**UNIVERSITY OF SOUTHAMPTON**

FACULTY OF ENGINEERING, SCIENCE AND MATHEMATICS

SCHOOL OF ELECTRONICS AND COMPUTER SCIENCE

# Near-Capacity Co-located and Distributed MIMO Systems

*by*

Lingkun Kong

*B.Eng., M.Eng.*

*A doctoral thesis submitted in partial fulfilment of*
*the requirements for the award of Doctor of Philosophy*
*at the University of Southampton*

October 2010

SUPERVISOR: *Prof. Lajos Hanzo*

FREng, FIEEE, FIET, DSc, Chair of Telecommunications

and *Dr. Soon Xin Ng*

PhD, SMIEEE, MIET

School of Electronics and Computer Science

University of Southampton

Southampton SO17 1BJ

United Kingdom

**This thesis is dedicated to**

my beloved parents, sister
and parents in law
for their love and support
and my lovely wife Dr. Xiaoli LI
for her tremendous patience, love and care
as well as our unborn baby
for the joy he/she brings to us · · ·

UNIVERSITY OF SOUTHAMPTON

ABSTRACT

FACULTY OF ENGINEERING, SCIENCE AND MATHEMATICS
SCHOOL OF ELECTRONICS AND COMPUTER SCIENCE

Doctor of Philosophy

**Near-Capacity Co-located and Distributed MIMO Systems**

by
Lingkun Kong

Space-time transmission based colocated and distributed Multiple-Input Multiple-Output (MIMO) systems are investigated. Generally speaking, there are two types of fundamental gains, when using multiple antennas in wireless communications systems: the multiplexing gain and the diversity gain. Spatial multiplexing techniques such as the Vertical Bell-labs LAyered Space-Time (V-BLAST) scheme exploit the associated multiplexing gain in terms of an increased bit rate, whereas spatial diversity techniques such as Space-Time Coding (STC) aim for achieving a diversity gain, which results in a reduced error rate. Firstly, we concentrate our attention on a novel space-time transmission scheme, namely on Generalized Multi-Layer Space-Time Codes (GMLST), which may be viewed as a composite of V-BLAST and STC, hence they provide both multiplexing and diversity gains. The basic decoding procedure conceived for our GMLST arrangement is a certain ordered successive decoding scheme, which combines group interference nulling and interference cancellation. We apply a specifically designed power allocation scheme, in order to avoid the overall system performance degradation in the case of equal power allocation. Furthermore, the optimal decoding order is found, in order to enhance the system's performance with the aid of the channel state information (CSI) at the receiver. However, our decoding scheme relying on power allocation or on the optimal decoding order does not take full advantage of the attainable receive antenna diversity. In order to make the most of this source of diversity, an iterative multistage Successive Interference Cancellation (SIC) detected GMLST scheme was proposed, which may achieve the full receive diversity after a number of iterations, while imposing only a fraction of the computational complexity of Maximum Likelihood (ML)-style joint detection.

Furthermore, for the sake of taking full advantage of the available colocated MIMO channel capacity, we present a low-complexity iteratively detected space-time transmission architecture based on GMLST codes and IRregular Convolutional Codes (IRCCs). The GMLST arrangement is serially concatenated with a Unity-Rate Code (URC) and an IRCC, which are used to facilitate near-capacity operation with the aid of an EXtrinsic

Information Transfer (EXIT) chart based design. Reduced-complexity iterative multi-stage SIC is employed in the GMLST decoder instead of the significantly more complex ML detection. For the sake of approaching the maximum attainable rate, iterative decoding is invoked to achieve decoding convergence by exchanging extrinsic information across the three serially concatenated component decoders. Finally, it is shown that the iteratively detected IRCC-URC-GMLST scheme using SIC strikes an attractive trade-off between the complexity imposed and the effective throughput attained, while achieving a near-capacity performance.

The above-mentioned advances were also exploited in the context of near-capacity communications in distributed MIMO systems. Specifically, we proposed an Irregular Cooperative Space-Time Coding (Ir-CSTC) scheme, which combines the benefits of Distributed Turbo Codes (DTC) and serially concatenated schemes. Firstly, a serial concatenated scheme comprising an IRCC, a recursive URC and a STC was designed for the conventional single-relay-aided network for employment at the source node. The IRCC is optimized with the aid of EXIT charts for the sake of achieving a near-error-free decoding at the relay node at a minimum source transmit power. During the relay's transmit period, another IRCC is amalgamated with a further STC, where the IRCC employed at the relay is further improved with the aid of a joint source-and-relay mode design procedure for the sake of approaching the relay channel's capacity. At the destination node, a novel three-stage iterative decoding scheme is constructed in order to achieve decoding convergence to an infinitesimally low Bit Error Ratio (BER) at channel Signal-to-Noise Ratios (SNRs) close to the relay channel's capacity. As a further contribution, an extended Ir-CSTC scheme is studied in the context of a twin-relay aided network, where a successive relaying protocol is employed. As a benefit, the factor two multiplexing loss of the single-relay-aided network - which is imposed by the creation of two-phase cooperation - is recovered by the successive relaying protocol with the aid of an additional relay. This technique is more practical than the creation of a full-duplex system, which is capable of transmitting and receiving at the same time. The generalized joint source-and-relay mode design procedure advocated relies on the proposed procedure of finding the optimal cooperative coding scheme, which performs close to the twin-relay-aided network's capacity. The corresponding simulation results verify that our proposed Ir-CSTC schemes are capable of near-capacity communications in both the single-relay-aided and the twin-relay-aided networks.

Having studied diverse noise-limited single-user systems, we finally investigate a multiuser space division multiple access (SDMA) uplink system designed for an interference-limited scenario, where the multiple access interference (MAI) significantly degrades the overall system performance. For the sake of supporting rank-deficient overloaded sys-

tems, a maximum signal-to-interference-plus-noise ratio (MaxSINR) based SIC multiuser detection (MUD) algorithm is proposed for the multiple-antenna aided multi-user SDMA system, which is capable of striking a trade-off between the interference suppression and noise enhancement. Furthermore, the multiuser SDMA system is combined with channel codes, which assist us in eliminating the typical error floors of rank-deficient systems. Referring to the Ir-CSTC scheme designed for the single-user scenario, relaying techniques are invoked in our channel-coded SDMA systems, which benefit from extra spatial diversity gains. In contrast to the single-user Ir-CSTC schemes, interference suppression is required at both the base station (BS) and the relaying mobile station (MS). Finally, a more practical scenario is considered where the MSs have spatially correlated transmit antennas. In contrast to the conventional views, our simulation results suggest that the spatial correlation experienced at the transmitter is potentially beneficial in multiuser SDMA uplink systems, provided that efficient MUDs are invoked.

# Acknowledgements

I would like to express my heartfelt gratitude to my first supervisor Professor Lajos Hanzo for his outstanding supervision and support throughout my research. His guidance, inspiration and encouragement have greatly benefited me; especially his generous investment of time and energy deserve my utmost acknowledgement. Most importantly, I would like to thank him for his invaluable friendship.

Moreover, I would like to cordially thank my second supervisor Dr. Soon Xin Ng (Michael). It would simply not have been possible to produce this thesis without his extremely generous and friendly support in helping me with the program debugging and engaging in intensive and inspiring discussions, especially in the beginning phase of my Ph.D career. I also wish sincerely to thank Michael for his friendship.

Many thanks also to my colleagues and the staff of the Communications Group, both past and present, for their support, help and discussions throughout my research. Special thanks to my colleagues Dr. Robert Maunder and Dr. Ronald Yee Siong Tee for their fruitful discussions as well as for their friendship. The financial support of the China-UK Scholarship Council, as well as that of the EPSRC UK, the EU under the auspices of the Optimix project is gratefully acknowledged.

Finally, I thank my dear parents, lovely sister and parents in law who have been providing me love and motivation. Last but not least, I want to thank my beloved wife Dr. Xiaoli LI who has been supporting me all the time.

# Declaration of Authorship

I, **Lingkun Kong**, declare that the thesis entitled

**Near-Capacity Co-located and Distributed MIMO Systems**

and the work presented in it are my own and has been generated by me as the result of my own original research. I confirm that:

1. This work was done wholly or mainly while in candidature for a research degree at this University;
2. Where any part of this thesis has previously been submitted for a degree or any other qualification at this University or any other institution, this has been clearly stated;
3. Where I have consulted the published work of others, this is always clearly attributed;
4. Where I have quoted from the work of others, the source is always given. With the exception of such quotations, this thesis is entirely my own work;
5. I have acknowledged all main sources of help;
6. Where the thesis is based on work done by myself jointly with others, I have made clear exactly what was done by others and what I have contributed myself;
7. Parts of this work have been published as: [69-80].

**Signed**:
**Date**: 18 October 2010

# List of Publications

## Journal Papers:

1. **Lingkun Kong**, Soon Xin Ng, Ronald Y. S. Tee, Robert G. Maunder and Lajos Hanzo, "Reduced-Complexity Near-Capacity Downlink Iteratively Decoded Generalized Multi-Layer Space-Time Coding Using Irregular Convolutional Codes", IEEE Transactions on Wireless Communications, vol. 9, no. 2, pp. 684-695, February 2010.

2. **Lingkun Kong**, Soon Xin Ng, Robert G. Maunder and Lajos Hanzo, "Maximum-Throughput Irregular Distributed Space-Time Code for Near-Capacity Cooperative Communications", IEEE Transactions on Vehicular Technology, vol. 59, no. 3, pp. 1511-1517, March 2010.

3. **Lingkun Kong**, Soon Xin Ng, Robert G. Maunder and Lajos Hanzo, "Near-Capacity Cooperative Space-Time Coding Employing Irregular Design and Successive Relaying", IEEE Transactions on Communications, vol. 58, no. 8, pp. 2232-2241, August 2010.

4. Li Wang, **Lingkun Kong**, Soon Xin Ng and Lajos Hanzo, "Code-Rate-Optimized Differentially Modulated Near-Capacity Cooperation", submitted to IEEE Transactions on Communications.

5. Shinya Sugiura, Soon Xin Ng, **Lingkun Kong**, Sheng Chen and Lajos Hanzo, "Multiple-Relay Aided Differential Distributed Turbo Coding for Asynchronous Cooperative Networks", submitted to IEEE Transactions on Vehicular Technology.

## Conference Papers:

1. **Lingkun Kong**, Soon Xin Ng and Lajos Hanzo, "Near-Capacity Three-Stage Downlink Iteratively Decoded Generalized Layered Space-Time Coding with Low Complexity", in Proceedings of IEEE Globecom'08, (New Orleans, LA, USA), pp. 1-6, 30 Nov.-04 Dec. 2008.

2. **Lingkun Kong**, Soon Xin Ng, Robert G. Maunder and Lajos Hanzo, "Irregular Distributed Space-Time Code Design for Near-Capacity Cooperative Communications", in Proceedings of IEEE VTC'09 Fall, (Anchorage, Alaska, USA), pp. 1-6, 20-23 Sept. 2009.

3. **Lingkun Kong**, Soon Xin Ng, Robert G. Maunder and Lajos Hanzo, "Successive Relaying Aided Near-Capacity Irregular Distributed Space-Time Coding", in Proceedings of IEEE Globecom'09, (Honolulu, Hawaii, USA), pp. 1-5, 30 Nov.-04 Dec. 2009.

4. Wei Liu, **Lingkun Kong**, Soon Xin Ng and Lajos Hanzo, "Near-Capacity Iteratively Decoded Markov-Chain Monte-Carlo Aided BLAST System", in Proceedings of IEEE Globecom'09, (Honolulu, Hawaii, USA), pp. 1-5, 30 Nov.-04 Dec. 2009.

5. Li Wang, **Lingkun Kong**, Soon Xin Ng and Lajos Hanzo, "To Cooperate or Not: A Capacity Perspective", in Proceedings of IEEE VTC'10 Spring, (Taipei, Taiwan), pp. 1-5, 16-19 May 2010.

6. Li Wang, **Lingkun Kong**, Soon Xin Ng and Lajos Hanzo, "A Near-Capacity Differentially Encoded Non-Coherent Adaptive Multiple-Symbol-Detection Aided Three-Stage Coded Scheme", in Proceedings of IEEE VTC'10 Spring, (Taipei, Taiwan), pp. 1-5, 16-19 May 2010.

7. Shinya Sugiura, Soon Xin Ng, **Lingkun Kong**, Sheng Chen and Lajos Hanzo, "Multiple-Relay Aided Distributed Turbo Coding Assisted Differential Unitary Space-Time Spreading for Asynchronous Cooperative Networks", in Proceedings of IEEE VTC'10 Spring, (Taipei, Taiwan), pp. 1-5, 16-19 May 2010.

# Contents

# List of Symbols

## General notation

- The superscript $^*$ is used to indicate complex conjugation. Therefore, $a^*$ represents the complex conjugate of the variable $a$.
- The superscript $^T$ is used to indicate matrix transpose operation. Therefore, $\mathbf{a}^T$ represents the transpose of the matrix $\mathbf{a}$.
- The superscript $^H$ is used to indicate complex conjugate transpose operation. Therefore, $\mathbf{a}^H$ represents the complex conjugate transpose of the matrix $\mathbf{a}$.
- The notation $\hat{x}$ represents the estimate of $x$.

## Special symbols

$A(.)$: The $a\ priori$ information.

$A_E$: Area beneath a specific EXIT curve.

$A_i$: Area beneath the inner decoder's EXIT curve.

$A_o$: Area beneath the inverted EXIT curve of the outer decoder.

$B$: The input information bit stream of the GMLST scheme.

$C$: The channel capacity in [bits/sym].

$\bar{C}$: The attainable DCMC capacity in [bits/sym].

$C_{eff}$: The *effective* throughput in [bits/sym].

$\mathbf{C}_j$: The *codeword* matrix of the $j$-th layer in the GMLST scheme.

$\mathbb{C}$: The complex space.

$c_k$: The transmitted symbol at instance $k$.

$c_o$: The coded bit stream of the outer encoder.

$d_{rd}$: The geometrical distance between the relay and destination.

$d_{sd}$: The geometrical distance between the source and destination.

$d_{sr}$: The geometrical distance between the source and relay.

$E(.)$: The $extrinsic$ information.

$E_b$: Bit energy.

$E_j$: The power level (in linear scale) assigned to group $j$ of the GMLST scheme.

$E_s$: Symbol energy.

$E[k]$: The expected value of $k$.

$G_{rd}$: The power gain of the relay-to-destination link.

$G_{sd}$: The power gain of the source-to-destination link.

$G_{sr}$: The power gain of the source-to-relay link.

$h_{i,j}$: The channel impulse response between the $i$-th transmit antenna and the $j$-th receive antenna.

$\mathbf{H}$: The channel matrix.

$\overline{\mathbf{H}}$: The spatially correlated MIMO channel matrix.

$\mathbf{I}$: The identity matrix.

$I_a$: The mutual information between the *a priori* LLR values and the corresponding bit stream.

$I_e$: The mutual information between the *extrinsic* LLR values and the corresponding bit stream.

$I_p$: The mutual information between the *a posteriori* LLR values and the corresponding bit stream.

$I^r$: The number of iterations at the relay.

$I_i^d$: The number of inner iterations at the destination.

$I_o^d$: The number of outer iterations at the destination.

$K$: The symbol intervals during a GMLST frame.

$L$: The time instances in a STBC *codeword* matrix / the number of SDMA users.

$L_a$: The *a priori* LLR values.

$L_e$: The *extrinsic* LLR values.

$L_p$: The *a posteriori* LLR values.

$L_r$: The transmission symbol periods from the relay node.

$L_s$: The transmission symbol periods from the source node.

$\mathcal{M}$: The modulation levels.

$M$: The number of possible GMLST(STBC) *codeword* matrix combinations / the number of receive antennas at the BS in the multi-user SDMA uplink.

$n_k$: AWGN added to the transmitted signal at instance $k$.

$N_0$: Single-sided power spectral density of white noise.

$N_d$: The number of antennas at the destination node.

$N_r$: The number of receive antennas / the number of antennas at the relay node.

$N_s$: The number of antennas at the source node.

$N_t$: The number of transmit antennas per user.

$P_{ab}$: The path loss between nodes $a$ and $b$.

$P(.)$: The probability.

$p(.)$: The probability density function.

$q$: The number of GMLST layers.

$R$: Coding rate.

$R_o$: Coding rate of the outer code.

$R_i$: Coding rate of the inner code.

$R_s$: Coding rate at the source node.

$R_r$: Coding rate at the relay node.

$\mathbf{R}_{BS}$: The spatial correlation matrix at the base station.

$\mathbf{R}_{MS}$: The spatial correlation matrix at the mobile station.

$\mathbf{R}_n$: The interference covariance matrix.

$\mathbf{R}_s$: The signal covariance matrix.

$S$: The switch of the MS's transmitter.

$T$: The signalling period.

$T(.)$: The extrinsic information transfer function.

$T^{-1}(.)$: The inverse extrinsic information transfer function.

$u_i$: The uncoded bit stream of the inner encoder.

$u_o$: The uncoded bit stream of the outer encoder.

$\mathbf{w}_i$: The linear maximum SINR filter.

$W$: The bandwidth in Hz.

$\mathbf{W}_k^j$: The nulling matrix at the $j$-th SIC decoding stage at instance $k$.

$\mathbf{W}_{LS}$: The LS-based MUD's weight matrix.

$\mathbf{W}_{MMSE}$: The MMSE-based MUD's weight matrix.

$y_k$: The received symbol at instance $k$.

$\alpha_i$: The $i$-th weighting coefficient of the IRCC.

$\alpha(\grave{s})$: The standard state metric values in the forward recursions in the BCJR algorithm.

$\beta_j$: The $j$-th weighting coefficient of the IRCC at the relay node.

$\beta_{MS}$: The MS antenna correlation coefficient.

$\beta(s)$: The standard state metric values in the backward recursions in the BCJR algorithm.

$\sigma^2$: The complex AWGN noise's variance.

$\lambda$: The ratio of the first time slot duration to the total frame duration in half-duplex relay systems.

$\lambda_i$: The SINR of the maximum SINR filter output.

$\eta$: The bandwidth efficiency in [bit/sec/Hz].

$\pi$: Temporal interleaver.

$\pi^{-1}$: Temporal deinterleaver.

$\pi_s$: Temporal interleaver at the source node.

$\pi_s^{-1}$: Temporal deinterleaver at the source node.

$\pi_r$: Temporal interleaver at the relay node.

$\pi_r^{-1}$: Temporal deinterleaver at the relay node.

$\Theta$: The linear maximum SINR array processor.

$\Psi_j$: Vector-based temporal interleaver.

$\Pi$: Spatial interleaver.

Chapter 1

# Introduction

## 1.1 Historical Perspective on Colocated Multiple-Antenna Communications

Since Shannon's 1948 milestone-paper [1], the design of high-speed, high-quality wireless communication systems has become the most important challenge for researchers in the field of digital communications. There are two key requirements for modern wireless systems, namely achieving a high bit rate and a low error rate. However, as Shannon detailed in [1], the channel capacity of conventional single-input single-output (SISO) systems is limited. Hence it is hard to meet the increasing demand for higher data rates and improved bit error ratio (BER) in wireless communications. Given a fixed bandwidth, there exists a trade-off between the bit rate and error rate of a digital communication system. We may readily improve one of them at the cost of sacrificing the other, but it is challenging to accomplish both of these objectives at the same time in conventional SISO systems.

As a remedy, the concept of multiple antennas was proposed, resulting in a multiple-input multiple-output (MIMO) system [2]. In these MIMO systems, the previously unexploited spatial domain was also capitalized on, in addition to the classic time and frequency domain. Recent information theoretical studies have shown that the capacity of a MIMO system [3–6] is higher than that of a SISO system. Hence, multiple-antenna aided techniques are capable of improving the bit rate and/or the error rate.

The benefits of multiple antennas in wireless communication systems are summarized in Fig. 1.1. Basically, two types of fundamental gains can be achieved by using multiple antennas in a wireless communication system: the multiplexing gain and the diversity gain. Spatial multiplexing techniques, such as the Bell-labs LAyered Space-

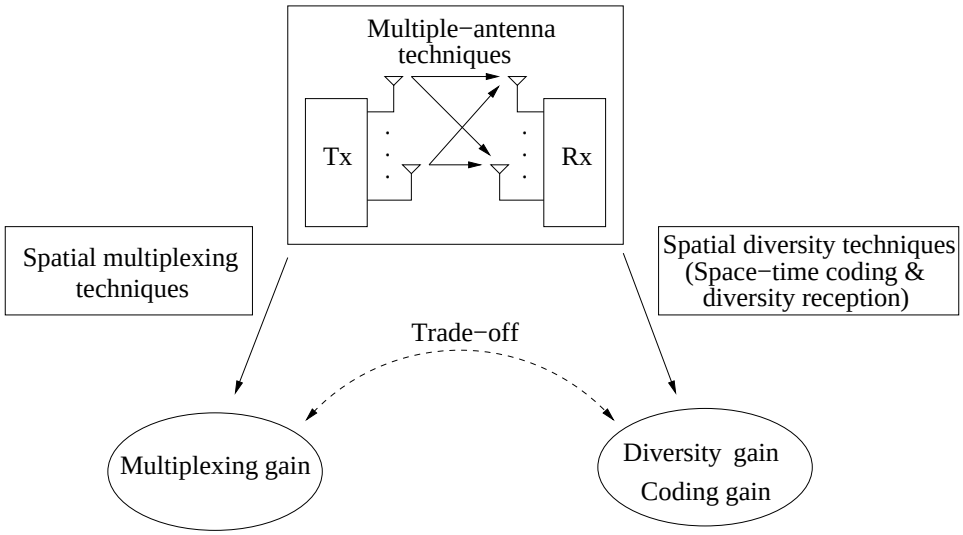


**Figure 1.1:** Benifits of multiple-antenna techniques for wireless communications.

Time (BLAST) architecture [7] aim for attaining a multiplexing gain, i.e., for an increased bit rate with respect to a single-antenna assisted system. In contrast to this, spatial diversity techniques such as space-time coding (STC) [8, 9] aim for achieving a diversity gain, which results in a reduced bit error rate. As shown in Fig. 1.1, there exists a potential trade-off between the spatial multiplexing and spatial diversity techniques. Hence we can design MIMO schemes, which are capable of striking a trade-off between the multiplexing and diversity gains [10, 11].

In the sequel, an overview of spatial multiplexing techniques, spatial diversity techniques and high-rate hybrid space-time techniques is provided. More details were presented in [12], for example.

**The Increased Bit Rate Potential of Spatial Multiplexing Techniques**

Spatial multiplexing techniques simultaneously transmit independent information sequences over multiple transmit antennas. Assuming that $n$ transmit and $m$ receive antennas are used, the overall bit rate is enhanced by a factor of $n$ compared to a single-antenna aided system, which is achieved without any bandwidth expansion or without extra transmission power. A well-known spatial multiplexing scheme is the BLAST arrangement [7]. For a single-antenna assisted system, given a fixed bandwidth, the channel capacity can only be increased upon increasing the transmit power. By contrast, for a MIMO system having $n$ transmit and $m$ receive antennas, it was shown in [3, 4, 7] that the capacity increases approximately linearly with the minimum of $n$ and $m$. This was unrealistic in the context of classic SISO schemes.

*Transmitter and Receiver Structure*

The idea of spatial multiplexing was first suggested in [13]. The basic principle of spatial multiplexing schemes is as follows. At the transmitter, the source information bit

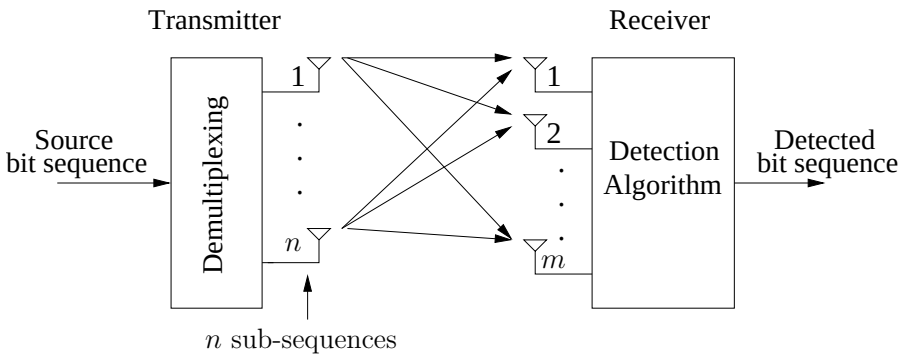


**Figure 1.2:** Basic principle of spatial multiplexing.

sequence is split into $n$ sub-sequences (demultiplexing). Then, these sub-sequences are modulated and transmitted simultaneously over the $n$ transmit antennas within the same frequency band. The received sequences are then detected by employing an interference cancellation algorithm. The basic architecture of a spatial multiplexing scheme is illustrated in Fig. 1.2.

Considering a frequency-flat fading channel scenario, there exist several optional detection algorithms for spatial multiplexing schemes. The optimum receiver based on the maximum-likelihood (ML) criterion performs an exhaustive search over all possible combinations of the $n$ transmitted symbols and opts for the most likely one as the transmitted symbol. The ML detector is capable of achieving the maximum attainable spatial diversity with respect to the number of receive antennas [14]. The major drawback of the ML detector is its high complexity, which increases exponentially with the number of transmit antennas and the number of bits per symbol of the modulation scheme employed. Owing to its potentially excessive complexity, the ML detector is often deemed impractical. For the BLAST scheme, an alternative detection strategy known as interference nulling (IN) and interference cancellation (IC) was proposed by Foschini *et al.* in [7, 15, 16]. In contrast to the ML detector, the $n$ sub-sequences, which are referred to as layers in BLAST systems, are detected successively layer by layer, instead of being detected jointly. The detection process consists of two steps: interference nulling and cancelling. During the nulling step, the BLAST detector first selects the specific layer having the largest post-suppression signal-to-noise ratio (SNR) and estimates the bits of that layer, while considering the interference imposed by all other layers to be zero, as in the linear zero-forcing (ZF) receiver [15, 17]. Alternatively, a linear minimum-mean-square-error (MMSE) receiver [18, 19] may be used during this phase, which avoids the noise-boosting of the ZF scheme. Then at the cancelling step, the influence of the just detected layer is subtracted from the composite multistream received signals. Based on the partially decontaminated received signals, interference nulling is performed once again, and the layer having the second highest post-suppression SNR is considered. This pro-

cedure is repeated, until all the $n$ layers are detected. This detection order is indeed the optimal one, as shown in [16]. It may also be observed that owing to the nulling operations, the number of receiver antennas $m$ must be at least equal to the number of transmit antennas $n$, i.e., we have $n \leq m$. Otherwise, the overall BER performance degrades dramatically [20]. As a matter of fact, the BER performance of the individual layers is typically different, which depends on the post-suppression SNR. In the case of low SNRs, error propagation effects arising from the previously detected layers may emerge. Hence, the specific layer detected first has the best performance. By contrast, the layers that are detected at a later stage have the advantage of a higher receive diversity order, since less interfering layers ought to be cancelled. Therefore, in the high SNR region, the layer detected last provides the best performance [21]. A more detailed performance analysis of BLAST systems was presented in [22].

*Channel Coded MIMOs*

In order to improve the performance of spatial multiplexing schemes, channel coding techniques may be introduced. Most spatial multiplexing schemes employ one-dimensional channel coding in the time domain [23]. This is in contrast to space-time coding techniques [8, 9], where two-dimensional coding is invoked in the context of both the time and spatial domains. Basically, there are three types of channel coding schemes utilized in conjunction with spatial multiplexing: horizontal coding, vertical coding and a combination of them. Horizontal coding implies that channel encoding is performed solely for individual layers after the demultiplexer of Fig. 1.2. The space-time $codeword$ associated with certain information bits is transmitted over the same antenna. At the receiver, channel decoding can be used separately for each layer after their detection. In the case of vertical coding, nonetheless, channel encoding is performed before the demultiplexer of Fig. 1.2, and the coded bits are demultiplexed and spread across the transmit antennas. Compared to horizontal coding, vertical coding offers an additional spatial diversity gain at the cost of an increased computational complexity in the process of joint decoding [12].

The combination of horizontal and vertical encoding for BLAST is referred to as diagonal coding [7]. Correspondingly, the original BLAST strategy is also known as diagonal BLAST (D-BLAST). As in the horizontal coding regime, channel encoding is performed separately for each layer of Fig. 1.2. Following this stage, a spatial block interleaver is employed in order to spread the coded bits from all layers across the time and antenna dimensions in a diagonal pattern. A comparative performance study of horizontal, vertical and diagonal space-time coding was presented in [23]. The BLAST system operating without any channel coding scheme was termed as the vertical BLAST (V-BLAST) in [15].

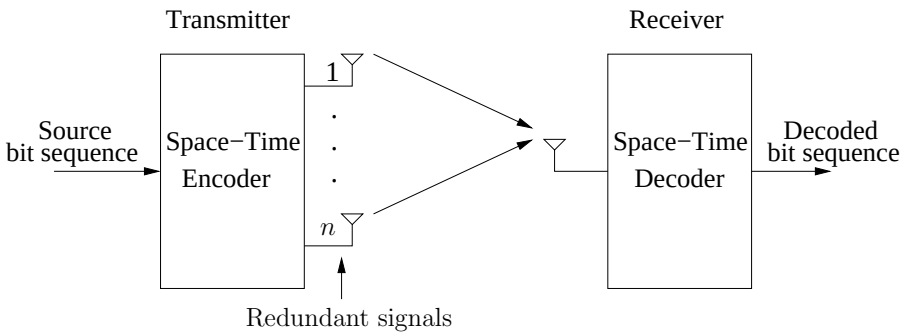


**Figure 1.3:** Basic principle of space-time coding.

### Reduced-BER Spatial Diversity Techniques

In contrast to spatial multiplexing techniques, which are capable of providing increased bit rates compared to a single-antenna system, spatial diversity techniques mainly aim for improving the BER performance. This can be achieved on the basis of attaining a diversity gain and a coding gain.

The basic philosophy of diversity is to exploit the random nature of radio propagation channels by finding more or less independently faded signalling branches for communication. If a specific propagating branch undergoes severe attenuation, other independent branches may have strong signals. A key parameter of diversity techniques is the maximum achievable diversity order, which is determined by the number of independent channel branches. The signals' error probability diminishes exponentially with the diversity order. Therefore, the attainable diversity order is one of the key performance indicators of fading channels. When considering a MIMO system having $n$ transmit and $m$ receive antennas for example, there are $mn$ independently fading spatial channels. Hence independently faded replicas of the same information can be transmitted. In this case, a maximum antenna diversity order of $mn$ may be achieved.

*Diversity Reception*

Diversity reception techniques are employed in systems having a single transmit and multiple receive antennas. For the sake of providing a diversity gain, they perform a linear combining of the individual received signals. In the case of frequency-flat fading, the optimum combining strategy is maximum ratio combining (MRC) [24], which is capable of maximizing the SNR at the combiner's output. There are several reduced-complexity suboptimal combining strategies in the literature, such as equal gain combining (EGC), where the fading effects imposed on the received signals are compensated by derotating the received signal according to the estimated inverted channel phases and then added up, or selective diversity (SD), where the received signal having the maximum instantaneous SNR is selected for detection regardless of all other received signals [24]. All three diversity combining techniques are capable of achieving the maximum attainable receive

antenna diversity order [25].

*Transmit Diversity and Space-Time Codes*

The main philosophy of transmit diversity is to provide a diversity or a coding gain by transmitting redundant signals over multiple transmit antennas. This is in contrast to spatial multiplexing, where independent bit sequences are transmitted. In transmit diversity aided systems, multiple antennas are only required at the transmitter, although multiple receive antennas can be utilized to further improve the attainable performance. In cellular networks, the downlink traffic is typically higher than the uplink traffic. When considering low cost and light weight mobile stations (MSs), it is more practicable to employ transmit diversity techniques at the base station (BS), where the size-limitation is less of problem.

The transmit diversity concept was first proposed in form of a low-complexity technique referred to as delay diversity [26,27]. However, the importance of transmit diversity was not recognized until Alamouti proposed a simple scheme for two transmit antennas in 1998 [8]. In the same year, Tarokh *et al*. invented space-time trellis codes (STTC) [9] which are regarded as two-dimensional coding schemes applied across both time slots and transmit antennas. These STTC schemes may be treated as a generalization of trellis coded modulation (TCM) [28, 29] to multiple transmit antennas. Compared to delay diversity and to Alamouti's scheme, which are only capable of providing a diversity gain, STTCs achieve both a diversity gain and a coding gain. Motivated by the concept of Alamouti's scheme, the novel family of orthogonal space-time block codes (OSTBC) was introduced in [30, 31] as a generalization of Alamouti's STBC scheme to more than two transmit antennas. Similarly to Alamouti's scheme, no additional coding gain is attained in OSTBC schemes. The basic structure of space-time coding schemes is illustrated in Fig. 1.3, where redundant signals are introduced in the encoder based on the specific space-time scheme considered.

**High-Rate Diversity-Oriented Space-Time Techniques**

We note that conventional space-time coding schemes, such as STTC and STBC achieve at most the same data rate as an uncoded single-antenna aided system. Their main objective is to improve the BER performance by offering a spatial diversity gain or a coding gain. Moreover, it is also possible to design increased-rate space-time techniques [10, 11, 32–35], which strike a compromise between the attainable spatial multiplexing and space-time coding gain.

More specifically, it was proposed in [10] to combine the STBC and V-BLAST techniques to provide both spatial diversity and multiplexing gains, where the antennas employed at the transmitter are partitioned into layers and each layer uses STBC. At the

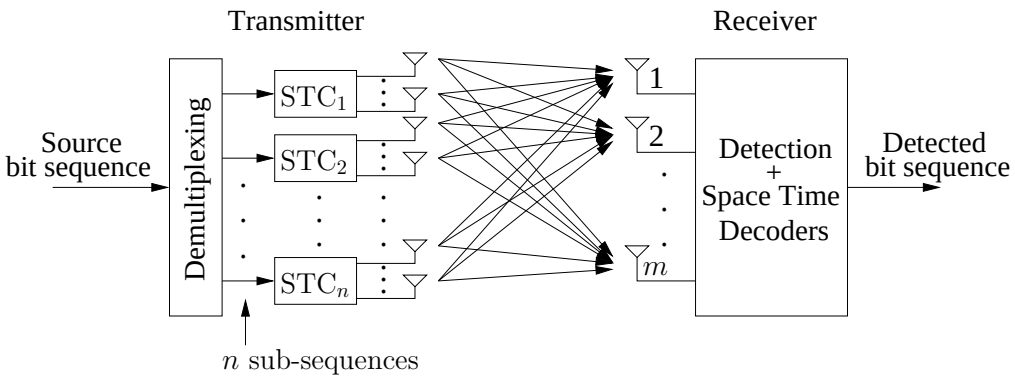


**Figure 1.4:** Basic principle of high-rate diversity-oriented space-time scheme.

receiver side, group-based successive interference cancellation (SIC) was employed before decoding the STBC signals of each layer. Compared to the pure V-BLAST scheme, an extra transmit diversity gain can be achieved by combining V-BLAST and STBC. On the other hand, the overall throughput is higher than that of pure STBC as a benefit of the independent symbol streams transmitted from different layers. In [36, 37], the STBC and interference cancellation arrangements were combined with code division multiple access (CDMA) for the sake of increasing the number of users supported by the system. Furthermore, [11] proposed a hybrid scheme combining V-BLAST with STTC schemes. Compared to the schemes of [10], extra coding gains were achieved by STTC scheme. An iterative SIC algorithm was also proposed in [11] for the sake of attaining the maximum attainable receive diversity gain for each layer of the combined scheme. The basic structure of these hybrid schemes is illustrated in Fig. 1.4.

## 1.2 Distributed Multiple-Antenna Aided Systems

In most publications on space-time coding and spatial multiplexing techniques, usually some restrictive assumptions are stipulated concerning the antenna spacing at the transmitter and receiver. It is typically assumed that the antenna spacing is sufficiently high, so as to justify the assumption of statistically independent fading on the individual transmission links. However, having a sufficiently high antenna spacing, which results in low spatial correlation cannot always be guaranteed in a practical system. The problem of correlation between the transmitted signals may be circumvented by introducing a new class of MIMOs, which are also referred to as distributed MIMOs in the context of cooperative communications [38, 39] (see Fig. 1.5 for an overview). The basic philosophy of cooperative communications can be traced back to the idea of the relay channel, which was introduced in 1971 by Van der Meulen [40]. Cover and El Gamal [41] characterised the relay channel from an information theoretic point of view. In [42] Sendonaris *et al.* generalised the conventional relay model, where there is a single source, a relay and a des-

tination, to multiple nodes that transmit their own data as well as serve as relays for each other. The scheme of [42] was referred to as "user cooperation diversity". Sendonaris *et al*. presented in [38, 39] a simple user-cooperation methodology based on the so-called Decode-and-Forward (DF) protocol using CDMA. In [43], Dohler *et al*. introduced the concept of Virtual Antenna Arrays (VAA) that emulates Alamouti's STBC for single-antenna-aided cooperating users. Space-time coded cooperative diversity protocols designed for exploiting the spatial diversity in a cooperative scenario were proposed in [44].

As a further advance, Hunter *et al*. [45] proposed the novel philosophy of coded cooperation aided schemes, which combine the idea of cooperation with classic channel coding methods. An extension of this coded cooperation framework was presented in [46], where the diversity gain of coded cooperation was increased with the aid of ideas borrowed from the area of space-time codes. Additionally, a turbo coded scheme was proposed in [46] in the framework of cooperative communications. Furthermore, the analysis of the performance benefits of channel codes in a coded cooperation aided scenario was performed in [47]. Laneman *et al*. [48] developed and analysed cooperative diversity protocols and compared the DF, Amplify-and-Forward (AF), selection based relaying and incremental relaying strategies. Furthermore, inspired by the classic turbo codes used in non-cooperative communication scenarios, Distributed Turbo Codes (DTC) [49] have been proposed for "distributed MIMO" systems, which benefit from a *turbo processing* gain. The idea of DTCs was further revisited in [50], where a three-component Distributed Turbo Trellis Coded Modulation (DTTCM) scheme has been proposed, which takes into consideration the realistic condition of having an imperfect source-to-relay communication link.

## 1.3 Iterative Detection and Near-Capacity Communications

Since Shannon's classic work in 1948 [1], the design of near-capacity communication systems has been one of the key problems for researchers in the area of coding. It was not until the discovery of turbo codes [51] that near-capacity systems employing simple constituent codes and efficient iterative decoding became a reality at a moderate complexity. Since then, the appealing iterative decoding of concatenated codes has inspired numerous researchers to extend the technique to other transmission schemes [52–54]. Specifically, the turbo principle was extended to multiple parallel concatenated codes in [52] and to serially concatenated codes in [53, 54]. Furthermore, the advent of turbo coding led to the "rediscovery" of Low Density Parity Check (LDPC) codes [55–57], which apply iterative decoding techniques to bipartite graphs [58] for the sake of facilitating near-capacity communications. Recently, irregular channel coding techniques [59–61] have been com-

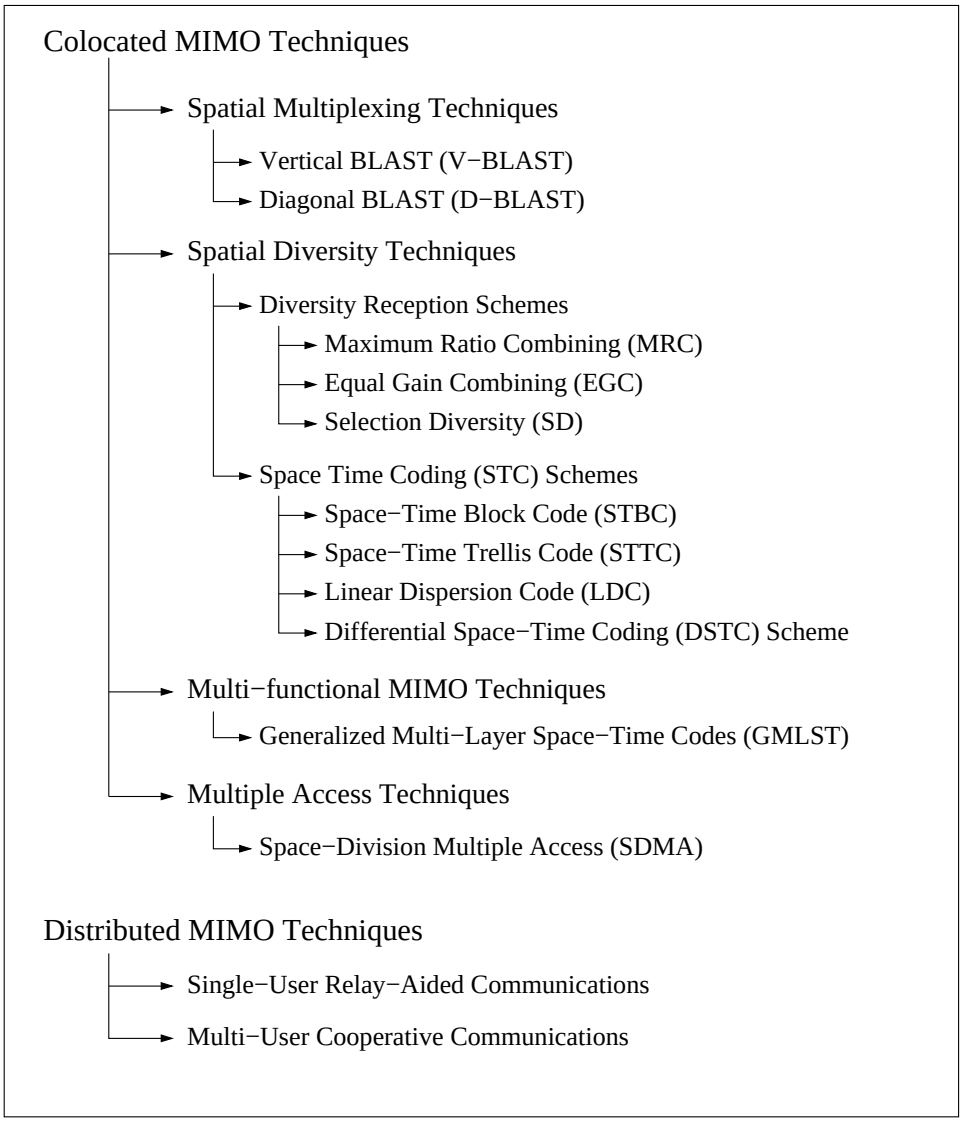


**Figure 1.5:** Classification of multiple-antenna techniques.

bined with iterative detection in order to enable near-capacity operation without imposing an excessive decoding complexity and latency. The serial concatenation and iterative decoding of an irregular outer code with a regular inner code was proposed by Tüchler and Hagenauer [61]. On the other hand, in analogy to classic turbo codes invoked in colocated MIMO systems, DTC [49] has been proposed for "distributed MIMO" systems for power-efficient cooperative communications. However, the original concept of DTC [49] fails to approach the corresponding relay channel's capacity. In [62] and [63], Zhang and Duman proposed several well-designed near-capacity turbo coding schemes for distributed MIMO systems, although the authors did not aim for finding the optimal coding schemes under different network configurations.

On the other hand, for the sake of analysing the iterative decoding process, in [64] ten Brink proposed the employment of the so-called EXtrinsic Information Transfer (EXIT)

chart to predict the convergence behaviour of iteratively decoded systems. The computation of EXIT charts was further simplified in [61] to a time averaging, when the Probability Density Functions (PDFs) of the information communicated between the input and output of the constituent decoders are both symmetric and consistent. A tutorial introduction to EXIT charts can be found in [65]. The concept of EXIT chart analysis has been extended to three-stage concatenated systems in [66–68]. In [61], the EXIT chart analysis was used to assist the process of irregular code design by employing a curve matching algorithm for the sake of "very-near-capacity" operation.

## 1.4 Outline of the Thesis

The outline of the thesis is presented below with reference to Fig. 1.6:

### 1.4.1 Chapter 2: Generalized Multi-Layer Space-Time Codes

In this chapter, a novel space-time transmission scheme, namely the concept of Generalized Multi-Layer Space-Time Codes (GMLST), is introduced. This scheme may be treated as a composite of V-BLAST and STC, in which the two fundamental schemes of horizontal GMLST (H-GMLST) and diagonal GMLST (D-GMLST) are included according to different symbol-to-antenna mapping schemes. We first discuss an appropriately ordered successive decoding procedure which combines group interference nulling and interference cancellation. The issues of power allocation and optimal decoding order are considered, in order to enhance the system's performance. Finally, an iterative multistage successive interference cancellation aided GMLST scheme is designed.

### 1.4.2 Chapter 3: Near-Capacity Iteratively-Decoded Generalized Multi-Layer Space-Time Codes

This chapter presents a low complexity iteratively detected space-time transmission architecture based on GMLST codes and IRregular Convolutional Codes (IRCCs). The GMLST is serially concatenated with a Unity-Rate Code (URC) and an IRCC which are used to facilitate near-capacity operation with the aid of an EXIT chart based design. Reduced-complexity iterative multistage successive interference cancellation is employed in the GMLST decoder, instead of the significantly more complex maximum likelihood detection. For the sake of approaching the maximum attainable rate, iterative decoding is invoked to achieve decoding convergence by exchanging extrinsic information across the three serial component decoders. Finally, it is shown that the SIC-based iteratively de-

tected IRCC-URC-GMLST system is capable of providing an attractive trade-off between the affordable computational complexity and the achievable system throughput.

### 1.4.3 Chapter 4: Irregular Cooperative Space-Time Coding Schemes

In this chapter, we firstly propose an Irregular Cooperative Space-Time Coding (Ir-CSTC) scheme designed for near-capacity communications in the conventional single-relay-aided network. The Discrete-input Continuous-output Memoryless Channel (DCMC) [14] capacity formula of Alamouti's STBC scheme for the two-hop single-relay-aided network is derived. At the source node, a serial concatenated scheme comprising an IRCC, a recursive URC and a STBC was designed for the sake of approaching the corresponding source-to-relay link capacity, where the IRCC was optimized with the aid of EXIT charts. At the relay node, another IRCC is concatenated serially with an identical STBC. The relay's IRCC is re-optimized based on EXIT chart analysis for the sake of approaching the relay channel's capacity, before transmitting the relayed information. It is demonstrated that the topology of the Ir-CSTC system coincides with that of a DTC. At the destination node, a novel three-stage iterative decoding scheme is constructed in order to achieve decoding convergence to an infinitesimally low BER. The corresponding simulation results show that our joint source-and-relay mode design based on EXIT chart analysis is capable of near-capacity communications in the single-relay-aided network.

Furthermore, an extended Ir-CSTC scheme is studied in the context of a twin-relay aided network, in which the successive relaying protocol is employed. The factor two multiplexing loss in the single-relay-aided network is recovered by the successive relaying protocol employed in conjunction with an additional relay. Tight upper and lower bounds of the successive relaying channel's capacity are given. The distributed codes employed at both the source and relays are jointly designed with the aid of EXIT charts for the sake of high-integrity operation at SNRs close to the corresponding twin-relay channel's capacity. Finally, it is shown that the extended Ir-CSTC scheme is still capable of near-capacity cooperative communications in the twin-relay aided network, while maintaining the same spectrum efficiency as the direct transmission.

### 1.4.4 Chapter 5: Relay-Assisted Multiple-Antenna Aided Multi-User SDMA Uplink

In this chapter, we investigate a multiuser space division multiple access (SDMA) uplink system in an interference-limited scenario, where the multiple access interference (MAI) imposed significantly degrades the overall system performance. For the sake of support-

ing rank-deficient systems, a maximum signal-to-interference-plus-noise ratio (MaxSINR) based SIC multiuser detection (MUD) algorithm is proposed for the multiple-antenna aided multi-user SDMA system, which strikes a trade-off between the interference suppression attained and noise enhancement imposed. Furthermore, the multiuser SDMA system is combined with channel codes, which eliminates the error floors encountered in rank-deficient systems. Referring to the Ir-CSTC scheme of Chapter 4 designed for the single-user scenario, relay techniques are incorporated in our channel-coded SDMA systems, which will benefit from extra spatial diversity and reduced-pathloss based geometrical gains. In contrast to the single-user Ir-CSTC schemes, interference suppression is required at both the base station (BS) and the relaying mobile station (MS). Finally, a more practical scenario is considered where the MSs have spatially correlated transmit antennas. In contrast to the conventional views, our simulation results show that the transmitter's spatial correlation is potentially beneficial in the multiuser SDMA uplink, when employing efficient MUDs.

### 1.4.5 Chapter 6: Conclusions and Future Work

This chapter summarises the main findings and contributions of each chapter and proposes some future research ideas.

## 1.5 Novel Contributions

The dissertation is based on the publications and manuscript submissions of [69–80]. The novel contributions of this thesis are summarized as follows:

1. In Chapter 2, we propose a GMLST code, which is a sophisticated multi-functional composite of the V-BLAST and STC arrangements, designed for the sake of striking an attractive trade-off between the multiplexing gain and diversity gain. Furthermore, in order to achieve the maximum attainable receive diversity gain, a novel low-complexity iterative multi-stage SIC scheme is designed, while imposing only a fraction of the ML's complexity [69].

2. In Chapter 3, the DCMC [14] capacity formula of GMLST schemes using STBC components is derived [76] and based on the area property of EXIT charts, the maximum achievable rates of various iterative multi-stage SIC and ML based GMLST schemes are obtained. Furthermore, an iteratively decoded near-capacity serially concatenated IRCC-URC-GMLST scheme is designed employing EXIT charts. On the other hand, in order to enhance the attainable performance, we redesign the

original IRCCs of Tüchler and Hagenauer [61,81], invoking more component codes in order to match the inner codes' EXIT functions more accurately. The computational complexity of this concatenated scheme is substantially reduced at the cost of a modest reduction in the maximum achievable rate compared to that of ML detection.

3. In Chapter 4, we propose near-capacity Ir-CSTC schemes for both the single-relay-aided [70,77] and twin-relay based successive relaying aided systems [71,78] using the proposed joint source-and-relay mode design procedures. The theoretical lower and upper bounds on the capacity of both the single-relay and successive-relaying channels are derived. More particularly, the single-relay-aided system's effective throughput is maximized as a benefit of the proposed design procedure [77], while the transmission efficiency of classic direct transmission is achieved by our twin-relay-aided system, when employing the successive relaying protocol of [78]. It is demonstrated that our joint source-and-relay mode design procedure is capable of finding the optimal near-capacity cooperative coding scheme in arbitrary relay network configurations in both single-relay-aided and twin-relay-aided networks.

4. In Chapter 5, the Ir-CSTC schemes of Chapter 4 are investigated in the context of an interference-limited multiuser SDMA scenario. In contrast to the noise-limited single-user scenario of Chapter 4, interference suppression is performed at both the base station and the relaying mobile station. Specifically, a MaxSINR-based SIC multiuser detector is proposed for the multiple-antenna aided multi-user SDMA uplink, which is capable of appropriately balancing the interference suppression attained and the noise enhancement tolerated, while supporting rank-deficient systems. In addition, the effects of the spatial antenna correlation of MS transmitters on the average system BER are studied in the context of multiuser scenarios.

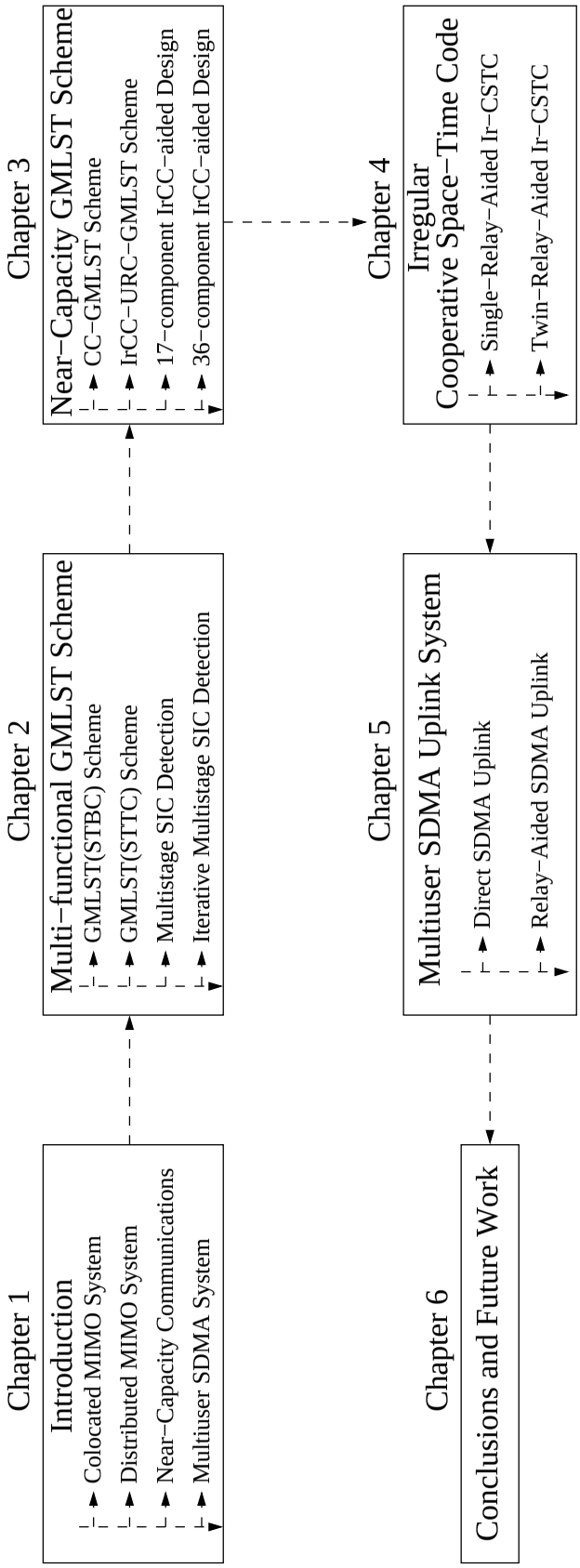


**Figure 1.6:** Thesis outline.

Chapter 2

# Generalized Multi-Layer Space-Time Codes

## 2.1 Introduction

Recent information theoretic studies have shown that the capacity of a Multiple-Input Multiple-Output (MIMO) system [3–6] is significantly higher than that of a Single-Input Single-Output (SISO) system. As mentioned in Chapter 1, there are two types of fundamental gains obtained by MIMO systems [2, 12, 82], namely the multiplexing gain and the diversity gain. In [16], Wolniansky *et al.* proposed the popular multi-layer MIMO structure, referred to as the Vertical Bell-labs LAyered Space-Time (V-BLAST) scheme, which is capable of increasing the achievable throughput without any increase in the system's bandwidth by mapping the information to be transmitted to multiple antennas. Although it was primarily designed for attaining transmit multiplexing gain, it is worth noting that upon increasing the number of antennas, typically the achievable transmit diversity gain also increases at the cost of an increased receiver complexity.

In contrast to spatial multiplexing techniques [7, 15, 16], Alamouti [8] discovered a transmit diversity scheme, referred to as a Space-Time Block Code (STBC), where the prime concern was achieving a diversity gain. The attractive benefits of Alamouti's design motivated Tarokh *et al.* [30, 31] to generalize Alamouti's scheme to an arbitrary number of transmit antennas. Another transmit diversity scheme, referred to as Space-Time Trellis Coding (STTC) was invented by Tarokh *et al.* in [9, 83], which is capable of achieving both spatial diversity gain and coding gain or time diversity gain. However, these conventional STBC and STTC schemes achieve at most the same data rate as an uncoded single-antenna system. Hence, a MIMO scheme attaining both multiplexing gain and diversity gain is attractive [82]. Various hybrid BLAST and STTC schemes have

been proposed in [10, 11]. A Generalized Multi-Layer Space-Time (GMLST) code may be constructed as a composite of the V-BLAST scheme and Space-Time Coding (STC), which strikes a flexible trade-off between the throughput and error probability attained.

The framework of the GMLST scheme is specified as follows. At the transmitter, the set of available antennas is divided into several groups and each group utilizes space-time coding as the component code. At the receiver, in order to avoid the potentially excessive complexity of all-group being joint detected (JD), as in the V-BLAST detection algorithm [15, 16], the space-time code of each individual group is processed successively beneficially, combining interference nulling and interference cancellation on a group-by-group basis, as detailed later in this chapter. Therefore, as mentioned above, the GMLST may be viewed as a beneficial combination of V-BLAST and STC, where the space-time codes employed achieve a higher spatial diversity than pure V-BLAST. As a further benefit, the overall system throughput is significantly higher than that of STC systems due to the multiplexing gain of BLAST. We can also see similar architectures in [10] and [18], where space-time trellis codes and space-time block codes were combined with V-BLAST, respectively. Furthermore, according to Tarokh's power allocation algorithm [10], two different signal-to-antenna mappings and an optimal detection order may be introduced to improve the overall system performance. Nevertheless, due to the constraints of BLAST-like detection, the maximum attainable receive diversity cannot be readily achieved with the aid of a serial detection scheme. Hence, in [11], iterative multistage Successive Interference Cancellation (SIC) was proposed in order to achieve the maximum receive diversity, attainable by classic Maximum Likelihood (ML) detection, while imposing only a fraction of the ML complexity.

*Against this backcloth, the novelty and rationale of this chapter may be summarized as follows:*

1. *We propose a Generalized Multi-Layer Space-Time (GMLST) code, which is regarded as a sophisticated multi-functional composite of the V-BLAST and Space-Time Coding (STC), for the sake of striking an attractive trade-off between the multiplexing gain and diversity gain. Hence, flexibility between the full-multiplexing and the full-diversity oriented system benefits is attained*

2. *A novel low-complexity iterative multi-stage Successive Interference Cancellation (SIC) scheme is designed, in order to achieve the maximum attainable receive diversity of the potentially excessive-complexity classic ML detection, while imposing only a fraction of the ML complexity.*

The rest of the chapter is organized as follows. In Section 2.2, an overview of the GMLST coding architecture is presented, where we assume that the wireless MIMO

channels we are using in this chapter are independently frequency non-selective Rayleigh fading channels. The encoding process of the GMLST schemes using STTC and STBC as the component STCs is detailed in Section 2.2.1 and Section 2.2.2, respectively. Furthermore, we introduce the multistage SIC-based detection of GMLST schemes in Section 2.3. Tarokh's power allocation scheme and the optimal detection ordering procedure are highlighted in Section 2.4 and Section 2.5, respectively. Finally, we specify the proposed iterative multistage SIC detection scheme in Section 2.6 and present our conclusions in Section 2.7.

## 2.2 GMLST Transmitter Architecture

Consider now a point-to-point wireless communication link equipped with $N_t$ transmit and $N_r$ receive antennas, where the signal to be transmitted over the $j$-th antenna at time instant $k$ is denoted by $c_k^j$. In this chapter, we consider transmissions over a non-dispersive Rayleigh fading channel. Therefore, the signal received by each antenna is constituted by the superposition of independently Rayleigh faded transmitted signals. The signal received by the $i$-th antenna at time instant $k$ is given by

$$y_k^i = \sum_{j=1}^{N_t} h_{i,j} c_k^j + n_k^i, \tag{2.1}$$

where $h_{i,j}$ is the complex-valued channel coefficient between the $j$-th transmit and the $i$-th receive antenna, which is modeled by the samples of independent complex Gaussian random variables having a zero mean and a variance of 0.5 per dimension. Furthermore, $n_k^i$ is the Additive White Gaussian Noise (AWGN) encountered by the $i$-th antenna at time instant $k$ and modeled by the samples of independent complex Gaussian random variables having a zero mean and a variance of $N_0/2$ per dimension.

Let us define $\mathbf{y}_k$, $\mathbf{c}_k$ and $\mathbf{n}_k$ as

$$\mathbf{y}_k = [y_k^1, y_k^2, \ldots, y_k^{N_r}]^T,$$

$$\mathbf{c}_k = [c_k^1, c_k^2, \ldots, c_k^{N_t}]^T,$$

and

$$\mathbf{n}_k = [n_k^1, n_k^2, \ldots, n_k^{N_r}]^T,$$

respectively. Then the channel model of Eq. (2.1) may be expressed using a more compact matrix notation as

$$\mathbf{y}_k = \mathbf{H}\mathbf{c}_k + \mathbf{n}_k, \tag{2.2}$$

where $\mathbf{H}$ is the $(N_r \times N_t)$-element channel matrix, which has the $(i,j)$-th entry $[\mathbf{H}]_{i,j} = h_{i,j}$. In this chapter, we consider quasi-static flat fading channels, assuming that the channel coefficients remain unchanged within a transmission frame of $K$ symbol intervals and are faded between frames randomly. Furthermore, we assume that the channel coefficients are perfectly estimated at the receiver, unless specified otherwise.

### 2.2.1 GMLST Transmitter Using STTCs

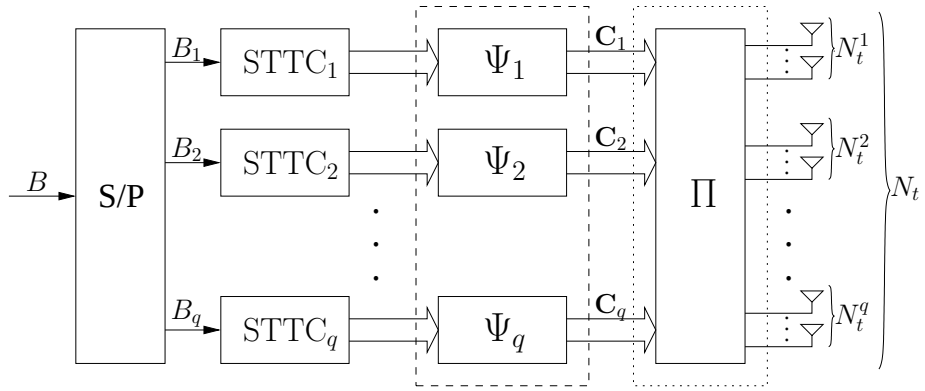


(a) The GMLST(STTC) transmitter architecture, where "$\Psi_j$" indicates a vector-based temporal interleaver and "$\Pi$" denotes the spatial interleaver

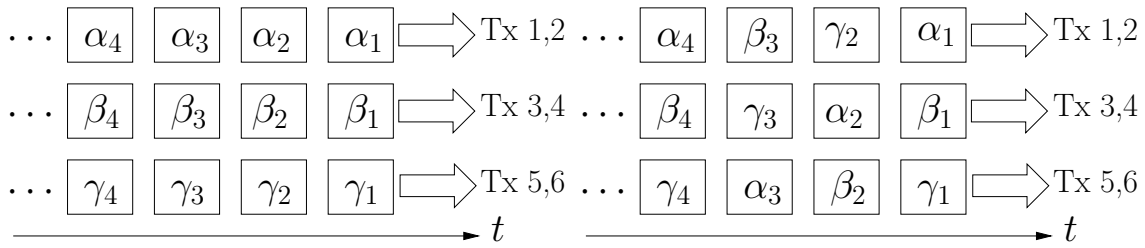


(b) H-GMLST (c) D-GMLST

**Figure 2.1:** Transmitter of the GMLST(STTC) architecture.

The encoding process of the GMLST coding schemes employing STTC [9] as the component STCs, which we refer to as the GMLST(STTC) arrangement, is illustrated in Fig. 2.1. We assume that a block of $B$ information bits is input to a serial-to-parallel (S/P) converter, which partitions this bit stream into $q$ groups, referred to as layers having lengths of $B_1, B_2, \ldots, B_q$, where we have $B_1 + B_2 +, \ldots, +B_q = B$ bits in total. Then, each group of $B_j$ bits, for $1 \leq j \leq q$, is separately encoded in Fig. 2.1(a) by a component encoder $STC_j$ associated with $N_t^j$ number of transmit antennas, where we have $N_t^1 + N_t^2 +, \ldots, +N_t^q = N_t$. The resultant $(N_t^j \times K)$-element *codeword* matrix $\mathbf{C}_j$ of $STTC_j$ will be transmitted by the $N_t^j$ transmit antennas of group $j$ of Fig. 2.1(a) during

$K$ symbol intervals. We refer to the $k$th column $\mathbf{c}_{j,k}$ of $\mathbf{C}_j$ as the *symbol vector* generated by group $j$ at time instant $k$. Following space-time encoding, the symbol vectors of each group are passed through an independent vector-based temporal interleaver $\Psi_j$. The vector-based temporal interleavers $\Psi_j$ represented by the dashed block of Fig. 2.1(a) are used for the *codewords* generated by the different groups, for the sake of eliminating the effects of bursty error propagation among the different groups during the detection iterations [11]. Furthermore, the spatial interleaver $\Pi$ represented by the dotted block of Fig. 2.1(a) may be considered to be a mapping of the space-time encoded *symbol vectors* to a certain group of transmit antennas, which provides additional spatial diversity. Two specific mapping schemes were considered in [11], namely, horizontal and diagonal mapping, which are shown in Fig. 2.1(b) and 2.1(c), respectively.

The philosophy of the horizontal mapping of Fig. 2.1(b) is that of passing all *symbol vectors* from one group to the corresponding group of transmit antennas. A simple example is seen in Fig. 2.1(b), where $\alpha_k$, $\beta_k$ and $\gamma_k$, with $k = 1, 2, \ldots$, represent the *symbol vectors* of three different groups and each group is mapped to two transmit antennas. Thus, the transmitted *symbol vectors* from one of the groups generate a horizontal pattern of mapping, which is referred to as the H-GMLST scheme in Fig. 2.1(b) of this chapter. By contrast, in the diagonal mapping, the *symbol vectors* from each group are cyclically mapped to all available groups of antennas for each different symbol interval with a period of $p$. We present a simple example in Fig. 2.1(c) in conjunction with $p = q = 3$, where again, $q$ is the number of groups. Observe in Fig. 2.1(c) that the transmitted *symbol vectors* originating from every group are allocated across the space (antennas) and time dimensions in a diagonal pattern. Hence we may refer to this scheme as GMLST with diagonal allocation (D-GMLST). Compared to the H-GMLST arrangement of Fig. 2.1(b), an additional spatial diversity can be attained by the D-GMLST scheme, since the *symbol vectors* of each group are periodically mapped to independently fading channels. This additional spatial diversity results in an improved performance for the D-GMLST, as we will demonstrate in Section 2.3.2. Note that in [84,85] zero-padding was recommended at both the beginning and end of each transmission frame for the diagonal mapping, therefore the overall transmission efficiency was decreased to a degree, depending on the length of the transmission frame.

### 2.2.2 GMLST Transmitter Using STBCs

Fig. 2.2 illustrates the GMLST transmitter scheme employing STBCs [8, 30, 31] as the component STCs, which we refer to as the GMLST(STBC) arrangement. It is noted that when STBCs are employed as the components, the vector-based temporal interleavers

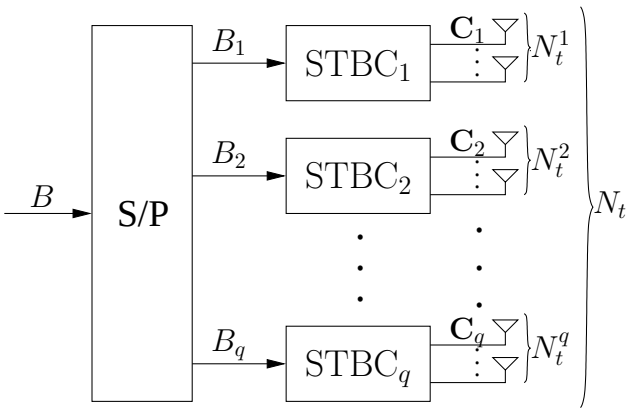


**Figure 2.2:** GMLST(STBC) transmitter architecture, where neither temporal nor spatial interleavers are needed.

in Fig. 2.1(a) are no longer employed, because they would destroy the structure of the STBC *codeword* matrix and would be of no use in eliminating the effects of bursty error propagation, since the different STBC *codeword* matrices are independent in a specific group. Furthermore, only the horizontal mapping scheme of Fig. 2.1(b) is considered in Fig. 2.2, since no additional spatial diversity can be achieved, while employing the diagonal mapping of Fig. 2.1(c) in the GMLST(STBC) schemes.

## 2.3 Multistage SIC Detection

Let us now rewrite Eq. (2.2) as:

$$\mathbf{y}_k = \mathbf{H}_{1,k}\mathbf{c}_{1,k} + \mathbf{H}_{2,k}\mathbf{c}_{2,k} + \cdots + \mathbf{H}_{q,k}\mathbf{c}_{q,k} + \mathbf{n}_k, \quad 1 \leq k \leq K, \tag{2.3}$$

where $\mathbf{H}_{j,k}$ denotes the $(N_r \times N_t^j)$-element subchannel matrix of group $j$ at time instant $k$, while $\mathbf{c}_{j,k} = [c_k^{N_t^1+\cdots N_t^{j-1}+1}, \ldots, c_k^{N_t^1+\cdots N_t^{j-1}+N_t^j}]^T$ is the the $k$th column of the *codeword* matrix $\mathbf{C}_j$ and $\mathbf{n}_k$ is the $N_r$-element complex-valued additive white Gaussian noise vector.

For the sake of maintaining an affordable computational complexity, a reduced complexity Successive Interference Cancellation (SIC) based detection scheme was proposed in [11] instead of ML detection. In order to maintain a low complexity, the signals are detected layer-by-layer in a multistage manner, instead of high-complexity ML-style joint-detection. In the spirit of the V-BLAST scheme [7], the detection order of the SIC-based scheme has a significant effect on the achievable performance of the GMLST system. The optimal successive detection order of GMLST systems will be discussed in Section 2.5. In this subsection, we assume that the detection order of Fig. 2.3(a) was already determined and without loss of generality we assume the natural detection order of $\{1', 2', \ldots, q'\}$.

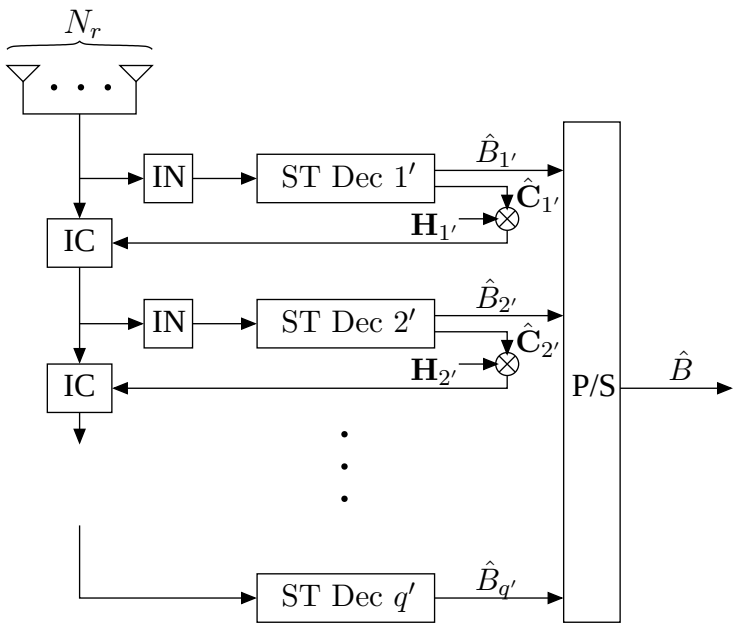


(a) main block diagram of the multistage SIC detection, where "IN" denotes the interference nulling module and "IC" indicates the interference cancellation module

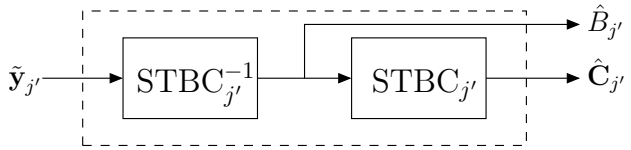


(b) sub-block diagram for the "ST Dec $j'$" component using STBC, where "$\text{STBC}_{j'}^{-1}$" denotes the $j'$-th linear STBC decoder and "$\text{STBC}_{j'}$" indicates the corresponding STBC recoder

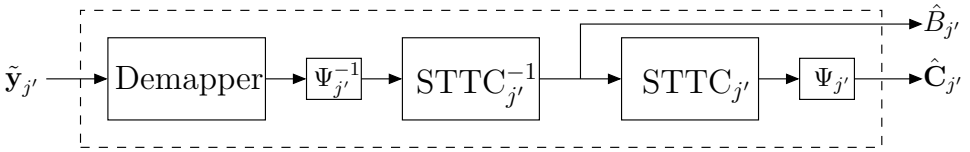


(c) sub-block diagram for the "ST Dec $j'$" component using STTC, where "$\text{STTC}_{j'}^{-1}$" denotes the $j'$-th STTC Viterbi decoder and "$\text{STTC}_{j'}$" indicates the corresponding STTC recoder

**Figure 2.3:** Multistage SIC detection in the GMLST STTC and STBC schemes.

Let us now present the SIC-based detection algorithm as follows.

During the first detection stage ($j = 1$), we let $\mathbf{y}_k^1 = \mathbf{y}_k$, for all $1 \leq k \leq K$.

During the $j$-th detection stage, given that the previous $(j-1)$ groups $1', 2', \ldots, (j-1)'$ have already been detected and their effects have been cancelled from the received signals, the resultant received signal $\mathbf{y}_k^j$ for $k = 1, \ldots, K$, which still contains the interference imposed by the 'not-yet-decoded' groups of $(j+1)', (j+2)', \ldots, q'$, can now be written as

$$\mathbf{y}_k^j = \mathbf{H}_{j',k}\mathbf{c}_{j',k} + \mathbf{H}_{(j+1)',k}\mathbf{c}_{(j+1)',k} + \cdots + \mathbf{H}_{q',k}\mathbf{c}_{q',k} + \mathbf{n}_k^j. \tag{2.4}$$

Then at the time instant $k$, we can find a set of orthonormal column vectors (not necessarily unique) in the null space of $[\mathbf{H}_{(j+1)',k}, \ldots, \mathbf{H}_{q',k}]^T$, and amalgamate their transposes into an $[(N_r - N_t + N_t^{1'} + \cdots + N_t^{j'}) \times N_r]$-element nulling matrix $\mathbf{W}_k^{j\,1}$ based on zero-forcing (ZF)[2]. Then, let both sides of Eq. (2.4) be left-multiplied by $\mathbf{W}_k^j$, which suppresses all the interfering signals imposed by the groups $(j+1)'$ to $q'$ and generates the interference-free equivalent 'sliced' signal of group $j'$

$$\tilde{\mathbf{y}}_k^j = \mathbf{W}_k^j \mathbf{y}_k^j = \mathbf{W}_k^j \mathbf{H}_{j',k} \mathbf{c}_{j',k} + 0 + \mathbf{W}_k^j \mathbf{n}_k^j = \tilde{\mathbf{H}}_{j',k} \mathbf{c}_{j',k} + \tilde{\mathbf{n}}_k^j. \tag{2.5}$$

We can see in Eq. (2.5) that $\tilde{\mathbf{H}}_{j',k}$ is the equivalent channel matrix having $(N_r - N_t + N_t^{1'} + \cdots + N_t^{j'}) \times N_t^{j'}$ elements at time instant $k$ for group $j'$, which has the same statistical properties as $\mathbf{H}_{j',k}$ due to the orthonormalizing effect of $\mathbf{W}_k^j$, i.e., the entries of $\tilde{\mathbf{H}}_{j',k}$ are independent and identically complex Gaussian distributed with a zero mean and a variance of 0.5 per dimension, as mentioned in Section 2.2. Assuming that perfect interference cancellation is achieved, the resultant noise vector $\tilde{\mathbf{n}}_k^j$ also contains independent and identically complex Gaussian distributed entries with mean of zero and variance of $N_0/2$ per dimension [10].

As for the nulling matrix $\mathbf{W}_k^j$, we have $\mathbf{W}_k^j = \mathbf{W}^j$ for all $1 \leq k \leq K$ in the case of the H-GMLST scheme of Fig. 2.1(b) as the channel 'seen' by each group is time-invariant in each transmission frame, since we assumed communications over a quasi-static Rayleigh fading channel. This implies that the nulling matrix only has to be calculated once for each frame. Otherwise, in the D-GMLST scheme of Fig. 2.1(c), we have $\mathbf{W}_k^j = \mathbf{W}_{k \bmod p}^j$ by each group varies with a period of $p$. Therefore, a total number of $p$ nulling matrices are required for each frame. Based on Eq. (2.5), the $j'$-layer *codeword*, which is denoted by $\hat{\mathbf{C}}_{j'}$ can be decoded using the ML space-time decoders of Fig. 2.3, which correspond to the Viterbi decoder [89] or simple linear processing [8] for space-time trellis codes and space-time block codes, respectively. Prior to moving on to the next detection stage, interference cancellation is carried out according to Fig. 2.3(a) by subtracting the contribution of the 'just-detected' group $j'$ from $\mathbf{y}_k^j$, which results in the 'partially decontaminated' received signal $\mathbf{y}_k^{j+1}$

$$\mathbf{y}_k^{j+1} = \mathbf{y}_k^j - \mathbf{H}_{j',k} \hat{\mathbf{c}}_{j',k}, \quad 1 \leq k \leq K, \tag{2.6}$$

where $\hat{\mathbf{c}}_{j',k}$ is the $k$th column of $\hat{\mathbf{C}}_{j'}$. Then the above procedure of Fig. 2.3 is repeated for $j = j+1$, until all groups are detected ($j = q$).

[1] The computation of the nulling matrix $\mathbf{W}_k^j$ is described in the Appendix.

[2] A more powerful Maximum Signal-to-Noise Ratio array processing algorithm was presented in [86–88].

### 2.3.1 Soft SIC Detection

In order to reduce the detrimental effects of error propagation, soft interference cancellation can be invoked, which means that instead of using the hard decisions $\hat{\mathbf{c}}_{j',k}$ in Eq. (2.6), the expectation value

$$\tilde{c}^i_{j',k} = \sum_{m=1}^{\mathcal{M}} x_m \cdot P(c^i_{j',k} = x_m|\tilde{\mathbf{y}}^j_k), \quad 1 \leq i \leq N_t^{j'} \tag{2.7}$$

is used, where $c^i_{j',k}$ is the $i$-th element of vector $\mathbf{c}_{j',k}$ and $P(c^i_{j',k} = x_m|\tilde{\mathbf{y}}^j_k)$ is the conditional probability that the $\mathcal{M}$-ary constellation point $x_m$ was transmitted, given the equivalent received signal vector $\tilde{\mathbf{y}}^j_k$. To elaborate a little further, based on Eq. (2.5) we can obtain the *a posteriori* probability $P(c^i_{j',k} = x_m|\tilde{\mathbf{y}}^j_k)$ using the Bayes' rule as follows:

$$\begin{aligned} P(c^i_{j',k} = x_m|\tilde{\mathbf{y}}^j_k) &= \frac{p(\tilde{\mathbf{y}}^j_k|c^i_{j',k} = x_m)P(c^i_{j',k} = x_m)}{p(\tilde{\mathbf{y}}^j_k)} \\ &= \frac{p(\tilde{\mathbf{y}}^j_k|c^i_{j',k} = x_m)P(c^i_{j',k} = x_m)}{\sum_{n=1}^{\mathcal{M}} p(\tilde{\mathbf{y}}^j_k|c^i_{j',k} = x_n)P(c^i_{j',k} = x_n)}, \quad 1 \leq i \leq N_t^{j'}. \end{aligned} \tag{2.8}$$

For GMLST(STBC) schemes, since the component STBC has no error correcting capability (no coding gain provided), Eq. (2.8) can be further simplified to

$$P(c^i_{j',k} = x_m|\tilde{\mathbf{y}}^j_k) = \frac{p(\tilde{\mathbf{y}}^j_k|c^i_{j',k} = x_m)}{\sum_{n=1}^{\mathcal{M}} p(\tilde{\mathbf{y}}^j_k|c^i_{j',k} = x_n)}, \quad 1 \leq i \leq N_t^{j'} \tag{2.9}$$

when the $\mathcal{M}$ signals are assumed to be equally probable, i.e. the *a priori* probabilities obey $P(c^i_{j',k} = x_n) = \frac{1}{\mathcal{M}}$ for all $n \in [1, \mathcal{M}]$. On the other hand, for the GMLST(STTC) schemes, the Maximum A-posteriori Probability (MAP) decoder [89] can be used instead of the Viterbi decoder for the component STTC to deliver more reliable *a posteriori* probabilities $P(c^i_{j',k}|\tilde{\mathbf{y}}^j_k)$, which can be implemented by invoking the so-called Bahl-Cocke-Jelinek-Raviv (BCJR) algorithm [90]. The MAP decoder takes the equivalent channel observations $\tilde{\mathbf{y}}^j_k$ and generates the Log Likelihood Ratio (LLR) [89] for each transmitted symbol $c^i_{j',k}$, $1 \leq i \leq N_t^{j'}$ based on the trellis structure of the $j'$-layer STTC code. Assuming that $P(c^i_{j',k} = x_1)$ is larger than all the other probabilities of $P(c^i_{j',k} = x_n)$, where $n \in (1, \mathcal{M}]$, we may glean the *a posteriori* LLR value of the transmitted symbol $c^i_{j',k}$ from the MAP decoder, which is expressed as

$$\begin{aligned} L(c^i_{j',k} = x_m|\tilde{\mathbf{y}}^j_k) &= \log\frac{P(c^i_{j',k} = x_m|\tilde{\mathbf{y}}^j_k)}{P(c^i_{j',k} = x_1|\tilde{\mathbf{y}}^j_k)} \\ &= \log\frac{p(c^i_{j',k} = x_m, \tilde{\mathbf{y}}^j_k)}{p(c^i_{j',k} = x_1, \tilde{\mathbf{y}}^j_k)} \\ &= \log\frac{\sum_{\mathbf{c}_{j',k} \in \Theta_{i,x_m}} \alpha(\grave{s})\beta(s)\exp(-\frac{\|\tilde{\mathbf{y}}^j_k - \tilde{\mathbf{H}}_{j',k}\mathbf{c}_{j',k}\|^2}{N_0})}{\sum_{\mathbf{c}_{j',k} \in \Theta_{i,x_1}} \alpha(\grave{s})\beta(s)\exp(-\frac{\|\tilde{\mathbf{y}}^j_k - \tilde{\mathbf{H}}_{j',k}\mathbf{c}_{j',k}\|^2}{N_0})}, \end{aligned} \tag{2.10}$$

where $\alpha(\grave{s})$ and $\beta(s)$ are the standard state metric values in the forward and backward recursions in the BCJR algorithm [90]. $\Theta_{i,x_m}$ and $\Theta_{i,x_1}$ denote the sets of trellis transitions with $c^i_{j',k} = x_m$ and $c^i_{j',k} = x_1$, respectively. Hence, the expectation value of $\tilde{c}^i_{j',k}$ for the soft SIC-based GMLST(STTC) schemes may be accordingly computed based on Eqs. (2.7) and (2.10). Since in case of reliable decisions soft-values close to the legitimate hard-decision-based constellation points are subtracted in Eq. (2.6), whereas in the case of unreliable decisions small values are subtracted, the effects of potential error propagation are significantly reduced.

### 2.3.2 Performance Characterization

It is noted that in contrast to V-BLAST, the requirement for the number of receive antennas in the GMLST system is $N_r \geq N_t - N_t^{1'} + 1$, where $N_t^{1'}$ is the number of transmit antennas of group $1'$. More particularly, when we consider the most appropriate detection order, which depends on the specific channel realization encountered at the receiver and to be detailed in Section 2.5, $1'$ may be any integer spanning from 1 to $q$. Thereby, we let $N_r \geq \max_j\{N_t - N_t^j\} + 1$ in order to guarantee that the proposed multistage SIC detection algorithm is applicable. Monte-Carlo simulations have been performed to evaluate the proposed multistage SIC algorithm of Fig. 2.3. Unless specified otherwise, the STCs utilized for all groups are identical in this chapter. For brevity, we use the notation $(N_t, N_r)$ from now on to denote a MIMO system having $N_t$ transmit and $N_r$ receive antennas. The simulation setup which will be used in all the simulations in this chapter is as follows. We assume having $N_t^1 = N_t^2 = \ldots = N_t^q$ and take two GMLST schemes as examples: a (4, 4)-element GMLST and an (8, 8)-element GMLST. For GMLST(STTC) schemes, both the H-GMLST and D-GMLST schemes of Fig. 2.1 are considered, while only the H-GMLST arrangement is invoked for the GMLST(STBC) schemes. Furthermore, we also assume that each group contains two transmit antennas for simplicity. The 2 b/s/Hz Quaternary Phase-Shift Keying (QPSK) modulated 16-state space-time trellis code proposed in [9, Fig. 5] is taken into account as the component code for all groups in the GMLST(STTC) scenario. By contrast, Alamouti's STBC [8] is considered in the GMLST(STBC) scenario of Fig. 2.2. The transmission rate of the half-rate-coded (4, 4) and (8, 8)-element systems is 4 and 8 b/s/Hz, respectively. As mentioned above, we consider quasi-static flat Rayleigh fading channels. The channel coefficients are assumed to be perfectly known at the receiver. Each transmission frame is composed of 130 half-rate-coded 2-bit-symbols from each transmit antenna, which corresponds to 520 and 1040 information bits per frame in the (4, 4) and (8, 8) systems, respectively. We outline the simulation parameters of our GMLST systems in Table 2.1.

| | |
|---|---|
| Modulation Scheme | QPSK |
| No. of Layers | $q = 2$ or 4 |
| No. of Tx per Layer | $N_t^j = 2, j \in [1, q]$ |
| No. of Rx | $N_r = 4$ or 8 |
| Frame Length | 130 symbols per transmit antenna |
| Channel | Quasi-static flat Rayleigh fading |
| GMLST(STBC) Component Codes | STBC [8] |
| GMLST(STTC) Component Codes | STTC [9, Fig. 5] |

**Table 2.1:** GMLST system parameters.

Fig. 2.4(a) and Fig. 2.4(b) depict the BER performances against the average received SNR per bit per receive antenna in the (4, 4) and (8, 8) systems, respectively. It can be observed for both systems that the H-GMLST(STBC) schemes slightly outperform the GMLST(STTC) arrangements in the low-SNR regime. This observation is due to the fact that in the low-SNR regime we encounter severe error propagations among the GMLST layers. Since the STTC codewords are correlated during the transmission frame, while the various STBC codewords are independent, stronger error propagation occurs among the GMLST(STTC) layers than among the GMLST(STBC) layers. On the other hand, since the error propagation is less pronounced in the high SNR regime as well as because the STTC provides useful coding gains, the GMLST(STTC) scheme exhibits a better performance than the GMLST(STBC) scheme. Furthermore, as expected we can see clearly in Fig. 2.4 that the D-GMLST(STTC) generally performs better than H-GMLST(STTC) in the context of both systems due to the additional spatial diversity induced by diagonal mapping. The improvement of the diagonal mapping over horizontal mapping is about 0.6 and 1.0 dB at a target BER of $10^{-4}$ in the (4, 4) and (8, 8) systems, respectively. Based on this observation, we can say that a higher additional diversity gain is attained in the (8, 8) system than in the (4, 4) system, since the former has four groups (layers), while the latter only has two groups (layers). Hence the (8, 8) system provides a higher transmit diversity gain when using the diagonal mapping. Fig. 2.4 also shows the BER performances of GMLST(STTC) schemes, when using soft SIC in both the (4, 4) and (8, 8) systems. Explicitly, it is demonstrated in Fig. 2.4(a) that a soft-SIC advantage of 0.2 dB was achieved at a target BER of $10^{-4}$ by the soft-SIC-based GMLST(STTC) schemes over its hard-SIC-based counterpart in the (4, 4) system at the cost of a higher computational complexity, since MAP decoders are employed. We have an even more

modest improvement of 0.1 dB at the target BER of $10^{-4}$ in the (8, 8) system, as shown in Fig. 2.4(b). Furthermore, when comparing Fig. 2.4(a) and Fig. 2.4(b), it is clearly seen that the (8, 8) GMLST schemes outperform the corresponding (4, 4) counterparts, while attaining a higher system throughput of 8 b/s/Hz. This is because the first two groups of the (8, 8) GMLST schemes share the same receive diversity order as the two groups in the (4, 4) counterparts, while the third and fourth group of the (8, 8) GMLST schemes benefit from a higher receive diversity order.

## 2.4 Group-Based Power Allocation

In the previous section, the detection order was predetermined and independent of the channel realizations at the receiver. As a result, group $j'$ detected at the $j$-th detection level has an overall antenna diversity order of $(N_r - N_t + N_t^{1'} + \cdots + N_t^{j'}) \times N_t^{j'}$, as mentioned in [7]. If all groups are assigned the same power, group $1'$ would have the worst performance. Naturally, this induces an overall performance degradation, which is usually predetermined by the group having the worst performance. Thus, improving the performance of group $1'$ would be beneficial in terms of enhancing the overall performance. The most straightforward approach is to allocate more power to the groups detected earlier and less to the groups detected later under the constraint of a constant total transmission power.

An unequal group-based power allocation approach was first proposed by Tarokh *et al.* in [10], which we hence refer to as Tarokh's power allocation. In this strategy, a 3 dB power reduction was applied to each successive group according to the predetermined detection order. For simplicity, the predetermined detection order is assumed to be $\{1, 2, \ldots, q\}$. Let $E_j$ denote the power level (on a linear scale) assigned to group $j$, where we satisfy the total power constraint of

$$\sum_{j=1}^{q} E_j = E, \tag{2.11}$$

while maintaining $E_j = 2E_{j+1}$ for $1 \leq j \leq q-1$ and $E$ indicates the total transmission power of the GMLST scheme.

### 2.4.1 Performance Characterization

Clearly, Tarokh's power allocation strategy is appealingly simple, apart from arranging for the power allocation to be unequal, no additional computational complexity is imposed. Despite this simplicity, the simulation results of Figs. 2.5 and 2.6 show that it is superior

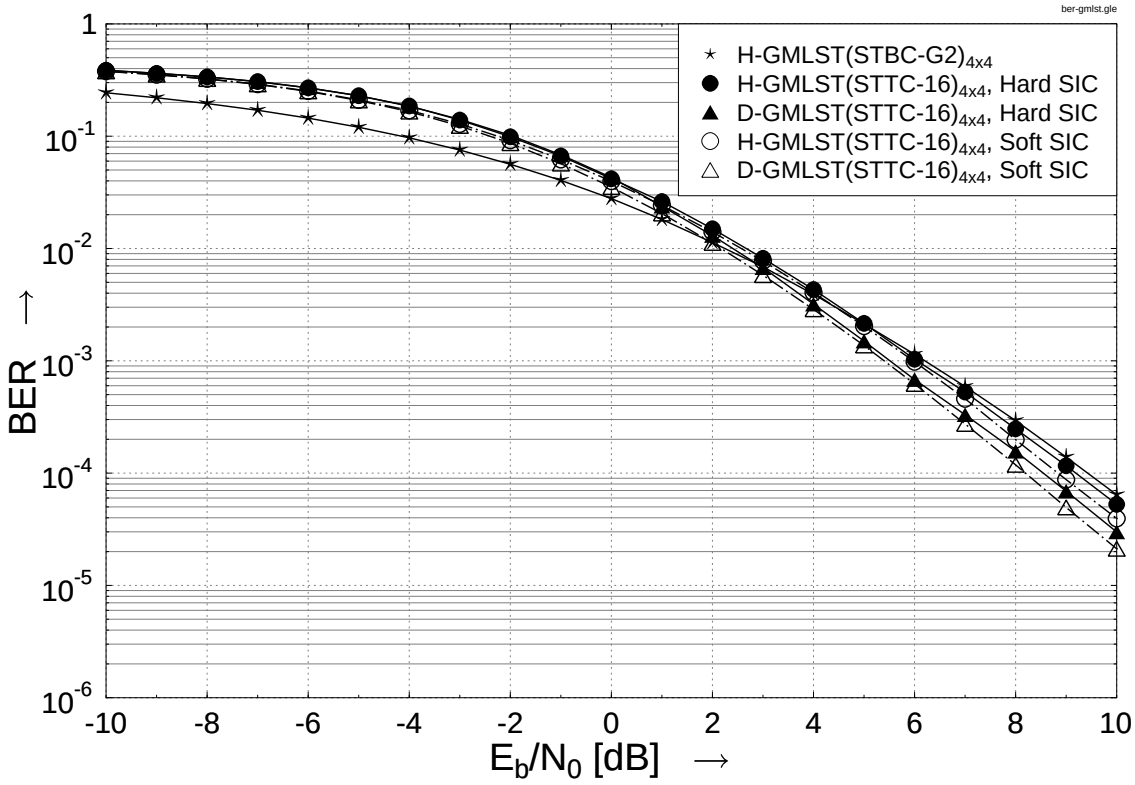


(a) BER performance of the (4, 4) system using the parameters of Table 2.1

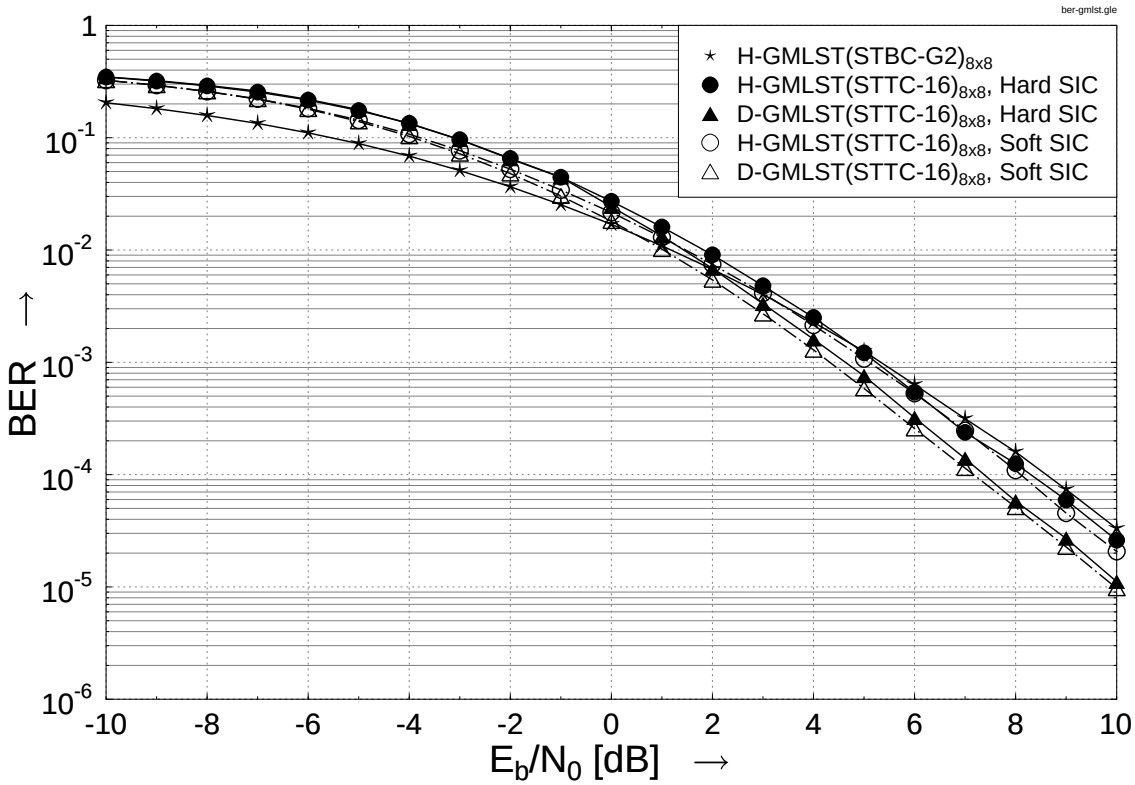


(b) BER performance of the (8, 8) system using the parameters of Table 2.1

**Figure 2.4:** Performance comparison in the (4, 4) and (8, 8) systems using the parameters of Table 2.1.

to the conventional equal-power allocation scheme in the high SNR regime. Fig. 2.5 and Fig. 2.6 show the BER performances of the GMLST schemes in the context of the (4, 4) and (8, 8) systems, respectively. Again, the GMLST schemes employing Tarokh's power allocation scheme generally outperform their counterparts relying on equal power allocation at high SNRs, but perform slightly worse at low SNRs. This is due to the fact that Tarokh's PA was designed based on each layer's diversity order which is accurate only in high SNR regime. More specifically, an advantage of 1.0 dB was observed at the target BER of $10^{-4}$ for Tarokh's power allocation over the equal-power allocation regime in the context of the H-GMLST(STBC) schemes, as depicted in Fig. 2.5(a), when the system was configured as a (4, 4) arrangement. In Fig. 2.5(b), the Tarokh-Power-Allocation aided hard-SIC-based H-GMLST(STTC) scheme exhibits an approximately 0.9 dB gain over its Equal-Power-Allocation aided counterpart at the same BER of $10^{-4}$. Furthermore, it is observed that the Tarokh-Power-Allocation aided soft-SIC-based D-GMLST(STTC) scheme outperforms the equal-power benchmarker by nearly 2.0 dB. On the other hand, in the context of the (8, 8) system of Fig. 2.6, we observe that with the aid of Tarokh's power allocation, the BER performance was improved by about 2.0 dB at the target BER of $10^{-4}$ over equal power allocation for both the H-GMLST(STBC) and GMLST(STTC) schemes. By comparing the performance improvements of Tarokh's power allocation in the context of the (4, 4) and (8, 8) systems, we can readily conclude that in conjunction with more GMLST layers, increased gains can be achieved by Tarokh's power allocation regime.

Nevertheless, from the point of minimizing the bit error probability, Tarokh's power allocation is not the optimal strategy. The optimal power allocation minimizing the transmission frame error probability was proposed in [11]. In this novel scheme, the individual transmission frame error probability of group $j$ was expressed as a function of the allocated power $E_j$, which is denoted by $p_j(E_j)$, given that the previous $(j-1)$ groups were all detected successfully. The simulation results of [11, Fig. 3] showed that the optimal power allocation scheme provided certain performance improvements over Tarokh's power allocation strategy. However, this regime imposed a higher computational complexity, especially in the process of finding the function $p_j(E_j)$.

## 2.5 Optimal Detection Order

In the previous section, various group-based power allocation techniques were discussed, which are capable of enhancing the system performance, when the detection order is independent of the channel state information (CSI). In this section, we will demonstrate how to determine the most appropriate detection order based on the channel quality experienced

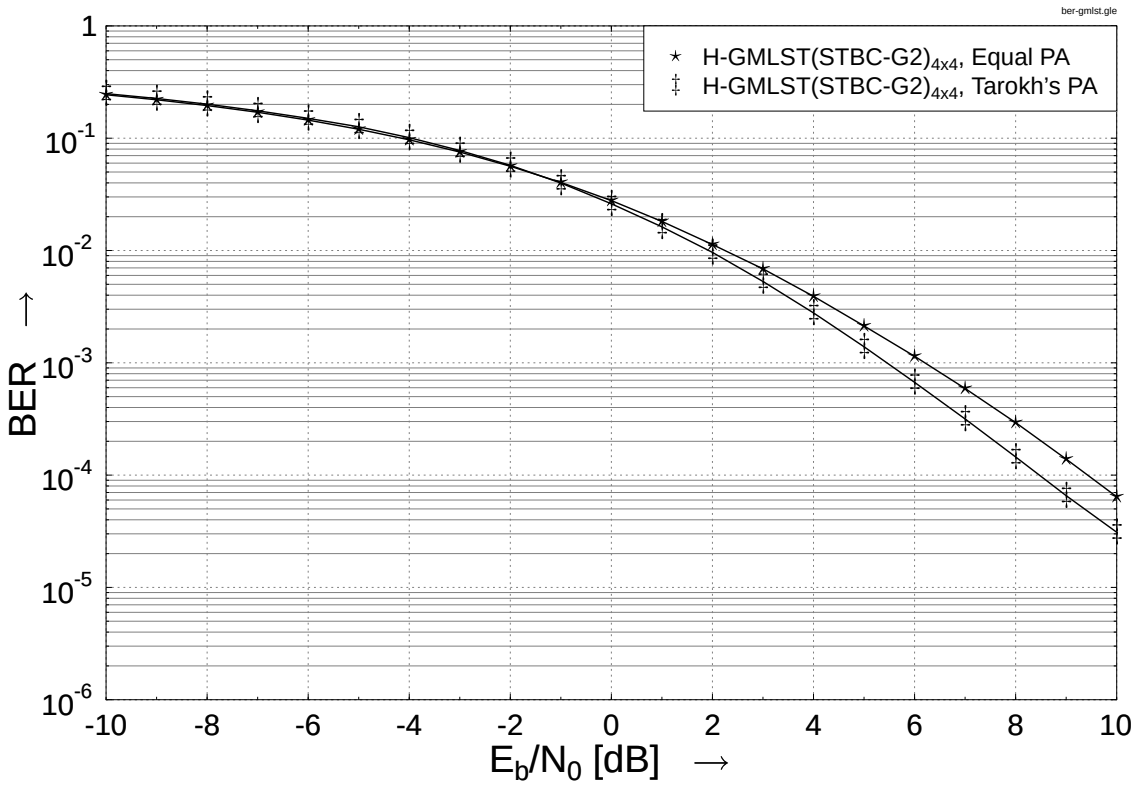


(a) BER performance of the H-GMLST(STBC) schemes of Fig. 2.2 using the parameters of Table 2.1

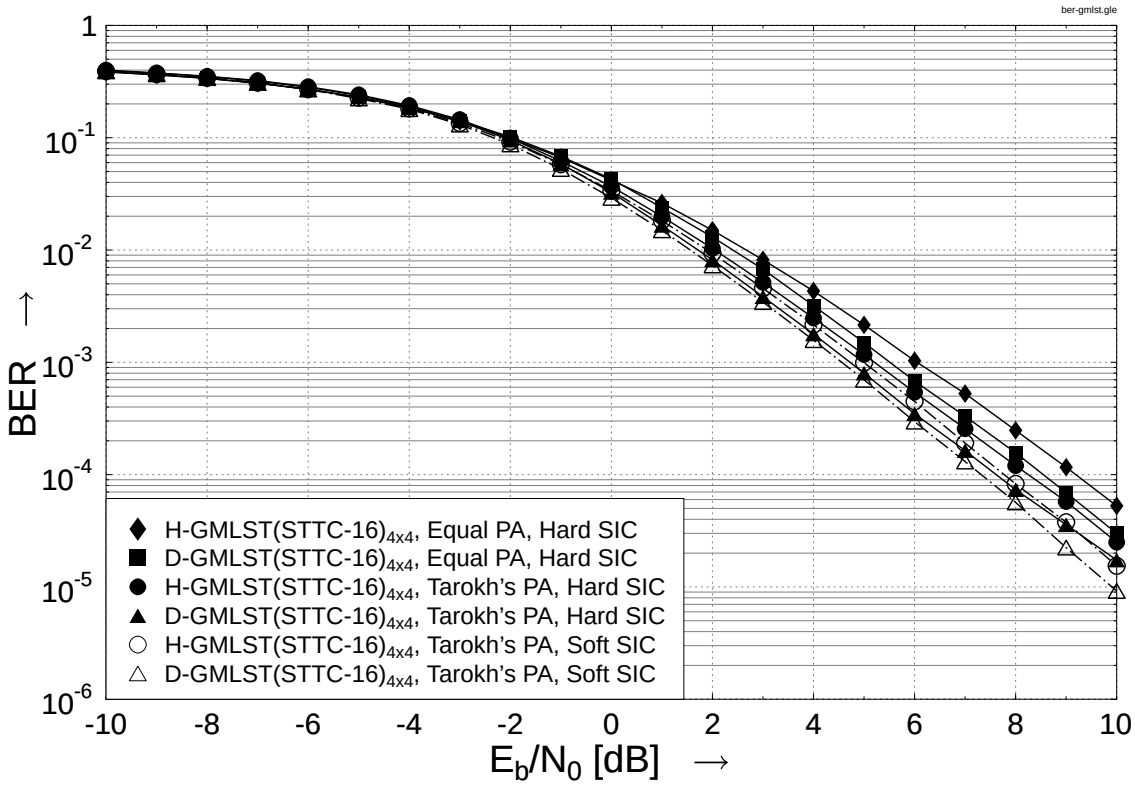


(b) BER performance of the GMLST(STTC) schemes of Fig. 2.1 using the parameters of Table 2.1

**Figure 2.5:** Performance comparison of different power allocation schemes in the (4, 4) system using the parameters of Table 2.1.

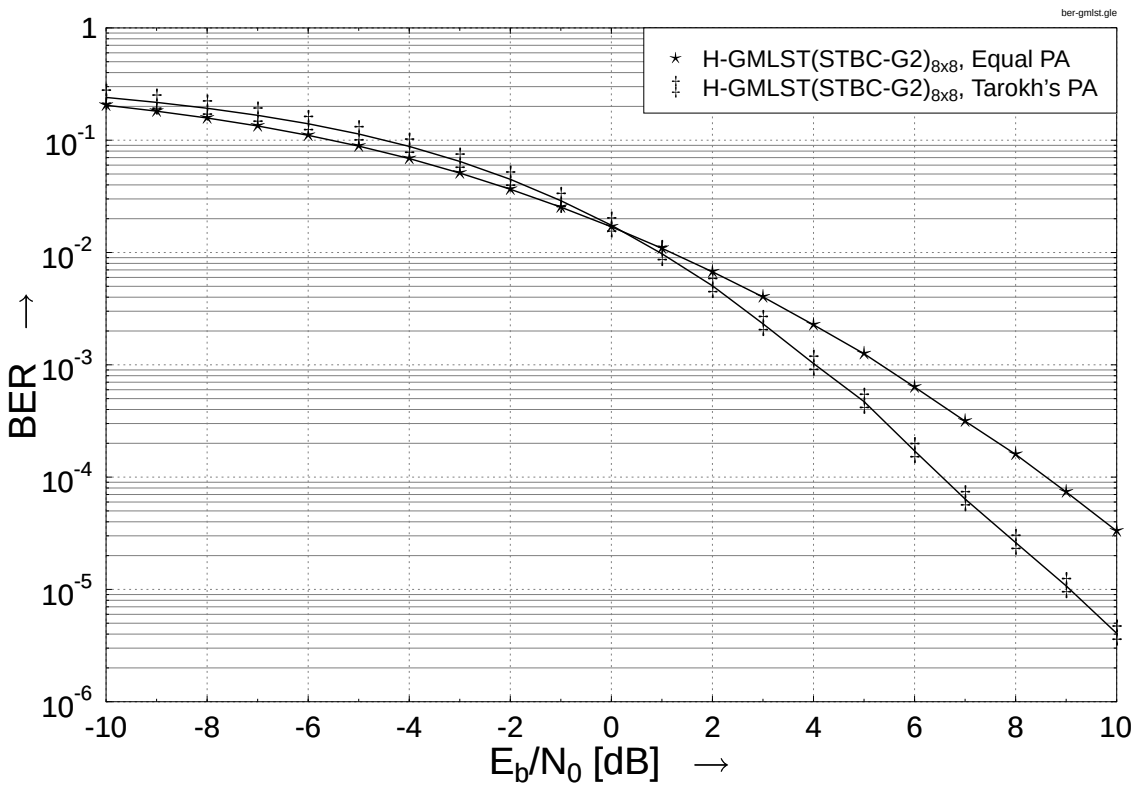


(a) BER performance of the H-GMLST(STBC) schemes of Fig. 2.2 using the parameters of Table 2.1

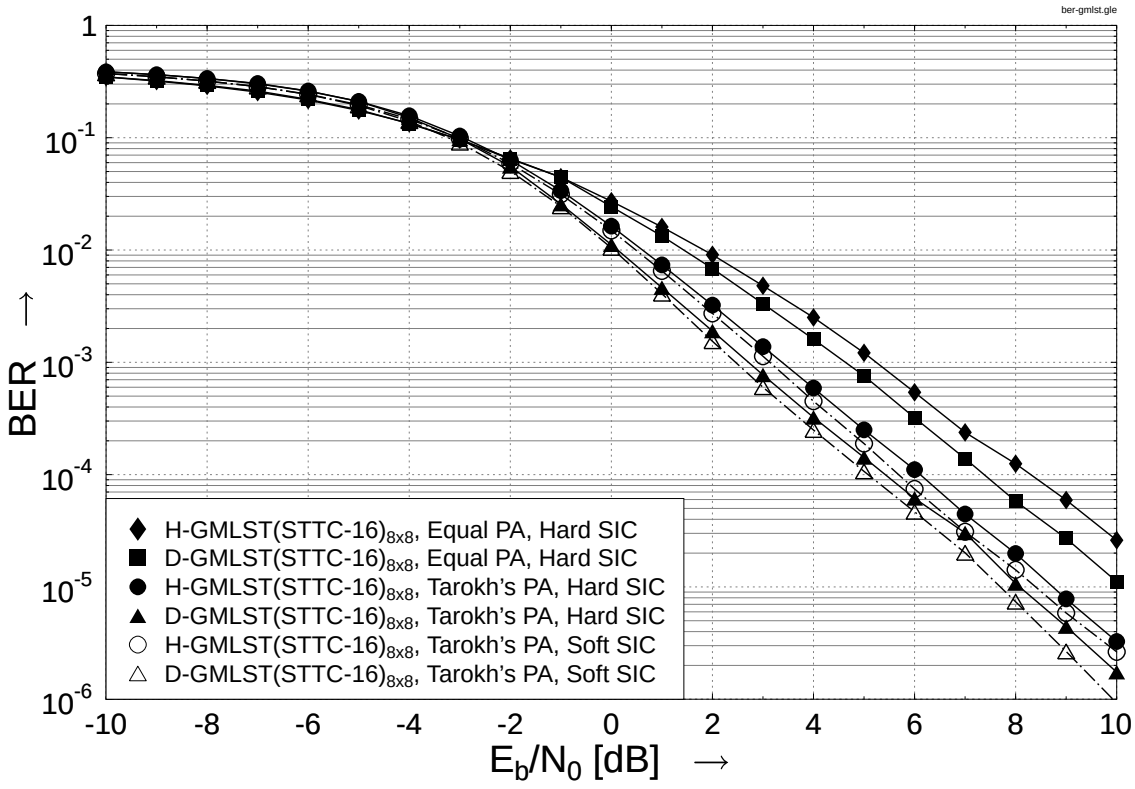


(b) BER performance of the GMLST(STTC) schemes of Fig. 2.1 using the parameters of Table 2.1

**Figure 2.6:** Performance comparison of different power allocation schemes in the (8, 8) system using the parameters of Table 2.1.

at the receiver, when equal power allocation is applied and quasi-static channels are considered. Note that the detection order is not important in the context of the D-GMLST schemes and can be arbitrary, since the different groups of the D-GMLST scheme experience the same time-varying channel quality. Hence we only consider the H-GMLST schemes of Fig. 2.1(b) in this section. The optimally ordered detection developed in [16] is investigated below in order to choose the layer associated with the largest post-nulling signal-to-noise ratio (SNR) instead of choosing an arbitrary layer to detect.

At the first detection level ($j = 1$), let $\mathbf{H}^1 = [\mathbf{H}_1, \ldots, \mathbf{H}_q]$, where $\mathbf{H}_l$ is the $\left(N_r \times N_t^l\right)$-element subchannel matrix corresponding to group $l$, and define the candidate group set as $S_1 \equiv \{l | 1 \leq l \leq q\}$.

At the $j$-th detection level, we find a set of orthonormal row vectors in the null space of $\mathbf{H}_l^j$ for each $l \in S_j$, where $\mathbf{H}_l^j$ indicates the matrix obtained by eliminating $\mathbf{H}_l$ from $\mathbf{H}^j$, and use them to construct an $[(N_r - N_t + N_t^{1'} \cdots + N_t^{(j-1)'} + N_t^l) \times N_r]$-element matrix $\mathbf{W}_l^j$. Then, left-multiply $\mathbf{H}_l$ by $\mathbf{W}_l^j$ in order to obtain the equivalent channel matrix of group $l$ at this detection level in the form of

$$\tilde{\mathbf{H}}_l^j = \mathbf{W}_l^j \mathbf{H}_l.$$

Since the nulling matrix $\mathbf{W}_l^j$ is orthonormal, the total output SNR of group $l$ after suppressing all the other groups becomes

$$SNR_l = \frac{\|\tilde{\mathbf{H}}_l^j\|^2 E_s}{N_0},$$

which is proportional to the squared Frobenius norm [91] of the corresponding equivalent channel matrix. Hence, we choose the specific candidate associated with the largest squared Frobenius norm as the group to be detected at this level, which is formulated as

$$j' = \arg\{\max_{l \in S_j} \| \tilde{\mathbf{H}}_l^j \|^2\}. \tag{2.12}$$

And then, by removing $j'$ from $S_j$, we update the candidate group set as

$$S_{j+1} = S_j \backslash \{j'\},$$

where we define $S_j \backslash \{j'\} \equiv \{l | l \in S_j, l \neq j'\}$. Correspondingly, by eliminating $\mathbf{H}_{j'}$ from $\mathbf{H}^j$, the channel matrix is changed to

$$\mathbf{H}^{j+1} = \mathbf{H}_{\bar{j}'}^j.$$

We carry out this process for $j = j + 1$, until the candidate group set becomes void. Finally, the detection order is obtained as $\{1', 2', \cdots, q'\}$, which is a certain permutation of $\{1, 2, \cdots, q\}$.

Observe by comparing that the procedure of finding the optimal detection order for the H-GMLST schemes of Fig. 2.1(b) is similar to that of the BLAST system's optimal detection ordering process. As the BLAST system's ordering was shown to be optimal in the sense of minimizing the probability of frame errors [17], the above-mentioned ordering procedure of Eq. (2.12) can also be similarly shown to be optimal in the same sense.

### 2.5.1 Complexity Analysis

Let us now compare the computational complexity of the multistage SIC of the H-GMLST schemes relying on arbitrary detection order, of the H-GMLST schemes invoking the optimal detection order and that of the D-GMLST(STTC) scheme associated with an arbitrary detection order. We consider the complexity of performing interference nulling quantified in terms of finding the null space basis of a two-dimensional complex matrix. At the $j$-th detection level of the H-GMLST scheme using an arbitrary detection order of, say $\{1, 2, \ldots, q\}$, it requires the computation of the null space basis of an $(N_t - N_t^1 - \cdots - N_t^j) \times N_r$ matrix. By contrast, at the $j$-th detection level of the H-GMLST scheme associated with the optimal detection order of $\{1', 2', \ldots, q'\}$, in order to determine which particular group will be detected, the null space basis of an $(N_t - N_t^{1'} - \cdots - N_t^{(j-1)'} - N_t^l) \times N_r$ matrix has to be found for every $l \in S_j$. Finally, at the $j$-th detection level of the D-GMLST scheme relying on an arbitrary detection order of, say $\{1, 2, \ldots, q\}$, it requires the computation of the null space basis of $p$ different $(N_t - N_t^1 - \cdots - N_t^j) \times N_r$ matrices. In order to simplify our discussions, we treat the complexity of performing interference nulling in the H-GMLST scheme relying on an arbitrary detection order as our benchmark. Then, at the $j$-th detection level, $1 \leq j \leq q-1$, the complexity of the D-GMLST scheme associated with an arbitrary detection order and that of the H-GMLST scheme relying on the optimal detection order is $p = q$ and $q - j - 1$ times higher, respectively. Since the complexity of computing the squared Frobenius norm of $\| \tilde{\mathbf{H}}_l^j \|^2$ in the H-GMLST scheme using the optimal detection order is negligible compared to that of finding the null space basis, we may argue that the D-GMLST scheme has the highest complexity, while the H-GMLST arrangement associated with an arbitrary detection order has the lowest complexity, when disregarding the component STCs' decoding processes.

### 2.5.2 Performance Characterization

Fig. 2.7 and Fig. 2.8 characterize the BER performances of the optimally ordered detection schemes in the context of the (4, 4) and (8, 8) H-GMLST systems, respectively. We can see that in conjunction with the optimally ordered detection, the system performances

were improved by approximately 1.9 dB and 3.3 dB at the target BER of $10^{-4}$ in the (4, 4) and (8, 8) systems, respectively, regardless of whether the H-GMLST(STBC) or the H-GMLST(STTC) schemes were considered. Furthermore, let us now compare Fig. 2.7 and Fig. 2.8 to Fig. 2.5 and Fig. 2.6 of Section 2.4 one by one. It may be observed that the H-GMLST scheme relying on optimally ordered detection performs slightly better than the H-GMLST and D-GMLST arrangements invoking Tarokh's power allocation in the (4, 4) system. Similarly, in the context of the (8, 8) system, the performance gain of H-GMLST relying on optimally ordered detection over D-GMLST using Tarokh's power allocation was around 0.8 dB in the range of high $E_b/N_0$ values.

## 2.6 Iterative Multistage SIC Detection

Although the group-based power allocation of Section 2.4 and the optimal detection ordering of Section 2.5 have the potential of recovering some SNR loss compared to the arbitrary ordering schemes combined with equal-power allocation, the above-mentioned multistage SIC-based detection scheme fails to achieve the maximum attainable receive diversity order. More particularly, the receive antenna diversity order of group $j'$ detected at the $j$-th detection level is only $N_r - N_t + N_t^{1'} + \cdots + N_t^{j'}$. It clearly transpires from the discussions of Section 2.5 that the earlier a layer is detected, the lower its receive diversity order is. Therefore, in order to exploit the maximum attainable receive diversity order for all layers, an efficient iterative multistage SIC detection scheme was proposed in [11]. For GMLST(STTC) schemes, it may be observed from Fig. 2.9 that different temporal interleavers are used for creating the codewords of the different groups for the sake of eliminating the effects of burst error propagation among groups during the consecutive iterations. The temporal interleavers are vector based, where the vector size is determined by the spatial dimension of the relevant codeword, which guarantees the rank of the STTCs in each group remains unaffected.

The corresponding schematic of the iterative detection procedure is depicted in Fig. 2.9. Without loss of generality, the serial detection order in this figure is assumed to be $\{1', 2', \cdots, q'\}$ for both the optimally and arbitrarily ordered detection processes. We can see in Fig. 2.9 that the first iteration is the same as described above, except that temporal interleaving and deinterleaving should be carried out accordingly, which substantially reduces the effects of burst error propagation among the groups for the GMLST(STTC) schemes. In the subsequent iterations, the interference nulling (IN) stage of Eq. (2.5) and Fig. 2.3(a) is no longer needed since all groups have already been detected, while the interference cancellation (IC) is still performed for all groups, which results in a theoretical receive diversity order of $N_r$ for each group. Each iteration consists of $q$ layers and each STC-

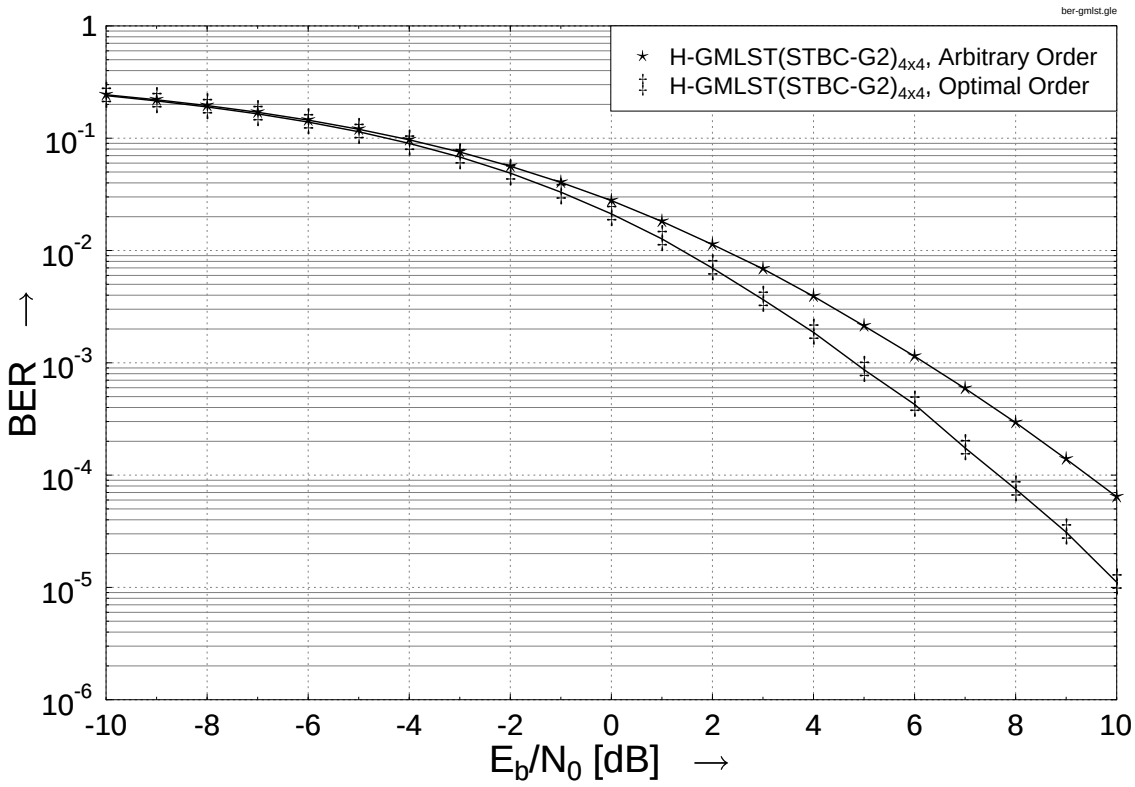


(a) BER performance of the H-GMLST(STBC) schemes of Fig. 2.2 using the parameters of Table 2.1

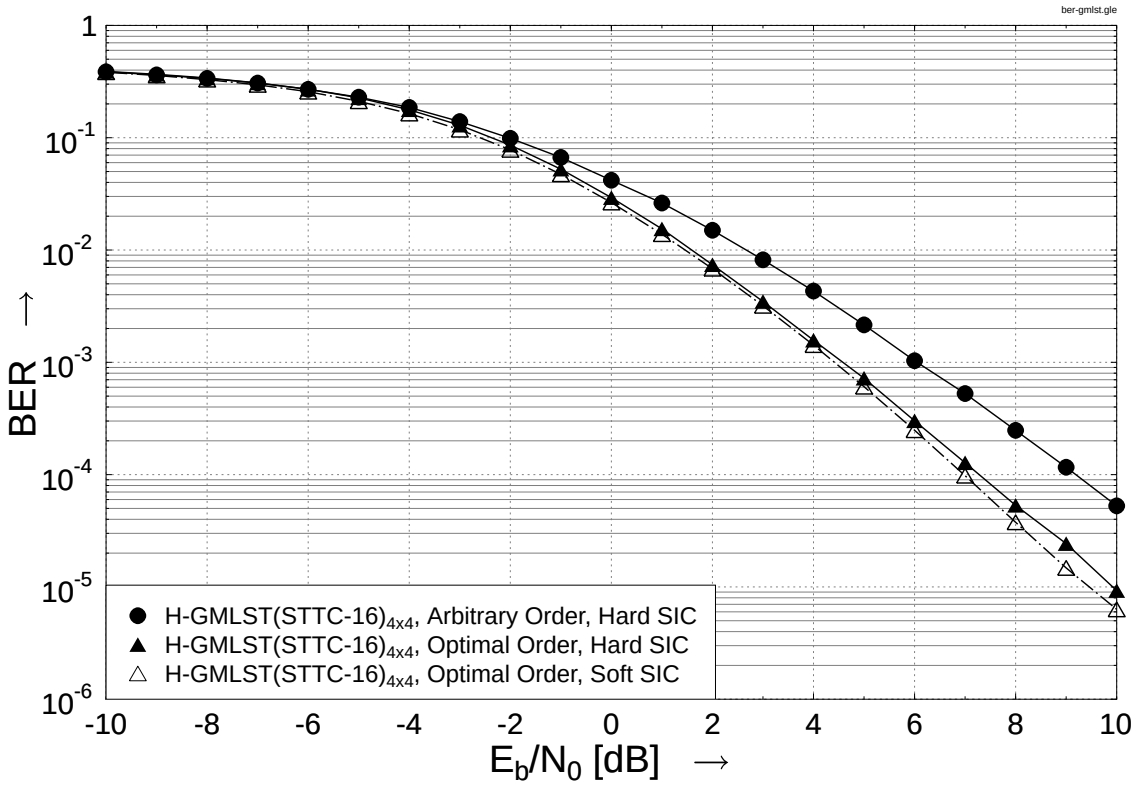


(b) BER performance of the H-GMLST(STTC) schemes of Fig. 2.1 using the parameters of Table 2.1

**Figure 2.7:** Performance comparison of ordered detection in the (4, 4) H-GMLST systems using the parameters of Table 2.1.

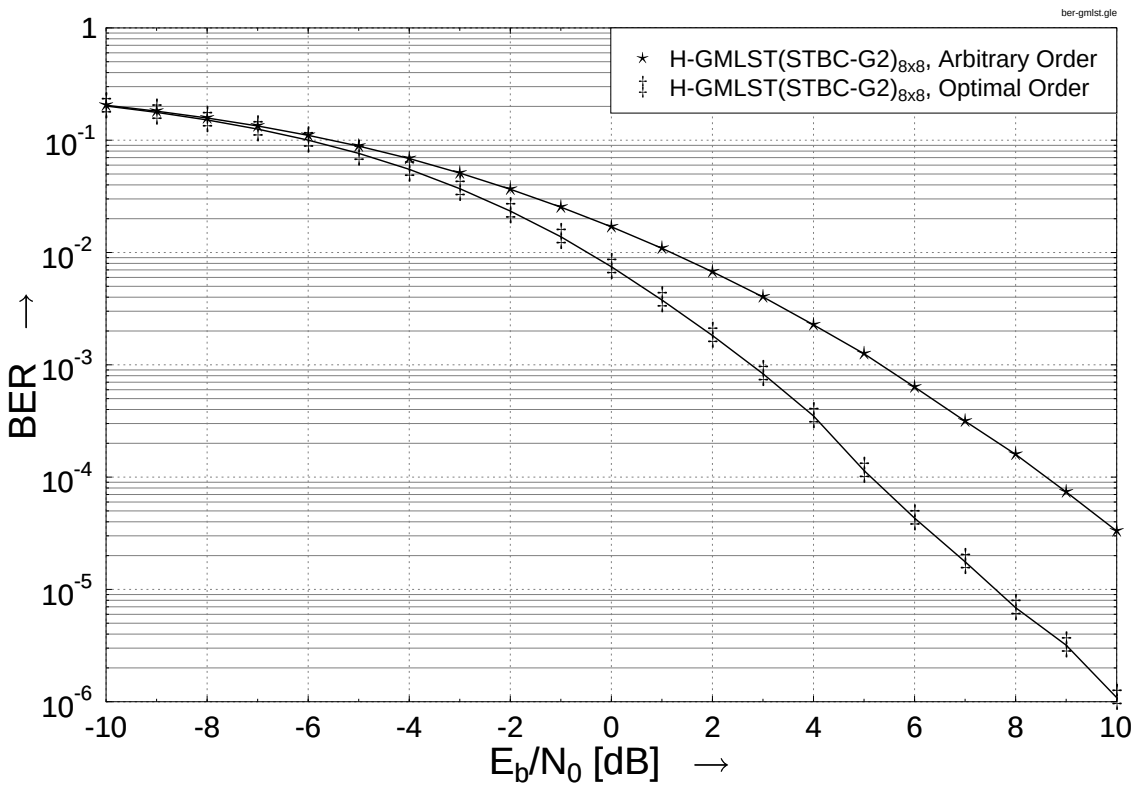


(a) BER performance of the H-GMLST(STBC) schemes of Fig. 2.2 using the parameters of Table 2.1

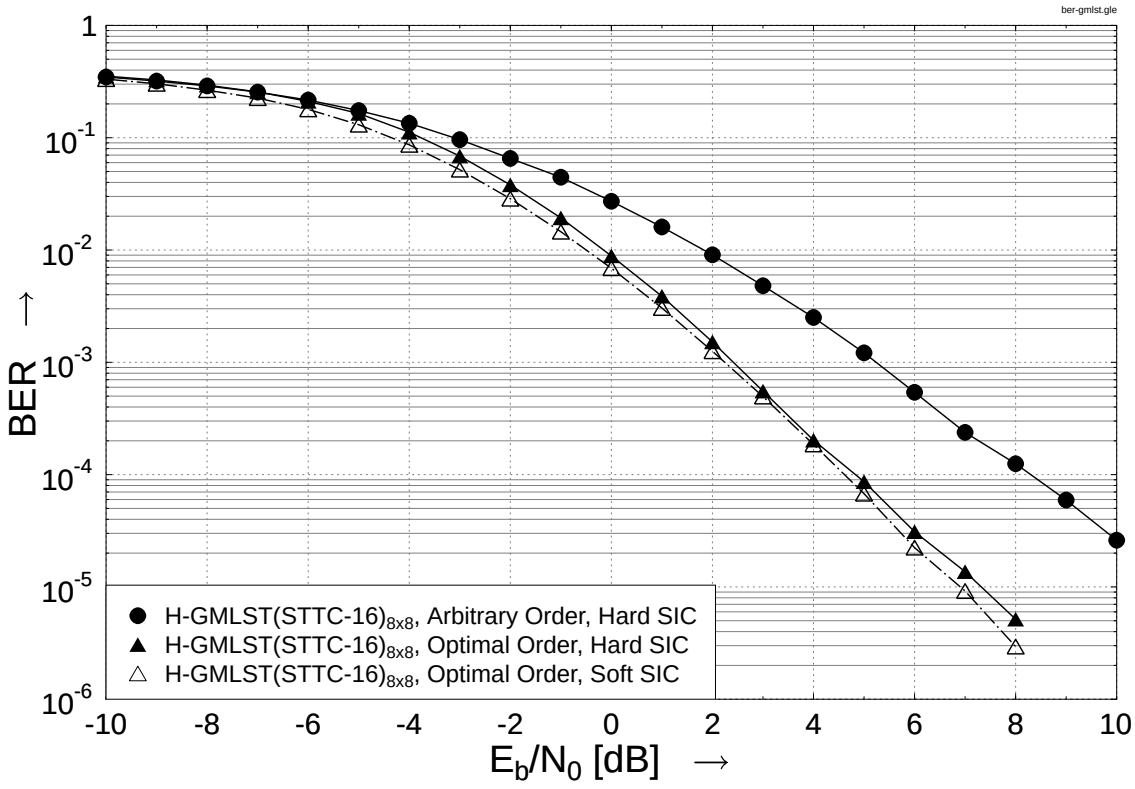


(b) BER performance of the H-GMLST(STTC) schemes of Fig. 2.1 using the parameters of Table 2.1

**Figure 2.8:** Performance comparison of ordered detection in the (8, 8) H-GMLST systems using the parameters of Table 2.1.

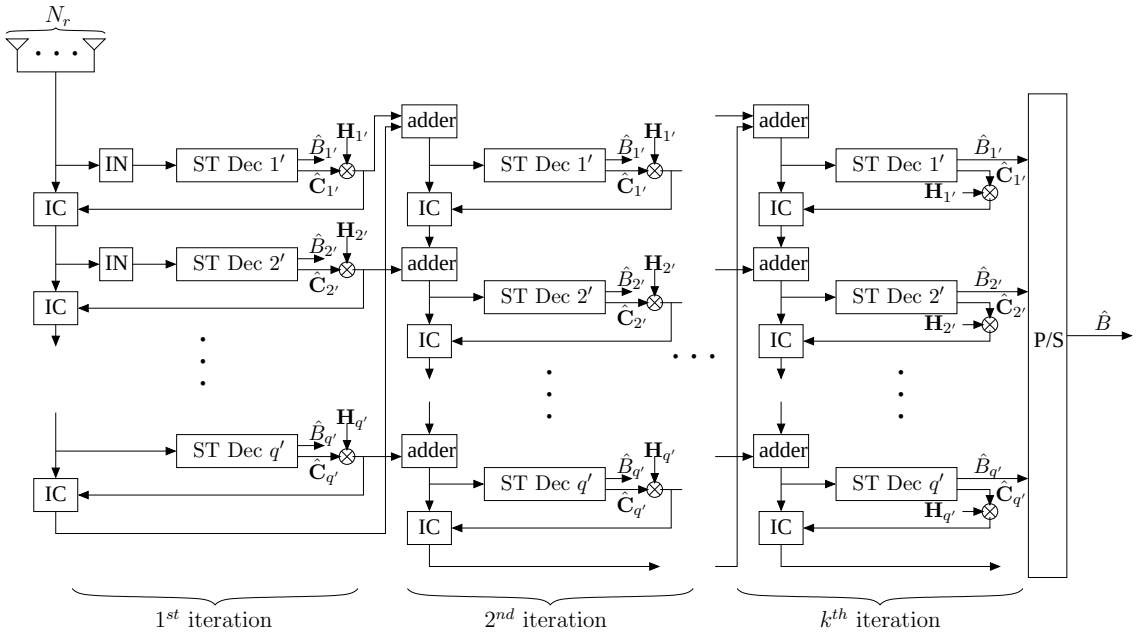


**Figure 2.9:** Iterative multistage SIC detection of GMLST schemes, where the "ST Dec $j'$" module is the same as in Fig. 2.3.

protected layer is processed successively, in the same order as during the first iteration. At level $j$, we subtract the interference induced by group $1', \cdots, (j-1)', (j+1)', \cdots, q'$ from the original received signals and re-decode group $j'$. Once decoded, the new decision of group $j'$ is fed back to the next level for detecting group $(j+1)'$. A full iteration is deemed to be completed when all the $q$ levels are completed. Based on Eq. (2.3), the detection of group $j'$ at the $j$-th detection stage of the $m$-th iteration can be written as

$$\mathbf{y}_k^m = \mathbf{H}_{j',k}\mathbf{c}_{j',k} + \sum_{a=1}^{j-1} \mathbf{H}_{a',k}(\mathbf{c}_{a',k} - \hat{\mathbf{c}}_{a',k}^m) + \sum_{b=j+1}^{q} \mathbf{H}_{b',k}(\mathbf{c}_{b',k} - \hat{\mathbf{c}}_{b',k}^{m-1}) + \mathbf{n}_k, \quad (2.13)$$

where the superscript $m$ and $m-1$ denote SIC iteration indices. After a number of iterations, the maximum attainable receive diversity order of $N_r$ may indeed be achieved for all layers, when the residual error propagation among different groups becomes negligible. The iterative process can be stopped, when the detected signals have become sufficiently reliable. Compared to ML detection, this iterative detection scheme is capable of approaching the same receive diversity order, despite imposing only a fraction of the computational complexity of ML-style joint detection.

### 2.6.1 Performance Characterization

The simulation results of the iterative-multistage-SIC-detected GMLST schemes are presented in Fig. 2.10 and Fig. 2.11 for the (4, 4) and (8, 8) systems, respectively. We first

consider the H-GMLST scheme associated with the optimal detection order, for example. Fig. 2.10(a) and Fig. 2.11(a) characterize the achievable performance improvements of iterative multistage SIC detection in the context of the GMLST(STBC) schemes. It is observed in Figs. 2.10(a) and 2.11(a) that, when two SIC operations are invoked, iterative gains of approximately 1.0 dB and 1.8 dB are achieved at the target BER of $10^{-4}$ in the context of the (4, 4) and (8, 8) systems, respectively, where according to Fig. 2.9 the maximum attainable receive diversity order has been achieved. Furthermore, no substantial additional improvements may be attained after two SIC iterations in either of these systems, since the remaining inter-group interference propagating across the groups is independently distributed across $K/2$ consecutive G2 *codeword* block periods during $K$ symbol intervals and hence cannot be eliminated by SIC operations.

On the other hand, we note in Fig. 2.1 for the GMLST(STTC) schemes that all the temporal vector-based interleavers are pseudo-random having a depth of the frame length, which are not used in the GMLST(STBC) arrangements. Consider the (4, 4) H-GMLST(STTC) scheme characterized in Fig. 2.10(b), where it is observed that the iterative SIC schematic of Fig. 2.9 uses an interleaver in order to dramatically enhance the system's performances. After three hard-decision-aided SIC iterations it achieves a 2.5 dB gains at a target BER of $10^{-3}$ compared to the performance of the optimally ordered detection characterized in Fig. 2.7(b). Furthermore, an even higher soft-SIC gain of 3.0 dB was recorded in Fig. 2.10(b) for the same number of iterations. The simulation results recorded for the iterative detection without the interleaver portrayed in the schematic of Fig. 2.9 may also be compared to those achieved with the aid of interleavers for quantifying the beneficial effect of the interleaver. We see in Fig. 2.10(b) that the interleaver provides only a modest gain, which is only apparent at high $E_b/N_0$ values after the first iteration, but brings about significant gains during the following iterations.

As discussed in Section 2.3, the first iteration is constituted by a simple detection operation. Hence the achievable performance is limited by that of the group detected first, which only benefits from the lowest receive antenna diversity order. As the interleavers seen in the schematic of the GMLST(STTC) schemes of Fig. 2.1 are developed to mitigate the potential burst error propagation among groups, they are of no benefit for the first group and have a negligible effect on the first iteration. Nevertheless, from the second iteration on, the interleaver helps significantly in mitigating the burst errors propagation among groups. We can see that in conjunction with three iterations, the attainable performance improvement of the system relying on the interleaver of Fig. 2.10(b) is around 1.0 dB at a target BER of $10^{-3}$ over the system operating without an interleaver, since the latter suffers from severe error propagation. We also see in Fig. 2.10(b) that the achievable performance improvement becomes less and less upon increasing the number of itera-

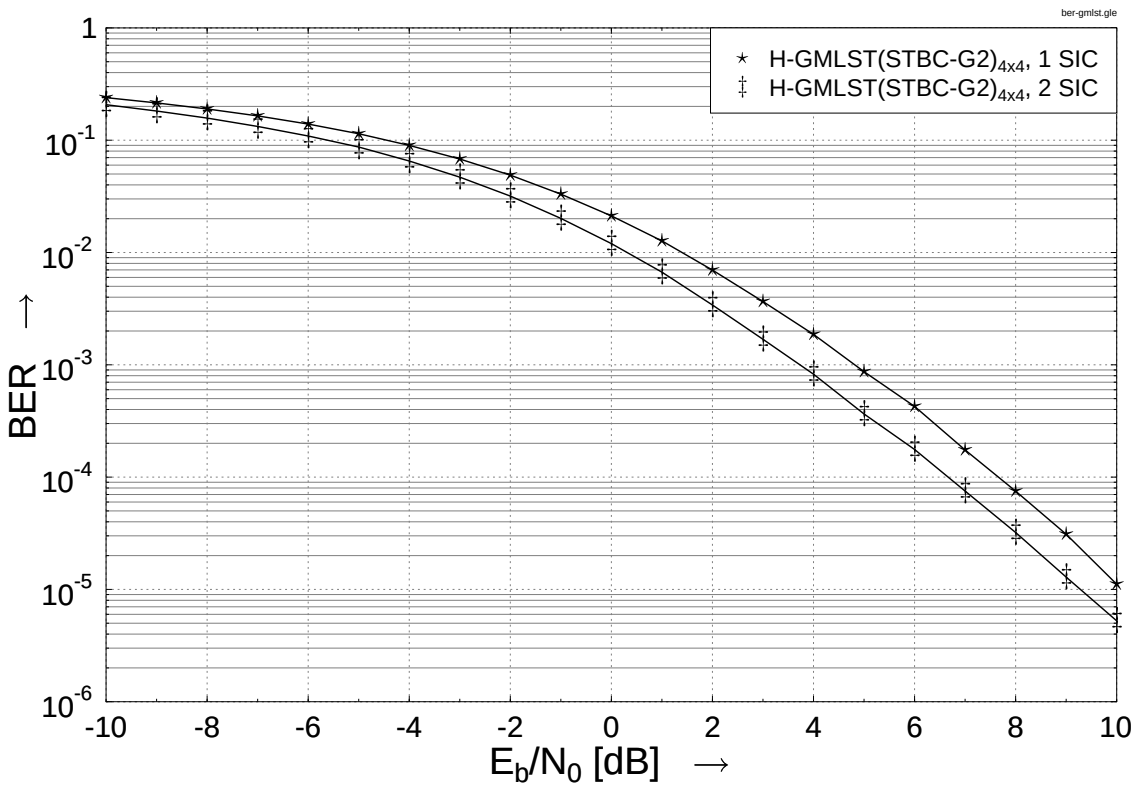


(a) BER performance of the H-GMLST(STBC) schemes of Fig. 2.2 using the parameters of Table 2.1

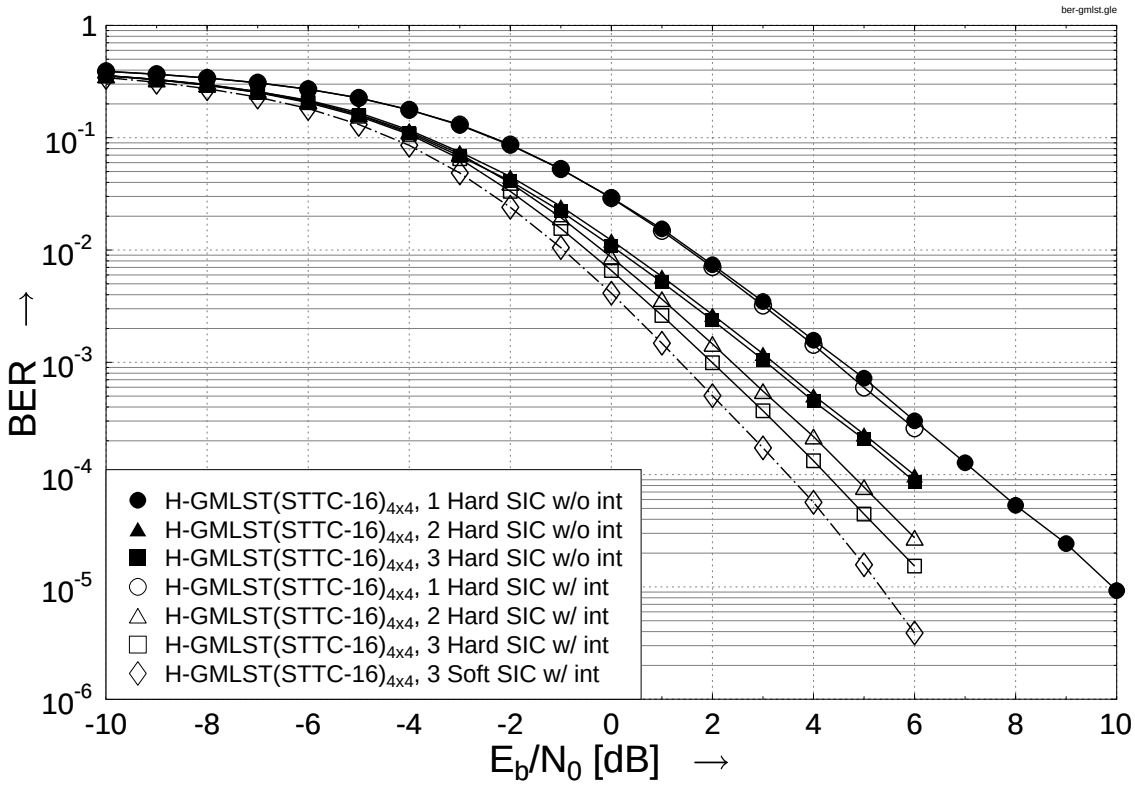


(b) BER performance of the H-GMLST(STTC) schemes of Fig. 2.1 using the parameters of Table 2.1

**Figure 2.10:** Performance of iterative multistage SIC detection in the (4, 4) H-GMLST systems using the parameters of Table 2.1.

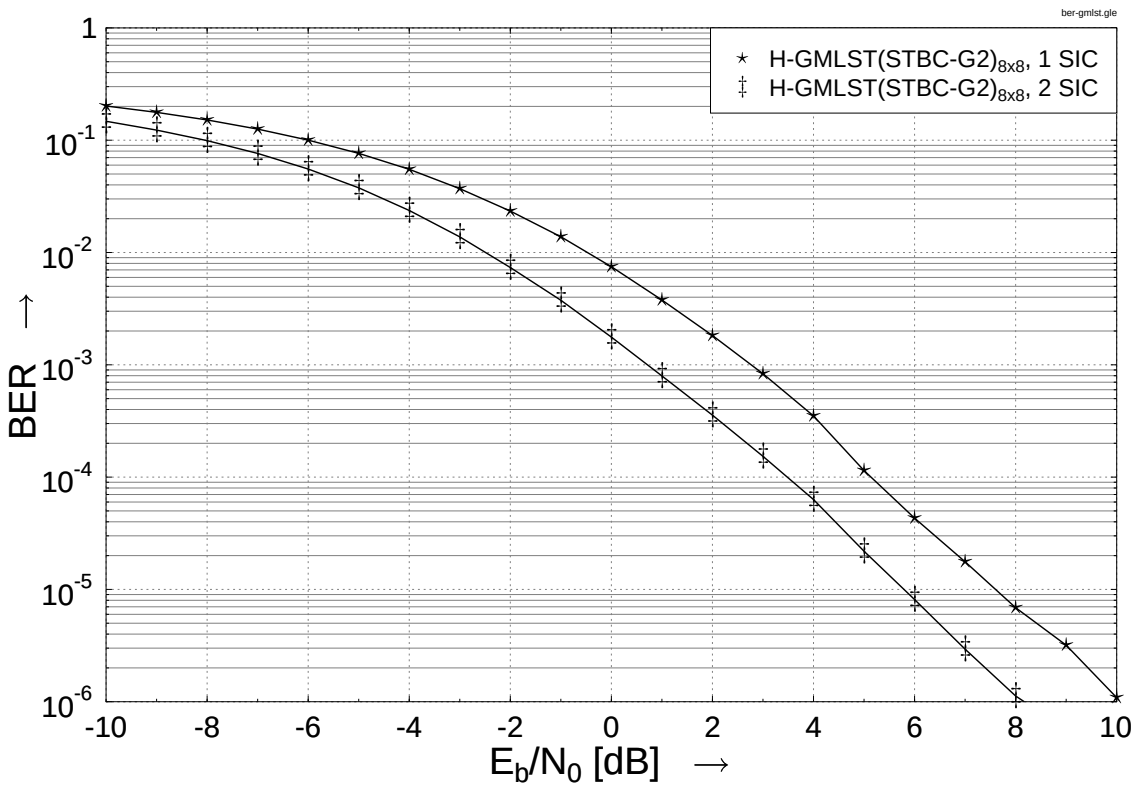


(a) BER performance of the H-GMLST(STBC) schemes of Fig. 2.2 using the parameters of Table 2.1

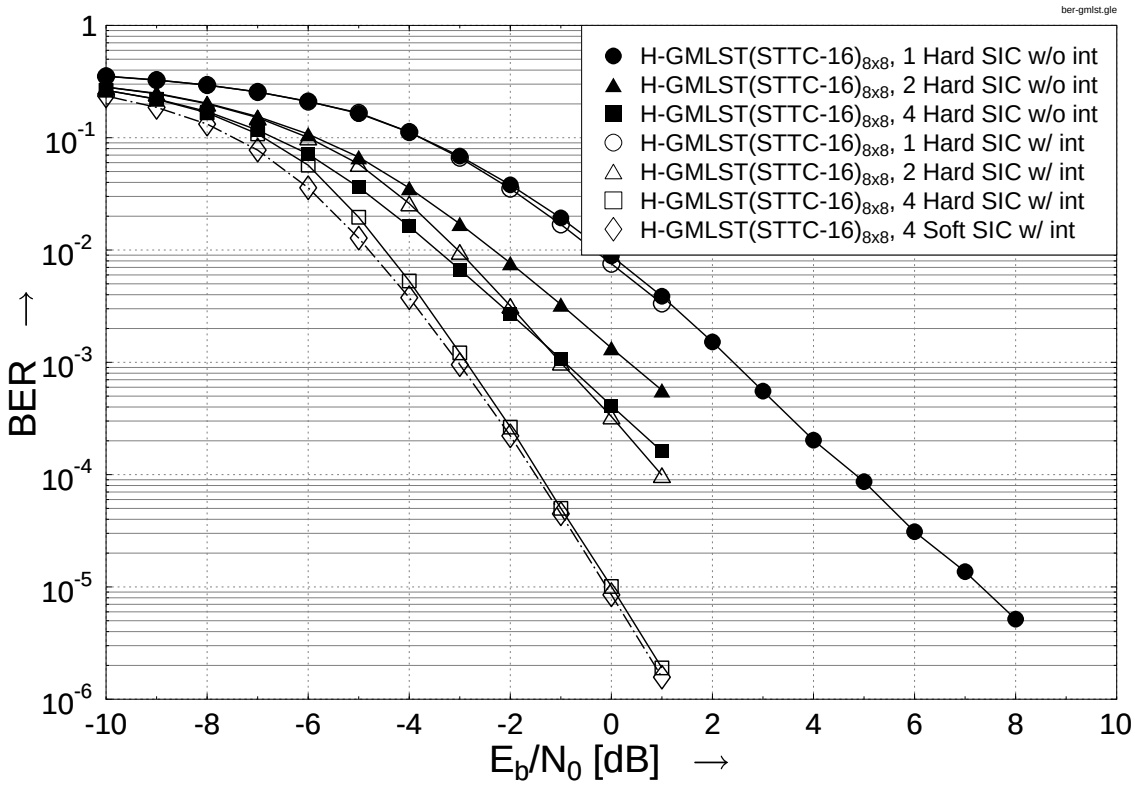


(b) BER performance of the H-GMLST(STTC) schemes of Fig. 2.1 using the parameters of Table 2.1

**Figure 2.11:** Performance of iterative multistage SIC detection in the (8, 8) H-GMLST systems using the parameters of Table 2.1.

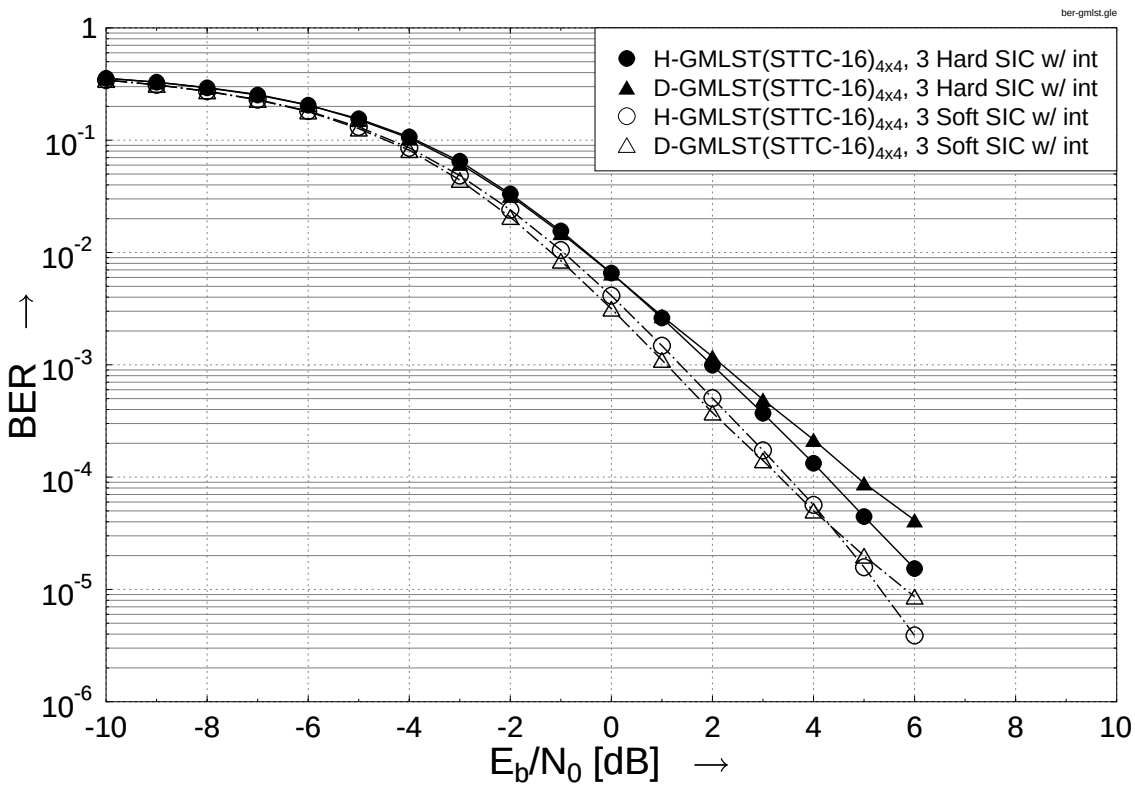


(a) BER performance of the (4, 4) system using the parameters of Table 2.1

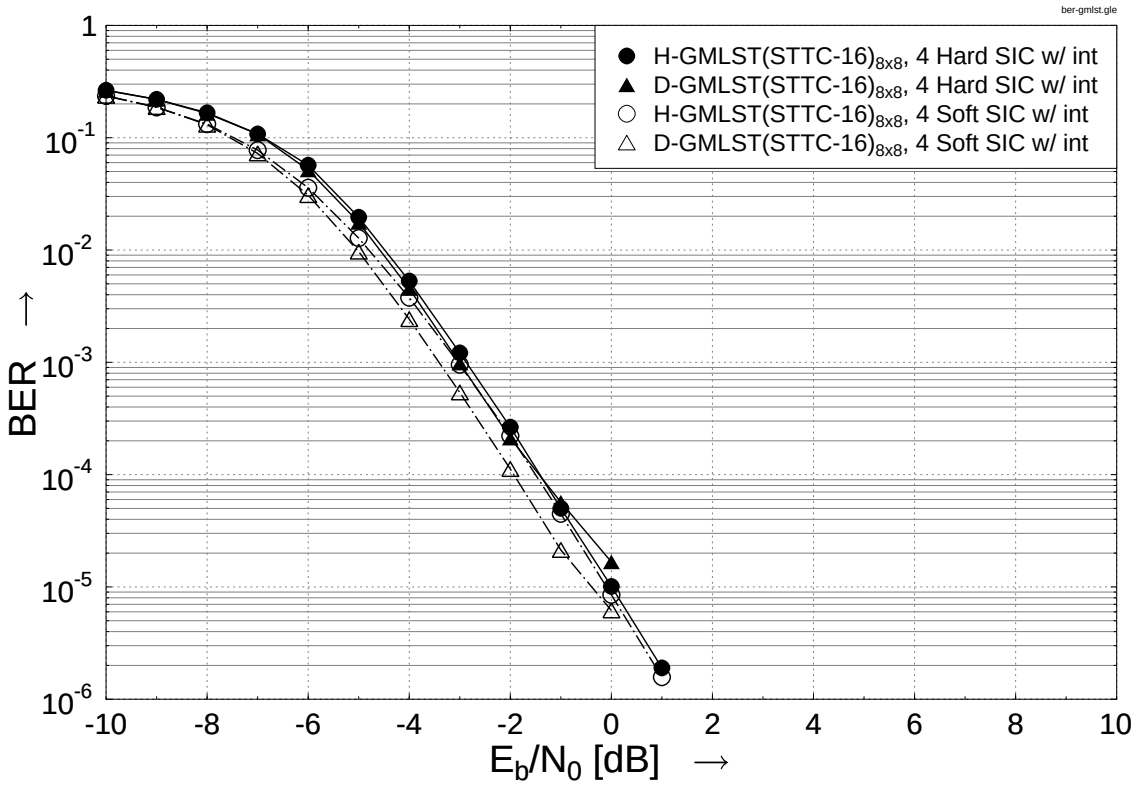


(b) BER performance of the (8, 8) system using the parameters of Table 2.1

**Figure 2.12:** Performance comparison of the H-GMLST(STTC) and D-GMLST(STTC) schemes using iterative multistage SIC detection in the (4, 4) and (8, 8) systems using the parameters of Table 2.1.

tions. Similar performance comparisons were conducted for the (8, 8) H-GMLST(STTC) system in Fig. 2.11(b). The performance improvements achieved by the iterative detection relying on the interleaver of Fig. 2.11(b) becomes larger. When using four hard SIC iterations, we achieve a gain of around 4.5 dB over the first iteration, which is also shown in Fig. 2.8(b) in conjunction with the optimally ordered detection at the target BER of $10^{-2}$. It is also observed from Fig. 2.11(b) that the interleavers have a key impact on the success of the iterative detection procedure. When using four iterations, the attainable performance of the interleaved system is improved by almost 2.0 dB at the target BER of $10^{-3}$ over the system operating without interleavers. Similarly observe in Fig. 2.11(b) that the iterative soft SIC operation attains more substantial performance advantages than its hard-decision-aided counterpart and the gain achieved after four SIC iterations becomes marginal.

The achievable performance of the interleaved D-GMLST(STTC) scheme of Fig. 2.1(c) using both the optimally and arbitrarily ordered detection is characterized in Fig. 2.12 for both the (4, 4) and (8, 8) systems for comparison. It is clearly seen from the BER curves that the (8, 8) system benefits from a higher diversity order than that in the (4, 4) system. We can also see in Fig. 2.12 that at the same number of iterations, the H-GMLST(STTC) scheme performs slightly worse than the D-GMLST(STTC) arrangement in the range of low $E_b/N_0$ values, but outperforms the D-GMLST(STTC) regime at high $E_b/N_0$ values.

## 2.7 Chapter Conclusion

In this chapter, a combination of V-BLAST and STCs designed for MIMO systems were investigated, which we referred to as Generalized Multi-Layer Space-Time Coding. Two fundamental schemes were designed, namely the GMLST(STBC) and GMLST(STTC) arrangements of Figs. 2.1 and 2.2, where STBCs and STTCs were used as the component space-time codes, respectively. According to the different mapping of the signals to the antennas, the GMLST(STTC) regime was further divided into two schemes, namely H-GMLST(STTC) and D-GMLST(STTC) arrangements. On the other hand, for the GMLST(STBC) scheme of Fig. 2.2, only horizontal mapping was considered, since no additional spatial diversity can be obtained, when employing diagonal mapping. The basic detection procedure devised for the GMLST schemes is constituted by the ordered successive detection scheme combining group-based interference nulling and interference cancellation, as portrayed in Fig. 2.3. Furthermore, in Section 2.4 we introduced Tarokh's power allocation regime for detection using an arbitrary order, which outperformed the conventional schemes relying on equal-power allocation at the same compu-

| GMLST Schemes | | Diversity Order | SNR Loss |
|---|---|---|---|
| H-GMLST(STBC) | ZF-SIC | $\approx (N_r - N_t + N_t^j) \times N_t^j$ | High |
| | PA aided SIC | $\approx (N_r - N_t + N_t^j) \times N_t^j$ | Low |
| | Ordered SIC | $\geq (N_r - N_t + N_t^j) \times N_t^j$ | Low |
| | Iterative SIC | $\approx N_r \times N_t^j$ | Low |
| | ML | $= N_r \times N_t^j$ | Zero |
| H-GMLST(STTC) | ZF-SIC | $\approx (N_r - N_t + N_t^j) \times N_t^j$ | High |
| | PA aided SIC | $\approx (N_r - N_t + N_t^j) \times N_t^j$ | Low |
| | Ordered SIC | $\geq (N_r - N_t + N_t^j) \times N_t^j$ | Low |
| | Iterative SIC | $\approx N_r \times N_t^j$ | Low |
| | Iterative Soft SIC | $\approx N_r \times N_t^j$ | Lower |
| | ML | $= N_r \times N_t^j$ | Zero |
| D-GMLST(STTC) | ZF-SIC | $> (N_r - N_t + N_t^j) \times N_t^j$ | High |
| | PA aided SIC | $> (N_r - N_t + N_t^j) \times N_t^j$ | Low |
| | Iterative SIC | $\geq N_r \times N_t^j$ | Low |
| | Iterative Soft SIC | $\geq N_r \times N_t^j$ | Lower |
| | ML | $> N_r \times N_t^j$ | Zero |

**Table 2.2:** Summary of comparative performance of GMLST schemes.

tational complexity. For the H-GMLST systems of Figs. 2.1(b) and 2.2, which relied on equal-power allocation, in Section 2.5 we also discussed the optimal detection order based on the assumption that the channel coefficients are perfectly known at the receiver. Finally, in Section 2.6 an iterative SIC-based detection scheme was advocated for both the GMLST(STTC) and GMLST(STBC) arrangements, in order to exploit the potential of full receive antenna diversity. The simulation results of Figs. 2.10 and 2.11 show that the iterative detection scheme is capable of approaching the same receive diversity order as ML-style joint detection while imposing only a fraction of the computational complexity of ML-style joint detection. Table 2.2 summarizes the performance versus complexity of various GMLST schemes, where the SNR loss is caused by the SIC-induced error propagation among different layers of the GMLST scheme. In conclusion, the iterative SIC-based GMLST scheme of Fig. 2.9 provides a promising practical solution for high-data-rate, high-integrity communications in MIMO systems, especially when the number of antennas is high.

In the next chapter, we will demonstrate that further performance improvements may be attained by the concatenation of the GMLST schemes with channel codes and upon performing iterative detection by exchanging extrinsic information between the different

component decoders/demodulators at the receiver side. Furthermore, we will use EXtrinsic Information Transfer (EXIT) charts to analyze the convergence behaviour of the iteratively detected system.

Chapter 3

# Near-Capacity Iteratively-Decoded Generalized Multi-Layer Space-Time Codes

## 3.1 Introduction

In Chapter 2, a Generalized Multi-Layer Space-Time (GMLST) coding scheme was proposed. It was shown that the GMLST scheme of Fig. 2.1 may be viewed as a beneficial amalgam of a V-BLAST and a STC scheme. With the advent of the STC employed, the GMLST architecture is capable of achieving a higher spatial diversity than the conventional V-BLAST scheme. Furthermore, as an added benefit, the system's overall throughput becomes significantly higher than that of the STC scheme, owing to its BLAST-like layered architecture. Despite these merits, the system performance of a stand-alone uncoded GMLST scheme is far from the achievable MIMO channel capacity. On the other hand, it is well known that turbo codes [51] benefit from an *iterative processing* gain and are capable of facilitating near-capacity operation without imposing an excessive decoding complexity or latency. This is achieved using the iterative exchange of so-called 'soft' information between the component decoders. With each iteration, the quality of the exchanged soft information gradually improves upon iterating, but starts to saturate closer to the system's capacity until eventually no further improvements can be obtained. The general turbo principle [92, 93] was extended to multiple parallel concatenated codes in [52], to serially concatenated codes in [94] and to multiple serially concatenated codes in [95]. Hence, the performance of the GMLST coding scheme can be enhanced by combining it with iterative detection aided schemes in a serial fashion, where iterative decoding is carried out by exchanging extrinsic information between the

different constituent decoders.

In the past few years, studying the convergence behaviour of iterative decoding has drawn considerable attention [64, 65, 96–104]. In [64], Stephan ten Brink proposed the employment of the so-called EXtrinsic Information Transfer (EXIT) characteristics between a concatenated decoder's input and output for characterizing the flow of extrinsic information through the Soft-Input Soft-Output (SISO) constituent decoders. A tutorial introduction to EXIT charts can be found in [65].

Recently, irregular coding techniques [59–61] have enabled 'very-near-capacity' operation. In [61, 81], Tüchler and Hagenauer proposed the employment of IRregular Convolutional Codes (IRCCs) in serially concatenated schemes, which are constituted by a family of convolutional codes having different rates, in order to design a near-capacity system. Hence, for the sake of decoding convergence at near-capacity Signal-to-Noise Ratios (SNRs), the GMLST scheme is serially concatenated with the IRCC as the outer code. The decoding convergence of iteratively decoded schemes can be analysed using EXIT charts [61, 64, 101]. The IRCCs were specifically designed with the aid of EXIT charts to improve the achievable convergence behaviour of our iteratively decoded GMLST scheme.

Furthermore, it was shown in [67, 105, 106] that a recursive code is needed as an intermediate code, when the inner code is non-recursive, in order to achieve decoding convergence to an infinitesimally low bit error ratio (BER) at low SNRs, while avoiding the formation of a BER floor when employing iterative decoding. Therefore, as a further advance, a recursive Unity-Rate Code (URC) [67, 105–108] can be employed as an intermediate code in order to improve the attainable decoding convergence of the three-stage serially concatenated GMLST scheme.

*Against this backcloth, the novel contribution of this chapter can be summarized as follows:*

1. *We derive the Discrete-input Continuous-output Memoryless Channel (DCMC) [14] capacity formula of GMLST(STBC) schemes and based on the area property of EXIT charts, the maximum achievable rates of various iterative multi-stage SIC and ML based GMLST schemes are obtained as well.*

2. *Once the DCMC capacity and the maximum achievable rates were attained, we use EXIT charts to design an iteratively decoded near-capacity serially concatenated IRCC-URC-GMLST scheme. A recursive Unity-Rate Code (URC) is invoked as an intermediate code, which changes only the shape of the EXIT curve, but not the area under the EXIT curve of the inner GMLST decoder in order to completely eliminate*

*the system's error-floor and to improve the attainable decoding convergence.*

3. *In order to enhance the attainable performance, we redesigned the original IRCCs of Tüchler and Hagenauer, invoking more component codes to match the inner codes' EXIT functions more accurately.*

4. *The computational complexity of this concatenated scheme is substantially reduced at the cost of a modest reduction in the maximum achievable rate compared to that of ML detection, owing to the employment of the low-complexity but suboptimum SIC in the GMLST decoder.*

The rest of the chapter is organised as follows. An overview of the serially concatenated and iteratively decoded channel-coded GMLST scheme is presented in Section 3.2, where the *A Posteriori Probability* (APP)-based iterative multistage SIC detection of Fig. 3.2 and the iterative ML detection of Fig. 3.3 are employed for the GMLST schemes. In Section 3.2.2 we introduce the EXIT chart analysis technique and illustrate how to generate EXIT charts for visualizing the interaction of the inner as well as of the outer codes. In Section 3.3, a three-stage serially concatenated IRCC- and URC-coded GMLST scheme is proposed for the sake of near-capacity communications, which is designed systematically based on EXIT chart analysis. Specifically, we derive the DCMC capacity formula of GMLST(STBC) schemes and quantify the maximum achievable rate of different GMLST schemes in Section 3.3.2. The proposed EXIT chart aided iterative system design is detailed in Section 3.3.3, while our simulation results and discussions are provided in Section 3.3.4. Finally, we conclude this chapter in Section 3.4.

## 3.2 Iteratively-Decoded Channel-Coded GMLST Scheme

In this chapter, we consider transmissions over a temporally uncorrelated flat Rayleigh fading channel. The point-to-point wireless communication link is equipped with $N_t$ transmit and $N_r$ receive antennas. When complex-valued $\mathcal{M}$-ary PSK/QAM is employed, the received signal vector of the MIMO system can be written as:

$$\mathbf{y} = \mathbf{H}\mathbf{c} + \mathbf{n} \,, \tag{3.1}$$

where $\mathbf{y} = [y_1, \ldots, y_{N_r}]^T$ is an $N_r$-element vector of the received signals, $\mathbf{H}$ is an $(N_r \times N_t)$-element channel matrix, the entries of which are independent and identically complex Gaussian distributed with a zero mean and a variance of 0.5 per dimension, $\mathbf{c} = [c_1, \ldots, c_{N_t}]^T$ is an $N_t$-element vector of the transmitted signals and $\mathbf{n} = [n_1, \ldots, n_{N_r}]^T$ is an $N_r$-element noise vector. Each element of $\mathbf{n}$ is an Additive White Gaussian Noise (AWGN) process having a zero mean and a variance of $N_0/2$ per dimension.

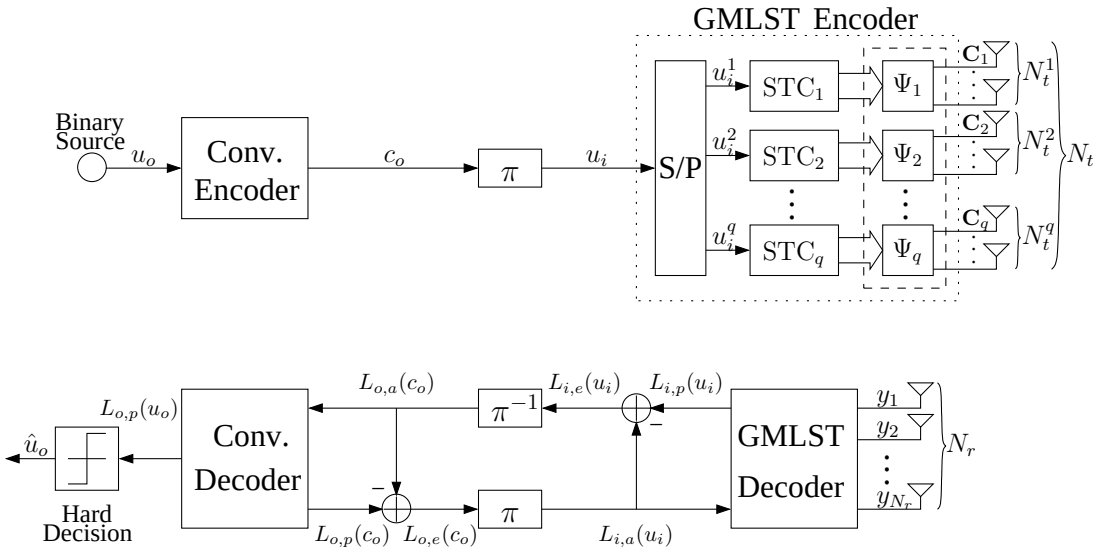


**Figure 3.1:** Iteratively-decoded GMLST system block diagram.

A high level block diagram of the iteratively-decoded GMLST system is depicted in Fig. 3.1, where the transmitted binary source bit stream $u_o$ is encoded by a 1/2-rate Recursive Systematic Convolutional (RSC) code and then interleaved by a random bit-wise interleaver $\pi$. After channel interleaving, the RSC coded bit stream $c_o$ is taken as the information bit stream $u_i$ of the GMLST encoder, which is illustrated at the top right of Fig. 3.1. Note that the spatial interleaver of Fig. 2.1(a) in Chapter 2 is not needed here, since the inherent time diversity of the fast fading channel is dominant. The information bit stream $u_i$ is input to a serial-to-parallel (S/P) converter, which partitions this bit stream into $q$ groups having lengths of $u_i^1, u_i^2, \ldots, u_i^q$, respectively. Then, each group of $u_i^j$ bits, for $1 \leq j \leq q$, is separately encoded by a component encoder $STC_j$ associated with $N_t^j$ number of transmit antennas, where we have $N_t^1 + N_t^2 + \ldots + N_t^q = N_t$. The resultant $(N_t^j \times K)$-element *codeword* matrix $\mathbf{C}_j$ of $STC_j$ will be transmitted by the $N_t^j$ transmit antennas during $K$ symbol intervals. Similarly to the definition in Section 2.2 of Chapter 2, we also refer to the $k$th column $\mathbf{c}_{j,k}$ of $\mathbf{C}_j$ as the *symbol vector* generated by group $j$ at time instant $k$. Furthermore, as presented in Chapter 2, when the STBC is employed as the component space-time code, the vector-based temporal interleavers represented by the dashed block of Fig. 3.1 are not needed any more.

At the receiver side of Fig. 3.1, the SISO APP-based RSC decoder iteratively exchanges extrinsic information with the APP-based GMLST decoder. The RSC decoder invokes the Bahl-Cocke-Jelinek-Raviv (BCJR) algorithm [90] for the bit-based trellis [109]. All BCJR calculations are performed in the logarithmic domain and use a lookup table for correcting the Jacobian approximation in the Log Maximum A-posteriori Probability (Log-MAP) algorithm [89, 110]. The extrinsic soft information, represented in the

form of Logarithmic Likelihood Ratios (LLRs) [111], is iteratively exchanged between the RSC decoder and the GMLST decoder for the sake of assisting each other's operation, as detailed in [112]. In Fig. 3.1, $L(.)$ denotes the LLRs of the bits concerned, where the subscript $i$ relates to the inner GMLST decoder, while $o$ corresponds to outer RSC decoding. Additionally, the subscripts $a$, $p$ and $e$ denote the nature of the LLRs, with $a$, $p$ and $e$ indicating *a priori*, *a posteriori* and extrinsic information, respectively.

As shown in Fig. 3.1, the received signal vectors $\mathbf{y}$ are detected by the GMLST decoder based on their LLR representation for each of the interleaved channel-coded bits $u_i$. The *a priori* LLR values $L_{i,a}(u_i)$ of the GMLST decoder are subtracted from the *a posteriori* LLR values $L_{i,p}(u_i)$ for the sake of generating the extrinsic LLR values $L_{i,e}(u_i)$, and then the LLR values $L_{i,e}(u_i)$ are deinterleaved by a soft-bit deinterleaver represented by $\pi^{-1}$, as seen in Fig. 3.1. Next, the soft bits $L_{o,a}(c_o)$ are passed to the SISO RSC decoder in order to compute the *a posteriori* LLR values $L_{o,p}(c_o)$ provided by the Log-MAP algorithm [110] for all the channel-coded bits. During the last iteration, only the LLR values $L_{o,p}(u_o)$ of the source information bits $u_o$ are required, which are passed to the hard decision block of Fig. 3.1 in order to determine the estimated source information bits $\hat{u}_o$. As seen in Fig. 3.1, the extrinsic information $L_{o,e}(c_o)$ is generated by subtracting the *a priori* information $L_{o,a}(c_o)$ from the *a posteriori* information $L_{o,p}(c_o)$, which is then fed back to the GMLST decoder as the *a priori* information $L_{i,a}(u_i)$ after appropriately reordering them using the soft-bit interleaver $\pi$ of Fig. 3.1. The GMLST decoder of Fig. 3.1 exploits the *a priori* information $L_{i,a}(u_i)$ in conjunction with the received signals $\mathbf{y}$ for the sake of providing improved *a posteriori* LLR values $L_{i,p}(u_i)$, which are then passed to the RSC channel decoder and then back to the GMLST decoder for further iterations.

### 3.2.1 APP-Based Iterative Detection of GMLST Schemes

It is clearly seen in Fig. 3.1 that the soft decoded information of the GMLST decoder is required for facilitating the iterative decoding process. Recall from Fig. 2.9 of Section 2.6 that an efficient hard-decision based iterative multistage SIC detection algorithm was proposed for the sake of achieving the maximum attainable receive diversity for all layers of the GMLST scheme, where no soft information was exploited. Hence, in Section 3.2.1.1, an APP-based iterative multistage SIC detection scheme will be proposed, where the APP-based SISO STC decoders are considered instead of the conventional hard-decision space-time decoders of Fig. 2.9. For comparison, in Section 3.2.1.2 we also propose an iterative ML detection scheme for our GMLST(STTC) arrangement, which imposes a potentially excessive complexity owing to jointly detecting all groups.

### 3.2.1.1 APP-Based Iterative Multistage SIC Detection

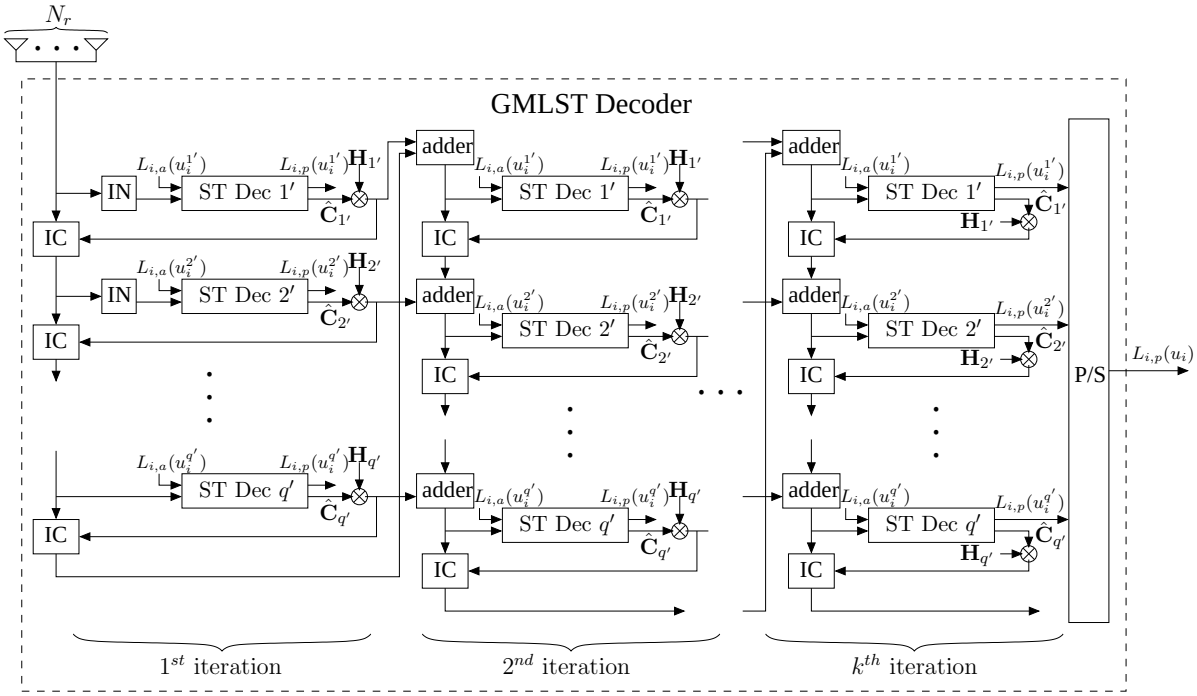


(a) main block diagram

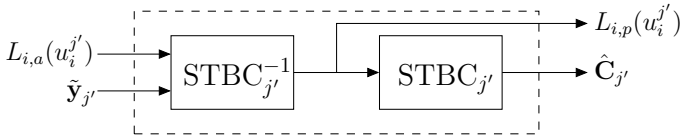


(b) sub-block diagram for the "ST Dec $j'$" component for STBC, where $\mathrm{STBC}_{j'}^{-1}$ represents the STBC decoder which outputs the soft *a posteriori* LLR values $L_{i,p}(u_i^{j'})$ and $\mathrm{STBC}_{j'}$ is the corresponding STBC recoder

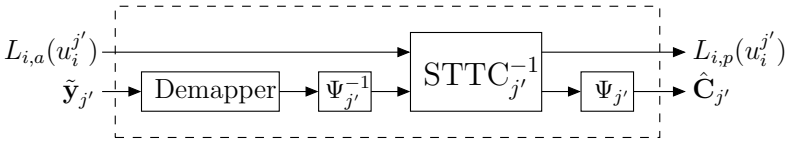


(c) sub-block diagram for the "ST Dec $j'$" component for STTC, where $\mathrm{STTC}_{j'}^{-1}$ represents soft-input soft-output APP-based STTC decoder and $L_{i,a}(u_i^{j'})$ correspond to the *a priori* LLR values of the information bits $u_i^{j'}$

**Figure 3.2:** GMLST receiver schematic employing iterative multistage APP-based SIC detection, where "IN" and "IC" denote the group interference nulling module and the group interference cancellation module, respectively.

As presented in Section 2.6, the GMLST coding scheme of Fig. 3.1 may rely on a reduced-complexity iterative multistage SIC detection algorithm, which is capable of achieving the maximum attainable receive diversity. Again, in this section, a reduced-complexity APP-based iterative SIC detection scheme is proposed in Fig. 3.2 for the sake of facilitating the iterative decoding process of Fig. 3.1 as well as maintaining an affordable computational complexity. In order to maintain a low complexity, the signals are

detected layer-by-layer in a multistage manner, as in Fig. 2.9 of Chapter 2, instead of using high-complexity ML-style joint-detection. We note that in contrast to the discussions in Chapter 2, the specific decoding order of the iterative SIC-based scheme of Fig. 3.2 has no effect on the attainable performance of the GMLST arrangement since the signals transmitted from the different GMLST layers experience the same time-varying channels in a fast-fading scenario, hence can be arbitrary. Similarly, the decoding order in Fig. 3.2 is assumed to be $\{1', 2', \ldots, q'\}$ without any loss of generality.

The APP-based iterative multistage SIC detection procedure of Fig. 3.2 is generally similar to that of Fig. 2.9, except that the corresponding APP-based STC decoders are used instead of the previous hard-decision STC decoders of Fig. 2.3 in Chapter 2. It is clearly seen in Fig. 3.2(a) that, at the $j$-th decoding stage encountered during a specific SIC iteration, the $j'$-layer *codeword* is denoted by $\hat{\mathbf{C}}_{j'}$, which is decoded using the APP-based space-time decoders of Fig. 3.2(b) and Fig. 3.2(c) for the STBCs and STTCs, respectively, in conjunction with the *a priori* LLR values $L_{i,a}(u_i^{j'})$ gleaned from the outer channel decoder of Fig. 3.1. The decoded soft output LLR values $L_{i,p}(u_i^{j'})$ are subtracted by the corresponding *a priori* LLRs $L_{i,a}(u_i^{j'})$ and then used as the *a priori* information of the outer channel decoder in Fig. 3.1. Note that in Fig. 3.2(c), the corresponding STTC recoders of Fig. 2.3(c) discussed in Chapter 2 are no longer needed, which apparently results in a computational complexity reduction.

#### 3.2.1.2 Iterative ML Detection

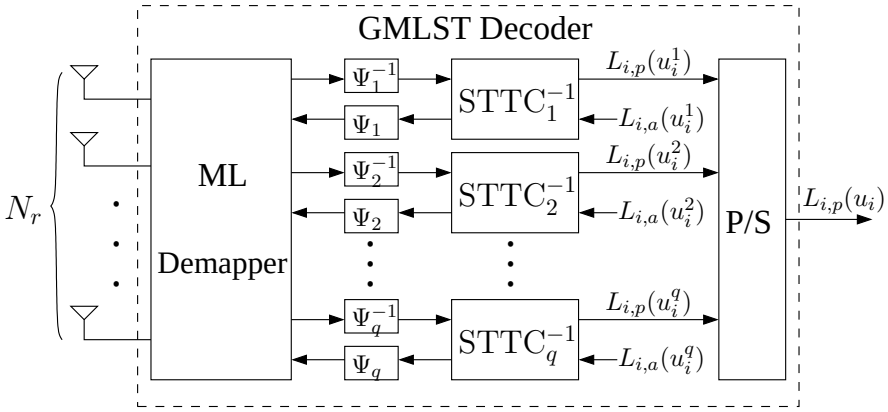


**Figure 3.3:** Iterative ML detection of the GMLST(STTC) scheme, where $\Psi_j$ is the corresponding temporal interleaver, $\text{STTC}_j^{-1}$ represents $j$-layer soft-input soft-output APP-based space-time decoder and $L_{i,a}(u_i^j)$ correspond to the *a priori* LLR values of the information bits $u_i^j$.

For comparison, we also present a significantly more complex iterative ML detection scheme designed for the GMLST(STTC) schemes of Fig. 3.1. The iterative ML detection procedure is shown in Fig. 3.3. Firstly, the $N_t$ transmitted $\mathcal{M}$-ary symbols are jointly detected as a combined $[N_t \times \log_2 \mathcal{M}]$-bit symbol by an ML demapper. Then, the probability

vector of each $[N_t \times \log_2 \mathcal{M}]$-bit symbol is converted to $q$ number of probability vectors corresponding to the $q$ number of $[N_t^j \times \log_2 \mathcal{M}]$-bit symbols of the different layers. The resultant probability vectors are then fed to the component STTC decoders.

Similar to the concept of Bit-Interleaved Coded Modulation schemes using Iterative Decoding (BICM-ID) [113–118], an iterative detection gain can be attained, since the EXIT curve of the ML demapper seen in Fig. 3.3 is a sloping line. However, it is not guaranteed that the DCMC capacity to be detailed in Section 3.3.2 can be achieved with the aid of iterative ML detection, because the maximum achievable rate of the iterative ML detection scheme is dependent on the EXIT curve shapes of the various space-time trellis codes.

On the other hand, the ML detection of GMLST(STBC) schemes is conceptually straightforward but implementationally complex. A specific GMLST scheme using identical STBCs as the component space-time codes is designed for encoding over $L$ transmission symbols, assuming that the channel's envelope may be considered quasi-static over this period. Based on Eq. (3.1), the signal received during $L$ symbol periods can be written as:

$$\mathbf{Y} = \mathbf{HC} + \mathbf{N} \,, \tag{3.2}$$

where $\mathbf{Y} = [\mathbf{y}_1, \ldots, \mathbf{y}_L] \in \mathbb{C}^{N_r \times L}$ is the sampled received signal matrix, $\mathbf{H} \in \mathbb{C}^{N_r \times N_t}$ is the quasi-static channel matrix, which is constant over $L$ symbol periods, $\mathbf{C} = [\mathbf{c}_1, \ldots, \mathbf{c}_L] \in \mathbb{C}^{N_t \times L}$ is the GMLST(STBC) *codeword* matrix and $\mathbf{N} = [\mathbf{n}_1, \ldots, \mathbf{n}_L] \in \mathbb{C}^{N_r \times L}$ represents the additive white Gaussian noise matrix.

Let us assume that we have a total of $M$ possible GMLST(STBC) *codeword* matrix combinations for $L$ consecutive symbol periods. Based on Eq. (3.2), the conditional probability of receiving a signal matrix $\mathbf{Y}$, given that an $M$-ary GMLST(STBC) *codeword* matrix of $\mathbf{C}^m$, $m \in \{1, \ldots, M\}$, was transmitted over uncorrelated flat Rayleigh fading channels is determined by the Probability Density Function (PDF) of the noise, yielding:

$$\begin{aligned} p(\mathbf{Y}|\mathbf{C}^m) &= \frac{1}{(\pi N_0)^{LN_r}} \exp\left(\frac{-\|\mathbf{Y} - \mathbf{HC}^m\|^2}{N_0}\right), \\ &= \prod_{k=1}^{L} \prod_{r=1}^{N_r} \frac{1}{\pi N_0} \exp\left(\frac{-|y_{r,k} - \sum_{t=1}^{N_t} h_{r,t} c_{t,k}^m|^2}{N_0}\right). \end{aligned} \tag{3.3}$$

Similarly, once the conditional probability $p(\mathbf{Y}|\mathbf{C}^m)$ was obtained, the iterative decoding process can be activated between the outer channel decoder and the GMLST(STBC) ML decoder using the iterative BICM-ID procedure [114, 118].

### 3.2.2 EXIT Chart Analysis

The concept of EXIT charts was proposed in [64, 101], which assist us in predicting the convergence behaviour of iterative decoders by examining the evolution of the input/output mutual information exchange either between the inner and outer decoders of a serially concatenated scheme or between the upper and lower decoders of a parallel concatenated arrangement during the consecutive iterations. The application of EXIT charts is based on two main assumptions, which are realistic when using long interleavers, namely that the *a priori* LLR values are fairly uncorrelated and that the Probability Density Function (PDF) of the *a priori* LLR values can be modelled by the Gaussian distribution. Additionally, a number of EXIT chart variations have been proposed in the literature. These include three-dimensional EXIT charts [67] developed for characterizing the iterative decoding convergence properties of three-stage serial concatenations. Furthermore, non-binary EXIT charts [119] may be employed to characterize concatenated schemes, where the iteratively exchanged soft information pertains to symbol values, rather than bit values.

#### 3.2.2.1 Transfer Characteristics of the GMLST Decoder

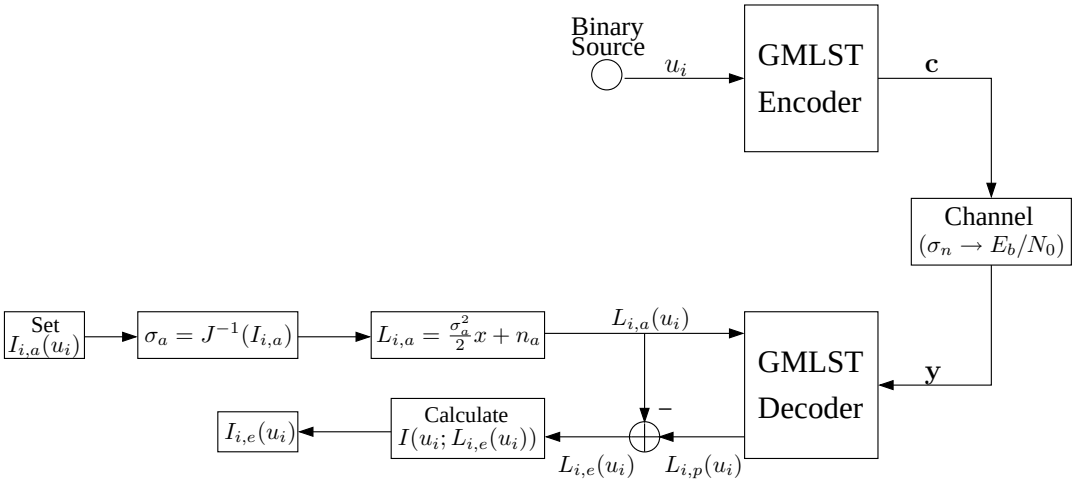


**Figure 3.4:** The GMLST decoder's transfer characteristics evaluation procedure block diagram.

As seen in Fig. 3.1, the inputs of the GMLST decoder are the noise-contaminated channel output observations $\mathbf{y}$ and the *a priori* information $L_{i,a}(u_i)$ generated by the outer channel decoder. The GMLST decoder of Fig. 3.1 outputs the *a posteriori* information $L_{i,p}(u_i)$, subtracts the *a priori* information and hence produces the extrinsic information $L_{i,e}(u_i)$. Based on the above-mentioned two assumptions, the *a priori* input $L_{i,a}(u_i)$ can be modelled by applying an independent zero-mean Gaussian random variable having a variance of $\sigma_a^2$. In conjunction with the outer channel coded and interleaved bits $u_i \in \{0, 1\}$ of Fig. 3.1 or equivalently $x \in \{-1, +1\}$, the *a priori* input $L_{i,a}(u_i)$ can be written

as [64]

$$L_{i,a} = \frac{\sigma_a^2}{2} \cdot x + n_a, \tag{3.4}$$

since $L_{i,a}$ is an LLR-value obeying the Gaussian distribution [111]. Accordingly, the conditional PDF of the *a priori* input $L_{i,a}(u_i)$ is

$$p_a(\zeta|X=x) = \frac{1}{\sqrt{2\pi}\sigma_a} \cdot \exp\left(-\frac{\left(\zeta - \frac{\sigma_a^2}{2} \cdot x\right)^2}{2\sigma_a^2}\right). \tag{3.5}$$

The mutual information $I_{i,a}(u_i) = I[u_i; L_{i,a}(u_i)]$ or equivalently $I_{i,a}(u_i) = I[x; L_{i,a}(u_i)]$ between the outer coded and interleaved bit stream $u_i$ and the *a priori* LLR values $L_{i,a}(u_i)$ is used to quantify the information content of the *a priori* knowledge [120] as follows:

$$I_{i,a}(u_i) = \frac{1}{2} \cdot \sum_{X=-1,+1} \int_{-\infty}^{+\infty} p_a(\zeta|X) \cdot \log_2 \frac{2 \cdot p_a(\zeta|X)}{p_a(\zeta|X=-1) + p_a(\zeta|X=+1)} d\zeta. \tag{3.6}$$

Using Eq. (3.5), Eq. (3.6) can be expressed as

$$I_{i,a}(\sigma_a) = 1 - \frac{1}{\sqrt{2\pi}\sigma_a} \int_{-\infty}^{+\infty} \exp\left(-\frac{\left(\zeta - \frac{\sigma_a^2}{2}\right)^2}{2\sigma_a^2}\right) \cdot \log_2\left[1 + e^{-\zeta}\right] d\zeta. \tag{3.7}$$

For notational simplicity and in order to highlight the dependence of $I_{i,a}$ on $\sigma_a$, we define [64, 101]

$$J(\sigma) := I_{i,a}(\sigma_a = \sigma) \tag{3.8}$$

with

$$\lim_{\sigma \to 0} = 0, \quad \lim_{\sigma \to \infty} = 1, \quad \sigma > 0. \tag{3.9}$$

The function $J(\sigma)$ is monotonically increasing [120] and thus reversable. Furthermore, it was shown in [61] that the mutual information between the equiprobable bits $X$ and their respective LLRs $L$ for *symmetric* and *consistent*[1] $L$-values always simplifies to

$$\begin{aligned} I(X;L) &= 1 - \int_{-\infty}^{+\infty} p(L|X=+1) \cdot \log_2\left[1 + e^{-L}\right] dL \\ I(X;L) &= 1 - E_{X=+1}\left\{\log_2\left[1 + e^{-L}\right]\right\}. \end{aligned} \tag{3.10}$$

In order to quantify the information content of the extrinsic LLR values $L_{i,e}(u_i)$ at the output of the GMLST decoder of Fig. 3.1, the mutual information $I_{i,e}(u_i) = I[u_i; L_{i,e}(u_i)]$

[1] The LLR values are symmetric if their PDF is symmetric $p(-\zeta|X=+1) = p(\zeta|X=-1)$. Additionally, all LLR values with symmetric distribution satisfy the consistency condition [61]: $p(-\zeta|X=x) = e^{-x\zeta} p(\zeta|X=x)$.

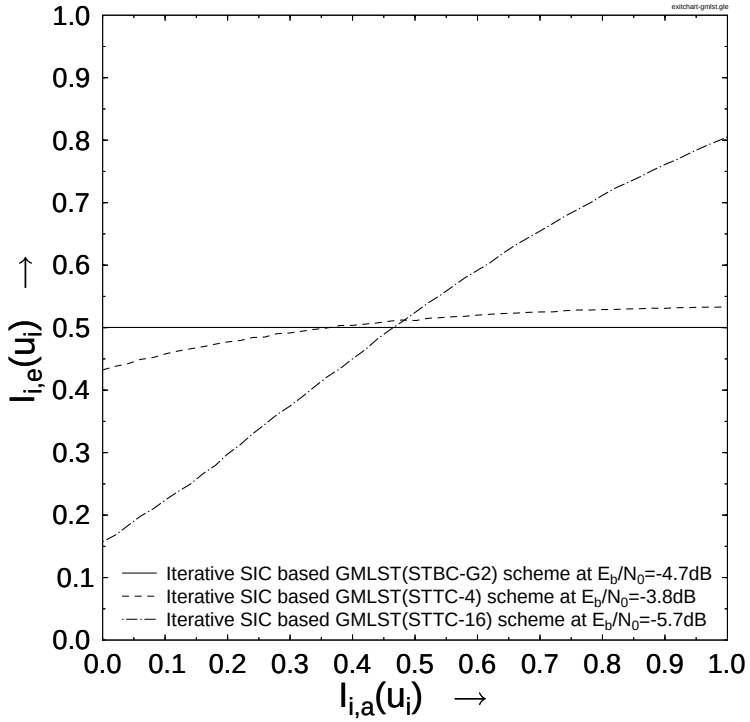


**Figure 3.5:** Extrinsic information transfer characteristics of various GMLST schemes using iterative SIC detection.

can be used, which is computed as in Eq. (3.6) using the PDF $p_e$ of the extrinsic output expressed as

$$I_{i,e}(u_i) = \frac{1}{2} \cdot \sum_{X=-1,+1} \int_{-\infty}^{+\infty} p_e(\zeta|X) \cdot \log_2 \frac{2 \cdot p_e(\zeta|X)}{p_e(\zeta|X=-1) + p_e(\zeta|X=+1)} d\zeta. \quad (3.11)$$

Considering $I_{i,e}(u_i)$ as a function of both $I_{i,a}(u_i)$ and the $E_b/N_0$ value encountered, the GMLST decoder's extrinsic information transfer characteristic is defined as [64, 101]

$$I_{i,e}(u_i) = T_i[I_{i,a}(u_i), E_b/N_0]. \quad (3.12)$$

Fig. 3.4 illustrates how the EXIT characteristic $I_{i,e}(u_i)$ is calculated for a specific $[I_{i,a}(u_i), E_b/N_0]$ input combination. First, the wireless channel's noise variance $\sigma_n$ is computed according to the specific $E_b/N_0$ value considered. Then, a specific value of $I_{i,a}(u_i)$ is selected to compute $\sigma_a$, where the EXIT curve has to be evaluated using $\sigma_a = J^{-1}(I_{i,a})$. Afterwards, Eq. (3.4) is used to generate $L_{i,a}(u_i)$, as shown in Fig. 3.4, which is applied as the *a priori* LLR input of the GMLST decoder. Finally, the mutual information of $I_{i,e}(u_i) = I(u_i; L_{i,e}(u_i))$, $0 \leq I_{i,e}(u_i) \leq 1$, between the outer coded and interleaved bit stream $u_i$ and the LLR values $L_{i,e}(u_i)$ is calculated using Eq. (3.11) with the aid of the PDF $p_e$ of the extrinsic output $L_{i,e}(u_i)$. This requires the determination of the distribution $p_e$ by means of Monte Carlo simulations. However, according to [65], upon invoking the ergodicity theorem of Eq. (3.10), namely upon replacing the expected value by the

time average, the mutual information can be estimated using a sufficiently large number of samples even for non-Gaussian or unknown distributions, which may be expressed as [65]

$$I\left(u_i; L_{i,e}(u_i)\right) = 1 - E_{X=+1}\left\{\log_2\left[1 + e^{-L_{i,e}(u_i)}\right]\right\} \approx 1 - \frac{1}{N}\sum_{n=1}^{N}\log_2\left[1 + e^{-x(n)\cdot L_{i,e}(u_i(n))}\right]. \quad (3.13)$$

Fig. 3.5 shows the extrinsic information transfer characteristics of various iterative SIC based GMLST decoders for example, where STTC-4 and STTC-16 denote the 4-state based STTC [9, Fig. 4] and 16-state based STTC [9, Fig. 5], respectively, while STBC-G2 indicates Alamouti's STBC scheme [8]. As seen in the figure, iterative SIC detection does not provide any iteration gain upon increasing the mutual information at the input of the GMLST(STBC) decoder, since the extrinsic transfer curve of the GMLST(STBC) decoder is a horizontal line. On the other hand, the slopes seen in Fig. 3.5 representing the extrinsic information transfer characteristics of the GMLST(STTC) schemes illustrate that substantial iterative gains may be achieved, which will benefit the iteratively-decoded GMLST scheme of Fig. 3.1.

#### 3.2.2.2 Transfer Characteristics of the Outer Decoder

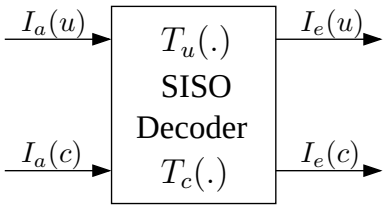


**Figure 3.6:** The soft-input soft-output decoder module, which describes the extrinsic information transfer characteristics of the outer decoder between the input and output of uncoded bits $u$ and coded bits $c$.

The extrinsic transfer characteristic of the outer channel decoder of Fig. 3.1 bears similarity to that of the inner GMLST decoder. The outer decoder is typically a four-terminal SISO module [121] as seen in Fig. 3.6. The mutual information quantifies the relationship of the *extrinsic* output $(I_{o,e}(u_o), I_{o,e}(c_o))$ and the *a priori* input $(I_{o,a}(u_o), I_{o,a}(c_o))$ for both the original uncoded information bit stream $u_o$ and for the coded bit stream $c_o$, respectively. Hence, the mutual information can be represented with the aid of the functions $I_{o,e}(u_o) = T_{o,u}[I_{o,a}(u_o), I_{o,a}(c_o)]$ as well as $I_{o,e}(c_o) = T_{o,c}[I_{o,a}(u_o), I_{o,a}(c_o)]$ of Fig. 3.6.

As seen in Fig. 3.1, the input of the outer channel decoder of the serially concatenated GMLST scheme consists only of the *a priori* input $L_{o,a}(c_o)$ provided by the GMLST

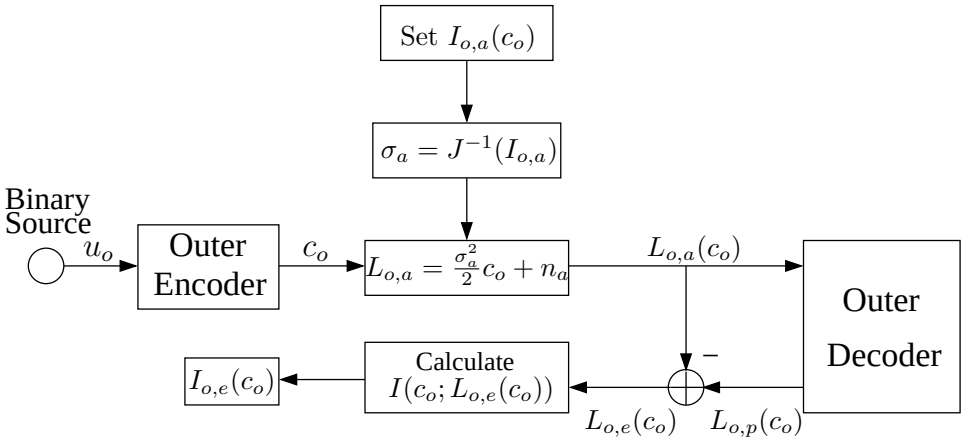


**Figure 3.7:** Evaluation of the outer channel decoder transfer characteristics.

decoder after appropriately reordering the corresponding extrinsic LLRs $L_{i,e}(u_i)$. Therefore, the extrinsic transfer characteristic of the outer channel decoder seen in Fig. 3.1 only describes the relationship between the outer channel decoder's LLR input $L_{o,a}(c_o)$ and the extrinsic output $L_{o,e}(c_o)$. Furthermore, the extrinsic information transfer characteristic of the outer channel decoder is independent of the $E_b/N_0$ value and hence $I_{o,e}(c_o)$ may be written as

$$I_{o,e}(c_o) = T_o[I_{o,a}(c_o)], \tag{3.14}$$

where $I_{o,a}(c_o) = I[c_o; L_{o,a}(c_o)]$, $0 \leq I_{o,a}(c_o) \leq 1$, is the mutual information between the outer channel coded bit stream $c_o$ and the *a priori* LLR values $L_{o,a}(c_o)$. Similarly, $I_{o,e}(c_o) = I[c_o; L_{o,e}(c_o)]$, $0 \leq I_{o,e}(c_o) \leq 1$, represents the mutual information between the outer channel coded bit stream $c_o$ and the extrinsic LLR values $L_{o,e}(c_o)$. The computational model of evaluating the EXIT characteristics of the outer channel decoder is shown in Fig. 3.7. As seen in the figure, the procedure is similar to that of the GMLST decoder shown in Fig. 3.4, except that its value is independent of the $E_b/N_0$ value. Again, $I_{o,e}(c_o) = I[c_o; L_{o,e}(c_o)]$ may be computed either by evaluating the histogram based approximation of the PDF of the extrinsic output $p_e$ [64, 101] and then applying Eq. (3.11) or, more conveniently, by the time averaging method [65] of Eq. (3.13) as

$$\begin{aligned} I\left[c_o; L_{o,e}(c_o)\right] &= 1 - E\left\{\log_2\left[1 + e^{-L_{o,e}(c_o)}\right]\right\} \\ &\approx 1 - \frac{1}{N}\sum_{n=1}^{N} \log_2\left[1 + e^{-c_o(n)\cdot L_{o,e}[c_o(n)]}\right]. \end{aligned} \tag{3.15}$$

In the system of Fig. 3.1, we employ a 1/2-rate memory-4 Recursive Systematic Convolutional (RSC) code as the outer channel code, which is defined by the generator polynomial $(1, g_1/g_0)$, where $g_0 = 1 + D + D^4$ is the feedback polynomial and $g_1 = 1 + D^2 + D^3 + D^4$ is the feedforward one. According to the procedure of Fig. 3.7,

we plot the extrinsic information transfer characteristic of the 1/2-rate memory-4 RSC code in Fig. 3.8. It is clearly seen in Fig. 3.8 that the extrinsic information transfer characteristic is symmetric to the $(I_{o,a}, I_{o,e}) = (0.5, 0.5)$ point. Furthermore, Fig. 3.8 also demonstrates that the RSC code converges fastest upon increasing $I_{o,a}$ in the range of $0.4 < I_{o,a} < 0.8$.

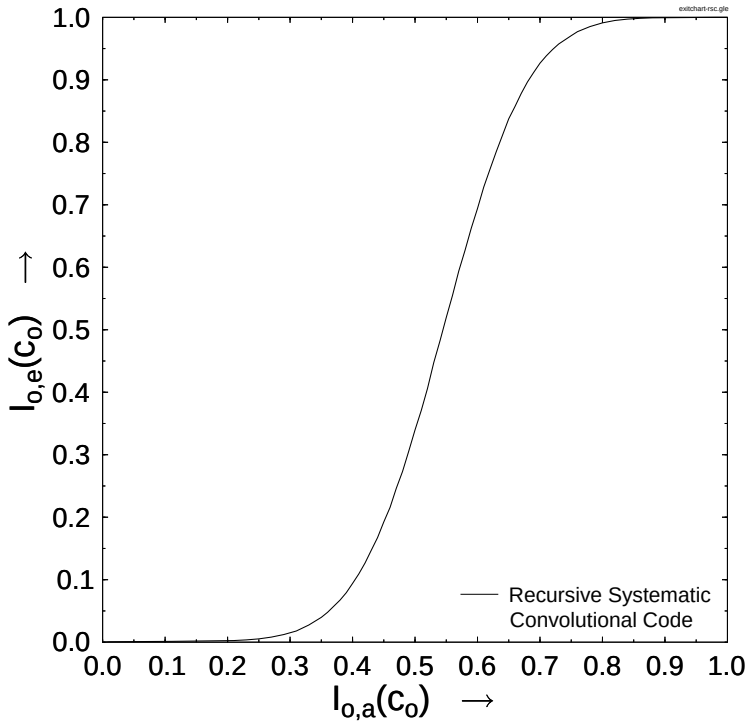


**Figure 3.8:** Extrinsic information transfer characteristic of a 1/2-rate memory-4 RSC code.

#### 3.2.2.3 Extrinsic Information Transfer Chart Results

The exchange of extrinsic information in the system of Fig. 3.1 can be visualized by plotting the EXIT characteristics of the inner GMLST decoder and the outer RSC decoder in a joint diagram, which is known as the EXIT chart [64, 101]. The outer RSC decoder's extrinsic output information $I_{o,e}(c_o)$ becomes the inner GMLST decoder's *a priori* input information $I_{i,a}(u_i)$, which is represented on the $x$-axis of the EXIT chart. Similarly, on the $y$-axis we plot the inner GMLST decoder's extrinsic output information $I_{i,e}(u_i)$, which becomes the outer RSC decoder's *a priori* input information $I_{o,a}(c_o)$. Accordingly, the axes of Figs. 3.5 and 3.8 are swapped intentionally for the sake of creating the EXIT chart, as seen in Fig. 3.9.

More explicitly, Fig. 3.9 shows the EXIT chart of the iteratively detected serially concatenated RSC-coded GMLST(STTC-16) scheme, where three SIC operations are performed within the GMLST(STTC-16) decoder. Ideally, in order for the exchange of extrinsic information between the GMLST decoder and the outer RSC decoder to converge

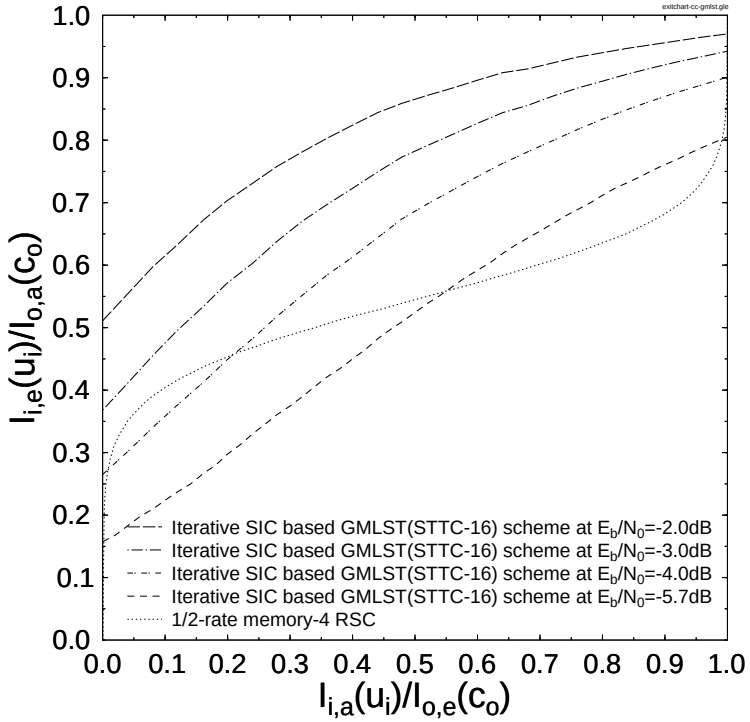


**Figure 3.9:** Extrinsic information transfer characteristic of 1/2-rate RSC code.

at a specific $E_b/N_0$ value, the EXIT curve of the GMLST decoder at the $E_b/N_0$ value of interest and the extrinsic transfer characteristic of the outer RSC decoder should only intersect at the (1.0, 1.0) point. If this condition is satisfied, then an open *convergence tunnel* [64, 101] appears in the EXIT chart, which implies that an infinitesimally low BER is achievable for the iteratively detected system. However, if the two extrinsic transfer characteristics intersect at a point close to the line at $I_{o,e}(c_o) = 1.0$ rather than at the (1.0, 1.0) point, then a moderately low BER may be still achieved, although a higher error floor occurs than for the schemes, where the intersection is at the (1.0, 1.0) point. Observe in Fig. 3.9 that the inner and outer EXIT curves intersect at a point very close to the vertical $I_{o,e}(c_o) = 1.0$ line at $E_b/N_0$=-3.0 dB. This implies that according to the predictions of the EXIT chart seen in Fig. 3.9, the iterative detection process is expected to converge to a moderately low BER at an $E_b/N_0$ value between -3.0 dB and -4.0 dB. In practice, the EXIT chart based convergence predictions are usually verified by the actual Monte-Carlo simulation based iterative decoding trajectory, as will be discussed in Section 3.3.

#### 3.2.2.4 Area Properties of EXIT Charts

Let us now discuss the relevance of the EXIT chart area $A_i$ beneath the inner code's EXIT characteristic and the area $A_o$ beneath the inverted outer EXIT characteristic. In [122, 123], the area $A_o$ beneath the inverted EXIT characteristic of an *optimal* outer APP-based

SISO decoder having a coding rate of $R_o$ was shown to be given by

$$A_o = R_o. \tag{3.16}$$

In the scenario where this outer code is serially concatenated with a $R_i$-rate inner code that is employed for protecting $\mathcal{M}$-ary modulated transmissions, the *effective* throughput $C_{eff}$ in bits per symbol is given by

$$C_{eff} = R_o \cdot R_i \cdot \log_2(\mathcal{M}) = A_o \cdot R_i \cdot \log_2(\mathcal{M}). \tag{3.17}$$

As described in Section 3.2.2.3, maintaining an open EXIT chart tunnel is a necessary condition for achieving iterative decoding convergence to an infinitesimally low BER. Since an open EXIT chart tunnel can only be created if the EXIT chart area beneath the inverted outer EXIT characteristic $A_o$ is less than that beneath the inner code's EXIT characteristic $A_i$, we have $A_o < A_i$. Hence maintaining

$$C_{eff} < A_i \cdot R_i \cdot \log_2(\mathcal{M}) \tag{3.18}$$

constitutes a necessary condition for iterative decoding convergence to an infinitesimally low BER to be supported.

In the case where we have $R_i = 1$ and an *optimal* inner APP-based SISO decoder is employed, the authors of [122, 123] showed that

$$A_i \cdot R_i \cdot \log_2(\mathcal{M}) = C \tag{3.19}$$

holds, where $C$ is the Discrete-input Continuous-output Memoryless Channel's (DCMC) capacity [14] expressed in bits per symbol. Hence, when $R_i = 1$ and an *optimal* inner APP-based SISO decoder is employed, maintaining

$$C_{eff} < C \tag{3.20}$$

constitutes a necessary condition for iterative decoding convergence to an infinitesimally low BER to be supported. Note that naturally this is in line with Shannon's lesson stated in his seminal publication of 1948 [1].

However, when we have $R_i < 1$ or a *sub-optimal* inner APP-based SISO decoder is employed, the authors of [122, 123] showed that

$$A_i \cdot R_i \cdot \log_2(\mathcal{M}) = \bar{C} \leq C, \tag{3.21}$$

where $\bar{C}$ is the attainable DCMC capacity (maximum achievable bandwidth efficiency/rate). More explicitly, in this case, some capacity loss occurs, since the necessary condition for iterative decoding convergence to an infinitesimally low BER to be supported becomes

$$C_{eff} < \bar{C}. \tag{3.22}$$

In conclusion, the properties of EXIT charts can be summarized as follows:

**Rate property:** *The area under the inverted EXIT curve of an optimal outer APP-based SISO decoder is equal to its code rate.*

**Capacity property:** *The area beneath the EXIT curve of the inner decoder is equal to the DCMC capacity, provided that the inner code rate is 1 and the optimal inner APP-based SISO decoder is used.*

**Convergence property:** *The trajectory approaches the (1.0, 1.0) point of the EXIT chart indicates the decoding convergence to an infinitesimally low BER.*

Note that the EXIT chart area of $A_i - A_o$ within an open EXIT chart tunnel is proportional to the discrepancy between the *effective* throughput and the (attainable) DCMC capacity. Hence, we may conclude that near-capacity transmissions are facilitated, when a narrow, marginally open EXIT chart tunnel can be created for facilitating convergence to an infinitesimally low BER. This motivates the employment of irregular coding techniques, which deliberately shape the EXIT curve of the outer code with the aid of using diverse outer code components, leading to the concept of EXIT chart matching, as will be discussed in the following section.

## 3.3 Near-Capacity IRCC- and URC-Coded GMLST Schemes

As presented in Section 3.2.2.3, the employment of conventional two-stage iteratively-detected GMLST schemes typically result in an intersection of the inner and outer components' EXIT curves in the EXIT chart of Fig. 3.9 and hence they suffer from a BER floor, preventing them from achieving infinitesimally low BER values, since the inner coding stage is of non-recursive nature. In this section we circumvent this deficiency by proposing a three-stage iteratively-detected GMLST scheme, where a recursive Unity-Rate Code (URC) [67, 105, 106] is employed as the intermediate code in order for the inner code's EXIT curve to reach the (1.0, 1.0) point of perfect convergence and hence to achieve an infinitesimally low BER. On the other hand, irregular coding [59, 60] has been proposed for reliable communications at SNRs that are close to the channel capacity, which was further applied for example in the context of serial concatenated schemes using iterative decoding in [61]. Therefore, we apply an IRregular Convolutional Code (IRCC) [61, 81] as the outer code of our proposed three-stage serially concatenated scheme for the sake of near-capacity communications.

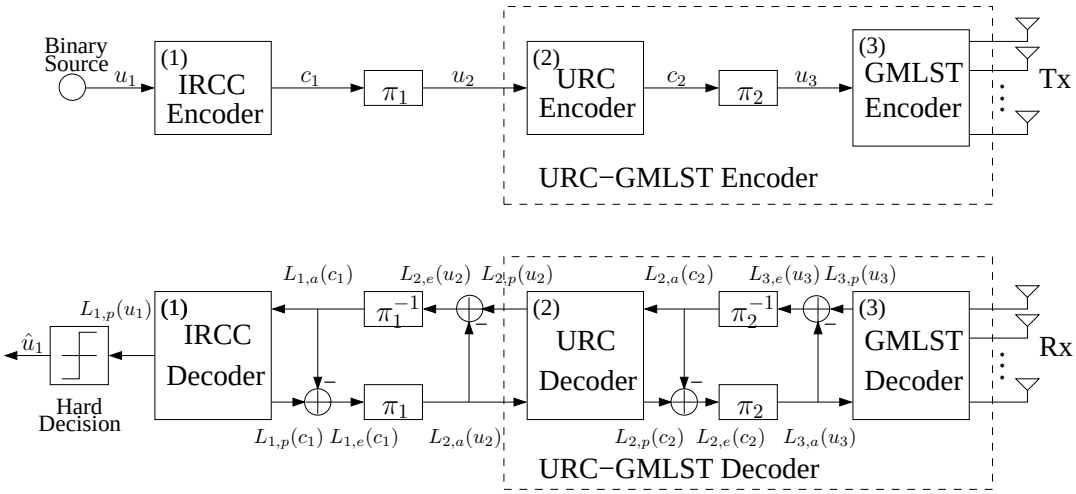


**Figure 3.10:** Schematic of the proposed IRCC-URC-GMLST scheme.

### 3.3.1 System Overview

The schematic of the proposed three-stage serially concatenated system is illustrated in Fig. 3.10. At the transmitter side, IRCCs [61, 81] having an overall code rate of $R_1$ are employed for encoding specifically optimized fractions of the input stream, where each fraction's code rate was designed for achieving a near-capacity performance with the aid of EXIT charts [101]. A recursive URC was amalgamated with the above-mentioned GMLST in Fig. 3.10 as the inner code for assisting the non-recursive GMLST scheme in achieving decoding convergence to an infinitesimally low BER at near-capacity SNRs. The GMLST encoder partitions the long bit stream emanating from the intermediate URC encoder into several substreams and each substream is separately space-time encoded. Two different high-length bit-wise interleavers are introduced between the three component encoders so that the input bits of the URC and GMLST encoders can be rendered independent of each other, which is one of the necessary conditions for achieving a good match between the performance predictions of EXIT charts analysis and of classic bit-by-bit Monte-Carlo simulations [101]. For simplicity, we refer to the proposed serially concatenated system as the IRCC-URC-GMLST scheme.

At the receiver side, according to Fig. 3.10, an iterative decoding procedure is operated, which employs three *A Posteriori Probability* (APP)-based decoders. The received signals are first decoded by the APP-based GMLST decoder in order to produce the *a priori* Log-Likelihood Ratio (LLR) values $L_{2,a}(c_2)$ of the coded bits $c_2$. The URC decoder of Fig. 3.10 processes the information forwarded by the GMLST decoder in conjunction with the *a priori* LLR values $L_{2,a}(u_2)$ of the information bits $u_2$ in order to generate the *a posteriori* LLR values $L_{2,p}(u_2)$ and $L_{2,p}(c_2)$ of the information bits $u_2$ and the coded bits $c_2$, respectively. In the scenario, when iterations are needed within the amalgamated "URC-GMLST" decoder so as to achieve a near-capacity performance, the *a priori* LLRs

$L_{2,a}(c_2)$ are subtracted from the *a posteriori* LLR values $L_{2,p}(c_2)$ and then they are fed back to the GMLST decoder as the *a priori* information $L_{3,a}(u_3)$ through the interleaver $\pi_2$. Similarly, the *a priori* LLR values of the URC decoder are subtracted from the *a posteriori* LLR values produced by the Maximum A-posteriori Probability (MAP) algorithm [89], for the sake of generating the extrinsic LLR values $L_{2,e}(u_2)$ seen in Fig. 3.10. Next, the soft bits $L_{1,a}(c_1)$ are passed to the IRCC decoder in order to compute the *a posteriori* LLR values $L_{1,p}(c_1)$ of the IRCC encoded bits $c_1$. During the last iteration, only the LLR values $L_{1,p}(u_1)$ of the original information bits $u_1$ are required, which are passed to the hard-decision block in order to estimate the source bits. As seen in Fig. 3.10, the extrinsic information $L_{1,e}(c_1)$ is generated by subtracting the *a priori* information from the *a posteriori* information, which is fed back to the URC decoder as the *a priori* information $L_{2,a}(u_2)$ through the interleaver $\pi_1$. For the sake of clarity, in the iterative detection procedure, we define the initial decoding process passing information from the inner decoder to the outer decoder as the first iteration between the two decoders.

### 3.3.2 Capacity and Maximum Achievable Rate

Let us now consider a Discrete-input Continuous-output Memoryless Channel (DCMC) in the context of discrete-amplitude QAM and PSK [14] modulation. In order to design a near-capacity coding scheme, in this section we derive the DCMC capacity formula for GMLST(STBC), which refers to the GMLST schemes using STBC [8, 31] as the component STCs. Additionally, the maximum achievable bandwidth efficiency/rate of various iterative SIC and ML based GMLST schemes is derived for transmission over the DCMC based on the area properties of EXIT charts [122].

#### 3.3.2.1 DCMC Capacity of "GMLST(STBC)"

As mentioned in Section 3.2.1.2, a specific GMLST scheme using an identical STBC as its component STBCs is designed for encoding over $L$ transmission symbols, assuming that the channel's envelope may be considered quasi-static over this period. Let us rewrite Eq. (3.2) as follows

$$\mathbf{Y} = \mathbf{HC} + \mathbf{N}\,, \tag{3.23}$$

where $\mathbf{Y} = [\mathbf{y}_1, \ldots, \mathbf{y}_L] \in \mathbb{C}^{N_r \times L}$ is the sampled received signal matrix, $\mathbf{H} \in \mathbb{C}^{N_r \times N_t}$ is the quasi-static channel matrix, which is constant over $L$ symbol periods, $\mathbf{C} = [\mathbf{c}_1, \ldots, \mathbf{c}_L] \in \mathbb{C}^{N_t \times L}$ is the GMLST(STBC) *codeword* matrix and $\mathbf{N} = [\mathbf{n}_1, \ldots, \mathbf{n}_L] \in \mathbb{C}^{N_r \times L}$ represents the additive white Gaussian noise matrix.

In this section, we only consider STBCs having square-shaped *codeword* matrices [8,

124–127] as the component STBCs of the GMLST schemes of Fig. 2.2, where we have $L = N_t/q$. For example, when Alamouti's G2 space-time scheme [8] is used as the component STBC, the GMLST(STBC) *codeword* matrix is as follows:

$$\mathbf{C}_{GMLST(STBC)} = \begin{pmatrix} c_{1,1} & c_{1,2} & \dots & c_{j,1} & c_{j,2} & \dots & c_{q,1} & c_{q,2} \\ -\bar{c}_{1,2} & \bar{c}_{1,1} & \dots & -\bar{c}_{j,2} & \bar{c}_{j,1} & \dots & -\bar{c}_{q,2} & \bar{c}_{q,1} \end{pmatrix}^T, \quad (3.24)$$

where the columns represent $L = 2$ different time slots, while the rows represent $qL$ different transmit antennas, and $\begin{pmatrix} c_{j,1} & c_{j,2} \\ -\bar{c}_{j,2} & \bar{c}_{j,1} \end{pmatrix}^T$ is the $j$-layer STBC *codeword* matrix. Hence, when complex-valued $\mathcal{M}$-ary PSK/QAM is employed in a GMLST(STBC) scheme, we have a total of $M = \mathcal{M}^{qL}$ possible GMLST(STBC) *codeword* matrix combinations for $L$ consecutive symbol periods. Based on Eq. (3.23), the conditional probability of receiving a signal matrix $\mathbf{Y}$, given that an $M$-ary GMLST(STBC) *codeword* matrix $\mathbf{C}^m$, $m \in \{1, \dots, M\}$, was transmitted over uncorrelated flat Rayleigh fading channels is determined by the Probability Density Function (PDF) of the noise, yielding:

$$p(\mathbf{Y}|\mathbf{C}^m) = \frac{1}{(\pi N_0)^{LN_r}} \exp\left(\frac{-\|\mathbf{Y} - \mathbf{H}\mathbf{C}^m\|^2}{N_0}\right), \quad (3.25)$$
$$= \prod_{k=1}^{L} \prod_{r=1}^{N_r} \frac{1}{\pi N_0} \exp\left(\frac{-|y_{r,k} - \sum_{t=1}^{N_t} h_{r,t} c_{t,k}^m|^2}{N_0}\right).$$

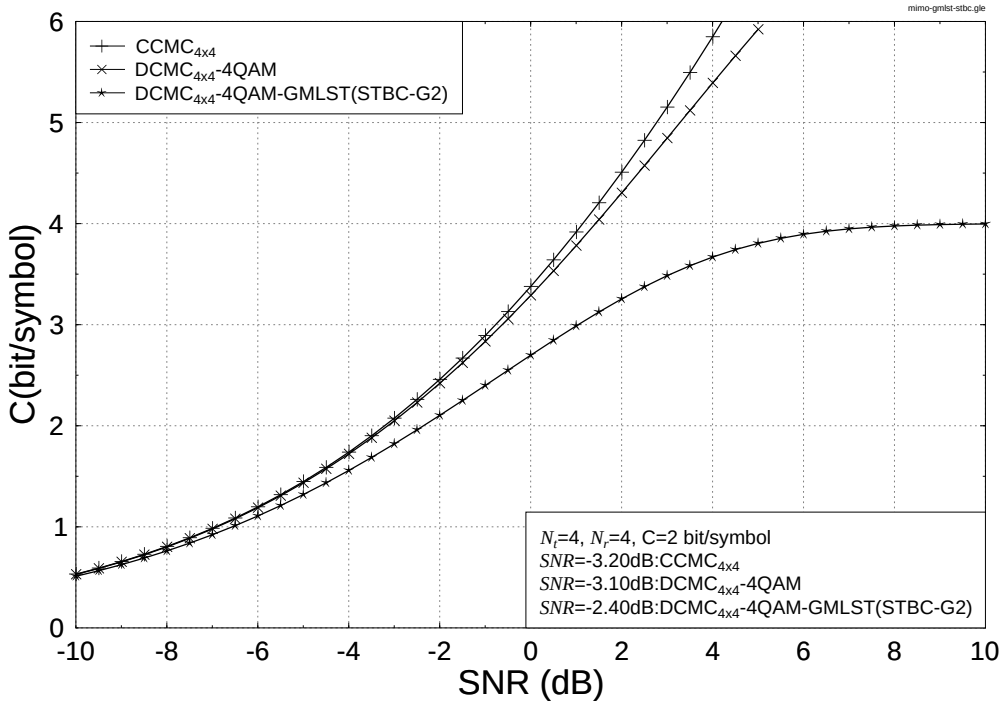


**Figure 3.11:** The capacity of GMLST(STBC-G2) schemes obeying the architecture of Fig. 2.2, when communicating over uncorrelated flat Rayleigh fading channels employing $N_t = 4$ transmit antennas and $N_r = 4$ receive antennas.

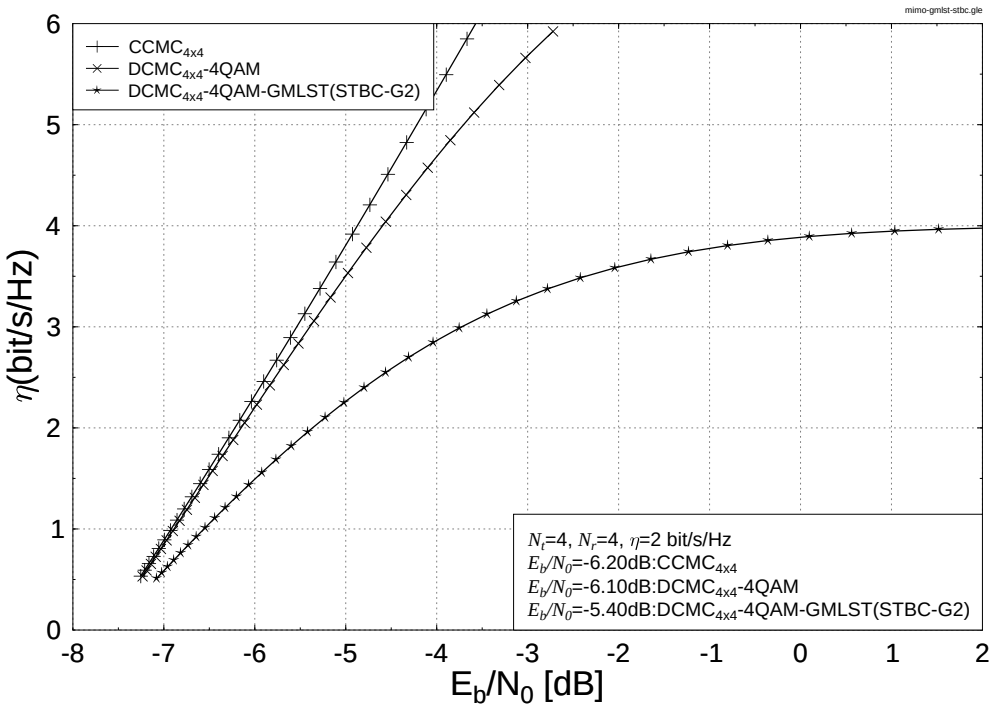


**Figure 3.12:** The bandwidth efficiency of GMLST(STBC-G2) schemes obeying the architecture of Fig. 2.2, when communicating over uncorrelated flat Rayleigh fading channels employing $N_t = 4$ transmit antennas and $N_r = 4$ receive antennas.

The channel capacity per symbol period evaluated for the GMLST(STBC) scheme, when using complex-valued $\mathcal{M}$-ary PSK/QAM for transmission over the DCMC can be shown to be [127]:

$$C_{\text{DCMC}}^{\text{GMLST(STBC)}} = \frac{1}{L} \max_{p(\mathbf{C}^1)\ldots p(\mathbf{C}^M)} \sum_{m=1}^{M} \int_{\mathbf{Y}} p(\mathbf{Y}|\mathbf{C}^m) p(\mathbf{C}^m) \cdot \log_2 \left( \frac{p(\mathbf{Y}|\mathbf{C}^m)}{\sum_{n=1}^{M} p(\mathbf{Y}|\mathbf{C}^n) p(\mathbf{C}^n)} \right) d\mathbf{Y}, \tag{3.26}$$

where the right hand side of Eq. (3.26) is maximized, when we have $p(\mathbf{C}^m) = 1/M$ for $m \in \{1, \ldots, M\}$. Hence, Eq. (3.26) can be simplified to:

$$C_{\text{DCMC}}^{\text{GMLST(STBC)}} = \frac{\log_2(M)}{L} - \frac{1}{ML} \sum_{m=1}^{M} E\left[ \log_2 \sum_{n=1}^{M} \exp(\Psi_{m,n}) \,\middle|\, \mathbf{C}^m \right], \tag{3.27}$$

where $E[A|\mathbf{C}^m]$ is the expectation of $A$ conditioned on $\mathbf{C}^m$ and the expectation in Eq. (3.27) is taken over $\mathbf{H}$ and $\mathbf{N}$, while $\Psi_{m,n}$ is given by:

$$\Psi_{m,n} = \frac{-\|\mathbf{H}(\mathbf{C}^m - \mathbf{C}^n) + \mathbf{N}\|^2 + \|\mathbf{N}\|^2}{N_0}. \tag{3.28}$$

Based on the DCMC capacity formula of Eq. (3.27) we can compute the capacity of any GMLST(STBC) scheme by substituting the corresponding GMLST(STBC) *codeword* matrix $\mathbf{C} \in \mathbb{C}^{N_t \times L}$ into Eq. (3.28).

The resultant bandwidth efficiency is computed by normalising the channel capacity given by Eq. (3.27), with respect to the product of the bandwidth $W$ and the signalling period $T$, yielding:

$$\eta = \frac{C}{WT} \text{ [bit/s/Hz]} , \tag{3.29}$$

where $WT = 1$ for PSK/QAM schemes, when assuming zero Nyquist excess bandwidth. The bandwidth efficiency, $\eta$, is typically plotted against the SNR per bit given by: $E_b/N_0 = \text{SNR}/\eta$.

In this chapter, we consider the scenario when $N_t = 4$ transmit and $N_r = 4$ receive antennas are used, where $N_t^1 = N_t^2 = 2$. Based on Eq. (3.27), the Monte-Carlo-based evaluation of the GMLST(STBC-G2)'s DCMC capacity is illustrated in Fig. 3.11, which is indicated by the label $\text{DCMC}_{4\times4}$-4QAM-GMLST(STBC-G2). The DCMC capacity curves of the multiplexing-based MIMO scheme which employed a ML detector, and of the unrestricted Continuous-input Continuous-output Memoryless Channel (CCMC) [6, 14] are depicted in Fig. 3.11 for comparison. Furthermore, the bandwidth efficiency/rate curves are shown in Fig. 3.12.

#### 3.3.2.2 Maximum Achievable Rate Based on EXIT Charts

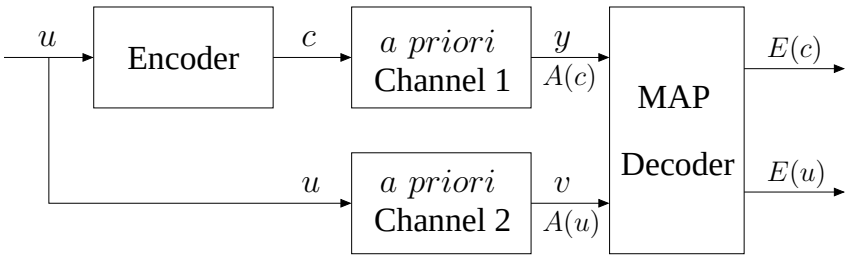


**Figure 3.13:** The encoding and decoding processes of an intermediate encoder whose input bits $u$ emanate from an outer encoder and whose output symbols $c$ are fed to an inner encoder. The $a\ priori$ channels are used to model the outer and inner decoders, whereas the upper $a\ priori$ channel can be replaced by the communication channel to model the inner decoder. The notations $A(.)$ and $E(.)$ represent the $a\ priori$ and $extrinsic$ information, respectively.

According to the discussions of Section 3.2.2.4, the maximum achievable bandwidth efficiency/rate of the system is equal to the area under the EXIT curve of the inner code, provided that the channel's input is independently and uniformly distributed, assuming furthermore that the inner code rate is 1 and that the *optimum* or *sub-optimum* APP-based decoding algorithm is used. This area property of the EXIT charts may be exploited by considering Fig. 3.13 as in [122]. Explicitly, the area under the EXIT curve of the inner code quantifies the capacity of the communication channel (the upper $a\ priori$ Channel 1 in Fig. 3.13), when the communication channel's input is independently and uniformly

distributed, while the $a\ priori$ channel (the lower $a\ priori$ Channel 2 in Fig. 3.13) is modeled by a Binary Erasure Channel (BEC). This area property was experimentally shown to be valid for arbitrary inner codes and communication channels, provided that the $a\ priori$ Channel 2 is a BEC. Furthermore, there is experimental evidence that the area property of EXIT charts is also valid when the $a\ priori$ Channel 2 is modeled by an AWGN channel, as it was originally demonstrated in [101].

Based on the area property of EXIT charts, the maximum achievable rate curves of various iterative SIC and ML based GMLST schemes of Figs. 3.2 and 3.3 are shown in Figs. 3.14-3.16 together with the CCMC and DCMC capacity curves of the multiplexing-based MIMO scheme. As mentioned above, we consider the scenario when $N_t = 4$ transmit and $N_r = 4$ receive antennas are used, where we have $N_t^1 = N_t^2 = 2$. For simplicity, the component STCs utilized in the schematic of Fig. 2.1 for all groups are assumed to be identical. Specifically, we use STBC-G2 [8], 4-state based STTC-4 [9, Fig. 4] and 16-state based STTC-16 [9, Fig. 5] as the component STCs of the GMLST schemes of Fig. 2.1, respectively. As shown in Figs. 3.14-3.16, the DCMC capacity of the multiplexing-based MIMO scheme employing 4QAM ($\text{DCMC}_{4\times4}$-4QAM) is higher than that of all the GMLST schemes and may be regarded as the tight capacity upper bound of the $(4 \times 4)$-element 4QAM MIMO systems. On the other hand, the DCMC capacity curve of the GMLST scheme of Fig. 2.2 using STBC-G2, namely $\text{DCMC}_{4\times4}$-4QAM-GMLST(STBC-G2), is also plotted in Fig. 3.14 for comparison. It is clearly seen in Fig. 3.14 that the bandwidth efficiency curve of the ML-based GMLST(STBC-G2) scheme exactly matches the $\text{DCMC}_{4\times4}$-4QAM-GMLST(STBC-G2) capacity curve, which verifies the area property of the EXIT chart presented in Section 3.2.2.4. Observe by comparing Fig. 3.14 with Fig. 3.16 that the $\text{DCMC}_{4\times4}$-4QAM-GMLST(STBC-G2) capacity curve is below that of the ML-based GMLST(STTC-16) scheme using three iterations. This is due to the loss of temporal diversity within the STBC-G2 orthogonal code of each group [6].

Furthermore, it is seen in Fig. 3.14 that upon invoking two SIC operations in the GMLST(STBC-G2) scheme of Fig. 2.2, the maximum achievable rate curve approaches the $\text{DCMC}_{4\times4}$-4QAM-GMLST(STBC-G2) rate curve, since the maximum attainable receive diversity has been approached. However, no substantial further improvements are attained beyond two SICs, since the remaining inter-group interference propagating across the groups is independently distributed across $K/2$ consecutive G2 *codeword* block periods during $K$ symbol intervals and hence cannot be eliminated by SIC operations. By contrast, for the GMLST(STTC) schemes of Fig. 2.1 characterized in Figs. 3.15 and 3.16, the maximum achievable rate improves steadily up to three SIC operations, although the maximum attainable receive diversity has already been achieved during the second itera-

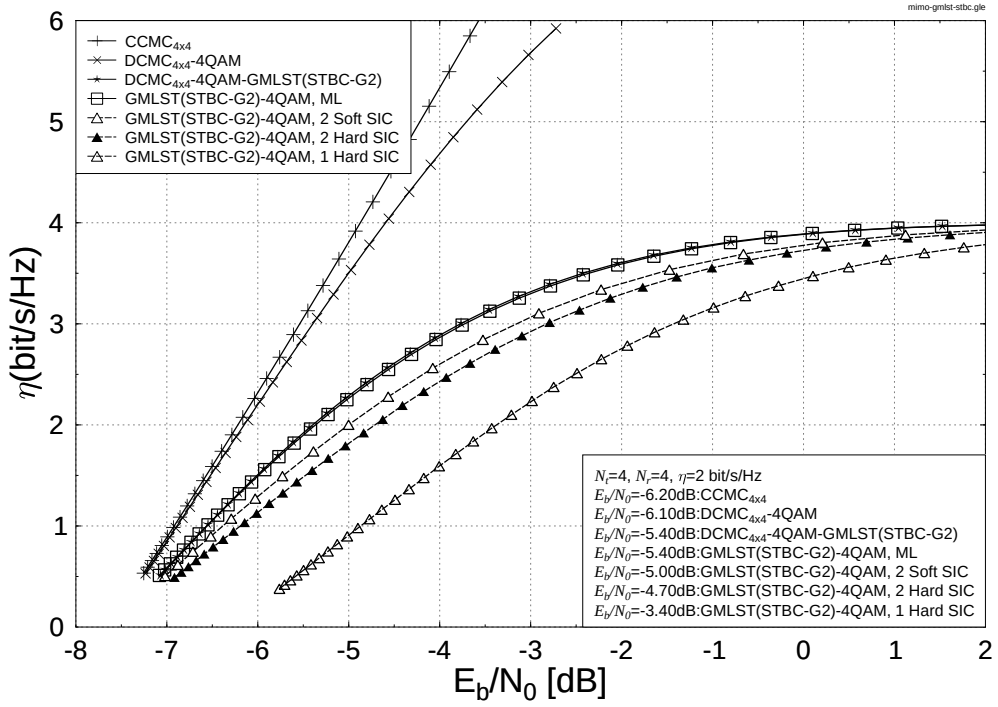


**Figure 3.14:** The bandwidth efficiency of various iterative SIC and ML based GMLST(STBC-G2) schemes obeying the architecture of Fig. 2.2, when communicating over uncorrelated flat Rayleigh fading channels employing $N_t = 4$ transmit antennas and $N_r = 4$ receive antennas. The system parameters are summarized in Table 3.1.

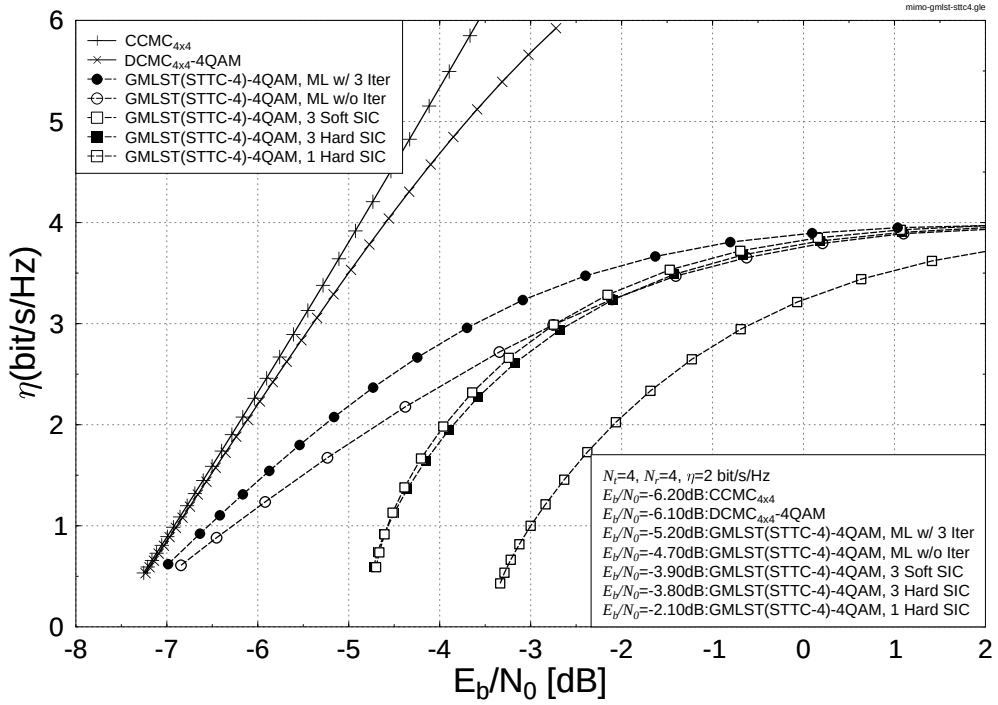


**Figure 3.15:** The bandwidth efficiency of various iterative SIC and ML based GMLST(STTC-4) schemes obeying the architecture of Fig. 2.1, when communicating over uncorrelated flat Rayleigh fading channels employing $N_t = 4$ transmit antennas and $N_r = 4$ receive antennas. The system parameters are summarized in Table 3.1.

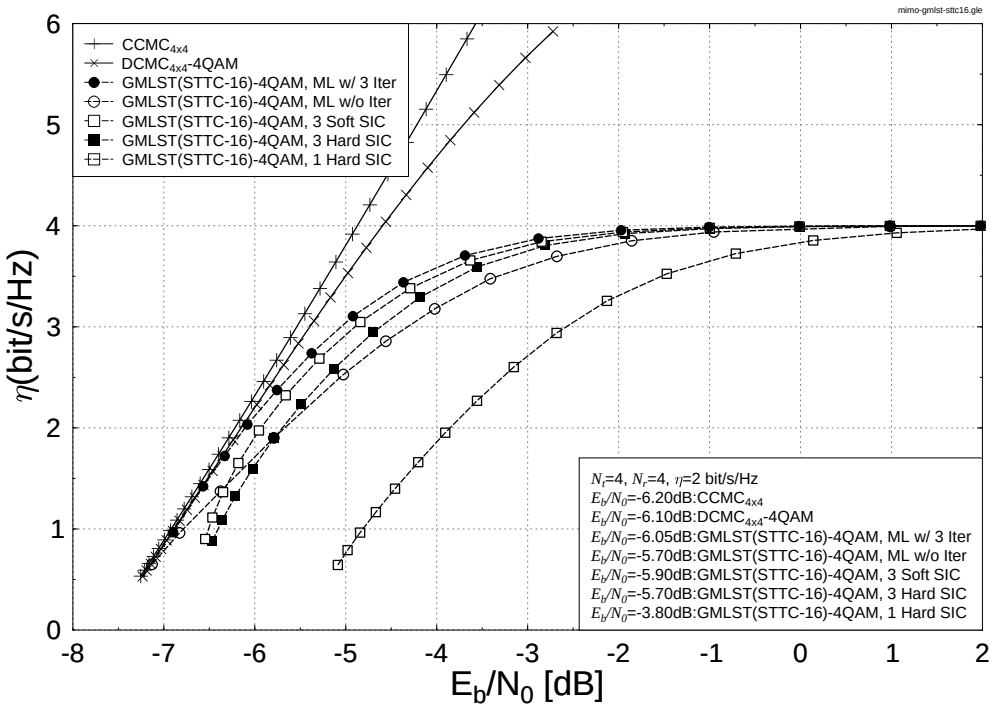


**Figure 3.16:** The bandwidth efficiency of various iterative SIC and ML based GMLST(STTC-16) schemes obeying the architecture of Fig. 2.1, when communicating over uncorrelated flat Rayleigh fading channels employing $N_t = 4$ transmit antennas and $N_r = 4$ receive antennas. The system parameters are summarized in Table 3.1.

tion. This is due to the strong error-correcting capability of the STTC associated with temporal vector-based interleavers. Observe in Figs. 3.15 and 3.16 that beyond three SICs, the additional performance improvements remain marginal. For the sake of attaining further improvements, soft interference cancellation may be invoked for both the GMLST(STBC) and GMLST(STTC) schemes, which is explicitly demonstrated in Figs. 3.14-3.16 as well.

Since no iterations can be carried out between the SIC-based demodulator and the STTC decoder when using SIC-based detection, some mutual information or throughput loss occurs, which cannot be recovered. For comparison, the maximum achievable rate of the ML-based iteratively detected GMLST(STTC) schemes of Fig. 3.3 are also quantified in Figs. 3.15 and 3.16. The number of iterations between the ML demapper and the GMLST component STTC decoders was fixed to three for both the GMLST(STTC-4) and GMLST(STTC-16) cases, which is the same as the number of SIC iterations. Hence, both the SIC-based and ML-based schemes of Figs. 3.2 and 3.3 invoke the same number of STTC decoder operations, but the ML demapper exhibits a higher complexity than the SIC operation. As shown in Figs. 3.15 and 3.16, the ML-based schemes of Fig. 3.3 provide a higher maximum achievable rate than that of the SIC-based arrangement.

| | |
|---|---|
| Modulation Scheme | 4QAM |
| No. of GMLST Layers | 2 |
| No. of Tx per GMLST Layer | 2 |
| No. of Rx | 4 |
| Channel | Temporally uncorrelated flat Rayleigh fading |
| GMLST(STBC) Component Codes | STBC [8] |
| No. of GMLST(STBC) SIC Iterations | 2 (hard and soft) |
| GMLST(STTC) Component Codes | STTC-4 [9, Fig. 4] and STTC-16 [9, Fig. 5] |
| No. of GMLST(STTC) SIC Iterations | 3 (hard and soft) |
| No. of GMLST(STTC) ML Iterations | 3 |
| Interleaver Length | 508000 bits |
| URC Generator | $(1, g_1/g_0) = (1, \frac{1}{1+D})$ |
| IRCC Coding Rate | 0.5 |
| IRCC Components | 17 or 36 |

**Table 3.1:** Iteratively-decoded IRCC-URC-GMLST system parameters used in the system architecture of Fig. 3.10.

### 3.3.3 EXIT Chart Aided System Design and Analysis

The main objective of employing EXIT charts [101] is to analyse the convergence behaviour of iterative decoders by examining the evolution of the input/output mutual information exchange between the inner and outer decoders during the consecutive iterations. As mentioned in Section 3.2.2.4, the area under the EXIT curve of the inner decoder is approximately equal to the channel capacity, when the channel's input is independently and uniformly distributed. Similarly, the area under the inverted EXIT curve of the outer code is approximately equal to the outer code rate. In this section, we will further exploit the well-understood properties of EXIT charts that a narrow, but marginally open EXIT-tunnel indicates a high probability of achieving a near-capacity performance, which was concluded in Section 3.2.2.4, for the sake of designing a near-capacity iteratively-decoded IRCC-URC-GMLST system. In what follows, all the results presented characterize the GMLST schemes using $N_t = 4$ transmit and $N_r = 4$ receive antennas in conjunction with the system parameters outlined in Table 3.1.

#### 3.3.3.1 EXIT Function of the Amalgamated "URC-GMLST" Decoder

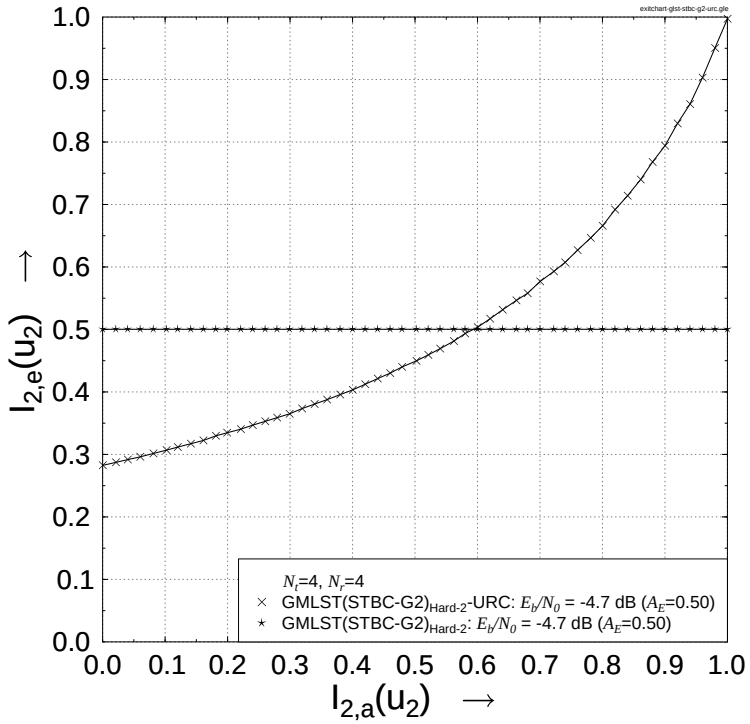


**Figure 3.17:** The EXIT chart curves for the stand-alone GMLST(STBC-G2) decoder and the amalgamated GMLST(STBC-G2)$_{\text{Hard}}$-URC decoder of Fig. 3.10 using the parameters of Table 3.1. The notation GMLST(STBC-G2)$_{\text{Hard-2}}$ indicates 2 hard SIC iterations within the GMLST decoder. By contrast no iterations are needed between the GMLST(STBC-G2)$_{\text{Hard}}$ and URC decoders, since the EXIT curve of the GMLST(STBC-G2)$_{\text{Hard}}$ detector is a horizontal line.

The original three-stage arrangement of the IRCC-URC-GMLST scheme seen in Fig. 3.10 would require a 3D EXIT chart analysis [67], which is hard to interpret visually. However, our experimental results show that an intermediate URC changes only the shape, but not the area under the EXIT curve of the inner code after a sufficiently high number of inner iterations. Hence, the inner URC and GMLST decoder pair seen in Fig. 3.10 requires only a few inner iterations between them, so that our three-stage system reaches the (1.0, 1.0) point of perfect convergence. Generally speaking, we continue invoking inner iterations between them until we succeed in generating sufficiently reliable mutual information, before activating the outer iterations. We can therefore view these two blocks as an amalgamated inner decoder using several inner iterations, which is portrayed by the lower dashed box in Fig. 3.10. This allows us to simplify the 3D EXIT analysis [67] to 2D EXIT functions [64], while using the most beneficial activation order of the iterative decoder components.

Let $I_{\cdot,a}(x), 0 \leq I_{\cdot,a}(x) \leq 1$, denote the mutual information between the *a priori* LLRs $L_{\cdot,a}(x)$ as well as the corresponding bits $x$ and let $I_{\cdot,e}(x), 0 \leq I_{\cdot,e}(x) \leq 1$, denote the mutual information between the *extrinsic* LLRs $L_{\cdot,e}(x)$ and the corresponding

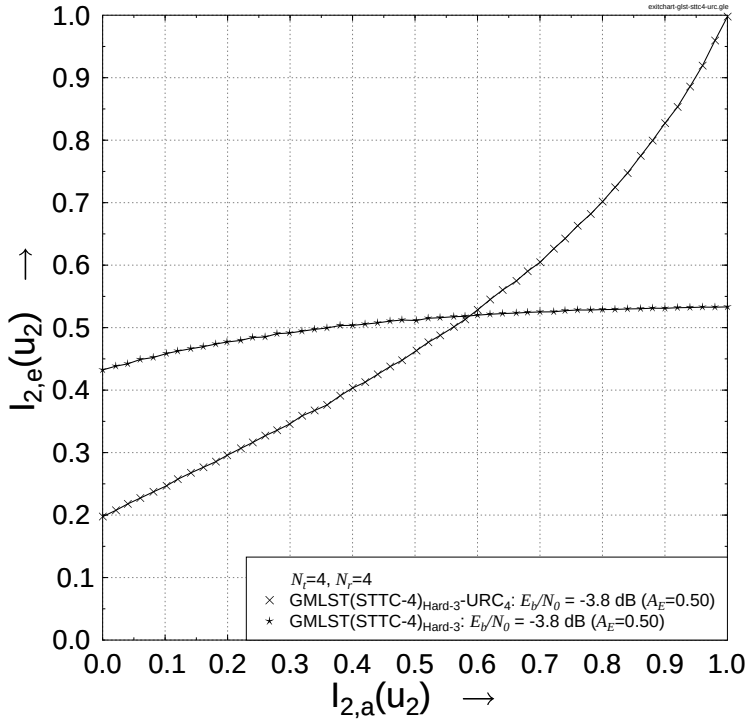


**Figure 3.18:** The EXIT chart curves for the stand-alone GMLST(STTC-4) decoder and the amalgamated GMLST(STTC-4)$_{\text{Hard}}$-URC decoder of Fig. 3.10 using the parameters of Table 3.1. The notation GMLST(STTC-4)$_{\text{Hard-3}}$ indicates 3 hard SIC iterations within the GMLST decoder and the subscript of URC denotes the number of iterations between the GMLST(STTC-4)$_{\text{Hard}}$ and URC decoders.

bits $x$. Considering the simplified two-stage iterative detection of Fig. 3.10, the EXIT characteristics of Decoder 2 and Decoder 1 can be described by the following two EXIT functions [64, 68]:

$$I_{2,e}\left(u_2\right) = T_{2,u_2}\left[I_{2,a}\left(u_2, E_b/N_0\right)\right] \tag{3.30}$$

$$I_{1,e}\left(c_1\right) = T_{1,c_1}\left[I_{1,a}\left(c_1\right)\right]. \tag{3.31}$$

Figs. 3.17-3.19 show the EXIT curves of the stand-alone SIC-based GMLST decoders and the amalgamated "URC-GMLST" decoders. We assume that the area under the EXIT curve of the stand-alone GMLST decoder or of the amalgamated "URC-GMLST" decoder of Fig. 3.10 is represented by $A_E$. It is observed in Fig. 3.17 that no inner iterations are needed between the GMLST(STBC-G2) and URC decoders, since the EXIT curve of the SIC-based GMLST(STBC-G2) detector is a horizontal line. The area under the EXIT curve of the GMLST(STBC-G2) decoder of Fig. 3.10 is equal to that beneath the EXIT curve of the amalgamated "URC-GMLST(STBC-G2)" decoder, which implies that no information loss occurs, when a URC is employed as the intermediate code. On the other hand, it is seen in Fig. 3.18 and 3.19 that the GMLST(STTC) decoders of Fig. 3.10 have slanted EXIT curves, hence extrinsic information exchange using decoding itera-

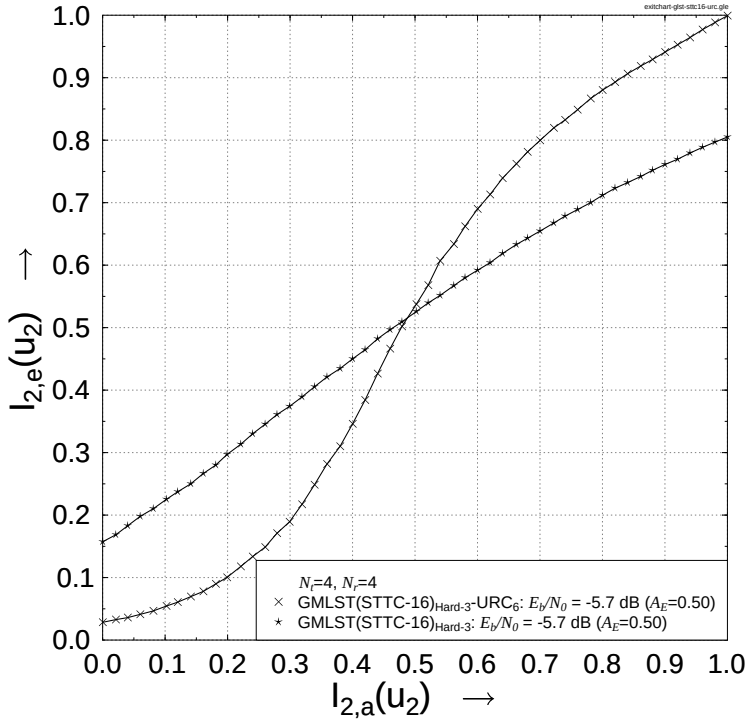


**Figure 3.19:** The EXIT chart curves for the stand-alone GMLST(STTC-16) decoder and the amalgamated GMLST(STTC-16)$_{\text{Hard}}$-URC decoder of Fig. 3.10 using the parameters of Table 3.1. The notation GMLST(STTC-16)$_{\text{Hard-3}}$ indicates 3 hard SIC iterations within the GMLST decoder and the subscript of URC denotes the number of iterations between the GMLST(STTC-16)$_{\text{Hard}}$ and URC decoders.

tions between the URC decoder and the GMLST(STTC) decoder is required to produce the maximum mutual information. After a sufficiently high number of inner iterations, the area under the EXIT curve of the amalgamated "URC-GMLST(STTC)" decoder of Fig. 3.10 is maximized, which is equal to that under the EXIT curve of the stand-alone GMLST(STTC) decoder.

#### 3.3.3.2 17-Component IRCC Aided System Design

Let $A_1$ be the area under the inverted EXIT-curve of Decoder 1 of Fig. 3.10. Then the area property of EXIT charts mentioned in Section 3.2.2.4 can be expressed as

$$A_1 = \int_0^1 T_{1,c_1}^{-1}(i)\mathrm{d}i = R_1, \tag{3.32}$$

which implies that the lowest SNR convergence threshold occurs, when we have $A_2 = R_1 + \epsilon$, where $A_2$ is defined as the area under the EXIT-curve of the URC Decoder 2 of Fig. 3.10 and $\epsilon$ is an infinitesimally small number, provided that the following convergence constraints hold [81]:

$$T_{2,u_2}(0, E_b/N_0) > 0, \;\; T_{2,u_2}(1, E_b/N_0) = 1, \;\; T_{2,u_2}(i, E_b/N_0) > T_{1,c_1}^{-1}(i), \;\; \forall i \in [0, 1) \tag{3.33}$$

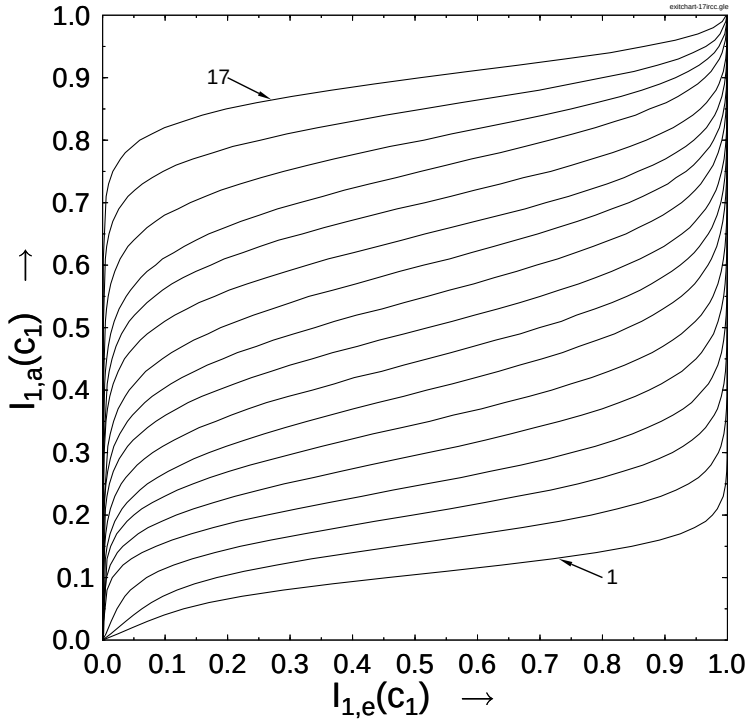


**Figure 3.20:** The EXIT curves for 17 original IRCC component codes.

Hence we invoke IRCCs [61, 81] in Fig. 3.10 as outer codes, because they exhibit flexible EXIT characteristics, which can be optimised to closely match the EXIT curve $T_{2,u_2}(i)$ of the amalgamated "URC-GMLST" decoder in Fig. 3.10, rendering the near-capacity code optimization a simple curve-fitting process.

The original IRCC scheme constituted by a set of $P = 17$ subcodes was constructed in [81] from a systematic, rate-1/2, memory-4 mother code defined by the generator polynomial $(1, g_1/g_0)$, where $g_0 = 1 + D + D^4$ is the feedback polynomial and $g_1 = 1 + D^2 + D^3 + D^4$ is the feedforward one. Each of the $P = 17$ subcodes have a different code rate $R_1^i, \forall i \in [1, 17]$, where puncturing was employed to obtain the rates of $R_1^i > 0.5$ and the code rates of $R_1^i < 0.5$ were created by adding more generators and by puncturing under the constraint of maximizing the achievable free distance. The two additional generators employed in [81] are $g_2 = 1+D+D^2+D^4$ and $g_3 = 1+D+D^3+D^4$, where the resultant $P = 17$ subcodes have coding rates spanning $0.1, 0.15, 0.2, \ldots,$ to 0.9. Each of these $P = 17$ subcodes encodes a specific fraction of the information bit stream according to a specific weighting coefficient $\alpha_i$, where $i = 1, 2, \ldots, 17$. More specifically, assume that there are $N$ number of encoded bits, where each subcode $i$ encodes a fraction of $\alpha_i R_1^i N$ information bits and generates $\alpha_i N$ encoded bits using a coding rate of $R_1^i$. As for the $P = 17$ number of subcodes, given the target overall average code rate of

$R_1 \in (0,1)$, the weighting coefficients $\alpha_i$ must satisfy:

$$1 = \sum_{i=1}^{P=17} \alpha_i, \quad R_1 = \sum_{i=1}^{P=17} \alpha_i R_1^i, \text{ and } \alpha_i \in [0,1], \ \forall i. \tag{3.34}$$

The EXIT function $T_{1,c_1}[I_{1,a}(c_1)]$ of Eq. (3.31) corresponding to the IRCC may be constructed from the EXIT functions of the $P = 17$ subcodes, $T^i_{1,c_1}[I_{1,a}(c_1)], i = 1, \ldots, P$. More specifically, the EXIT function $T_{1,c_1}[I_{1,a}(c_1)]$ of the IRCC is the weighted superposition of the $P = 17$ EXIT functions $T^i_{1,c_1}[I_{1,a}(c_1)], i = 1, \ldots, P$, which is expressed as follows [81]

$$T_{1,c_1}(I_{1,a}(c_1)) = \sum_{i=1}^{P=17} \alpha_i T^i_{1,c_1}[I_{1,a}(c_1)]. \tag{3.35}$$

Fig. 3.20 shows the EXIT functions of the original $P = 17$ subcodes used in [81]. Hence the coefficients $\alpha_1$ are optimised with the aid of the iterative algorithm of [61], so that the EXIT curve of the resultant IRCC is appropriately shaped and hence closely matches the EXIT curve $T_{2,u_2}(i)$ at the specific $E_b/N_0$ value considered. More explicitly, we intend to minimize the EXIT-tunnel area represented by the square of the error function $e(i) = [T_{2,u_2}(i, E_b/N_0) - T^{-1}_{1,c_1}(i)]$ over all $i \in [0,1]$, namely

$$J(\alpha_1, \ldots, \alpha_P) = \int_0^1 e(i)^2 \mathrm{d}i, \quad e(i) > 0, \forall i \in [0,1), \tag{3.36}$$

which is subject to the constraints of Eq. (3.34).

In this section, we consider an average coding rate of $R_1 = 0.5$ for the outer IRCC code. Hence the effective throughput is $2 \times R_1 \log_2 4 = 2$ bit/s/Hz, when 4QAM is employed by the above-mentioned two-layer GMLST schemes of Fig. 2.1. The maximum achievable rates of different GMLST schemes computed according to the properties of EXIT charts [81, 122] at a throughput of $\eta = 2$ bit/s/Hz are depicted in Figs. 3.14-3.16. The exchange of extrinsic information in the schematic of Fig. 3.10 is visualised by plotting the EXIT characteristics of the inner amalgamated "URC-GMLST" decoder and the specificly optimized outer IRCC decoder in Figs. 3.21-3.29.

Note that for the GMLST(STBC-G2) scheme of Fig. 2.2 characterized in Figs. 3.21 and 3.22, a near-capacity performance may be achieved without extrinsic information exchange using decoding iterations between the URC decoder and the GMLST(STBC-G2) decoder, since the EXIT curve of the SIC-based GMLST(STBC-G2) decoder is a horizontal line. As seen in Figs. 3.21, 3.22 and 3.23, when we employ the 17 original outer subcodes of [81] in our IRCC design, the outer IRCC is capable of accurately matching the EXIT curve of the inner amalgamated "URC-GMLST" decoder with the aid of the matching algorithm of [61]. On the other hand, observe in Figs. 3.24-3.29,

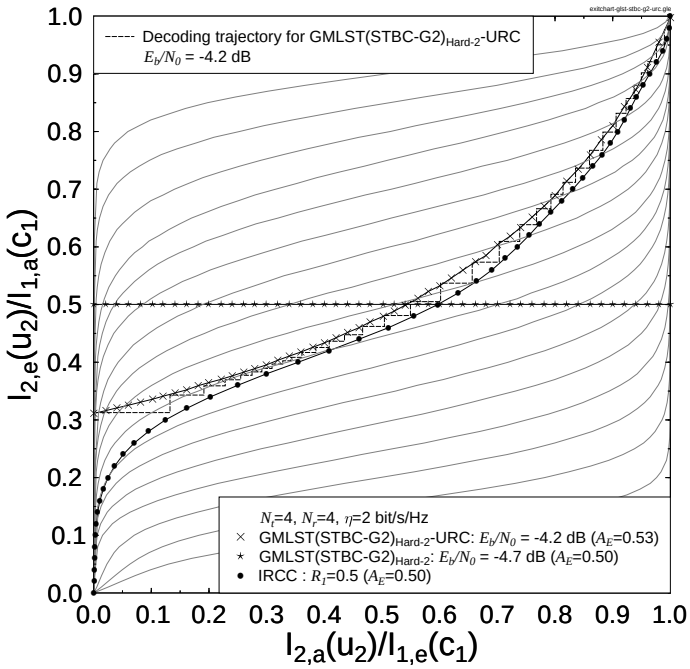


**Figure 3.21:** The EXIT chart curves for the GMLST(STBC-G2)$_{\text{Hard}}$-URC of Fig. 3.10 using a 17-component IRCC having weighting coefficients $[\alpha_1, \cdots, \alpha_{17}]$ = [0, 0, 0.0131465, 0.01553, 0, 0, 0.48839, 0.215005, 0, 0, 0, 0, 0.198844, 0, 0, 0, 0.0691192] and of the 17 original IRCC subcodes, when using the parameters of Table 3.1. The notation GMLST(STBC-G2)$_{\text{Hard-2}}$ indicates 2 hard SIC iterations within the GMLST decoder and no iteration is needed between the GMLST(STBC-G2)$_{\text{Hard}}$ and URC decoders, since the EXIT curve of the GMLST(STBC-G2)$_{\text{Hard}}$ detector is a horizontal line.

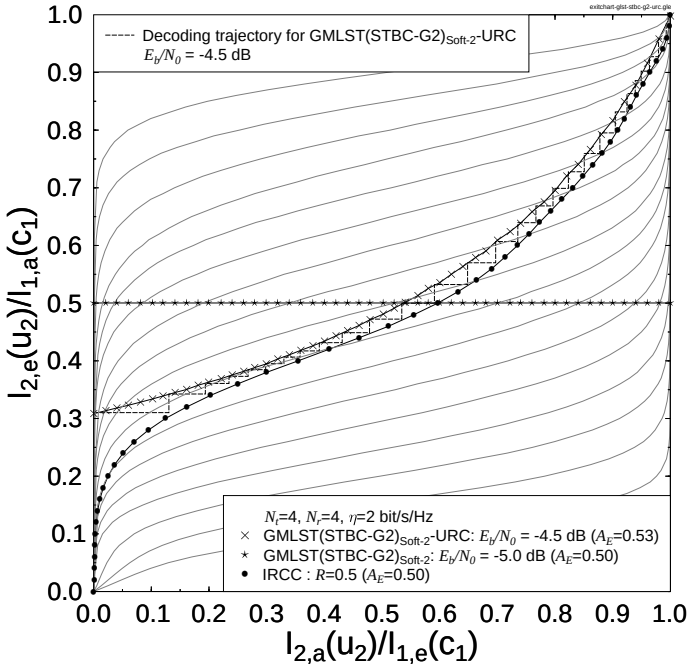


**Figure 3.22:** The EXIT chart curves for the GMLST(STBC-G2)$_{\text{Soft}}$-URC of Fig. 3.10 using a 17-component IRCC having weighting coefficients $[\alpha_1, \cdots, \alpha_{17}]$ = [0, 0, 0.0131465, 0.01553, 0, 0, 0.48839, 0.215005, 0, 0, 0, 0, 0.198844, 0, 0, 0, 0.0691192] and of the 17 original IRCC subcodes, when using the parameters of Table 3.1.

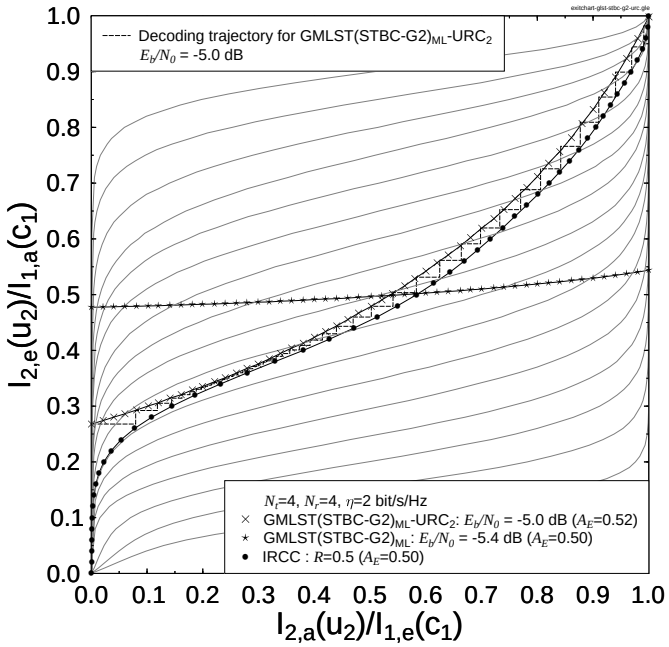


**Figure 3.23:** The EXIT chart curves for the GMLST(STBC-G2)$_{\mathrm{ML}}$-URC of Fig. 3.10 using a 17-component IRCC having weighting coefficients $[\alpha_1, \cdots, \alpha_{17}]$ = [0, 0, 0, 0, 0, 0.327442, 0.186505, 0.113412, 0, 0.0885527, 0, 0.0781214, 0.0962527, 0.0114205, 0.0346015, 0.0136955, 0.0500168] and of the 17 original IRCC subcodes, when using the parameters of Table 3.1. The notation GMLST(STBC-G2)$_{\mathrm{ML}}$ indicates the ML decoder for the GMLST(STBC-G2) scheme and the subscript of URC denotes the number of iterations between the GMLST(STBC-G2)$_{\mathrm{ML}}$ and URC decoders.

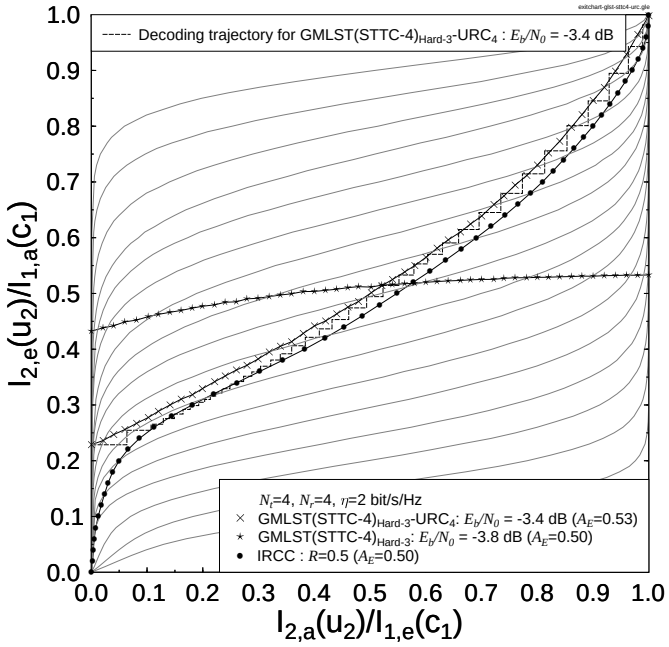


**Figure 3.24:** The EXIT chart curves for the GMLST(STTC-4)$_{\mathrm{Hard}}$-URC of Fig. 3.10 using a 17-component IRCC having weighting coefficients $[\alpha_1, \cdots, \alpha_{17}]$ = [0.0226959, 0, 0, 0, 0.0665581, 0.381315, 0, 0, 0, 0.284711, 0, 0.0311994, 0.0769669, 0, 0.0935122, 0, 0.0430583] and of the 17 original IRCC subcodes, when using the parameters of Table 3.1. The notation GMLST(STTC-4)$_{\mathrm{Hard\text{-}3}}$ indicates 3 hard SIC iterations within the GMLST decoder.

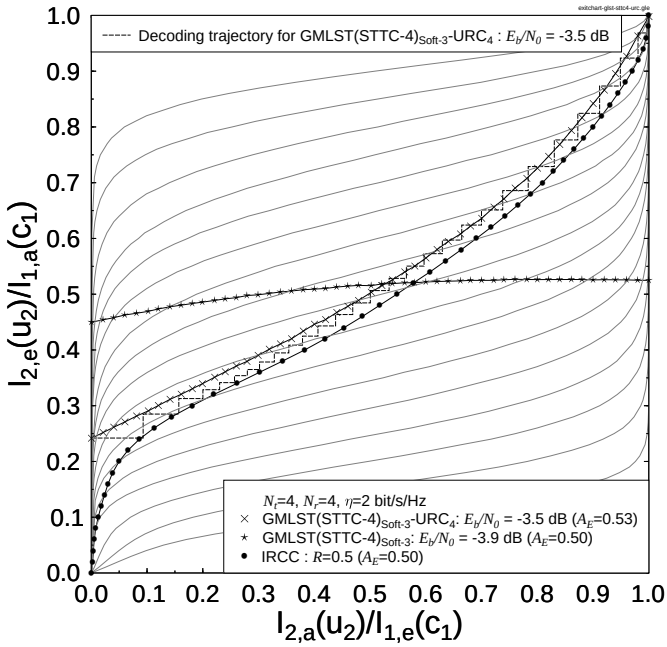


**Figure 3.25:** The EXIT chart curves for the GMLST(STTC-4)$_{\text{Soft}}$-URC of Fig. 3.10 using a 17-component IRCC having weighting coefficients $[\alpha_1, \cdots, \alpha_{17}]$ = [0.0226959, 0, 0, 0, 0.0665581, 0.381315, 0, 0, 0, 0.284711, 0, 0.0311994, 0.0769669, 0, 0.0935122, 0, 0.0430583] and of the 17 original IRCC subcodes, when using the parameters of Table 3.1. The notation GMLST(STTC-4)$_{\text{Soft-3}}$ indicates 3 soft SIC iterations within the GMLST decoder.

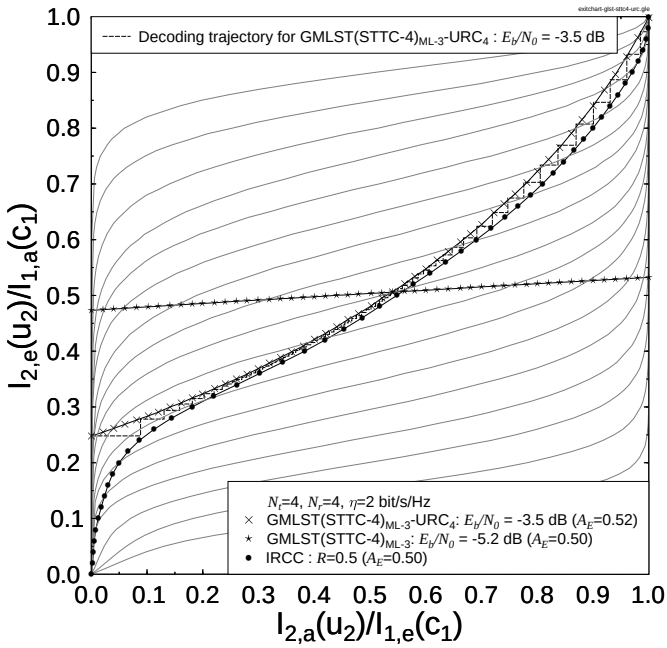


**Figure 3.26:** The EXIT chart curves for the GMLST(STTC-4)$_{\text{ML}}$-URC of Fig. 3.10 using a 17-component IRCC having weighting coefficients $[\alpha_1, \cdots, \alpha_{17}]$ = [0.0226959, 0, 0, 0, 0.0665581, 0.381315, 0, 0, 0, 0.284711, 0, 0.0311994, 0.0769669, 0, 0.0935122, 0, 0.0430583] and of the 17 original IRCC subcodes, when using the parameters of Table 3.1. The notation GMLST(STTC-4)$_{\text{ML-3}}$ indicates 3 iterations between ML demapper and GMLST component decoders.

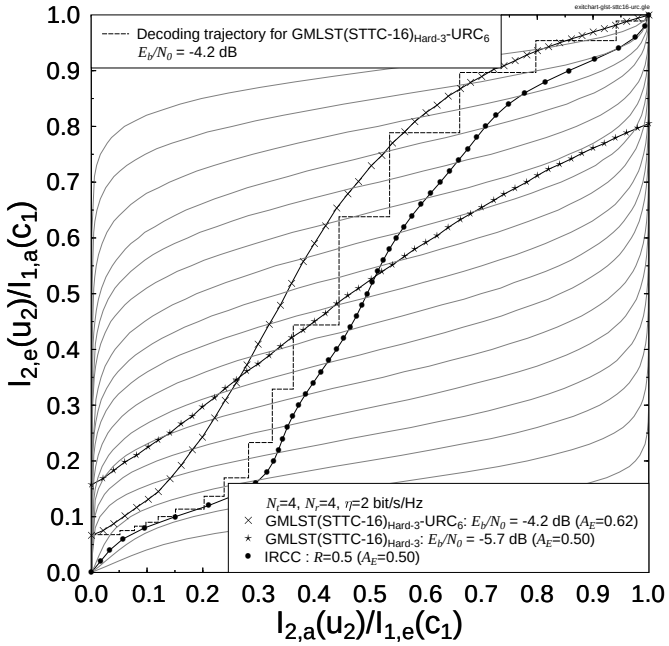


**Figure 3.27:** The EXIT chart curves for the GMLST(STTC-16)$_{\text{Hard}}$-URC of Fig. 3.10 using a 17-component IRCC having weighting coefficients $[\alpha_1, \cdots, \alpha_{17}]$ = [0.327965, 0, 0, 0, 0, 0.099581, 0.0735821, 0, 0, 0, 0, 0.080471, 0.129813, 0, 0, 0, 0.288618] and of the 17 original IRCC sub-codes, when using the parameters of Table 3.1. The notation GMLST(STTC-16)$_{\text{Hard-3}}$ indicates 3 hard SIC iterations within the GMLST decoder, and the subscript of URC denotes the number of iterations between the GMLST(STTC-16)$_{\text{Hard}}$ and URC decoders.

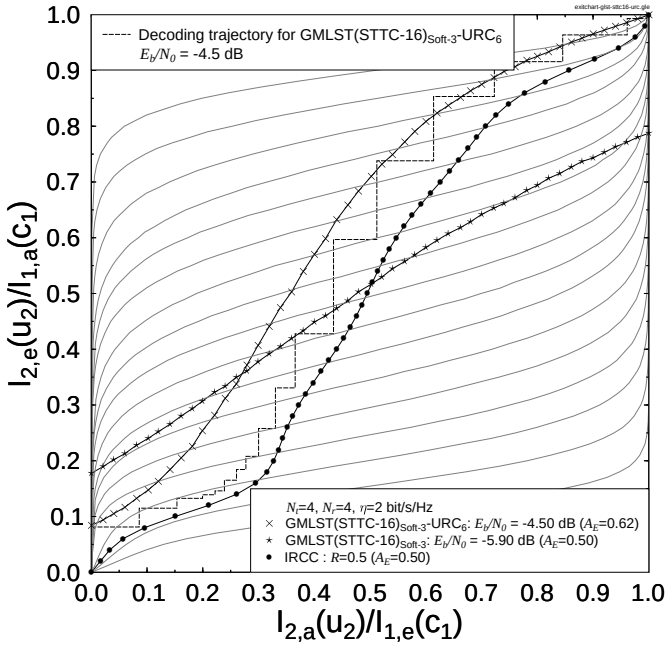


**Figure 3.28:** The EXIT chart curves for the GMLST(STTC-16)$_{\text{Soft}}$-URC of Fig. 3.10 using a 17-component IRCC having weighting coefficients $[\alpha_1, \cdots, \alpha_{17}]$ = [0.327965, 0, 0, 0, 0, 0.099581, 0.0735821, 0, 0, 0, 0, 0.080471, 0.129813, 0, 0, 0, 0.288618] and of the 17 original IRCC sub-codes, when using the parameters of Table 3.1. The notation GMLST(STTC-16)$_{\text{Soft-3}}$ indicates 3 soft SIC iterations within the GMLST decoder, and the subscript of URC denotes the number of iterations between the GMLST(STTC-16)$_{\text{Soft}}$ and URC decoders.

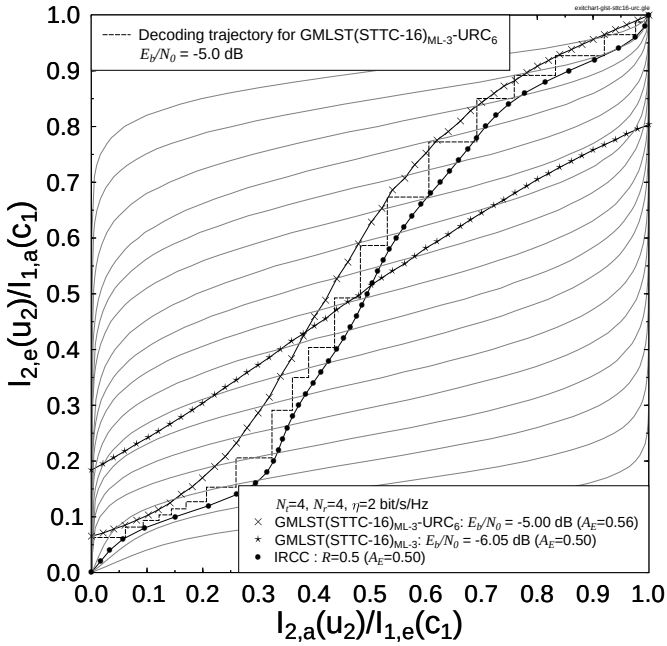


**Figure 3.29:** The EXIT chart curves for the GMLST(STTC-16)$_{\text{ML}}$-URC of Fig. 3.10 using a 17-component IRCC having weighting coefficients $[\alpha_1, \cdots, \alpha_{17}]$ = [0.327965, 0, 0, 0, 0, 0.099581, 0.0735821, 0, 0, 0, 0, 0.080471, 0.129813, 0, 0, 0, 0.288618] and of the 17 original IRCC subcodes, when using the parameters of Table 3.1. The notation GMLST(STTC-16)$_{\text{ML-3}}$ indicates 3 iterations between ML demapper and GMLST component decoders.

for the GMLST(STTC) scheme of Fig. 2.1 that the EXIT curve of the GMLST(STTC) decoder is a slanted line, hence extrinsic information exchange using decoding iterations between the URC decoder and the GMLST(STTC) decoder is needed in order to achieve a near-capacity performance. When there is no iteration between the URC decoder and the GMLST(STTC) decoder, the EXIT curve shape of the URC decoder depends on the $I_{3,e}(u_3)$ value of the GMLST(STTC) decoder observed in Figs. 3.24-3.29 at $I_{3,a}(u_3) = 0$. Hence, the URC-GMLST(STTC) scheme of Fig. 3.10 requires a higher $E_b/N_0$ value in order to maintain a normalised area of $A_E = 0.5$, as shown in Figs. 3.24-3.29. In other words, a certain mutual information i.e. throughput loss will occur, if there is no iteration between the URC decoder and the GMLST(STTC) decoder. It is noted that in Figs. 3.24-3.26, the outer IRCC is capable of accurately matching the EXIT curve of the inner amalgamated "URC-GMLST(STTC-4)" decoder. However, observe in Figs. 3.27-3.29 that due to the "S"-shape of the inner amalgamated "URC-GMLST(STTC-16)" decoder's EXIT curve the original IRCC using 17 subcodes cannot match this shape sufficiently accurately.

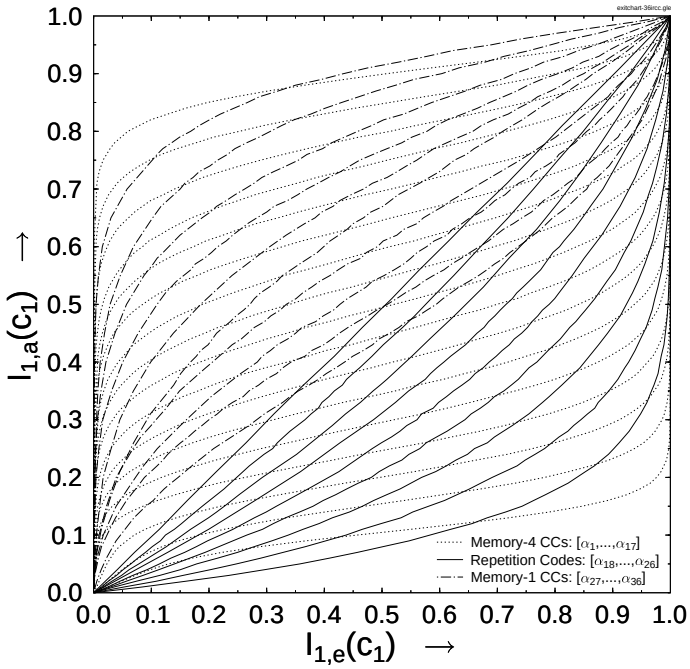


**Figure 3.30:** The EXIT curves for 36 IRCC component codes.

#### 3.3.3.3 36-Component IRCC Aided System Design

For the sake of more accurately matching the shape of the inner amalgamated "URC-GMLST" decoder's EXIT curves, in this section we introduce a novel outer irregular coding scheme using 36 component codes, which is constituted by a hybrid combination of irregular repetition codes and convolutional codes. Observe the EXIT functions of the 17 original subcodes shown in Fig. 3.20, where it is clearly seen that the original memory-4 IRCC exhibits a near-horizontal portion in the EXIT chart, which is typical of strong CCs having a memory of 4 associated with 16 trellis states. On the other hand, in order to match the shape of the inner codes' EXIT curves more accurately, the shape of the outer codes' EXIT functions can be adjusted in a way, which allows us to match a more diverse-shaped set of inner code EXIT functions. Hence we introduce a more diverse range of EXIT functions, particularly near the diagonal of the EXIT chart. This can be achieved by invoking weaker codes having a lower memory, which also impose a potentially reduced complexity.

Accordingly, memory-1 CCs are incorporated into the original IRCC scheme, which have a simple two-state trellis diagram. The generator polynomial of this rate-1/2 memory-1 mother code is defined by $(1, g_1/g_0)$, where $g_0 = D$ and $g_1 = 1$. For a lower code rate, an extra output generator polynomial, namely $g_2$ is used, where we have $g_2 = g_1$. For a higher code rate, the puncturing pattern of the original memory-4 IRCC is employed [81]. This way we generate 10 additional EXIT functions, which are shown by the dashed lines in Fig. 3.30, spanning the code-rate range of [0.45, 0.9] with a stepsize of 0.05. Fur-

thermore, a repetition code is a simple memoryless code, which consists of only two codewords, namely the all-zero and the all-one word. Since it has no memory, the EXIT functions of such repetition codes are diagonally-shaped. Hence, we also incorporate 9 different-rate repetition codes in our novel IRCC scheme, as indicated by the solid lines in Fig. 3.30 and spanning the code-rate range of [0.1, 0.5] with the rate-stepsize of 0.05.

Similarly, as for the $P = 17$ subcodes, Eq. (3.34) can be written for the 36-code scheme as follows:

$$1 = \sum_{i=1}^{P=36} \alpha_i, \quad R_1 = \sum_{i=1}^{P=36} \alpha_i R_1^i, \quad \text{and } \alpha_i \in [0,1], \ \forall i. \tag{3.37}$$

The EXIT functions of all $P = 36$ IRCC subcodes are shown in Fig. 3.30 and all the subcodes are summarized in Table 3.2. As a benefit, the proposed 36-component IRCC has a more diverse range of EXIT function shapes, hence it is capable of providing more accurately matching EXIT curves to fit that of the inner amalgamated "URC-GMLST" decoders, as evidenced in Figs. 3.31, 3.32 and 3.33.

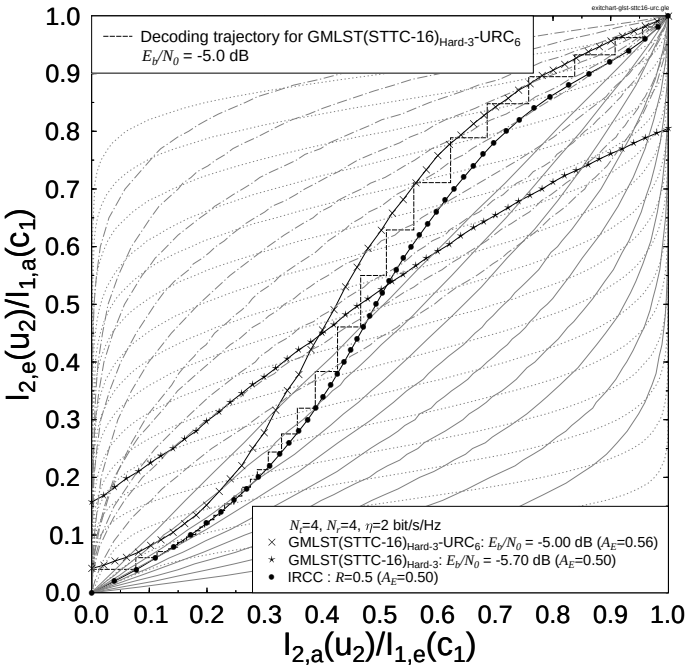


**Figure 3.31:** The EXIT chart curves for the GMLST(STTC-16)$_{\text{Hard}}$-URC of Fig. 3.10 using a 36-component IRCC having weighting coefficients $[\alpha_1, \cdots, \alpha_{36}]$ = [0, 0, 0, 0, 0, 0, 0, 0, 0, 0, 0, 0.0238076, 0.0654278, 0.0108539, 0, 0.0736835, 0.0251597, 0.124231, 0.0829128, 0, 0.140577, 0.0983615, 0.134327, 0.109642, 0, 0, 0, 0, 0, 0, 0, 0, 0, 0, 0, 0.00875876, 0.102257] and of the 36 IRCC subcodes, when using the parameters of Table 3.1. The notation GMLST(STTC-16)$_{\text{Hard-3}}$ indicates 3 hard SIC iterations within the GMLST decoder.

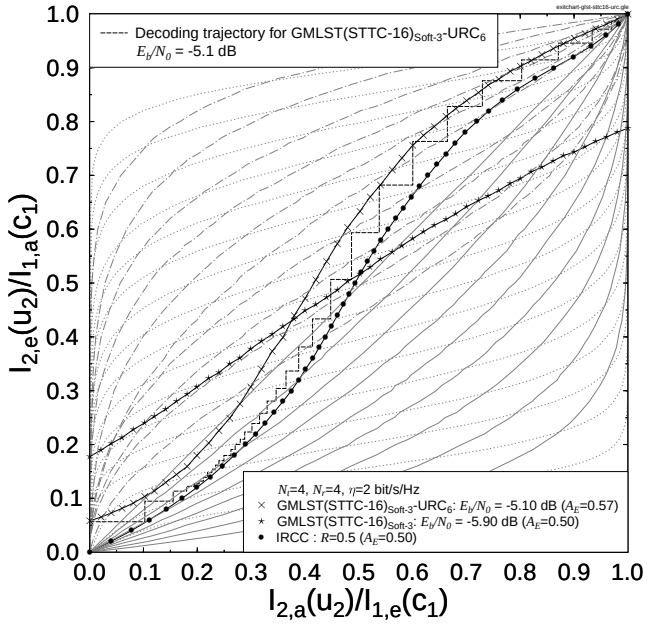


**Figure 3.32:** The EXIT chart curves for the GMLST(STTC-16)$_{\text{Soft}}$-URC of Fig. 3.10 using a 36-component IRCC having weighting coefficients $[\alpha_1, \cdots, \alpha_{36}]$ = [0, 0, 0, 0, 0, 0, 0, 0, 0, 0, 0.0238076, 0.0654278, 0.0108539, 0, 0.0736835, 0.0251597, 0.124231, 0.0829128, 0, 0.140577, 0.0983615, 0.134327, 0.109642, 0, 0, 0, 0, 0, 0, 0, 0, 0, 0, 0.00875876, 0.102257] and of the 36 IRCC subcodes, when using the parameters of Table 3.1. The notation GMLST(STTC-16)$_{\text{Soft-3}}$ indicates 3 soft SIC iterations within the GMLST decoder.

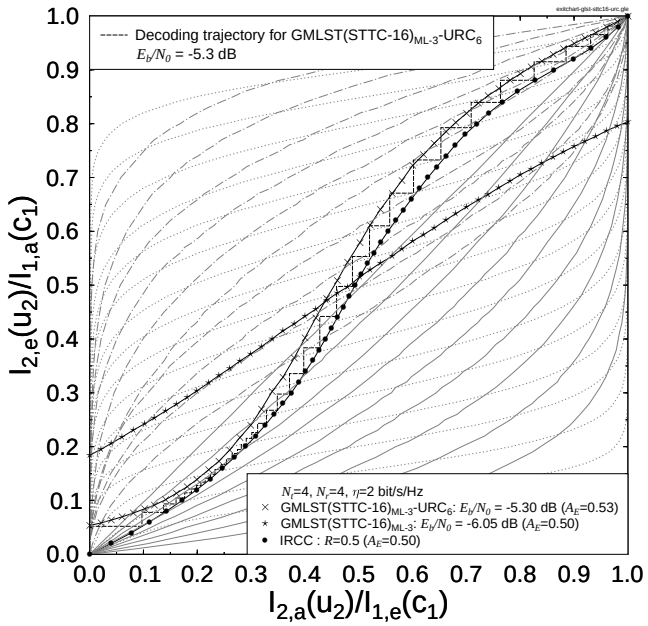


**Figure 3.33:** The EXIT chart curves for the GMLST(STTC-16)$_{\text{ML}}$-URC of Fig. 3.10 using a 36-component IRCC having weighting coefficients $[\alpha_1, \cdots, \alpha_{36}]$ = [0, 0, 0, 0, 0, 0, 0, 0, 0, 0, 0.0238076, 0.0654278, 0.0108539, 0, 0.0736835, 0.0251597, 0.124231, 0.0829128, 0, 0.140577, 0.0983615, 0.134327, 0.109642, 0, 0, 0, 0, 0, 0, 0, 0, 0, 0, 0.00875876, 0.102257] and of the 36 IRCC subcodes, when using the parameters of Table 3.1. The notation GMLST(STTC-16)$_{\text{ML-3}}$ indicates 3 iterations between ML demapper and GMLST component decoders, and the subscript of URC denotes the number of iterations between the GMLST(STTC-16)$_{\text{ML}}$ and URC decoders.

| Code Index $i$ | Type | Coding Rate | Code Index $i$ | Type | Coding Rate |
|---|---|---|---|---|---|
| 1 | CC mem-4 | 0.10 | 19 | Rep. Code | 0.15 |
| 2 | CC mem-4 | 0.15 | 20 | Rep. Code | 0.20 |
| 3 | CC mem-4 | 0.20 | 21 | Rep. Code | 0.25 |
| 4 | CC mem-4 | 0.25 | 22 | Rep. Code | 0.30 |
| 5 | CC mem-4 | 0.30 | 23 | Rep. Code | 0.35 |
| 6 | CC mem-4 | 0.35 | 24 | Rep. Code | 0.40 |
| 7 | CC mem-4 | 0.40 | 25 | Rep. Code | 0.45 |
| 8 | CC mem-4 | 0.45 | 26 | Rep. Code | 0.50 |
| 9 | CC mem-4 | 0.50 | 27 | CC mem-1 | 0.45 |
| 10 | CC mem-4 | 0.55 | 28 | CC mem-1 | 0.50 |
| 11 | CC mem-4 | 0.60 | 29 | CC mem-1 | 0.55 |
| 12 | CC mem-4 | 0.65 | 30 | CC mem-1 | 0.60 |
| 13 | CC mem-4 | 0.70 | 31 | CC mem-1 | 0.65 |
| 14 | CC mem-4 | 0.75 | 32 | CC mem-1 | 0.70 |
| 15 | CC mem-4 | 0.80 | 33 | CC mem-1 | 0.75 |
| 16 | CC mem-4 | 0.85 | 34 | CC mem-1 | 0.80 |
| 17 | CC mem-4 | 0.90 | 35 | CC mem-1 | 0.85 |
| 18 | Rep. Code | 0.10 | 36 | CC mem-1 | 0.90 |

**Table 3.2:** The 36 irregular component codes used in the hybrid IRCC scheme, where each subcode index $i$ corresponds to the weighting coefficient $\alpha_i$.

### 3.3.4 Results and Discussions

As we can see from Figs. 3.24, 3.25, 3.27, 3.28, 3.31 and 3.32, the bit-by-bit Monte-Carlo simulation based decoding trajectory of the IRCC-URC-GMLST(STTC) schemes using SIC detection within the GMLST (STTC) decoder has a slight mismatch with respect to their EXIT curves. This is due to the trellis structure of STTCs, which results in correlated error propagation between the different layers in the process of SIC operation. We found that the higher the correlation of the STTC coded bits owing to the trellis structure, the higher the decoding trajectory mismatch. Furthermore, as the number of trellis states increases from 4 to 16, the correlation of the STTC-16 coded bits becomes higher, because the code imposes more correlation. As a result, the STTC-16 scheme will impose a higher correlation than the STTC-4 scheme, when there is error propagation between the different layers due to the imperfect SIC operation. Hence, the decoding trajectory of the GMLST(STTC-16)-URC-IRCC scheme of Fig. 3.10 has a higher mismatch in its EXIT

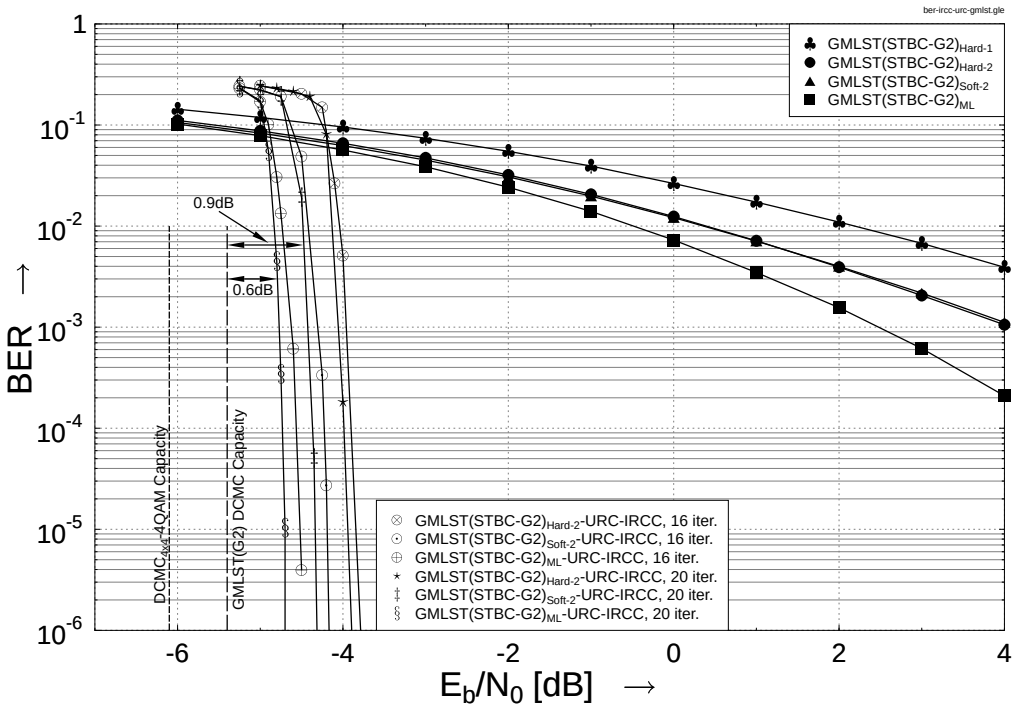


**Figure 3.34:** The BER performance comparison of the IRCC-URC-GMLST(STBC-G2) schemes of Fig. 3.10 and of the stand-alone GMLST(STBC-G2) schemes of Fig. 2.2 using the parameters of Table 3.1.

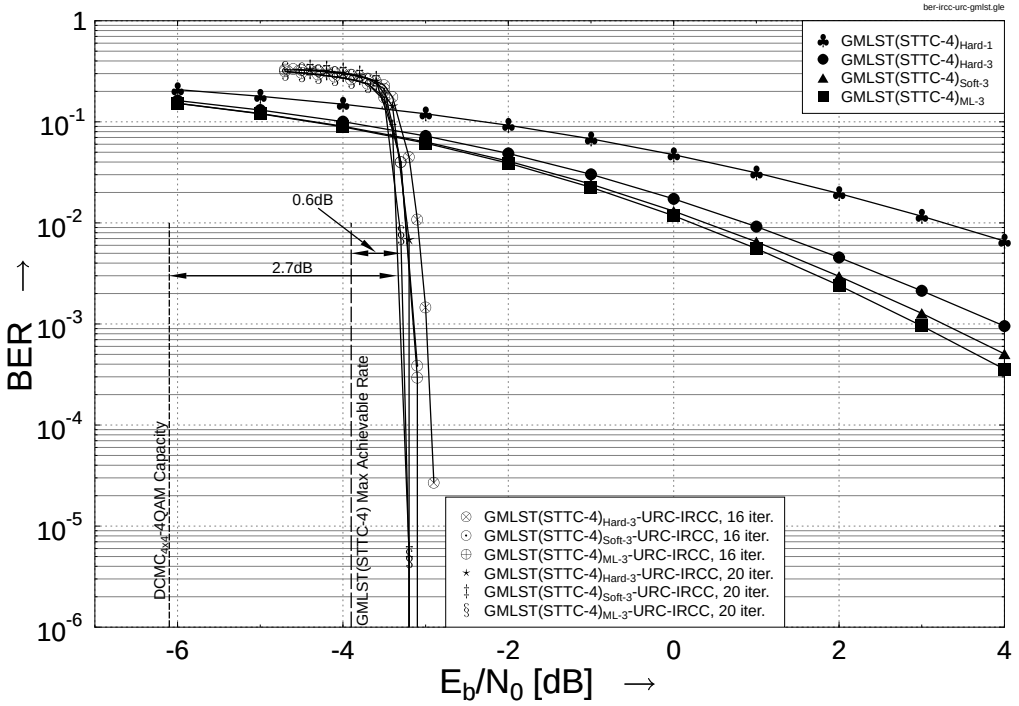


**Figure 3.35:** The BER performance comparison of the IRCC-URC-GMLST(STTC-4) schemes of Fig. 3.10 and of the stand-alone GMLST(STTC-4) schemes of Fig. 2.1 using the parameters of Table 3.1.

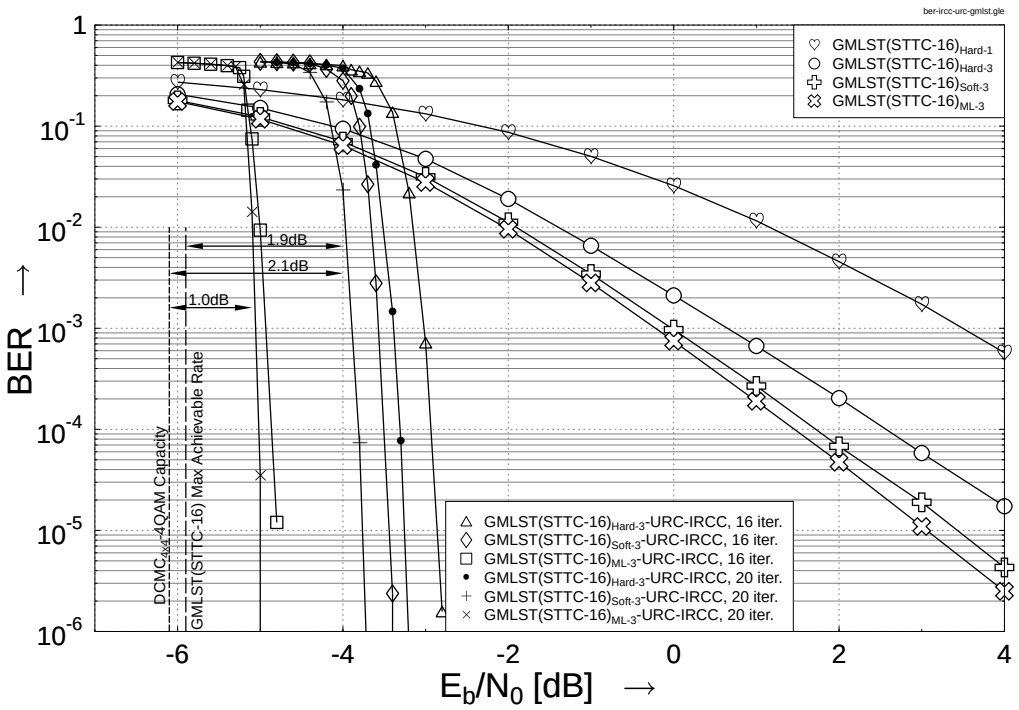


**Figure 3.36:** The BER performance comparison of the IRCC-URC-GMLST(STTC-16) schemes of Fig. 3.10 where the original 17-component IRCC is employed and of the stand-alone GMLST(STTC-16) schemes of Fig. 2.1 using the parameters of Table 3.1.

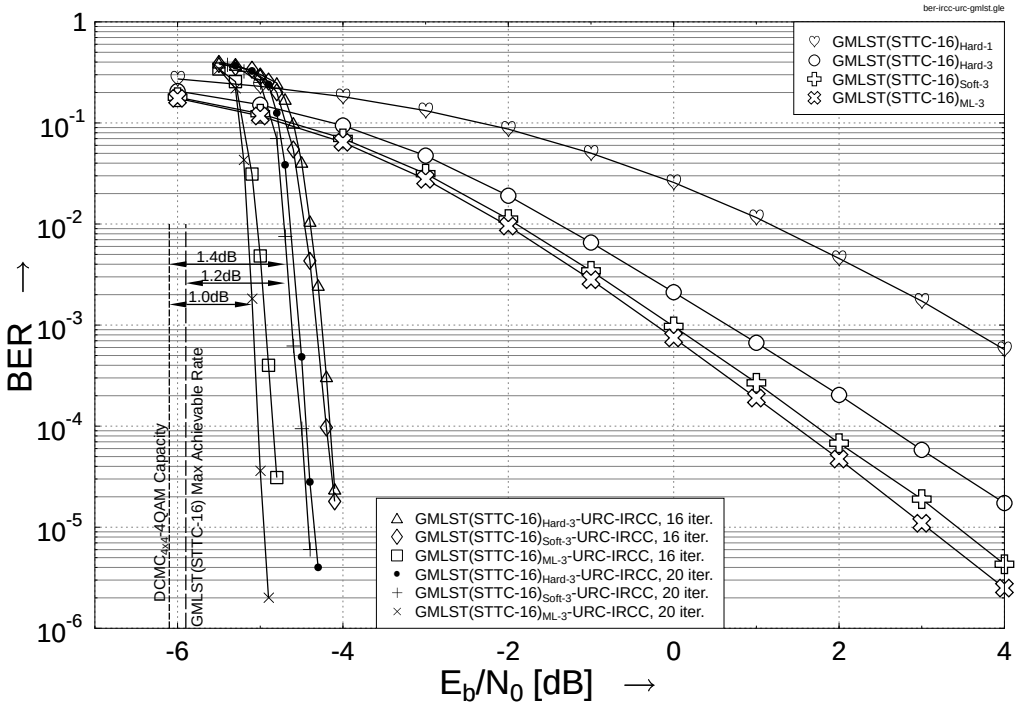


**Figure 3.37:** The BER performance comparison of the IRCC-URC-GMLST(STTC-16) schemes of Fig. 3.10 where the 36-component IRCC is employed and of the stand-alone GMLST(STTC-16) schemes of Fig. 2.1 using the parameters of Table 3.1.

chart, as seen in Figs. 3.27, 3.28, 3.31 and 3.32. By contrast, the decoding trajectory of the IRCC-URC-GMLST(STBC-G2) scheme of Fig. 3.10 characterized in Fig. 3.21 and 3.22 using hard and soft SIC accurately matches both the inner and the outer EXIT curves owing to the uncorrelated error propagation. For comparison, Fig. 3.23 presents the decoding trajectory of the IRCC-URC-GMLST(STBC-G2) scheme of Fig. 3.10 using an ML decoder. On the other hand, the decoding trajectory of the IRCC-URC-GMLST(STTC) schemes of Fig. 3.10 employing ML detection is presented in Figs. 3.26, 3.29 and 3.33. Again, we use three iterations between the ML demapper and GMLST component decoders so that the number of STTC decoder operations invoked remains the same as that of the scheme employing three SIC iterations. Since there is no error propagation in the ML-based scheme, the decoding trajectory of the ML-based scheme closely matches its EXIT curve. However, the error propagation was avoided in the ML-based scheme at the price of a higher complexity.

Figs. 3.34-3.37 present the BER performance of both the near-capacity IRCC-URC-GMLST of Fig. 3.10 and of the stand-alone GMLST schemes of Figs. 2.1 and 2.2 employing various space-time codes combined with SIC and ML detection. It is observed that for three SIC operations, the performance of both the GMLST(STTC-4) and GMLST(STTC-16) schemes significantly improves as a benefit of attaining the maximum achievable receive diversity, whereas the soft-SIC based scheme approaches the performance of the ML-detected GMLST(STTC) scheme more closely, since the residual error propagation is further mitigated. On the other hand as seen in Fig. 3.34, the GMLST(STBC-G2) scheme using two SIC operations exhibits a 1.6 dB gain over a single hard-output SIC iteration at the BER of $10^{-2}$. Although not explicitly shown here, our investigations indicate that no more improvements are attained beyond two SIC operations, since the residual interference propagating among groups is independently distributed across $K/2$ consecutive G2 *codeword* block periods during $K$ symbol intervals and hence it cannot be eliminated by further SIC operations. Observe in Figs. 3.34-3.37 that the throughput of the stand-alone GMLST schemes is relatively far from the corresponding DCMC capacity. For the concatenated systems of Fig. 3.10, it is clearly shown in Fig. 3.34 that the IRCC-URC-GMLST(STBC-G2) scheme is capable of performing within 0.9 dB of the corresponding DCMC capacity of the GMLST(STBC-G2) scheme, when soft SIC is employed. On the other hand, observe in Figs. 3.31 and 3.32 that the IRCC-URC-GMLST(STTC-16) scheme of Fig. 3.10 exhibits a mismatch between the decoding trajectory and the EXIT curve, but performs closer to the DCMC$_{4\times4}$-4QAM capacity, as shown in Fig. 3.37. This improvement is achieved at the price of a significantly higher complexity, than that of the IRCC-URC-GMLST(STBC-G2) scheme. The BER performance of the most complex ML-detected IRCC-URC-GMLST(STTC-16) scheme is also depicted in Fig. 3.37, where

we can see a 0.4 dB gain over the soft SIC based scheme. However, the complexity of the ML-based scheme may be unaffordable, especially when the number of GMLST layers is high.

## 3.4 Chapter Conclusion

In this chapter, we proposed the novel serially concatenated IRCC-URC-GMLST system of Fig. 3.10 that exploits the advantages of both iterative detection as well as those of the GMLST schemes using STBC and STTC as the component space-time codes. In Section 3.2.1.1, an APP-based iterative multistage SIC detection algorithm has been invoked for the GMLST schemes instead of the previous Viterbi-decoding-aided SIC detection for the sake of supporting the iterative detection process at the receiver side. Furthermore, in Section 3.2.1.2 we presented the significantly more complex iterative ML detection scheme designed for the GMLST(STTC) schemes of Fig. 2.1 in the context of serially concatenated systems for comparison, which invokes a concept similar to that of classic BICM-ID schemes. On the other hand, the benefit of URC precoders was characterized in Section 3.3.3.1, which was used as an intermediate code and assisted us in eliminating the system's error-floor and hence improved the attainable decoding convergence. Moreover, our investigations demonstrated in Section 3.3.3 that the proposed low-complexity SIC-based iteratively decoded IRCC-URC-GMLST scheme of Fig. 3.10 is capable of achieving a near-capacity performance, when designed with the aid of EXIT chart analysis. Table 3.3 presents the achievable coding gains, the SNR-distance from the maximum achievable rate limit as well as that from the DCMC capacity limit for the various near-capacity iteratively-decoded IRCC-URC-GMLST systems. Based on these simulation results, we found that the iterative IRCC-URC-GMLST scheme of Fig. 3.10 using SIC detection strikes an attractive trade-off between the complexity imposed and the effective throughput achieved. In conclusion, we summarize our design procedure as follows:

1. We derived the DCMC capacity formula of the GMLST(STBC) schemes of Fig. 2.2 and quantified the maximum achievable rates of the GMLST schemes using STTCs with the aid of EXIT charts.

2. We generated the EXIT curve of the inner decoder, which is constituted here by the GMLST decoder and URC decoder of Fig. 3.10.

3. We designed an IRCC outer code to match the EXIT curve of the inner code. The resultant scheme was capable of approaching the capacity determined for the high-complexity, but optimum ML detector.

| GMLST(STBC) Using 17-Component IrCC | Coding Gain | Distance from Max. Achiev. Rate | Distance from DCMC Capacity | Extracted from Fig. |
|---|---|---|---|---|
| Iterative Hard SIC | 12.5 dB | 0.7 dB | 2.1 dB | (3.34) |
| Iterative Soft SIC | 12.9 dB | 0.6 dB | 1.7 dB | |
| ML | 10.7 dB | 0.7 dB | 1.4 dB | |
| GMLST(STTC-4) Using 17-Component IrCC | Coding Gain | Distance from Max. Achiev. Rate | Distance from DCMC Capacity | Extracted from Fig. |
| Iterative Hard SIC | 11.2 dB | 0.6 dB | 2.9 dB | (3.35) |
| Iterative Soft SIC | 10.2 dB | 0.7 dB | 2.9 dB | |
| Iterative ML | 9.7 dB | 0.7 dB | 2.9 dB | |
| GMLST(STTC-16) Using 17-Component IrCC | Coding Gain | Distance from Max. Achiev. Rate | Distance from DCMC Capacity | Extracted from Fig. |
| Iterative Hard SIC | 7.4 dB | 2.5 dB | 2.9 dB | (3.36) |
| Iterative Soft SIC | 7.2 dB | 2.1 dB | 2.3 dB | |
| Iterative ML | 8.0 dB | 1.0 dB | 1.1 dB | |
| GMLST(STTC-16) Using 36-Component IrCC | Coding Gain | Distance from Max. Achiev. Rate | Distance from DCMC Capacity | Extracted from Fig. |
| Iterative Hard SIC | 8.6 dB | 1.3 dB | 1.7 dB | (3.37) |
| Iterative Soft SIC | 7.9 dB | 1.4 dB | 1.6 dB | |
| Iterative ML | 8.0 dB | 1.0 dB | 1.1 dB | |

**Table 3.3:** Performance summary of the iteratively-decoded IRCC-URC-GMLST systems of Fig. 3.10 at the target BER of $10^{-5}$.

4. We reduced the complexity imposed by the ML detector by using the lower-complexity SIC detector of Fig. 3.2, while avoiding any substantial performance degradation by redesigning the IRCC scheme using 36 component codes, which hence matches the EXIT curve of the SIC inner decoder more accurately.

5. This design procedure is generically applicable, regardless of the specific choice of the inner and outer decoder components, as exemplified by other detectors, such as Sphere Detectors (SD), Markov Chain Monte Carlo (MCMC) detectors as well as by other outer codes, such as an irregular Low Density Parity Check (LDPC) code, etc.

Chapter 4

# Irregular Cooperative Space-Time Coding Schemes

## 4.1 Introduction

In previous chapters, classic Multiple-Input Multiple-Output (MIMO) systems have been investigated, where the multiple antenna elements are colocated. As discussed in Chapter 1, the antenna elements in colocated MIMO systems are assumed to be positioned sufficiently far apart to ensure that the signals transmitted from each antenna element experience independent fading. Otherwise, the spatial fading correlation imposed by insufficient antenna spacing and large-scale shadow fading [128] result in a degraded capacity as well as BER performance for MIMO systems. However, the assumption of having a sufficiently high antenna spacing may be impractical for hand-held wireless devices, which are typically limited in size and hardware complexity. Hence, the conventional colocated MIMO schemes presented in previous chapters are not readily applicable to compact wireless devices due to the above-mentioned size and complexity constraints.

In the past few years, cooperative communication schemes [38, 39, 44, 46, 48, 129, 130] have been intensively studied, which combine the benefits of MIMO systems with relay-aided techniques in order to eliminate the correlation amongst the spatial diversity paths. Since the MIMO transmitter's elements in such a network are distributed, the network forms a "distributed MIMO" system. Relaying techniques may be employed in diverse communication scenarios, such as cellular networks, wireless ad-hoc and sensor networks, and wireless local area networks, in order to improve the attainable transmission efficiency and/or reliability. Specifically, in a relay aided network where the nodes (users) are equipped with either single or multiple antennas, cooperative communications allow the nodes (users) to assist each other in forwarding (relay) all messages to the destina-

tion, rather than transmitting only their own messages. Specifically, two main aspects of relay-aided networks have been investigated in the literatures, namely the fundamental limits of transmissions over relay channels [131–137], and the development of practical cooperative protocols and transmission schemes [48, 138, 139].

The information theoretic study of the relay aided channel's capacity was pioneered by Cover and El Gamal [131]. Specifically, they derived the exact capacity expression under certain conditions and evaluated both the lower and upper bounds of the achievable modem-mode-related information rates. Recent information theoretic studies considered the Gaussian relay channel in the context of multiple relay nodes [136], and relay nodes operating in either full- or half-duplex mode [132], as well as multi-antenna aided relaying systems [140] and two-way relay channels [137]. In addition to the information theoretic investigations, there are numerous studies on practical transmission schemes designed for relaying systems. For the sake of improving the attainable diversity gain of relay-aided networks, numerous cooperative protocols [38, 39, 44, 48, 138] have been proposed. According to the Amplify-and-Forward (AF) protocol [130], the source information is simply amplified and forwarded by a relay to the destination. By contrast, in the Decode-and-Forward (DF) protocol [130], the relayed signal is first detected, reencoded/remodulated and then forwarded to the destination. However, a strong channel code is required for avoiding or at least mitigating the potential error propagation in the DF scheme. Furthermore, the novel class of coded cooperation [139] was proposed by Hunter *et al.*, which combines the concept of cooperative communications and channel coding. Similarly to DF relaying, a sophisticated code design is needed to improve the efficiency of coded cooperation.

On the other hand, inspired by the family of classic turbo codes used in non-cooperative communication scenarios, Distributed Turbo Codes (DTC) [49] have been proposed for "distributed MIMO" systems, where the relay interleaves and re-encodes the message prior to forwarding it to the destination. Hence, a *turbo processing* gain may be achieved at the destination. However, DTCs suffer from having an imperfect communication link between the source and relay nodes. In [50], a three-component Distributed Turbo Trellis Coded Modulation (DTTCM) scheme has been proposed, which takes into consideration the realistic condition of having an imperfect source-to-relay communication link. The DTTCM scheme [50] designed using EXtrinsic Information Transfer (EXIT) chart analysis [64, 101] is capable of minimizing the decoding error probability at the relay node and performs close to its idealized counterpart that assumes perfect decoding at the relay node. However, the DTTCM of [50] fails to approach the corresponding relay channel's capacity. On the other hand, several near-capacity turbo coding schemes were proposed in [62] and [63] by Zhang and Duman for full-duplex and half-duplex relay-aided systems, re-

spectively, although the authors did not aim for finding the optimal coding schemes under different relay/network configurations.

Against this background, our objective here is to design a near-capacity cooperative scheme using a proposed joint source-and-relay mode design procedure, which is suitable for arbitrary relay network configurations. Furthermore, the relay system's effective throughput is maximized as a benefit of the proposed design procedure. For the sake of approaching the relay channel's capacity, we first derive the theoretical lower and upper bounds on the Continuous-input Continuous-output Memoryless Channel's (CCMC) [6, 14] capacity as well as of the Discrete-input Continuous-output Memoryless Channel (DCMC) [6, 14] capacity (constrained information rate) with independent and uniformly distributed (i.u.d.) inputs. A new Irregular Cooperative Space-Time Coding (Ir-CSTC) scheme is proposed, where two IRregular Convolutional Codes (IRCC) [61, 81] having different IRCC weighting coefficients are employed at the source and relay nodes, respectively, which are designed for supporting near-capacity cooperative communications.

On the other hand, since in most three-terminal cooperative scenarios, a significant *multiplexing loss* will be incurred compared to direct transmissions due to the half-duplex constraint[1] of practical transceivers, a successive relaying protocol was proposed in [141] for the sake of recovering the multiplexing loss by incorporating an additional relay in the network and arranging for the two relays to transmit in turn. In order to achieve a near-capacity performance in the context of twin-relay aided network, we extend the three-terminal Ir-CSTC scheme to suit the four-terminal network where the successive relaying protocol is employed. Similarly, we also derive both the upper and lower bounds of the CCMC capacity as well as the bounds of the information rates constrained by i.u.d. discrete inputs for the successive relaying aided uncorrelated Rayleigh fading channel. Furthermore, the joint source-and-relay mode design procedure is generalized for the twin-relay aided network. Specifically, the distributed code components used at the source and relays are optimally designed. As a benefit, the Ir-CSTC scheme becomes capable of approaching the DCMC capacity (constrained information rate) in the context of the successive relaying aided network, when the frame length is sufficiently long (e.g. $10^5$ bits), while approaching the transmission efficiency of classic direct transmission operating without relaying. Most importantly, it will be demonstrated that the joint source-and-relay mode design procedure is capable of finding the optimal cooperative

[1]The reason of assuming half-duplex terminals relies on the fact that current limitations in radio transceiver implementations preclude the terminals from full-duplex operation, i.e. from transmitting and receiving at the same time in the same frequency band. To elaborate a little further, indeed, it would be beneficial in capacity terms to transmit and receive at the same time, but this would result in the following problems. The received signal may be almost 100dB lower than the transmit signal. Hence the smallest leakage of the transmitted signal would desensitize the receiver's Automatic Gain Control (AGC), hence potentially drowning the received signal.

coding scheme under arbitrary relay network configuration in both single-relay-aided and twin-relay-aided networks.

The rest of this chapter is organised as follows. Section 4.2 focuses on single-relay-aided cooperative communications. The system model of the single-relay-aided network is described in Section 4.2.1. Section 4.2.2 specifies the encoding and decoding processes of the novel Ir-CSTC scheme. The single relay channel's capacity computation and the EXIT chart aided joint source-and-relay mode design are detailed in Section 4.2.3, while the corresponding simulation results and discussions are provided in Section 4.2.4. Furthermore, a twin-relay-based successive relaying aided cooperative communication scenario is considered in Section 4.3, where the extended Ir-CSTC scheme conceived for our four-terminal network is optimally designed for near-capacity operation with the aid of EXIT chart analysis. We provide our simulation results in Section 4.3.5 for the twin-relay-based successive relaying aided network. Finally, we conclude this chapter in Section 4.4.

## 4.2 Single-Relay-Aided Cooperative Communications

### 4.2.1 Single-Relay-Aided Network Model

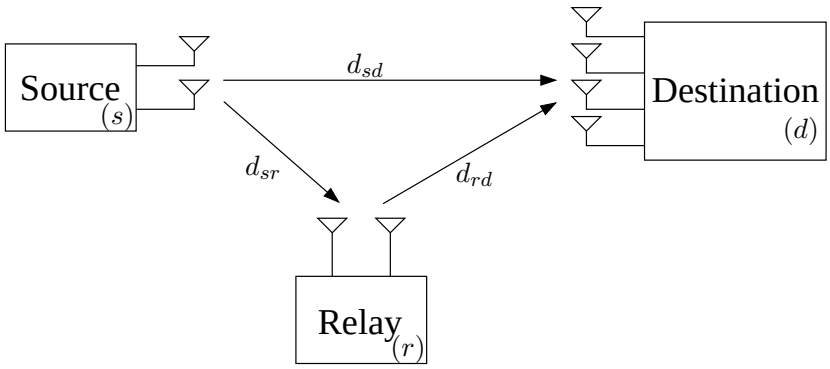


**Figure 4.1:** Schematic of a single relay aided multi-antenna system, where $d_{ab}$ is the geographical distance between node $a$ and node $b$.

We consider a two-hop relay-aided network, which has a single source node having $N_s$ antennas, a single relay node equipped with $N_r$ antennas and a destination node having $N_d$ antennas, where all nodes obey the half-duplex constraint, i.e. a node cannot transmit and receive simultaneously. The schematic of the proposed system is shown in Fig. 4.1, which typically entails two phases. In *Phase I*, the source node ($s$) broadcasts the information both to the relay node ($r$) and to the destination node ($d$). The relay node ($r$) processes the received information and forwards it to the destination node ($d$) in *Phase II*, while the source node ($s$) remains silent. The destination performs decoding based on the messages it received in both phases. As in [142], we model the communication links in

Fig. 4.1 as being subjected to both long-term free-space path loss as well as to short-term uncorrelated Rayleigh fading.

Let $d_{ab}$ and $P_{ab}$ denote the geometrical distance and the path loss between nodes $a$ and $b$. The path loss and the geometrical distance can be related by [142]

$$P_{ab} = \frac{K}{d_{ab}^{\alpha}}, \tag{4.1}$$

where $K$ is a constant that depends on the environment and $\alpha$ is the path-loss exponent. For a free space scenario, we have $\alpha = 2$. The relationship between the energy $E_{sr}$ received at the relay node and that of the destination node $E_{sd}$ can be expressed as

$$E_{sr} = \frac{P_{sr}}{P_{sd}} E_{sd} = G_{sr} E_{sd}, \tag{4.2}$$

where $G_{sr}$ is the power-gain (or geometrical-gain) [142] experienced by the source-to-relay link with respect to the source-to-destination link as a benefit of the commensurately reduced distance and path loss, which can be expressed as

$$G_{sr} = \left(\frac{d_{sd}}{d_{sr}}\right)^2. \tag{4.3}$$

Similarly, the geometrical-gain at the relay-to-destination link with respect to the source-to-destination link can be formulated as

$$G_{rd} = \left(\frac{d_{sd}}{d_{rd}}\right)^2. \tag{4.4}$$

Naturally, the geometrical-gain at the source-to-destination link with respect to itself is unity, i.e. $G_{sd} = 1$. Therefore, owing to the triangle inequality applied in Fig. 4.1, the geometrical-gains $G_{sr}$ and $G_{rd}$ have to satisfy

$$G_{sr} + G_{rd} + 2\sqrt{G_{sr} G_{rd}} \geq G_{sr} G_{rd}. \tag{4.5}$$

We assume that the relay node is closer to the source node than to the destination node, while both the source and relay are far away from the destination, namely we have $G_{sr} > G_{rd}$. In this scenario, the relay benefits from a higher received signal power than the destination. This assumption facilitates the employment of near-perfect DF relaying (similar arguments can be found in [132, 143]), otherwise other relaying modes might be better choices (e.g. Amplify-and-Forward (AF) and Compress-and-Forward (CF)). Hence, the vector hosting the received signal at the relay node during *Phase I*, which consists of $L_s$ number of symbol periods, can be formulated as

$$\mathbf{y}_r = \sqrt{G_{sr}} \mathbf{H}_{sr} \mathbf{c}_s + \mathbf{n}_r, \tag{4.6}$$

where $\mathbf{y}_r = [y_{r,1}, \ldots, y_{r,N_r}]^T$ is the $N_r$-element vector of the received signals at the relay node, $\mathbf{H}_{sr}$ is the $(N_r \times N_s)$-element channel matrix, the entries of which are independent

and identically complex Gaussian distributed with a zero mean and a variance of 0.5 per dimension. Furthermore, $\mathbf{c}_s = [c_{s,1}, \ldots, c_{s,N_s}]^T$ is an $N_s$-element vector of the signals transmitted from the source node at an average power of $P_0$ and $\mathbf{n}_r = [n_{r,1}, \ldots, n_{r,N_r}]^T$ is an $N_r$-element noise vector. Each element of $\mathbf{n}_r$ is an Additive White Gaussian Noise (AWGN) process having a zero mean and a variance of $N_0/2$ per dimension. By contrast, the signal vector received at the destination node during *Phase I* can be expressed as

$$\mathbf{y}_d^I = \sqrt{G_{sd}}\mathbf{H}_{sd}\mathbf{c}_s + \mathbf{n}_d, \tag{4.7}$$

and the signal vector received at the destination node during *Phase II*, when $L_r$ number of symbols are transmitted from the relay node, is formulated as

$$\mathbf{y}_d^{II} = \sqrt{G_{rd}}\mathbf{H}_{rd}\mathbf{c}_r + \mathbf{n}_d, \tag{4.8}$$

where $\mathbf{y}_d^I = [y_{d,1}^I, \ldots, y_{d,N_d}^I]^T$ and $\mathbf{y}_d^{II} = [y_{d,1}^{II}, \ldots, y_{d,N_d}^{II}]^T$ are both $N_d$-element vectors of the signals received during *Phase I* and *Phase II* at the destination node, $\mathbf{H}_{sd} \in \mathbb{C}^{N_d \times N_s}$ and $\mathbf{H}_{rd} \in \mathbb{C}^{N_d \times N_r}$ are the corresponding channel matrices, the entries of which are independent and identically complex Gaussian distributed with a zero mean and a variance of 0.5 per dimension. Finally, $\mathbf{c}_r = [c_{r,1}, \ldots, c_{r,N_r}]^T$ is an $N_r$-element vector of the signals transmitted from the relay node at the same power $P_0$ as that of $\mathbf{c}_s$ and $\mathbf{n}_d = [n_{d,1}, \ldots, n_{d,N_d}]^T$ is an $N_d$-element AWGN vector with each element having a zero mean and a variance of $N_0/2$ per dimension.

### 4.2.2 Irregular Cooperative Space-Time Codes

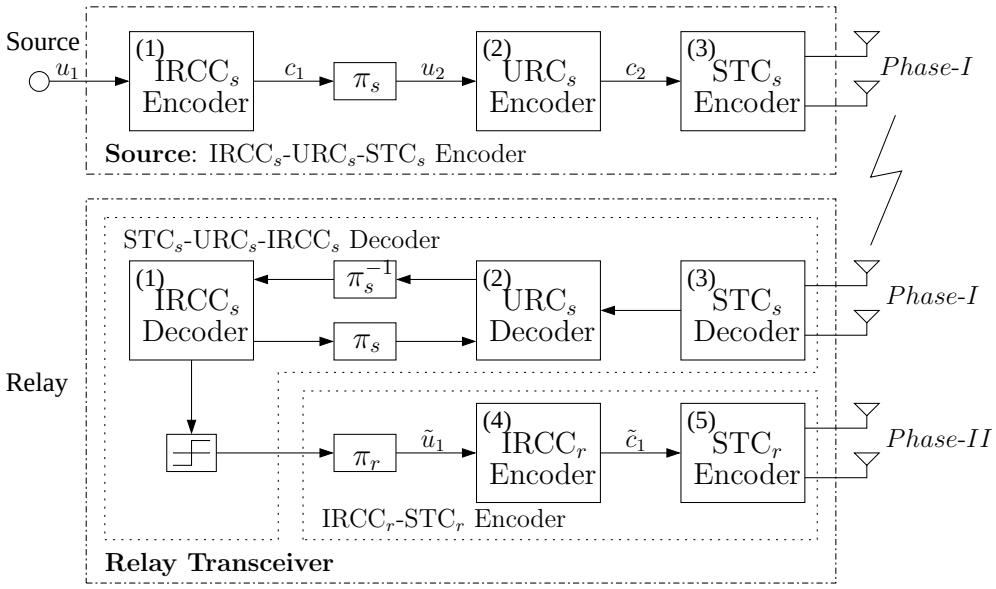


**Figure 4.2:** Schematic of the Ir-CSTC encoder. The corresponding decoder is shown in Fig. 4.3 and all system parameters are summarized in Table 4.1.

#### 4.2.2.1 Ir-CSTC Encoder

At the source node of the proposed two-hop relay-aided network as shown in Fig. 4.2, we use a Space-Time Code (STC) amalgamated with a recursive Unity-Rate Code (URC)[2] as the inner code, while an IRCC [61, 81] having an average code rate of $R_s$ is employed as the outer code, which is optimized with the aid of EXIT chart analysis for the sake of near-error-free decoding at channel SNRs close to the capacity of the source-to-relay link at the relay node during the relay's receive period of *Phase I*. On the other hand, as shown in Fig. 4.2, in the relay's transmit period of *Phase II* another IRCC having a code rate of $R_r$ is amalgamated with another STC, where the IRCC is further improved with the aid of a joint source-and-relay mode design procedure, as we will show in Section 4.2.3.2 for the sake of approaching the relay channel's capacity. Specifically, the notations $\pi_s$ and $\pi_r$ in Fig. 4.2 represent the bit-wise random interleaver used at the source node and the relay node, respectively. Compared to the topology of the DTC [49], it may be observed that the cooperative scheme seen in Fig. 4.2 combines the benefits of a serially concatenated scheme and of a DTC, which is referred to as an Irregular Cooperative Space-Time Coding (Ir-CSTC) scheme in this contribution.

#### 4.2.2.2 Three-Stage Iterative Decoding at the Destination

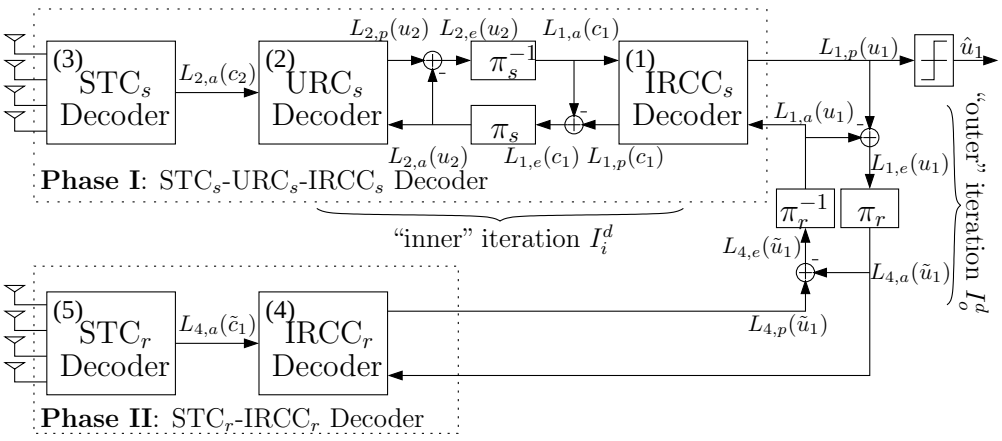


**Figure 4.3:** The three-stage iterative decoder of the Ir-CSTC scheme of Fig. 4.2, where all system parameters are summarized in Table 4.1.

The novel three-stage iterative decoder structure of the Ir-CSTC scheme is illustrated in Fig. 4.3. At the destination node, the signals received during *Phase I* are first de-

[2]URCs were proposed by Divsalar *et al.* [105] for the sake of extending the overall system's impulse response to an infinite duration, which efficiently spreads the extrinsic information, hence improves the achievable iterative detection gain.

coded by the amalgamated[3] "STC$_s$-URC$_s$" decoder in order to produce the *a priori* Log-Likelihood Ratio (LLR) values $L_{1,a}(c_1)$ of the coded bits $c_1$ by the Maximum A-posteriori Probability (MAP) algorithm [89]. The IRCC$_s$ decoder seen at the top right of Fig. 4.3 processes the information forwarded by the "STC$_s$-URC$_s$" decoder in conjunction with the *a priori* LLR values $L_{1,a}(u_1)$ of the information bits $u_1$ gleaned by the "STC$_r$-IRCC$_r$" relay-decoder in order to generate the *a posteriori* LLR values $L_{1,p}(u_1)$ and $L_{1,p}(c_1)$ of the information bits $u_1$ and of the coded bits $c_1$, respectively. As seen in Fig. 4.3, the *a priori* LLRs $L_{1,a}(c_1)$ are subtracted from the *a posteriori* LLR values $L_{1,p}(c_1)$ and then they are fed back to the "STC$_s$-URC$_s$" decoder as the *a priori* information $L_{2,a}(u_2)$ through the interleaver $\pi_s$. We term this information-exchange process seen in the top trace of Fig. 4.3 as the "inner" iteration[4]. Similarly, during the "outer" iterations, the *a priori* LLR values $L_{1,a}(u_1)$ fed into the IRCC$_s$ decoder are also subtracted from the *a posteriori* LLR values $L_{1,p}(u_1)$ for the sake of generating the extrinsic LLR values $L_{1,e}(u_1)$ as seen at the top right corner of Fig. 4.3. Then $L_{1,e}(u_1)$ is passed to the amalgamated "STC$_r$-IRCC$_r$" relay-decoder as the *a priori* information $L_{4,a}(\tilde{u}_1)$ through the interleaver $\pi_r$ in conjunction with the signals received during *Phase II* in order to compute the *a posteriori* LLR values $L_{4,p}(\tilde{u}_1)$ of the permuted information bits $\tilde{u}_1$ from the relay node. As seen in Fig. 4.3, the extrinsic information $L_{4,e}(\tilde{u}_1)$ is generated by subtracting the *a priori* information $L_{4,a}(\tilde{u}_1)$ from the *a posteriori* information $L_{4,p}(\tilde{u}_1)$, before $L_{4,e}(\tilde{u}_1)$ is fed back to the IRCC$_s$ decoder as the *a priori* information $L_{1,a}(u_1)$ through the de-interleaver $\pi_r^{-1}$. During the last "outer" iteration, only the LLR values $L_{1,p}(u_1)$ of the original information bits $u_1$ are required, which are passed to the hard-decision block of Fig. 4.3 in order to estimate the source bits.

### 4.2.3 Near-Capacity System Design and Analysis

In order to design a near-capacity coding scheme for the proposed two-hop relay-aided network, in Section 4.2.3.1 we first derive the upper and lower bounds on the relay channel's CCMC capacity as well as those of the DCMC capacity (constrained information rate) for Alamouti's STBC scheme, since the relay channel's exact capacity formula is unavailable. Then, our EXIT chart based joint source-and-relay mode design procedure will be detailed in Section 4.2.3.2.

[3]The terminology "amalgamated" is used here to indicate that although it might have some benefits to exchange extrinsic information between these two blocks, no iterations were used between them.

[4]Explicitly, at the destination node, the extrinsic information exchange between the amalgamated "STC$_s$-URC$_s$" decoder and the IRCC$_s$ decoder is referred to as the "inner" iteration, while that between the parallel amalgamated "STC$_s$-URC$_s$-IRCC$_s$" decoder and the amalgamated "STC$_r$-IRCC$_r$" relay-decoder is referred to as the "outer" iteration.

#### 4.2.3.1 Single-Relay Channel's Capacity

As presented in [132], a general upper bound on the CCMC capacity of a half-duplex[5] relay system is derived based on the original work on the full-duplex relay channels [131], which is given by

$$C_{\text{CCMC}}^{\text{coop}} \leq \max_{p(x_1,x_2,x)} \Bigg\{ \min \Big\{ \lambda E\left[I(X_1;Y_1,Y)\right] + (1-\lambda) E\left[I(X_2;Y_2|X)\right], \\ \lambda E\left[I(X_1;Y_1)\right] + (1-\lambda) E\left[I(X_2,X;Y_2)\right] \Big\} \Bigg\}, \quad (4.9)$$

where $p(x_1, x_2, x)$ indicates the joint probability of the signals transmitted from the source and the relay nodes, while $\lambda$ is the ratio of the first time slot duration to the total frame duration. The signals $X_1$ and $X_2$ are transmitted from the source node during the first and the second time slot, respectively, while $Y_1$ and $Y_2$ represent the corresponding signals received at the destination during the two consecutive time slots. Furthermore, $Y$ and $X$ are the received and transmitted signals at the relay node, respectively. On the other hand, another achievable rate definition for the DF protocol, which can be regarded as a lower bound on the CCMC capacity of the relay system, was provided in [132] in the form of

$$C_{\text{CCMC}}^{\text{coop}} \geq \max_{p(x_1,x_2,x)} \Bigg\{ \min \Big\{ \lambda E\left[I(X_1;Y)\right] + (1-\lambda) E\left[I(X_2;Y_2|X)\right], \\ \lambda E\left[I(X_1;Y_1)\right] + (1-\lambda) E\left[I(X_2,X;Y_2)\right] \Big\} \Bigg\}, \quad (4.10)$$

where $I(A;B)$ represents the mutual information between the channel's input $A$ and the corresponding output $B$, and $E(\cdot)$ denotes the expectation with respect to the fading coefficients.

In our half-duplex-constrained relay-aided system, the source node does not transmit during *Phase II*, i.e. $X_2 = 0$, we have $E[I(X_2;Y_2|X)] = 0$ and $E[I(X_2,X;Y_2)] = E[I(X;Y_2)]$ in (4.9) and (4.10). Hence, based on Eqs. (4.6)-(4.8) the upper and lower bounds of the single relay channel's capacity can be derived accordingly as

$$C_{\text{CCMC}}^{\text{coop}} \leq \max_{p(c_s,c_r)} \Bigg\{ \min \Big\{ \frac{L_s}{L_s+L_r} E\left[I(C_s;Y_d^I,Y_r)\right], \\ \frac{L_s}{L_s+L_r} E\left[I(C_s;Y_d^I)\right] + \frac{L_r}{L_s+L_r} E\left[I(C_r;Y_d^{II})\right] \Big\} \Bigg\} \quad (4.11)$$

[5] In [132], the source node continues transmission during the second time slot.

and

$$C_{\text{CCMC}}^{\text{coop}} \geq \max_{p(c_s,c_r)} \Bigg\{ \min\Big\{ \frac{L_s}{L_s+L_r} E\left[I(C_s;Y_r)\right], \\ \frac{L_s}{L_s+L_r} E\left[I(C_s;Y_d^I)\right] + \frac{L_r}{L_s+L_r} E\left[I(C_r;Y_d^{II})\right] \Big\} \Bigg\}, \quad (4.12)$$

respectively.

In addition to the CCMC capacity bounds, we also evaluate the information-rate bounds for the single relay channel in conjunction with i.u.d. discrete inputs. Thus, the upper and lower constrained information-rate bounds are given by

$$C_{\text{DCMC}}^{\text{coop}} \leq \min\Big\{ \frac{L_s}{L_s+L_r} E\left[I_d(C_s;Y_d^I,Y_r)\right], \\ \frac{L_s}{L_s+L_r} E\left[I_d(C_s;Y_d^I)\right] + \frac{L_r}{L_s+L_r} E\left[I_d(C_r;Y_d^{II})\right] \Big\} \quad (4.13)$$

and

$$C_{\text{DCMC}}^{\text{coop}} \geq \min\Big\{ \frac{L_s}{L_s+L_r} E\left[I_d(C_s;Y_r)\right], \\ \frac{L_s}{L_s+L_r} E\left[I_d(C_s;Y_d^I)\right] + \frac{L_r}{L_s+L_r} E\left[I_d(C_r;Y_d^{II})\right] \Big\}, \quad (4.14)$$

respectively, where the subscript $d$ indicates the i.u.d. discrete-input constraint.

In this contribution, we employ Alamouti's 4QAM-based G2 scheme at both the source and relay nodes, where the two-hop single-relay-aided network model is configured with $N_s = 2$, $N_r = 2$ and $N_d = 4$, as shown in Figs. 4.2 and 4.3. The *codeword* matrix of the G2 scheme is given by:

$$\mathbf{C}_{G2} = \begin{pmatrix} c_1 & c_2 \\ -\bar{c}_2 & \bar{c}_1 \end{pmatrix}^T. \quad (4.15)$$

Based on Eqs. (4.6)-(4.8), the signal received at the relay node during $V = 2$ consecutive symbol periods can be written as

$$\mathbf{Y}_r = \sqrt{G_{sr}}\mathbf{H}_{sr}\mathbf{C}_s + \mathbf{N}_r, \quad (4.16)$$

while the signals received at the destination node during $V = 2$ consecutive symbol periods in *Phase I* and *Phase II* are expressed as

$$\mathbf{Y}_d^I = \sqrt{G_{sd}}\mathbf{H}_{sd}\mathbf{C}_s + \mathbf{N}_d, \quad (4.17)$$

and

$$\mathbf{Y}_d^{II} = \sqrt{G_{rd}}\mathbf{H}_{rd}\mathbf{C}_r + \mathbf{N}_d, \quad (4.18)$$

respectively. Specifically, $\mathbf{Y}_r = [\mathbf{y}_{r,1}, \ldots, \mathbf{y}_{r,V}] \in \mathbb{C}^{N_r \times V}$, $\mathbf{Y}_d^I = [\mathbf{y}_{d,1}^I, \ldots, \mathbf{y}_{d,V}^I] \in \mathbb{C}^{N_d \times V}$ and $\mathbf{Y}_d^{II} = [\mathbf{y}_{d,1}^{II}, \ldots, \mathbf{y}_{d,V}^{II}] \in \mathbb{C}^{N_d \times V}$ are the matrices hosting the sampled signal received at the relay node and the destination node, respectively, while $\mathbf{H}_{sr} \in \mathbb{C}^{N_r \times N_s}$, $\mathbf{H}_{sd} \in \mathbb{C}^{N_d \times N_s}$ and $\mathbf{H}_{rd} \in \mathbb{C}^{N_d \times N_r}$ are the corresponding quasi-static channel matrices, which are constant over $V = 2$ consecutive symbol periods. Furthermore, $\mathbf{C}_s = [\mathbf{c}_{s,1}, \ldots, \mathbf{c}_{s,V}] \in \mathbb{C}^{N_s \times V}$ and $\mathbf{C}_r = [\mathbf{c}_{r,1}, \ldots, \mathbf{c}_{r,V}] \in \mathbb{C}^{N_r \times V}$ represent Alamouti's G2 matrices characterizing the transmissions of the source and relay nodes, while $\mathbf{N}_r = [\mathbf{n}_{r,1}, \ldots, \mathbf{n}_{r,V}] \in \mathbb{C}^{N_r \times V}$ and $\mathbf{N}_d = [\mathbf{n}_{d,1}, \ldots, \mathbf{n}_{d,V}] \in \mathbb{C}^{N_d \times V}$ represents the AWGN matrix incurred at the relay and the destination nodes, respectively.

Hence, we may readily derive the upper and lower bounds on the constrained information rate of the relaying channel with i.u.d. G2 *codeword*-matrix inputs as

$$C_{\text{DCMC}}^{\text{coop-g2}} \leq \min\Big\{ \frac{L_s}{L_s+L_r} E\left[I_d(\mathbf{C}_s; \mathbf{Y}_d^I, \mathbf{Y}_r)\right], \frac{L_s}{L_s+L_r} E\left[I_d(\mathbf{C}_s; \mathbf{Y}_d^I)\right] + \frac{L_r}{L_s+L_r} E\left[I_d(\mathbf{C}_r; \mathbf{Y}_d^{II})\right] \Big\} \quad (4.19)$$

and

$$C_{\text{DCMC}}^{\text{coop-g2}} \geq \min\Big\{ \frac{L_s}{L_s+L_r} E\left[I_d(\mathbf{C}_s; \mathbf{Y}_r)\right], \frac{L_s}{L_s+L_r} E\left[I_d(\mathbf{C}_s; \mathbf{Y}_d^I)\right] + \frac{L_r}{L_s+L_r} E\left[I_d(\mathbf{C}_r; \mathbf{Y}_d^{II})\right] \Big\}, \quad (4.20)$$

respectively.

Considering a relay channel associated with a perfect source-to-relay link, i.e. $G_{sr} = \infty$, where the relay node is very close to the source node and is capable of perfectly recovering all the information transmitted from the source node, we have

$$\max_{p(c_s,c_r)} E[I(C_s; Y_d^I, Y_r)] \to \infty, \quad \max_{p(c_s,c_r)} E[I(C_s; Y_r)] \to \infty, \quad (4.21)$$

and

$$E[I_d(\mathbf{C}_s; \mathbf{Y}_d^I, \mathbf{Y}_r)] = 2, \;\; E[I_d(\mathbf{C}_s; \mathbf{Y}_r)] = 2, \quad (4.22)$$

since the 4QAM-based G2 STC is used. Therefore, the CCMC capacity upper and lower bounds of (4.11) and (4.12) converge to

$$C_{\text{CCMC}}^{\text{coop}} = \max_{p(c_s,c_r)} \Big\{ \frac{L_s}{L_s+L_r} E\left[I(C_s; Y_d^I)\right] + \frac{L_r}{L_s+L_r} E\left[I(C_r; Y_d^{II})\right] \Big\}. \quad (4.23)$$

Similarly, the lower and upper bounds on the information rates constrained by the i.u.d. G2 $codeword$-matrix inputs converge to

$$C_{\text{DCMC}}^{\text{coop-g2}} = \min\Big\{ \frac{2L_s}{L_s+L_r}, \frac{L_s}{L_s+L_r} E\left[I_d(\mathbf{C}_s; \mathbf{Y}_d^I)\right] + \frac{L_r}{L_s+L_r} E\left[I_d(\mathbf{C}_r; \mathbf{Y}_d^{II})\right] \Big\}. \quad (4.24)$$

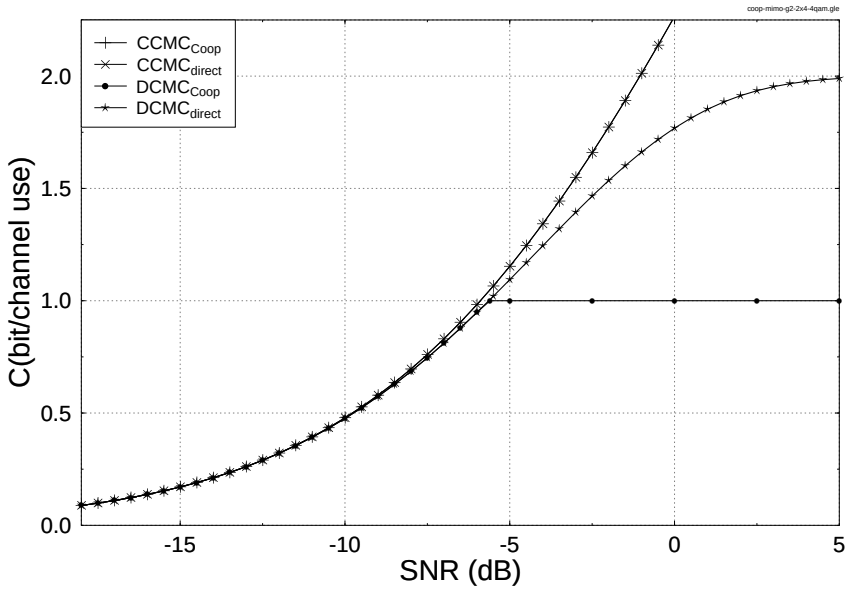


**Figure 4.4:** The CCMC capacity curve and constrained information rates employing Alamouti's G2 scheme in conjunction with $G_{sr} = \infty$ and $G_{rd} = 1$ as well as $L_s = L_r$ for the single-relaying channel of Fig. 4.1.

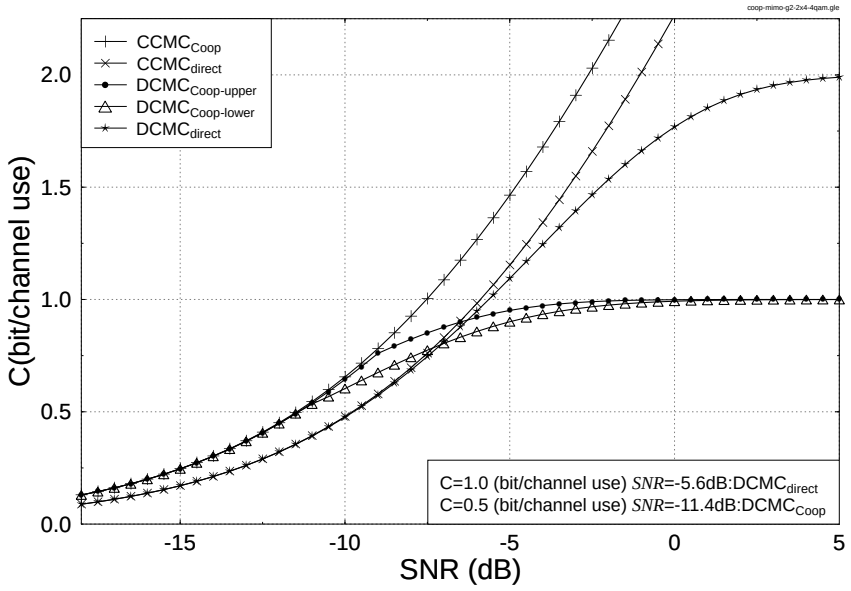


**Figure 4.5:** The relay channel's CCMC capacity and constrained information-rate bounds employing the 4QAM-modulated G2 scheme when the network of Fig. 4.1 is configured with $G_{sr} = 8$ and $G_{rd} = 2$ as well as $L_s = L_r$.

Finally, we reformulate (4.24) as follows

$$C_{\text{DCMC}}^{\text{coop-g2}}(\text{SNR}_e^{coop}) = \min\Big\{\frac{2L_s}{L_s+L_r}, \frac{L_s}{L_s+L_r} C_{\text{DCMC}}^{\text{s}\to\text{d}}\left(\text{SNR}_e^{s}\right) + \frac{L_r}{L_s+L_r} C_{\text{DCMC}}^{\text{r}\to\text{d}}\left(\text{SNR}_e^{r}, G_{rd}\right)\Big\}, \quad (4.25)$$

where we refer to $\text{SNR}_e^s$ and $\text{SNR}_e^r$ as the equivalent SNRs[6] at the source and relay, respectively, which are both equal to $P_0/N_0$, since they transmit at the same power of $P_0$. Furthermore, $\text{SNR}_e^{coop}$ is the equivalent overall SNR of the relay-aided network, which is defined by $\text{SNR}_e^{coop} = P_0/N_0$. The variables $C^{\text{s}\to\text{d}}$ and $C^{\text{r}\to\text{d}}$ represent the channel capacities of the direct source-to-destination link and of the relay-to-destination link, respectively. Furthermore, the corresponding constrained information rates of $E\left[I_d(\mathbf{C}_s; \mathbf{Y}_d^I, \mathbf{Y}_r)\right]$, $E\left[I_d(\mathbf{C}_s; \mathbf{Y}_r)\right]$, $E\left[I_d(\mathbf{C}_s; \mathbf{Y}_d^I)\right]$ and $E\left[I_d(\mathbf{C}_r; \mathbf{Y}_d^{II})\right]$ can be similarly evaluated with the aid of Monte-Carlo techniques based on Eq. (9) of [127].

An example is given in Fig. 4.4 for the single-relay-aided uncorrelated Rayleigh fading channel associated with $G_{rd} = 1$ and $L_s = L_r$. Based on Eqs. (4.23), (4.24) and (4.25), we characterize the CCMC capacity and the information rates obeying the i.u.d. 4QAM-based G2 $codeword$-matrix-input constraint. The capacity and information rates of the direct source-to-destination link channel are also depicted in Fig. 4.4, where we assume that the power constraint is $P_0$ for the direct transmission based benchmarker for the sake of a fair comparison. We can observe in Fig. 4.4 that the information-rate of the single-relay-aided channel is exactly the same as that of the direct transmission in the low-SNR regime, but only half of that in the high-SNR regime due to the multiplexing loss at the half-duplex single-relay-aided system.

Furthermore, we consider a more practical example for a specific network associated with $L_s = L_r$ as well as $G_{sr} = 8$ and $G_{rd} = 2$ in Fig. 4.5, where the source-to-relay link is imperfect. The CCMC capacity and the information rates obeying the i.u.d. 4QAM-modulated G2 *codeword*-matrix-input constraint are evaluated by the upper and lower bounds given in (4.11)-(4.12) and (4.19)-(4.20). We can see in Fig. 4.5 that the lower and upper bounds converge and exhibit a substantial capacity gain over conventional direct transmission in the low and medium SNR regimes below a certain convergence threshold, which is caused by the geometrical-gain of the relay-to-destination link. On the other hand, it is observed that the relay channel's DCMC capacity is only half of the direct transmission due to a factor of $\frac{L_s+L_r}{L_r} = 2.0$ multiplexing loss in the half-duplex scenario. The DCMC capacity provides the fundamental limits on the performance of a practical coding/decoding scheme. In Section 4.2.3.2, we will propose an optimal distributed coding scheme, which is capable of approaching the relay channel's limits under arbitrary relay network configuration.

[6]Here we introduced the terminology of equivalent $\text{SNR}_e$ to define the ratio of the signal power at the transmitter side with respect to the noise level at the receiver side, as in [142]. Although this does not have a direct physical interpretation, it simplifies our discussions.

#### 4.2.3.2 Joint Code Design for the Source-and-Relay Nodes Based on EXIT Charts

For the sake of analysing the convergence behaviours of iterative decoders employed by the two-hop relay-aided system, we use two EXIT charts [64, 101] to examine the evolution of the input/output mutual information exchanges between the inner amalgamated "STC$_s$-URC$_s$" decoder and the outer IRCC$_s$ decoder at the relay node, as well as between the parallel amalgamated "STC$_s$-URC$_s$-IRCC$_s$" decoder and the amalgamated "STC$_r$-IRCC$_r$" decoder at the destination node during the consecutive iterations. As has been investigated in [69, 108], a narrow but marginally open EXIT-tunnel between the EXIT curves of the inner amalgamated "STC$_s$-URC$_s$" decoder and the outer IRCC$_s$ decoder at the relay node indicates that a performance close to the capacity of the source-to-relay link could be achieved. Similarly, at the destination node, a narrow-but-open EXIT-tunnel between the EXIT curves of the parallel amalgamated "STC$_s$-URC$_s$-IRCC$_s$" decoder and the amalgamated "STC$_r$-IRCC$_r$" decoder indicates the possibility of achieving decoding convergence to an infinitesimally low Bit Error Ratio (BER) at SNRs close to the relay channel's capacity. Therefore, we propose a joint source-and-relay mode design procedure for supporting near-capacity cooperative communications as well as for maximizing the system's effective throughput, which can be simplified to two EXIT curve matching problems summarised as follows:

**Step 1:** Choose a specific average code rate $R_s$ for the IRCC$_s$ at the source node and employ the EXIT curve matching algorithm of [61] to obtain the optimized weighting coefficients $\alpha_i, i = 1, \ldots, 17$ of IRCC$_s$, where a narrow but marginally open EXIT-tunnel between the EXIT curves of the inner amalgamated "STC$_s$-URC$_s$" decoder and the outer IRCC$_s$ decoder emerges at the relay node. This implies that a near-capacity performance may be achieved for the source-to-relay communication link. Then we store the value of the corresponding transmit power required at the source node.

**Step 2:** Choose the same transmit power at the source as stored in **Step 1**. Fix the optimized weighting coefficients $\alpha_i, i = 1, \ldots, 17$ of the IRCC$_s$ obtained in **Step 1** at the source node, perform iterative decoding by exchanging extrinsic information between the amalgamated "STC$_s$-URC$_s$" decoder and the IRCC$_s$ decoder during *Phase I* at the destination node, until the further increase of the area $A_E$ under the EXIT curve of the amalgamated "STC$_s$-URC$_s$-IRCC$_s$" decoder becomes marginal, then stop this "inner" iterative decoding process.

| | |
|---|---|
| No. of Source Antennas $N_s$ | 2 |
| No. of Relay Antennas $N_r$ | 2 |
| No. of Destination Antennas $N_d$ | 4 |
| Channel | long-term path loss + short-term uncorrelated flat Rayleigh fading |
| STCs at the Source and Relay | STBC [8] |
| Modulation Scheme | 4QAM |
| Source Coding Rate $R_s$ | 0.5 |
| Geometrical Gain of $s$-to-$r$ link $G_{sr}$ | 8 |
| Geometrical Gain of $r$-to-$d$ link $G_{rd}$ | 2 |
| Frame Length | 250 000 bits |

**Table 4.1:** Single-relay-aided Ir-CSTC system parameters. The system's architecture was shown in Figs. 4.2 and 4.3.

**Step 3:** Assume perfectly error-free DF relaying and the same transmit power at the relay as that of the source in the second EXIT chart, which examines the evolution of the input/output mutual information exchanges in the three-stage iterative decoder of the Ir-CSTC scheme. Use the EXIT curve matching algorithm of [61] to match the SNR-dependent EXIT curve of the amalgamated "STC$_r$-IRCC$_r$" decoder to the target EXIT curve of the amalgamated "STC$_s$-URC$_s$-IRCC$_s$" decoder observed in **Step 2**. Obtain the maximized average code rate $R_r$ and the optimized weighting coefficients $\beta_j, j = 1, \ldots, 17$ of IRCC$_r$ when a narrow-but-open EXIT-tunnel emerges.

In the following part of this section, all the results presented characterize an Ir-CSTC scheme using the system parameters outlined in Table 4.1, where we consider an average code rate of $R_s = 0.5$ for the outer IRCC$_s$ at the source node and the specific relay network configuration associated with $G_{sr} = 8$ and $G_{rd} = 2$, which satisfies Eq. (4.5). The EXIT chart of the serially concatenated IRCC$_s$-URC$_s$-STBC$_s$ scheme of the source-to-relay link is depicted in Fig. 4.6, where $I_A$ and $I_E$ indicate the mutual information between the information bits and the $a\ priori$ LLR values as well as the corresponding $extrinsic$ LLR values, respectively. The EXIT curve of the outer IRCC$_s$ having optimized weighting coefficients $\alpha_i$ as shown in the caption of Fig. 4.6 was constructed using the curve matching algorithm of [61]. As we can see from Fig. 4.6, a narrow but marginally open EXIT tunnel emerges for the $2 \times 2$ source-to-relay communication link. A receive

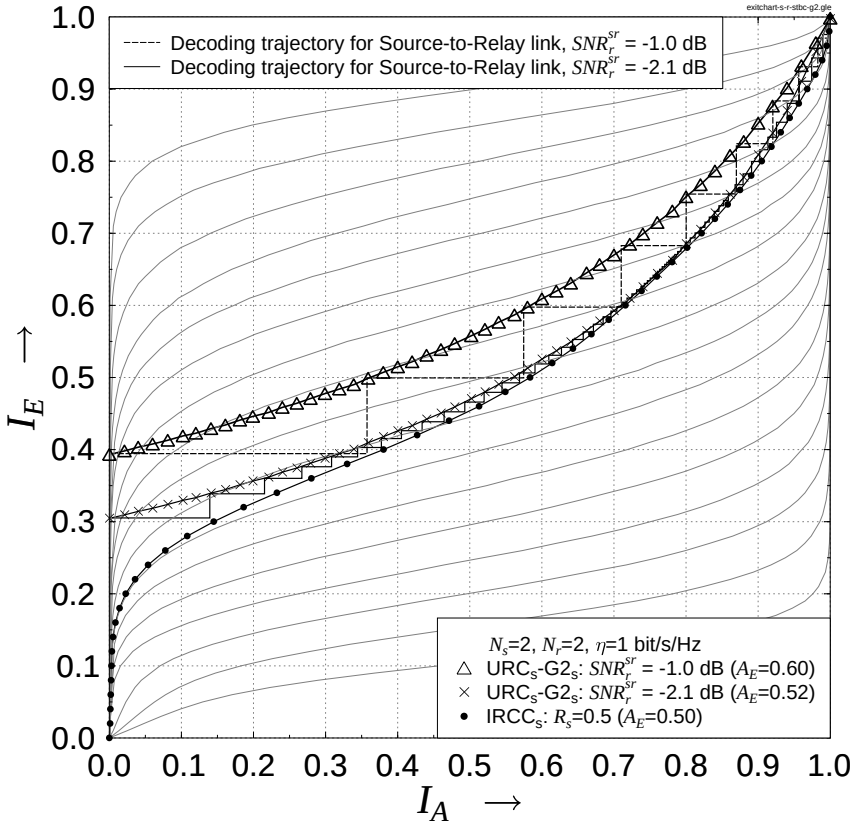


**Figure 4.6:** The EXIT chart curves of the URC$_s$-G2$_s$, the IRCC$_s$ with optimized weighting coefficients $[\alpha_1, \ldots, \alpha_{17}]$= [0, 0, 0, 0, 0, 0.327442, 0.186505, 0.113412, 0, 0.0885527, 0, 0.0781214, 0.0962527, 0.0114205, 0.0346015, 0.0136955, 0.0500168] and 17 IRCC subcodes for the $2 \times 2$ source-to-relay communication link. The transmitter's schematic is shown in Fig. 4.2 and the system parameters are summarized in Table 4.1.

SNR of about -2.1 dB is needed in order to attain a decoding convergence to an infinitesimally low BER. Due to the geometrical-gain of the source-to-relay link, the equivalent SNR at the source node can be computed as

$$\text{SNR}_e^s = \text{SNR}_r^{sr} - 10\log_{10}(G_{sr})[\text{dB}] \,, \tag{4.26}$$

where $\text{SNR}_r^{sr}$ is the receive SNR at the relay node. Hence, the minimum $\text{SNR}_e^s$ at the source node required for the sake of obtaining a near error-free performance at the relay node is -11.1 dB. As presented in Section 4.2.1, we assume that both the source and relay transmit their signals at the same transmit power, hence they have the same equivalent SNR. In order to avoid the potentially high computational complexity at the relay node, a wider-than-necessary EXIT tunnel[7] is created in the EXIT chart of Fig. 4.6 at the receive SNR of -1.0 dB at the relay node, which corresponds to an equivalent SNR of -10 dB based on Eq. (4.26) at both the source and relay nodes. As clearly seen in the EXIT

[7] A 'wider-than-necessary' EXIT tunnel indicates the possibility of reaching the convergence (1.0, 1.0) point for fewer iterations, which involves lower complexity.

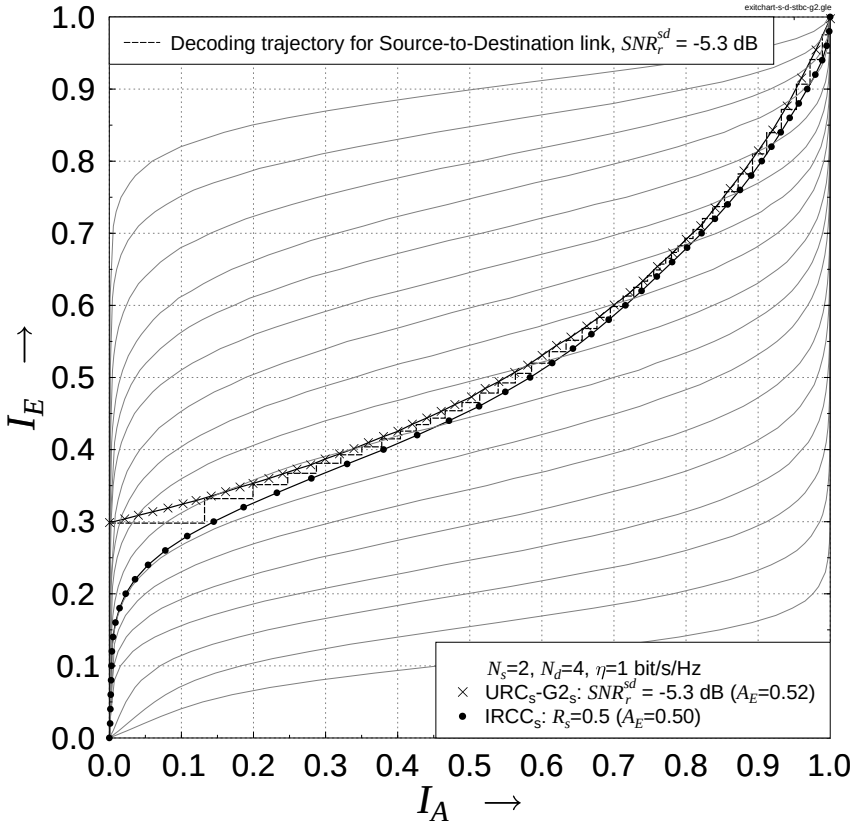


**Figure 4.7:** The EXIT chart curves for the URC$_s$-G2$_s$, the IRCC$_s$ with the same optimized weighting coefficients $[\alpha_1, \ldots, \alpha_{17}]$ = [0, 0, 0, 0, 0, 0.327442, 0.186505, 0.113412, 0, 0.0885527, 0, 0.0781214, 0.0962527, 0.0114205, 0.0346015, 0.0136955, 0.0500168] and 17 IRCC subcodes for the source-to-destination link in non-cooperative scenario where the SNR$_r^{sd}$ denotes the receive SNR of the source-to-destination link. The transmitter's schematic is shown in Fig. 4.2 and the system parameters are summarized in Table 4.1.

chart of Fig. 4.8 at the destination node, after 5 "inner" iterations between the IRCC$_s$ decoder and the amalgamated "STBC$_s$-URC$_s$" decoder, the increase of the area $A_E$ under the amalgamated "STBC$_s$-URC$_s$-IRCC$_s$" decoder becomes marginal. Hence, we fix the number of "inner" iterations to $I_i^d = 4$ at the destination node. Following the design procedure above, we obtain the resultant matching EXIT curve for the Ir-CSTC scheme in Fig. 4.8, where the IRCC$_r$ has the optimized weighting coefficients $\beta_j$ and a maximized average code rate of $R_r = 0.5$, hence we have $L_s = L_r$. It is clearly seen in Fig. 4.8 that a narrow-but-open EXIT-tunnel emerges, which indicates the possibility of achieving decoding convergence to an infinitesimally low BER at near-capacity SNRs for the Ir-CSTC scheme. This prediction is verified in Fig. 4.8 by plotting the corresponding Monte-Carlo simulation-related decoding trajectory, which indeed reaches the (1.0,1.0) point of the EXIT chart. On the other hand, since the code rate $R_r$ of the relay's IRCC has been maximized by the joint source-and-relay mode design procedure, the Ir-CSTC scheme achieves a maximum effective throughput of $\frac{L_s}{L_s+L_r} R_s \log_2 4 = 0.5$ bit/s/Hz, when the

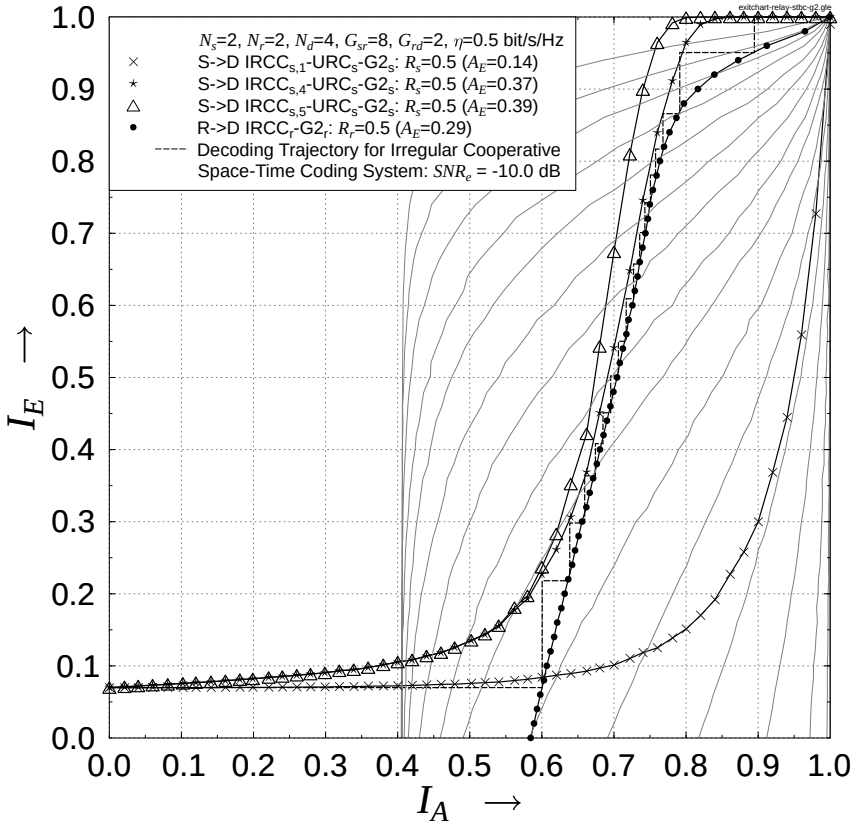


**Figure 4.8:** The EXIT chart curves for the IRCC$_s$-URC$_s$-G2$_s$ with various "inner" iterations, the IRCC$_r$-G2$_r$ with IRCC$_r$ having optimized weighting coefficients $[\beta_1, \ldots, \beta_{17}]$ = [0, 0, 0, 0, 0.233115, 0.0158742, 0.292084, 0.220065, 0.0151108, 0, 0, 0, 0, 0, 0, 0, 0.22375] and 17 SNR-dependent IRCC$_r$-G2$_r$ subcodes. The subscript of IRCC$_s$ denotes the number of "inner" iterations between the IRCC$_s$ and "G2$_s$-URC$_s$" decoders and the SNR$_e$ represents the equivalent SNR at both the source and relay nodes. The transmitter/receiver schematics are shown in Figs. 4.2 and 4.3, respectively, and the system parameters are summarized in Table 4.1.

4QAM-modulated G2 scheme is employed.

### 4.2.4 Simulation Results and Discussions

In this section, we present the BER versus equivalent SNR performance of both the perfect and imperfect relaying aided Ir-CSTC schemes as well as that of a non-cooperative serial concatenated IRCC-URC-STBC scheme in Fig. 4.9. For the Ir-CSTC scheme, according to the trajectory predictions seen in Figs. 4.6 and 4.8, the number of decoding iterations between the IRCC$_s$ decoder and the amalgamated "STBC$_s$-URC$_s$" decoder was fixed to $I^r = 13$ at the relay node. At the destination node, the number of "inner" decoding iterations was fixed to $I_i^d = 4$, while the number of "outer" decoding iterations between the parallel amalgamated "STBC$_s$-URC$_s$-IRCC$_s$" decoder and the amalgamated "STBC$_r$-IRCC$_r$" decoder was fixed to $I_o^d = 17$. On the other hand, for the non-cooperative serial

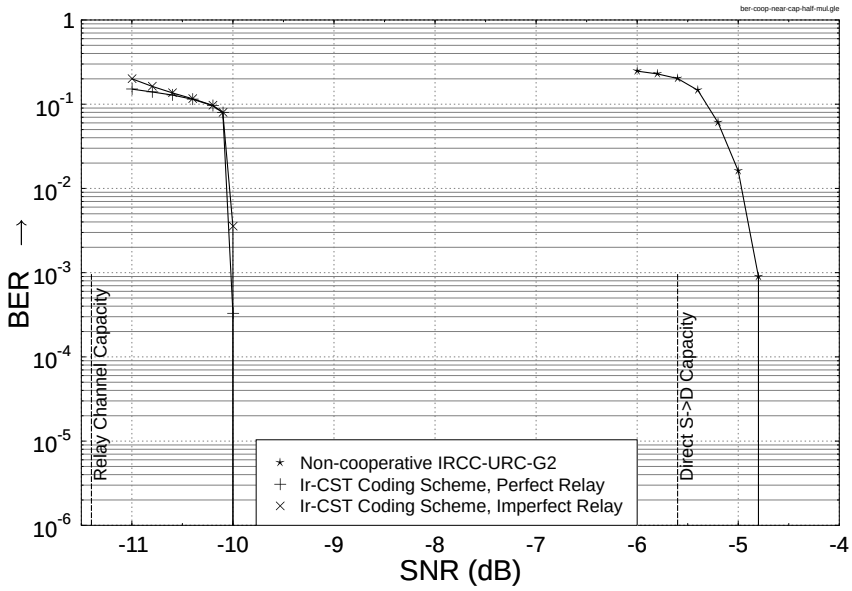


**Figure 4.9:** BER versus equivalent overall SNR performance of both perfect and imperfect relaying Ir-CSTC and non-cooperative IRCC-URC-G2 schemes for a frame length of 250 000 bits, where the cooperative network is configured with $G_{sr} = 8$ and $G_{rd} = 2$ as well as $L_s = L_r$ and the non-cooperative system is equipped with two transmit and four receive antennas. The transmitter/receiver schematics are shown in Figs. 4.2 and 4.3 and the system parameters are summarized in Table 4.1.

concatenated IRCC-URC-STBC scheme, we employ an outer IRCC, which has the same weighting coefficients $\alpha_i$ as that of the IRCC$_s$ in the cooperative system. The EXIT chart for the non-cooperative IRCC-URC-STBC scheme is shown in Fig. 4.7, where a narrow-but-open tunnel emerges at a receive SNR of about -5.3 dB at the destination node. For comparison, the number of decoding iterations exchanging extrinsic information between the outer IRCC decoder and the inner "STBC-URC" decoder in the non-cooperative scenario was fixed to $I_{non} = 13$ as well.

As seen in Fig. 4.9, the Ir-CSTC scheme outperforms the non-cooperative IRCC-URC-STBC scheme by approximately 5.1 dB in terms of the required equivalent SNR, which corresponds to a 3 dB lower value of 2.1 dB in terms of $E_b/N_0$ due to a factor two multiplexing loss in the half-duplex Ir-CSTC scheme. On the other hand, the performance of the perfect relaying-aided Ir-CSTC scheme matches the EXIT chart predictions of Fig. 4.8, while the imperfect relaying-aided Ir-CSTC scheme performs similarly to the perfect relaying scheme. This is due to the fact that the source information becomes near-error-free at the relay node after a sufficiently high number of decoding iterations. Furthermore, it is clearly shown in Fig. 4.9 that the Ir-CSTC scheme is capable of performing within 1.4 dB of the corresponding relay channel's DCMC capacity.

## 4.3 Twin-Relay-Aided Cooperative Communications

### 4.3.1 Twin-Relay-Aided Network Model

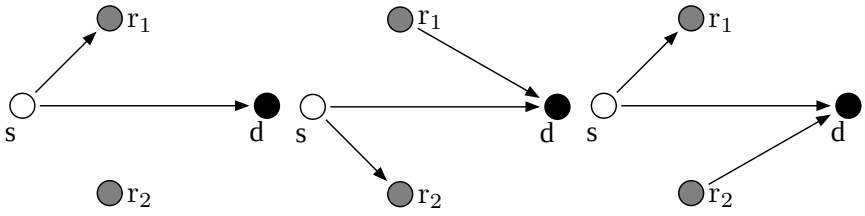


(a) Phase 1 (b) Phase 2 (c) Phase 3

**Figure 4.10:** System model for the successive relaying aided network, where the interference between the relays is negligible. This may be contrasted to the single-relay based architecture of Fig. 4.1.

In this section, we consider the four-terminal successive relaying aided network of Fig. 4.10, where a single source $s$ is equipped with $N_s$ antennas, and intends to communicate with the destination $d$ having $N_d$ antennas. The two relays $r_1$ and $r_2$ are equipped with $N_{r_1}$ and $N_{r_2}$ antennas, respectively, and each relay $r_i$ can be either a mobile user or a fixed relay. Compared to the conventional single-relay-aided scheme of Section 4.2.1, it is clearly seen that one additional relay is required to support the successive relaying, which potentially increases the overall infrastructure cost. However, this can be avoided, when the relays are constituted by inactive mobile users. As stated in Section 4.2, to obey the realistic limitations of practical transceivers, all nodes in the successive relaying network obey the half-duplex constraint as well. Furthermore, we consider a similar scenario to that of [144], where the relays were said to have "weak interconnections". In our case, the interference between the relays is considered to be negligible compared to the desired signal power, especially when no line-of-sight (LOS) transmission exists among the relays. Similarly, we model the communication links between the nodes of Fig. 4.10 as being subjected to both free-space path loss as well as to uncorrelated Rayleigh fading, except for the link between the relays. The proportional geometrical-gain [142] for the source-to-relay (SR) links and the relay-to-destination (RD) links with respect to the source-to-destination (SD) link are denoted by $G_{sr_1}$, $G_{sr_2}$ and $G_{r_1d}$, $G_{r_2d}$, respectively. In this section, we also assume that the relays are closer to the source than to the destination[8], while both the source and relays are far away from the destination, namely we have $G_{sr_i} > G_{r_id},\ i = 1, 2$.

[8] In [145] and [146], the effects of relay position were investigated and the authors considered the benefits of power allocation as a countermeasure.

### 4.3.2 Successive Relaying Protocol Description

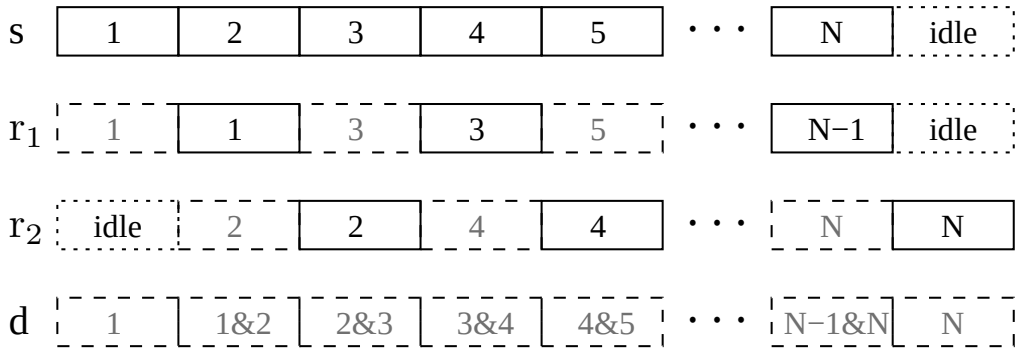


**Figure 4.11:** Frame structure of the successive relaying scheme of Fig. 4.10, solid box for transmitted signal, dashed box for received signal and dotted box for idle status.

We split the source transmissions into different identical-length frames. As illustrated in Fig. 4.10, the transmission scheduling of the successive relaying protocol can be described as follows[9]. In *Phase* 1 of Fig. 4.10(a), $s$ transmits frame 1; $r_1$ listens to $s$; $r_2$ remains silent and $d$ receives frame 1 from $s$. In *Phase* 2 of Fig. 4.10(b), $s$ transmits frame 2; $r_1$ decodes, re-encodes and forwards frame 1; $r_2$ listens to $s$ and $d$ receives frame 1 from $r_1$ and frame 2 from $s$. By contrast, during *Phase* 3 seen in Fig. 4.10(c), $s$ transmits frame 3; $r_2$ decodes, re-encodes and forwards frame 2; $r_1$ listens to $s$ and $d$ receives frame 2 from $r_2$ and frame 3 from $s$. This progress is repeated in this manner until *Phase* $N$. In *Phase* $(N+1)$, $s$ and $r_1$ (or $r_2$) keep silent. Then $r_2$ (or $r_1$) decodes, re-encodes and forwards frame $N$, while $d$ receives frame $N$ from $r_2$ (or $r_1$). The frame structure of the successive relaying scheme is further illustrated in Fig. 4.11. It is clearly seen that in our successive relaying scheme, $(N+1)$ communication phases are required to convey $N$ frames of information with the aid of two relays. Hence, the efficiency of classic direct transmission is approached, provided that $N$ is sufficiently high. The vector hosting the received signal at the relay $r_i$ can be formulated as:

$$\mathbf{y}_{r_i} = \sqrt{G_{sr_i}}\mathbf{H}_{sr_i}\mathbf{c}_s + \mathbf{n}_{r_i}. \tag{4.27}$$

By contrast, the signal vector received at the destination $d$ during the first and last transmission phase can be expressed as:

$$\mathbf{y}_d = \sqrt{G_{sd}}\mathbf{H}_{sd}\mathbf{c}_s + \mathbf{n}_d, \tag{4.28}$$

and

$$\mathbf{y}_d = \sqrt{G_{r_id}}\mathbf{H}_{r_id}\mathbf{c}_{r_i} + \mathbf{n}_d, \;\; i = 1 \text{ or } 2, \tag{4.29}$$

[9]In this contribution, we only consider the scenario, where the two relays are always active in assisting the source. The cooperative systems, where the relays are not always cooperating are investigated in [44] and [147].

respectively, while the signal received by $d$ from $s$ during the intermediate phase is contaminated by the interfering signals received from the relay, which is formulated as:

$$\mathbf{y}_d = \sqrt{G_{sd}}\mathbf{H}_{sd}\mathbf{c}_s + \sqrt{G_{r_id}}\mathbf{H}_{r_id}\mathbf{c}_{r_i} + \mathbf{n}_d, \;\; i = 1 \text{ or } 2, \tag{4.30}$$

where $\mathbf{y}_{r_i} = [y_{r_i,1}, \ldots, y_{r_i,N_{r_i}}]^T$ is the $N_{r_i}$-element vector of the signals received at relay $r_i$. Furthermore, $\mathbf{y}_d = [y_{d,1}, \ldots, y_{d,N_d}]^T$ is the $N_d$-element vector of the signals received at the destination, while $\mathbf{H}_{sr_i} \in \mathbb{C}^{N_{r_i} \times N_s}$, $\mathbf{H}_{sd} \in \mathbb{C}^{N_d \times N_s}$ and $\mathbf{H}_{r_id} \in \mathbb{C}^{N_d \times N_{r_i}}$ are the corresponding channel matrices having independent and identically complex Gaussian distributed elements with a zero mean and a variance of 0.5 per dimension. Furthermore, $\mathbf{c}_s = [c_{s,1}, \ldots, c_{s,N_s}]^T$ and $\mathbf{c}_{r_i} = [c_{r_i,1}, \ldots, c_{r_i,N_{r_i}}]^T$ are the $N_s$-element vector of the signals transmitted from the source $s$ and the $N_{r_i}$-element vector of signals transmitted from the relay $r_i$, respectively. For a fair comparison with the conventional single-relay-aided system of Section 4.2, in this section we assume that the source and relays transmit at the same power $P_0/2$. Finally, $\mathbf{n}_{r_i} = [n_{r_i,1}, \ldots, n_{r_i,N_{r_i}}]^T$ and $\mathbf{n}_d = [n_{d,1}, \ldots, n_{d,N_d}]^T$ are the corresponding $N_{r_i}$-element and $N_d$-element AWGN vectors, both with each element having a zero mean and a variance of $N_0/2$ per dimension.

### 4.3.3 Irregular Cooperative Space-Time Coding for Successive Relaying Network

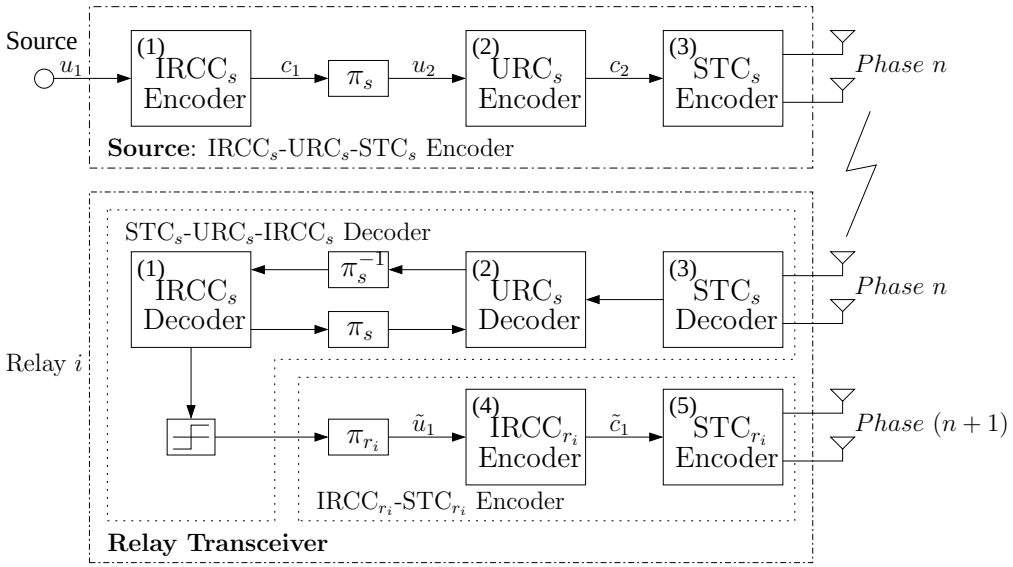


**Figure 4.12:** Schematic of the generalized Ir-CSTC encoder for the successive relaying aided network. The decoder's schematic can be found in Fig. 4.13, while the corresponding single-relay based transmitter may be contrasted by observing Fig. 4.2.

In Section 4.2, we have proposed a novel Ir-CSTC scheme for the three-terminal relay-aided network. In this section, we will extend this Ir-CSTC scheme for the four-terminal successive relaying aided network, which will be shown in Section 4.3.4 to be capable of approaching the DCMC capacity limit for the successive relaying channels.

#### 4.3.3.1 Distributed Encoding at the Source and Relays

As seen in Fig. 4.12, at the source of the four-terminal successive relaying aided network, we use a same three-component serial concatenated IRCC-URC-STC scheme. At both of the two relays, the same two-component serial concatenated IRCC-STC scheme is employed for the successive relaying aided network considered in this contribution, where the IRCCs at the relays may have different coding rates and weighting coefficients depending on the different relay topologies, and will assist us in attaining a near-capacity performance, as in Section 4.2.2. Since the frames transmitted and relayed from the source and relays have the same frame length, as seen in Fig. 4.11, we choose the same average code rate for the different IRCCs used at the source and relays of the twin-relay aided network, namely we have $R_s = R_{r_1} = R_{r_2}$. Note that there is no interference between the two relays during any of their transmission phases, as detailed in [144]. Hence, no interference suppression is needed at the relays, as seen in Fig. 4.12. However, at the destination, except for the first and last phase, suppression of the interference becomes a potential problem, which will be detailed in the next subsection.

#### 4.3.3.2 SIC-Aided Iterative Decoding at the Destination

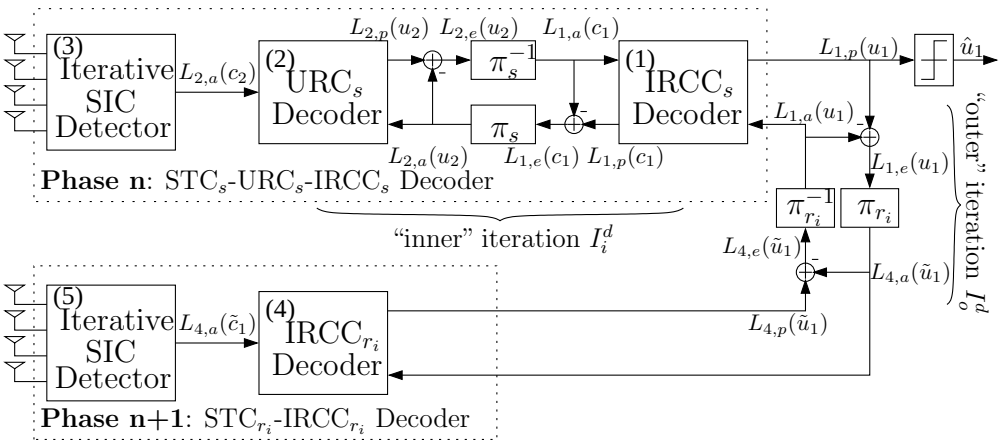


**Figure 4.13:** A frame-by-frame SIC aided iterative decoder of the generalized Ir-CSTC scheme of Fig. 4.12 at the destination. The corresponding single-relay based decoder may be contrasted by observing Fig. 4.3.

In contrast to the iterative decoder of the conventional single-relay-aided network of Section 4.2.2.2, Fig. 4.13 illustrates our novel frame-by-frame successive interference cancellation (SIC) aided iterative decoder designed for the generalized Ir-CSTC scheme of the successive relaying aided network. The SIC aided iterative decoder of Fig. 4.13 has two distinctive parts. Except for the first and last phase of the $(N+1)$-phase relaying protocol, in each intermediate phase, the destination first uses the iterative SIC algorithm [76]

to separate the signals received from the source and relays. For example, in *Phase* $n$ of Fig. 4.13, the destination receives the signals of frames $(n-1)$ and $n$ from the relay $r_j$, $j = 1$ or 2 as well as from the source $s$, respectively. It first detects the signals of frame $(n-1)$ using SIC, while treating the signals of frame $n$ as interference. After frame $(n-1)$ is detected, the destination subtracts it from the received signals and proceeds to detect frame $n$. As discussed in Section 2.6 of Chapter 2, after a sufficient number of SIC iterations near-optimum performance may be achieved for both frames $(n-1)$ and $n$. After the iterative SIC operations, the appropriately separated signals of frame $(n-1)$ received from the relay $r_j$ are used in the ensuing iterative decoding process of Fig. 4.13 in conjunction with the detected signals of frame $(n-1)$ received from the source $s$ in *Phase* $(n-1)$. The detected signals of frame $n$ are then decoded by the URC$_s$ decoder seen in the middle of the top part of Fig. 4.13 in order to produce the *a priori* Log-Likelihood Ratio (LLR) values $L_{1,a}(c_1)$ of the coded bits $c_1$ by the Maximum A-posteriori Probability (MAP) algorithm [89]. The IRCC$_s$ decoder seen at the top right of Fig. 4.13 processes the information forwarded by the URC$_s$ decoder in conjunction with the *a priori* LLR values $L_{1,a}(u_1)$ of the information bits $u_1$ gleaned by the "STC$_r$-IRCC$_r$" relay-decoder in order to generate the *a posteriori* LLR values $L_{1,p}(u_1)$ and $L_{1,p}(c_1)$ of the information bits $u_1$ and of the coded bits $c_1$, respectively. As seen in Fig. 4.13, the *a priori* LLRs $L_{1,a}(c_1)$ are subtracted from the *a posteriori* LLR values $L_{1,p}(c_1)$ and then they are fed back to the URC$_s$ decoder as the *a priori* information $L_{2,a}(u_2)$ through the interleaver $\pi_s$. We term this information-exchange process seen in the top trace of Fig. 4.13 as the "inner" iteration. Similarly, during the "outer" iterations, the *a priori* LLR values $L_{1,a}(u_1)$ fed into the IRCC$_s$ decoder are also subtracted from the *a posteriori* LLR values $L_{1,p}(u_1)$ for the sake of generating the extrinsic LLR values $L_{1,e}(u_1)$, as seen at the top right corner of Fig. 4.13. Then $L_{1,e}(u_1)$ is passed to the amalgamated "STC$_r$-IRCC$_r$" relay-decoder as the *a priori* information $L_{4,a}(\tilde{u}_1)$ through the interleaver $\pi_r$ in conjunction with the signals received from the relay $r_i$, $i = 2$ or 1 during *Phase* $(n+1)$ in order to compute the *a posteriori* LLR values $L_{4,p}(\tilde{u}_1)$ of the permuted information bits $\tilde{u}_1$. As seen in Fig. 4.13, the extrinsic information $L_{4,e}(\tilde{u}_1)$ is generated by subtracting the *a priori* information $L_{4,a}(\tilde{u}_1)$ from the *a posteriori* information $L_{4,p}(\tilde{u}_1)$, before $L_{4,e}(\tilde{u}_1)$ is fed back to the IRCC$_s$ decoder as the *a priori* information $L_{1,a}(u_1)$ through the de-interleaver $\pi_r^{-1}$. During the last "outer" iteration, the LLR values $L_{1,p}(u_1)$ of the original information bits $u_1$ are passed to the hard-decision block of Fig. 4.13 in order to estimate the source bits.

Similarly, in the subsequent *Phase* $(n+1)$, the signals of frame $n$ received from the relay $r_i$ and frame $(n+1)$ received from the source $s$ are detected consecutively by the iterative SIC algorithm at the destination. The detected signals of frame $n$ are passed to the amalgamated "STC$_{r_i}$-IRCC$_{r_i}$" decoder and are used in the ensuing iterative decoding

process. The separated signals of frame $(n+1)$ will then be used in the subsequent three-stage iterative decoding process in conjunction with the detected signals of frame $(n+1)$ in *Phase* $(n+2)$. This process continues, until the last frame is decoded.

### 4.3.4 Near-Capacity Coding Design

As presented in [70], the proposed Ir-CSTC scheme is capable of near-capacity cooperative communications in the context of a conventional single-relay-aided network. In this section, we will demonstrate that our general Ir-CSTC scheme is also capable of achieving decoding convergence to an infinitesimally low Bit Error Ratio (BER) at Signal-to-Noise Ratios (SNRs) close to the DCMC capacity limit (constrained information rate) of the successive relaying channel. We first derive the upper and lower bounds of the CCMC capacity as well as the constrained-information-rate bounds for the successive relaying system, when employing Alamouti's STBC scheme [8], as detailed in Section 4.3.4.1. Then, the EXIT chart based joint source-and-relay mode design will be carried out in Section 4.3.4.2. In Section 4.3.4.3, the EXIT chart analysis of a specific example will be given to demonstrate the proficiency of the code design procedure proposed in Section 4.3.4.2.

#### 4.3.4.1 Capacity and Information-Rate Bounds

Referring to the transmission frame structure of Fig. 4.11, the transmission arrangement of our twin-relay-aided successive relaying network can be treated as a superposition of the transmissions of two half-duplex three-terminal networks [132] minus a single direct source-to-destination link, provided that the number of frames is sufficiently high. Hence, according to Eqs. (4.9) and (4.10), we may readily derive the upper and lower bounds on the CCMC capacity of our successive relaying channel as

$$
\begin{aligned}
C_{\text{CCMC}}^{\text{coop}} \leq \max_{p(c_s,c_{r_1},c_{r_2})} \Bigg\{ & \min\Big\{ \frac{1}{2}E\left[I(C_s^1;Y_d^1,Y_{r_1})\right] + \frac{1}{2}E\left[I(C_s^2;Y_d^2|C_{r_1})\right], \\
& \qquad \frac{1}{2}E\left[I(C_s^1;Y_d^1)\right] + \frac{1}{2}E\left[I(C_s^2,C_{r_1};Y_d^2)\right] \Big\} \\
& + \min\Big\{ \frac{1}{2}E\left[I(C_s^1;Y_d^1,Y_{r_2})\right] + \frac{1}{2}E\left[I(C_s^2;Y_d^2|C_{r_2})\right], \\
& \qquad \frac{1}{2}E\left[I(C_s^1;Y_d^1)\right] + \frac{1}{2}E\left[I(C_s^2,C_{r_2};Y_d^2)\right] \Big\} \\
& \qquad - E\left[I(C_s;Y_d)\right] \Bigg\}
\end{aligned}
\tag{4.31}
$$

and

$$C_{\text{CCMC}}^{\text{coop}} \geq \max_{p(c_s,c_{r_1},c_{r_2})} \Bigg\{ \min\Big\{ \frac{1}{2}E\left[I(C_s^1;Y_{r_1})\right] + \frac{1}{2}E\left[I(C_s^2;Y_d^2|C_{r_1})\right], \\ \frac{1}{2}E\left[I(C_s^1;Y_d^1)\right] + \frac{1}{2}E\left[I(C_s^2,C_{r_1};Y_d^2)\right] \Big\} \\ + \min\Big\{ \frac{1}{2}E\left[I(C_s^1;Y_{r_2})\right] + \frac{1}{2}E\left[I(C_s^2;Y_d^2|C_{r_2})\right], \\ \frac{1}{2}E\left[I(C_s^1;Y_d^1)\right] + \frac{1}{2}E\left[I(C_s^2,C_{r_2};Y_d^2)\right] \Big\} \\ - E\left[I(C_s;Y_d)\right] \Bigg\}, \tag{4.32}$$

respectively, where $C_s = \begin{cases} C_s^1, & 1^{st} \text{ time slot} \\ C_s^2, & 2^{nd} \text{ time slot} \end{cases}$ and $Y_d = \begin{cases} Y_d^1, & 1^{st} \text{ time slot} \\ Y_d^2, & 2^{nd} \text{ time slot} \end{cases}$. Since the signals $C_s$ and $C_r$ are independent of each other in most practical scenarios, (4.31) and (4.32) can be simplified to

$$C_{\text{CCMC}}^{\text{coop}} \leq \max_{p(c_s,c_{r_1},c_{r_2})} \Bigg\{ \min\Big\{ \frac{1}{2}E\left[I(C_s^1;Y_d^1,Y_{r_1})\right], \frac{1}{2}E\left[I(C_s^2,C_{r_1};Y_d^2)\right] \Big\} \\ + \min\Big\{ \frac{1}{2}E\left[I(C_s^1;Y_d^1,Y_{r_2})\right], \frac{1}{2}E\left[I(C_s^2,C_{r_2};Y_d^2)\right] \Big\} \Bigg\} \tag{4.33}$$

and

$$C_{\text{CCMC}}^{\text{coop}} \geq \max_{p(c_s,c_{r_1},c_{r_2})} \Bigg\{ \min\Big\{ \frac{1}{2}E\left[I(C_s^1;Y_{r_1})\right], \frac{1}{2}E\left[I(C_s^2,C_{r_1};Y_d^2)\right] \Big\} \\ + \min\Big\{ \frac{1}{2}E\left[I(C_s^1;Y_{r_2})\right], \frac{1}{2}E\left[I(C_s^2,C_{r_2};Y_d^2)\right] \Big\} \Bigg\}, \tag{4.34}$$

respectively.

Similarly, we also evaluate the information-rate bounds for the successive relaying channel in conjunction with i.u.d. discrete inputs. Thus, the upper and lower constrained information-rate bounds are given by

$$C_{\text{DCMC}}^{\text{coop}} \leq \min\Big\{ \frac{1}{2}E\left[I_d(C_s^1;Y_d^1,Y_{r_1})\right], \frac{1}{2}E\left[I_d(C_s^2,C_{r_1};Y_d^2)\right] \Big\} \\ + \min\Big\{ \frac{1}{2}E\left[I_d(C_s^1;Y_d^1,Y_{r_2})\right], \frac{1}{2}E\left[I_d(C_s^2,C_{r_2};Y_d^2)\right] \Big\} \tag{4.35}$$

and

$$C_{\text{DCMC}}^{\text{coop}} \geq \min\Big\{\frac{1}{2}E\left[I_d(C_s^1;Y_{r_1})\right],\frac{1}{2}E\left[I_d(C_s^2,C_{r_1};Y_d^2)\right]\Big\} + \min\Big\{\frac{1}{2}E\left[I_d(C_s^1;Y_{r_2})\right],\frac{1}{2}E\left[I_d(C_s^2,C_{r_2};Y_d^2)\right]\Big\}, \tag{4.36}$$

respectively.

In this section, we also employ Alamouti's 4QAM-based G2 scheme at both the source and two relay nodes, where the network model is configured with $N_s = 2$, $N_{r_1} = N_{r_2} = 2$ and $N_d = 4$, as shown in Figs. 4.12 and 4.13. Based on Eqs. (4.27) and (4.30), the signal received at the relay node $r_i$ during $V = 2$ consecutive symbol periods can be written as:

$$\mathbf{Y}_{r_i} = \sqrt{G_{sr_i}}\mathbf{H}_{sr_i}\mathbf{C}_s + \mathbf{N}_{r_i}, \tag{4.37}$$

and except for the first and last phase, the signal received at the destination node during $V = 2$ consecutive symbol periods in the intermediate phase can be written as:

$$\mathbf{Y}_d = \sqrt{G_{sd}}\mathbf{H}_{sd}\mathbf{C}_s + \sqrt{G_{r_id}}\mathbf{H}_{r_id}\mathbf{C}_{r_i} + \mathbf{N}_d, \tag{4.38}$$

respectively, where $\mathbf{Y}_{r_i} = [\mathbf{y}_{r_i,1},\ldots,\mathbf{y}_{r_i,V}] \in \mathbb{C}^{N_{r_i}\times V}$ and $\mathbf{Y}_d = [\mathbf{y}_{d,1},\ldots,\mathbf{y}_{d,V}] \in \mathbb{C}^{N_d\times V}$ are the matrices hosting the sampled signal received at the relay node $r_i$ and the destination node, respectively. Furthermore, $\mathbf{C}_s = [\mathbf{c}_{s,1},\ldots,\mathbf{c}_{s,V}] \in \mathbb{C}^{N_s\times V}$ and $\mathbf{C}_{r_i} = [\mathbf{c}_{r_i,1},\ldots,\mathbf{c}_{r_i,V}] \in \mathbb{C}^{N_{r_i}\times V}$ represent Alamouti's G2 matrices characterizing the transmissions of the source and relay $r_i$, while $\mathbf{N}_{r_i} = [\mathbf{n}_{r_i,1},\ldots,\mathbf{n}_{r_i,V}] \in \mathbb{C}^{N_{r_i}\times V}$ and $\mathbf{N}_d = [\mathbf{n}_{d,1},\ldots,\mathbf{n}_{d,V}] \in \mathbb{C}^{N_d\times V}$ represents the AWGN matrix incurred at relay $r_i$ and the destination, respectively. Hence, the G2 *codeword*-matrix-input constrained information-rate bounds of (4.35) and (4.36) are given, respectively, by

$$C_{\text{DCMC}}^{\text{coop-g2}} \leq \min\Big\{\frac{1}{2}E\left[I_d(\mathbf{C}_s^1;\mathbf{Y}_d^1,\mathbf{Y}_{r_1})\right],\frac{1}{2}E\left[I_d(\mathbf{C}_s^2,\mathbf{C}_{r_1};\mathbf{Y}_d^2)\right]\Big\} + \min\Big\{\frac{1}{2}E\left[I_d(\mathbf{C}_s^1;\mathbf{Y}_d^1,\mathbf{Y}_{r_2})\right],\frac{1}{2}E\left[I_d(\mathbf{C}_s^2,\mathbf{C}_{r_2};\mathbf{Y}_d^2)\right]\Big\} \tag{4.39}$$

and

$$C_{\text{DCMC}}^{\text{coop-g2}} \geq \min\Big\{\frac{1}{2}E\left[I_d(\mathbf{C}_s^1;\mathbf{Y}_{r_1})\right],\frac{1}{2}E\left[I_d(\mathbf{C}_s^2,\mathbf{C}_{r_1};\mathbf{Y}_d^2)\right]\Big\} + \min\Big\{\frac{1}{2}E\left[I_d(\mathbf{C}_s^1;\mathbf{Y}_{r_2})\right],\frac{1}{2}E\left[I_d(\mathbf{C}_s^2,\mathbf{C}_{r_2};\mathbf{Y}_d^2)\right]\Big\}. \tag{4.40}$$

When we consider a relay channel associated with perfect source-to-relay links, i.e. $G_{sr} = \infty$, where the relay nodes are very close to the source node and are capable of perfectly recovering all the information transmitted from the source node, we have

$$\max_{p(c_s,c_r)} E[I(C_s;Y_d,Y_r)] \to \infty, \quad \max_{p(c_s,c_r)} E[I(C_s;Y_r)] \to \infty, \tag{4.41}$$

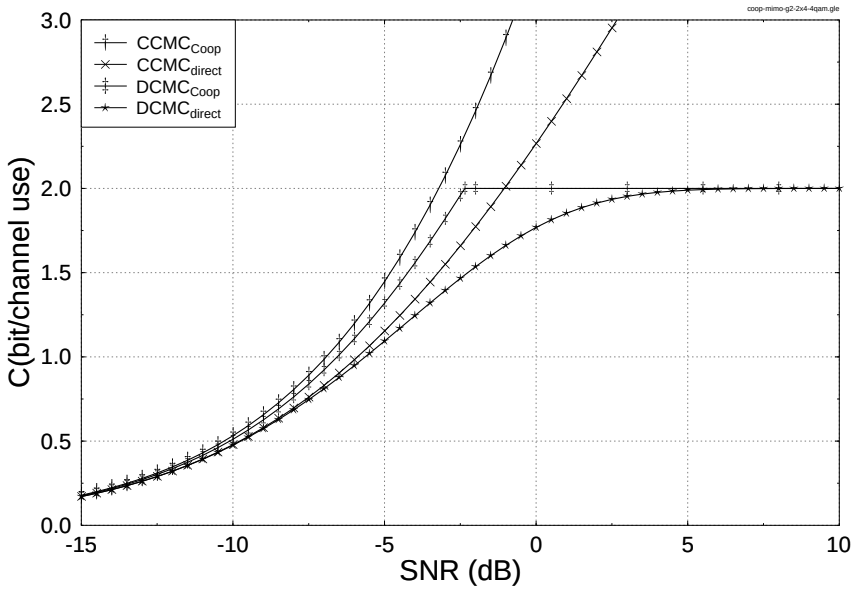


**Figure 4.14:** The CCMC capacity curve and constrained information rates employing Alamouti's G2 scheme in conjunction with $G_{sr_1} = G_{sr_2} = \infty$ and $G_{r_1 d} = G_{r_2 d} = 1$ for the successive relaying channel of Fig. 4.10. The corresponding single-relay based capacity curves may be contrasted by observing Fig. 4.4.

and

$$E[I_d(\mathbf{C}_s; \mathbf{Y}_d, \mathbf{Y}_r)] = 2, \;\; E[I_d(\mathbf{C}_s; \mathbf{Y}_r)] = 2, \tag{4.42}$$

since the 4QAM-based G2 STC is used. Therefore, the CCMC capacity upper and lower bounds of (4.33) and (4.34) converge to

$$C_{\text{CCMC}}^{\text{coop}} = \max_{p(c_s, c_{r_1}, c_{r_2})} \left\{ \frac{1}{2} E\left[ I(C_s^2, C_{r_1}; Y_d^2) \right] + \frac{1}{2} E\left[ I(C_s^2, C_{r_2}; Y_d^2) \right] \right\}. \tag{4.43}$$

Similarly, the lower and upper bounds on the information rates constrained by the i.u.d. G2 $codeword$-matrix inputs converge to

$$C_{\text{DCMC}}^{\text{coop-g2}} = \min\left\{ \frac{1}{2} E\left[ I_d(\mathbf{C}_s^2, \mathbf{C}_{r_1}; \mathbf{Y}_d^2) \right], 1 \right\} + \min\left\{ \frac{1}{2} E\left[ I_d(\mathbf{C}_s^2, \mathbf{C}_{r_2}; \mathbf{Y}_d^2) \right], 1 \right\}. \tag{4.44}$$

Finally, we reformulate (4.44) as follows

$$C_{\text{DCMC}}^{\text{coop-g2}}(\text{SNR}_e^{coop}) = \min\left\{ \frac{1}{2} C_{\text{DCMC}}^{\text{sr}_1 \to \text{d}}\left(\text{SNR}_e^s, \text{SNR}_e^{r_1}, G_{r_1 d}\right), 1 \right\} + \min\left\{ \frac{1}{2} C_{\text{DCMC}}^{\text{sr}_2 \to \text{d}}\left(\text{SNR}_e^s, \text{SNR}_e^{r_2}, G_{r_2 d}\right), 1 \right\}, \tag{4.45}$$

where the equivalent $\text{SNR}_e^s$, $\text{SNR}_e^{r_1}$ and $\text{SNR}_e^{r_2}$ at the source and relays are all equal to $P_0/2N_0$, since they transmit at the same power of $P_0/2$, as stated in Section 4.3.2. On the other hand, the equivalent overall SNR of the successive relaying aided network is defined by $\text{SNR}_e^{coop} = P_0/N_0$. The variables $C^{\text{sr}_1 \to \text{d}}$ and $C^{\text{sr}_2 \to \text{d}}$ represent the corresponding multiple-access channels' capacities, which can be similarly computed with the aid of Monte-Carlo techniques based on Eq. (11) of [76].

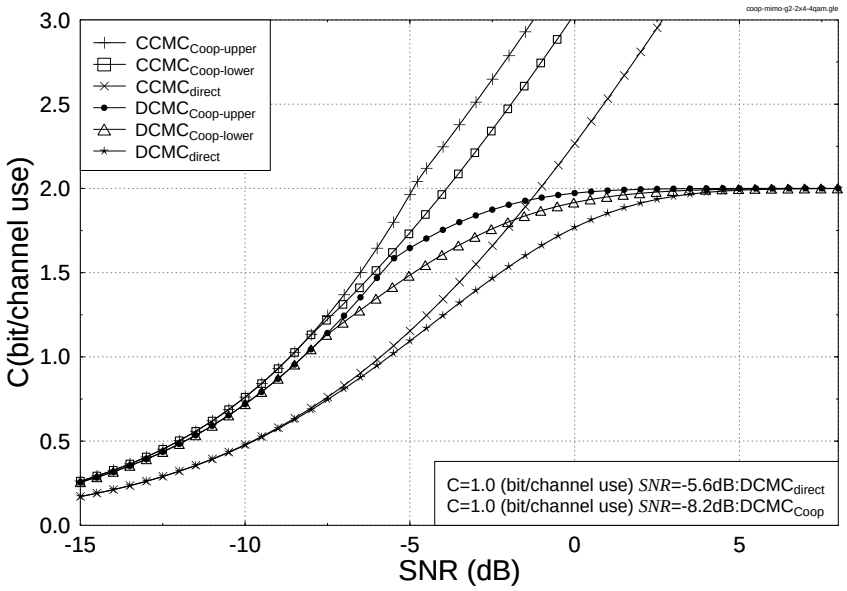


**Figure 4.15:** The CCMC capacity curve and constrained information rates employing Alamouti's G2 scheme in conjunction with $G_{sr_1} = G_{sr_2} = 8$ and $G_{r_1d} = G_{r_2d} = 2$ for the successive relaying channel of Fig. 4.10. The corresponding single-relay based capacity curves may be contrasted by observing Fig. 4.5.

In Fig. 4.14, we quantify the capacity of the successive relaying aided uncorrelated Rayleigh fading channel associated with $G_{r_1d} = G_{r_2d} = 1$. More explicitly, based on Eqs. (4.43), (4.44) and (4.45), we characterize the CCMC capacity and the information rates obeying the i.u.d. 4QAM-based G2 $codeword$-matrix-input constraint. The capacity and achievable information rates of the direct source-to-destination link channel are also depicted in Fig. 4.14, where we assume that the total power constraint is $P_0$ for the direct transmission based benchmarker for the sake of a fair comparison. We can observe in Fig. 4.14 that the attainable information-rate gain is substantial and the factor two multiplexing loss imposed by creating a separate transmit and receive slot is recovered compared to the classic direct transmission scheme.

Furthermore, we consider a more practical example for a specific network associated with $G_{sr_1} = G_{sr_2} = 8$ and $G_{r_1d} = G_{r_2d} = 2$ in Fig. 4.15, where the source-to-relay links are imperfect. The CCMC capacity and the information rates are evaluated by the upper and lower bounds given in (4.33)-(4.34) and (4.39)-(4.40). In this scenario, we can see in Fig. 4.15 that the lower and upper bounds converge in the low and medium SNR regimes below a certain convergence threshold. Next, we will show in Section 4.3.4.3 that the optimized cooperative coding scheme is capable of performing near-perfectly at the relay nodes, despite having imperfect source-to-relay links. The substantial capacity gains shown in Fig. 4.15 may be achieved by using successive relaying techniques instead of classic direct transmissions, partially, because the factor two multiplexing loss of [70] is recovered.

#### 4.3.4.2 Joint Code Design for the Source-and-Relay Nodes

For the sake of near-capacity cooperative communications in the successive relaying aided network in this section, we generalize the joint source-and-relay mode design procedure of Section 4.2.3.2 to suit our four-terminal network of Fig. 4.10, which is summarised as follows:

**Step 1:** Choose a specific average code rate $R$ for the IRCC$_s$ at the source and employ the EXIT curve matching algorithm of [61] at the relays in order to obtain the optimized weighting coefficients $\alpha_i, i = 1, \ldots, 17$ of IRCC$_s$, where a narrow but marginally open EXIT-tunnel is created between the EXIT curves of the inner amalgamated "STC$_s$-URC$_s$" decoder of Fig. 4.13 and the outer IRCC$_s$ decoder at the relays. This implies that a near-capacity performance may be achieved for the SR links. Then we store the value of the corresponding transmit power required at the source.

**Step 2:** Choose the same transmit power at the source as stored in **Step 1**. Fix the optimized IRCC$_s$ weighting coefficients $\alpha_i, i = 1, \ldots, 17$ obtained in **Step 1** at the source. Then perform iterative decoding by exchanging extrinsic information between the amalgamated "STC$_s$-URC$_s$" decoder of Fig. 4.13 and the IRCC$_s$ decoder at the destination, until the further increase of the area $A_E$ under the EXIT curve of the amalgamated "STC$_s$-URC$_s$-IRCC$_s$" decoder of Fig. 4.13 becomes marginal. Then stop this "inner" iterative decoding process.

**Step 3:** Assume perfectly error-free DF relaying and the same transmit power at the relay $r_1$ as that of the source in the second EXIT chart, which examines the evolution of the input/output mutual information exchanges in the three-stage iterative decoder of the Ir-CSTC scheme. Use the EXIT curve matching algorithm of [61] to match the SNR-dependent EXIT curve of the amalgamated "STC$_{r_1}$-IRCC$_{r_1}$" decoder of Fig. 4.13 to the target EXIT curve of the amalgamated "STC$_s$-URC$_s$-IRCC$_s$" decoder observed in **Step 2**. If an open EXIT-tunnel fails to appear, increase the transmit power at both the source $s$ and the relay $r_1$, until a narrow-but-open EXIT-tunnel emerges. Obtain the optimized weighting coefficients $\beta_j, j = 1, \ldots, 17$ of IRCC$_{r_1}$.

**Step 4:** Repeat the operations outlined in **Step 3** for relay $r_2$.

| | |
|---|---|
| Source Antennas No. $N_s$ | 2 |
| Relay $r_1$ Antennas No. $N_{r_1}$ | 2 |
| Relay $r_2$ Antennas No. $N_{r_2}$ | 2 |
| Destination Antennas No. $N_d$ | 4 |
| Channel | long-term path loss + short-term uncorrelated flat Rayleigh fading |
| STCs at the Source and Relays | STBC [8] |
| Modulation Scheme | 4QAM |
| IRCC$_s$ Coding Rate $R_s$ | 0.5 |
| IRCC$_{r_1}$ Coding Rate $R_{r_1}$ | 0.5 |
| IRCC$_{r_2}$ Coding Rate $R_{r_2}$ | 0.5 |
| Geometrical Gain of $s$-to-$r_1$ link $G_{sr_1}$ | 8 |
| Geometrical Gain of $s$-to-$r_2$ link $G_{sr_2}$ | 8 |
| Geometrical Gain of $r_1$-to-$d$ link $G_{r_1d}$ | 2 |
| Geometrical Gain of $r_2$-to-$d$ link $G_{r_2d}$ | 2 |
| Frame Length | 250 000 bits |

**Table 4.2:** Twin-relay-aided Ir-CSTC system parameters. The corresponding transmitter and receiver schemes are portrayed in Figs. 4.12 and 4.13.

**Step 5:** Finally, choose the higher of the two transmit power values obtained in **Step 3** and **Step 4** as the ultimate transmit power at the source and relays.

#### 4.3.4.3 EXIT Charts Analysis

In this section, we present simulation results for the twin-relay-aided Ir-CSTC scheme of Fig. 4.12 using the system parameters outlined in Table 4.2. We consider the same average code rate of 0.5 for the IRCCs at the source and relays, and the specific successive relaying aided network geometry associated with $G_{sr_1} = G_{sr_2} = 8$ and $G_{r_1d} = G_{r_2d} = 2$. Hence, the effective network throughput is $\frac{N}{N+1} R \log_2 4 \approx 1.0$ bit/s/Hz, when 4QAM is employed and provided that the number of frames $N$ is sufficiently high. Since the network is geographically symmetrical, for simplicity we will not differentiate the relays $r_1$ and $r_2$. Fig. 4.16 depicts the EXIT chart of the serial concatenated IRCC$_s$-URC$_s$-STBC$_s$ scheme of the SR link. The EXIT curve of the outer IRCC$_s$ having optimized weighting coefficients $\alpha_i$ was constructed using the curve matching algorithm of [61] as shown in

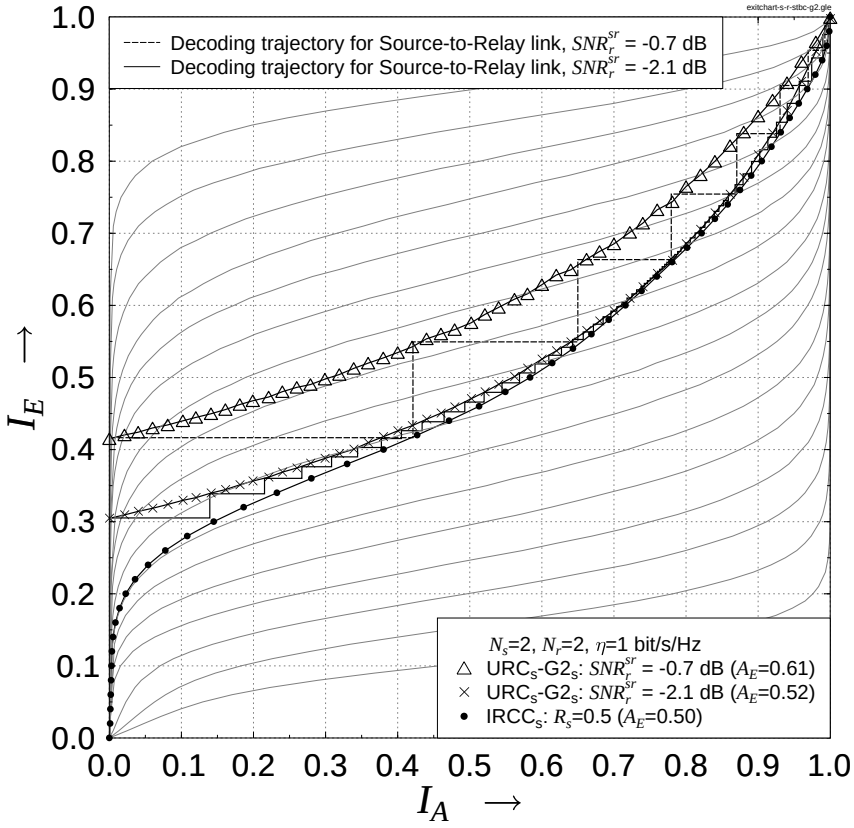


**Figure 4.16:** The EXIT chart curves of the URC$_s$-G2$_s$, the IRCC$_s$ with optimized weighting coefficients $[\alpha_1, \ldots, \alpha_{17}]$ = [0, 0, 0, 0, 0, 0.327442, 0.186505, 0.113412, 0, 0.0885527, 0, 0.0781214, 0.0962527, 0.0114205, 0.0346015, 0.0136955, 0.0500168] and 17 IRCC subcodes for the $(2 \times 2)$ SR link where the $\text{SNR}_r^{sr}$ is the receive SNR at the relay. The transmitter's schematic is shown in Fig. 4.12 and the system parameters are summarized in Table 4.2.

Fig. 4.16 and the Monte-Carlo-simulation based decoding trajectories are computed for a frame length of 250 000 bits. As seen from Fig. 4.16, a narrow but marginally open EXIT tunnel emerges for the $(2 \times 2)$ SR communication link. A receive SNR of about -2.1 dB is needed in order to attain a decoding convergence to an infinitesimally low BER. Hence, according to Eq. (4.26) the minimum $\text{SNR}_e^s$ at the source required for the sake of obtaining vanishingly low BERs at the relay is -11.1 dB. Since we assume that the source and relays transmit at the same power, we have $\text{SNR}_e^{coop} = \text{SNR}_e^s = \text{SNR}_e^r$. Following the design procedure of Section 4.3.4.2, a 'wider-than-necessary' EXIT tunnel is created in the EXIT chart of Fig. 4.16 at the receive SNR of -0.7 dB at the relay, which corresponds to an equivalent SNR of -9.7 dB based on Eq. (4.26) at the source and relays. Accordingly, it is clearly seen in the EXIT chart of Fig. 4.17 at the destination that after 5 "inner" iterations between the IRCC$_s$ decoder and the amalgamated "STBC$_s$-URC$_s$" decoder, the increase of the area $A_E$ under the amalgamated "STBC$_s$-URC$_s$-IRCC$_s$" decoder's EXIT curve becomes marginal. The resultant matching EXIT curve of the amalgamated "STBC$_r$-IRCC$_r$" decoder is shown in Fig. 4.17, where the IRCC$_r$ has the optimized

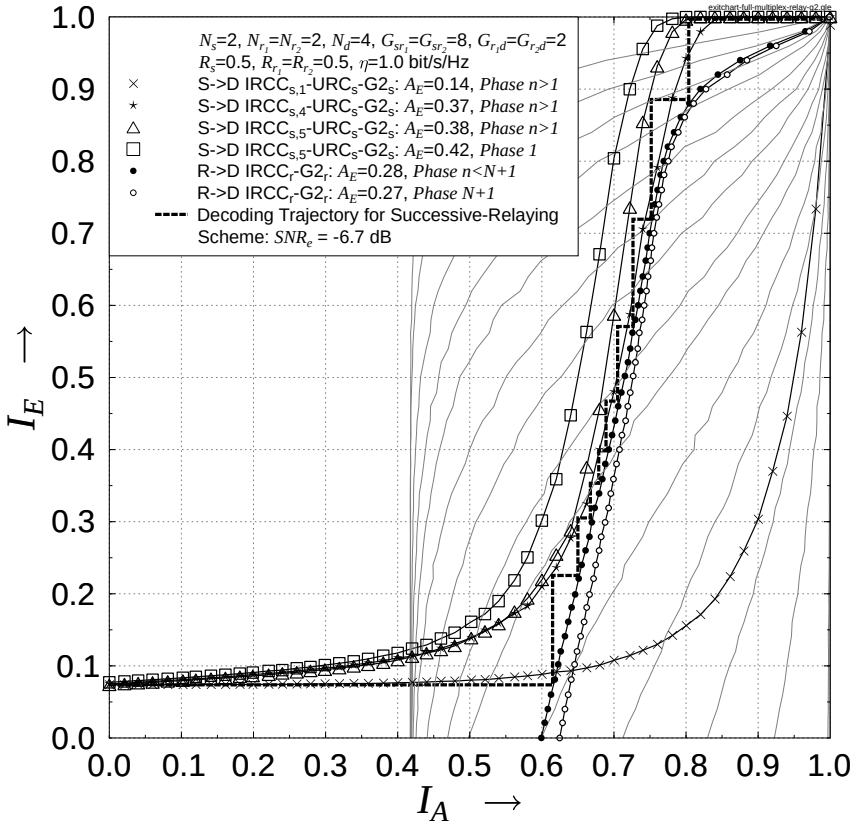


**Figure 4.17:** The EXIT chart curves for the IRCC$_s$-URC$_s$-G2$_s$ with various "inner" iterations, the IRCC$_r$-G2$_r$ with IRCC$_r$ having optimized weighting coefficients $[\beta_1, \ldots, \beta_{17}]$ = [0, 0, 0, 0, 0.233115, 0.0158742, 0.292084, 0.220065, 0.0151108, 0, 0, 0, 0, 0, 0, 0, 0.22375] and 17 SNR-dependent IRCC$_r$-G2$_r$ subcodes. The subscript of IRCC$_s$ denotes the number of "inner" iterations between the IRCC$_s$ and "G2$_s$-URC$_s$" decoders and the SNR$_e$ represents the equivalent overall SNR of the successive relaying aided network. The transmitter/receiver schematics are shown in Figs. 4.12 and 4.13 and the system parameters are summarized in Table 4.2.

weighting coefficients $\beta_j$, as summarized in Fig. 4.17. Similarly, as discussed in [70], the 'narrow-but-open' EXIT-tunnel of Fig. 4.17 indicates the possibility of achieving decoding convergence to an infinitesimally low BER at near-capacity SNRs for the Ir-CSTC scheme in the successive relaying aided network. This prediction is verified in Fig. 4.17 by plotting the corresponding Monte-Carlo simulation-based decoding trajectory, which indeed reaches the (1.0,1.0) point of the EXIT chart. Furthermore, we also plot the EXIT curves of the amalgamated "STBC$_s$-URC$_s$-IRCC$_s$" decoder in *Phase* 1 and the amalgamated "STBC$_r$-IRCC$_r$" decoder in *Phase* $(N+1)$ in Fig. 4.17, respectively. Since the tunnels in *Phase* 1 and *Phase* $(N+1)$ are wider, the trajectories can traverse through the tunnels at a reduced number of iterations to reach the (1.0,1.0) point.

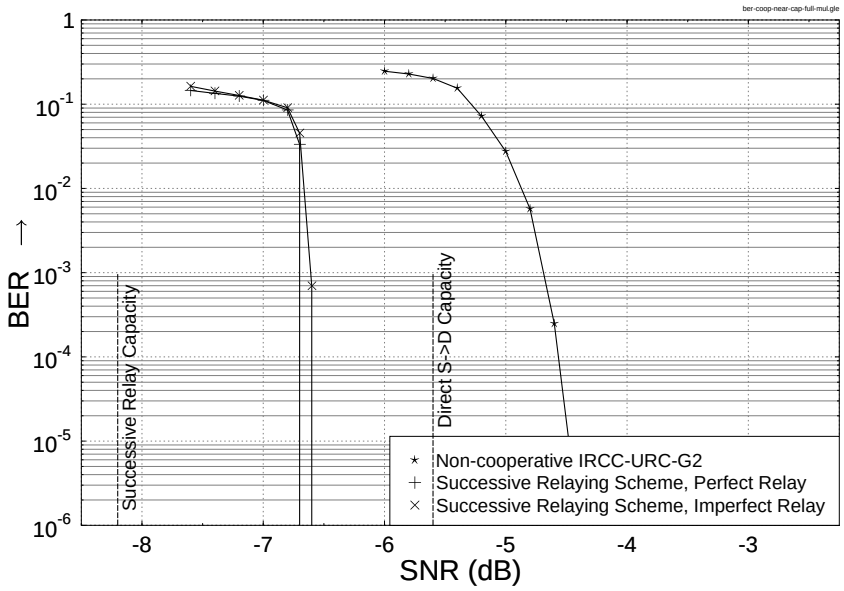


**Figure 4.18:** BER versus equivalent overall SNR performance of both perfect and imperfect relaying aided Ir-CSTC schemes in the successive relaying aided network for a frame length of 250 000 bits, while the performance of the non-cooperative system is also depicted here for comparison. The transmitter/receiver schematics are shown in Figs. 4.12 and 4.13 and the system parameters are summarized in Table 4.2.

### 4.3.5 Simulation Results and Discussions

In this section, we characterize the BER versus equivalent overall SNR performance of both the perfect and imperfect relaying aided Ir-CSTC schemes in the successive relaying aided network as well as that of a non-cooperative IRCC-URC-STBC scheme in Fig. 4.18. According to the trajectory predictions seen in Figs. 4.16 and 4.17, for the cooperative space-time coding scheme, the number of decoding iterations between the IRCC$_s$ decoder and the amalgamated "STBC$_s$-URC$_s$" decoder was fixed to $I^r = 11$ at the relays. At the destination, the number of "inner" decoding iterations was fixed to $I_i^d = 5$, while the number of "outer" decoding iterations between the parallel amalgamated "STBC$_s$-URC$_s$-IRCC$_s$" decoder and the amalgamated "STBC$_r$-IRCC$_r$" decoder was fixed to $I_o^d = 11$. On the other hand, for the non-cooperative serial concatenated IRCC-URC-STBC scheme, we employ an outer IRCC, which has the same weighting coefficients $\alpha_i$ as that of the IRCC$_s$ in the cooperative system. The number of decoding iterations exchanging extrinsic information between the outer IRCC decoder and the inner "STBC-URC" decoder was fixed to $I_{non} = 11$ as well. It is clearly seen in Fig. 4.18 that the performance of the perfect relaying-aided scheme matches the EXIT chart predictions of Fig. 4.17, while the imperfect relaying-aided scheme performs similarly to the perfect relaying scheme. This is due to the fact that the source information is detected without decoding errors after a sufficiently high number of decoding iterations at the relays. On the other hand,

the Ir-CSTC scheme employed in the successive relaying aided network outperforms the non-cooperative serial concatenated IRCC-URC-STBC scheme by about 2.2 dB, while maintaining the same effective throughput. As portrayed in Fig. 4.18, the Ir-CSTC scheme is capable of performing within 1.5 dB of the corresponding successive relaying channel's DCMC capacity.

## 4.4 Chapter Conclusion

In Section 4.2, we proposed an Ir-CSTC scheme designed for near-capacity communications in the conventional single-relay-aided network seen in Figs. 4.2 and 4.3. The encoding and decoding processes of Figs. 4.2 and 4.3 of the novel Ir-CSTC scheme were specified in Section 4.2.2, where we employed a serially concatenated three-component IRCC-URC-STBC scheme at the source and a two-component IRCC-STBC at the relay. In Section 4.2.3.1, we derived the CCMC capacity and the constrained information-rate bounds of Alamouti's G2 scheme for the half-duplex single-relay channel of Fig. 4.5. A joint source-and-relay mode design procedure designed with the aid of EXIT charts analysis was proposed in Section 4.2.3.2 for the sake of finding the optimal Ir-CSTC scheme, which performs closest to the single-relay channel's capacity as well as achieves the maximum effective throughput as an extra benefit of the joint mode design procedure. The numerical results seen in Fig. 4.9 of Section 4.2.4 demonstrated that the joint source-and-relay mode design based on EXIT chart analysis is capable of near-capacity cooperative communications in the single-relay-aided network.

Furthermore, in Section 4.3 an extended Ir-CSTC scheme was studied in the context of the twin-relay aided network of Fig. 4.10 in which the successive relaying protocol was employed. The factor two multiplexing loss of the single-relay-aided network was recovered by the successive relaying protocol, although this was achieved at the cost of an additional relay. Similarly, the CCMC capacity and the constrained information-rate bounds of Alamouti's STBC scheme were derived for the successive relaying aided schemes of Figs. 4.11 and 4.12 in Section 4.3.4.1. It was observed in Figs. 4.14 and 4.15 that the factor two multiplexing loss of the single-relay-aided network may be recovered by the successive relaying protocol with the aid of an additional relay, which is more practical than the assumption of a full-duplex system. The generalized joint source-and-relay mode design procedure advocated relies on the proposed procedure of finding the optimal cooperative coding scheme, which performs close to the capacity limit, in the context of twin-relay-aided network, as demonstrated by the BER performance results of Fig. 4.18 discussed in Section 4.3.5.

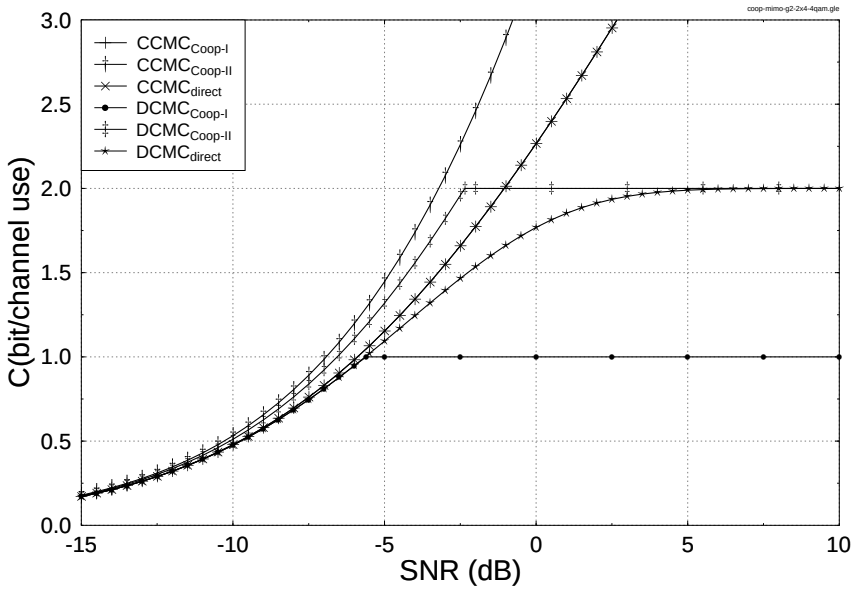


**Figure 4.19:** The CCMC capacity curve and constrained information rates of both the single-relay-aided and twin-relay-aided networks in conjunction with the network geometries of $G_{sr} = \infty$ and $G_{rd} = 1$, where Coop-I denotes the conventional single-relay-aided network of Fig. 4.1 and Coop-II indicates the successive relaying aided network of Fig. 4.10.

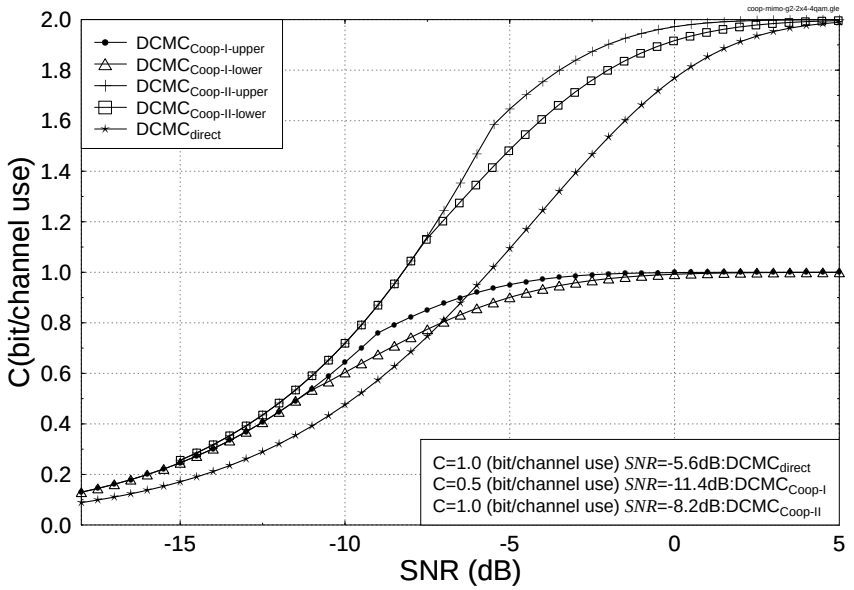


**Figure 4.20:** The CCMC capacity curve and constrained information rates of both the single-relay-aided and twin-relay-aided networks in conjunction with the network geometries of $G_{sr} = 8$ and $G_{rd} = 2$, where Coop-I denotes the conventional single-relay-aided network of Fig. 4.1 and Coop-II indicates the successive relaying aided network of Fig. 4.10.

Figs. 4.19-4.21 portrayed our performance comparisons of the Ir-CSTC schemes in the context of both the single-relay-aided and the twin-relay-aided networks in terms of the attainable capacity and BER performance. It may be clearly observed that although the twin-relay-aided Ir-CSTC scheme of Fig. 4.12 requires 0.3 dB higher $E_b/N_0$ to achieve decoding convergence to an infinitesimally low BER than its single-relay-aided counter-

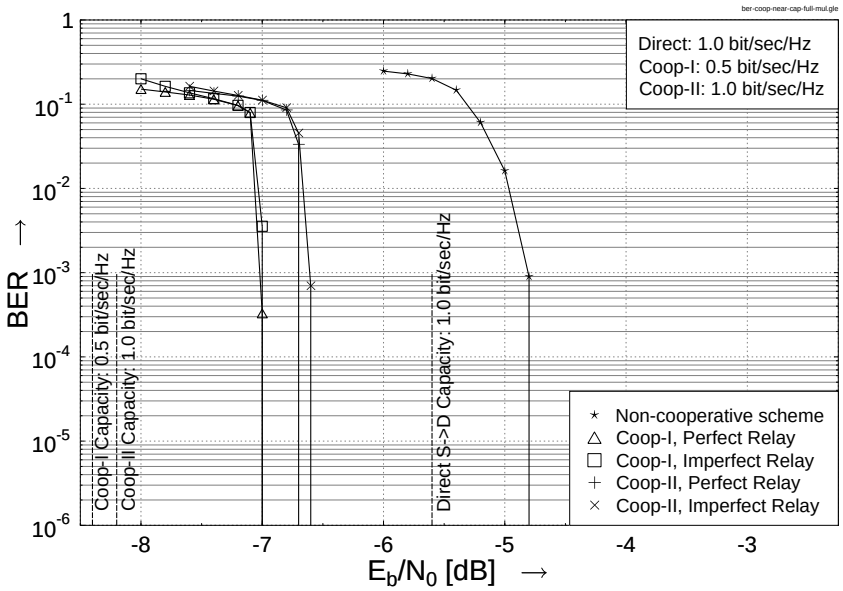


**Figure 4.21:** BER versus $E_b/N_0$ performance comparison of the Ir-CSTC scheme in the contexts of single-relay-aided and twin-relay-aided networks, where Coop-I denotes the conventional single-relay-aided network of Fig. 4.1 and Coop-II indicates the successive relaying aided network of Fig. 4.10. The Coop-I transmitter/receiver schematics are shown in Figs. 4.2 and 4.3 and the system parameters are summarized in Table 4.1, while Coop-II transmitter/receiver schematics are shown in Figs. 4.12 and 4.13 and the corresponding system parameters are summarized in Table 4.2. The performance of the non-cooperative system is also depicted for comparison.

part of Fig. 4.2, it maintains the same effective throughput as classic direct transmission, which is achieved with the aid of an additional relay used in conjunction with the proposed successive relaying protocol.

To summarize, the Ir-CSTC schemes of Figs. 4.2 and 4.12 proposed in this chapter are insensitive to the network's geometry. In other words, as long as the number of antennas as well as the space-time coding schemes used at the source and relays are fixed, the irregular components employed at the source and relays also remain unchanged, regardless of the network topology considered. This is because the EXIT curve shape of the inner decoder "STC$_s$-IRCC$_s$" of Fig. 4.3 employed at the relays as well as that of the amalgamated "STC$_s$-URC$_s$-IRCC$_s$" decoder of Fig. 4.3 invoked at the destination remains unaffected by the network's geometry. The topology only affects the transmit power thresholds to be used at the source and relays, when the EXIT tunnels open, as shown in Figs. 4.6-4.8 and 4.16-4.17. However, if the number of antennas, or the space-time coding schemes used at the source and relays are changed, say we replace the G2 STBC by a STTC, we have to redesign the irregular components both at the source and relays.

More specifically, the joint source-and-relay mode design procedures advocated in Sections 4.2.3.2 and 4.3.4.2 operate off-line in order to find the optimal distributed code components. In other words, they do not have to operate on-line in order to adapt the

parameters according to the instantaneous channel conditions. Once the irregular components at the source and relays were determined, they remain fixed during the transmit and receive periods. However, the knowledge of the channel state information is required during the off-line search procedure, which was assumed to be perfectly known at both the relay and destination in this chapter. Furthermore, the code design procedure is not limited to a specific networking scenario, but applicable under virtually any network configuration. Most importantly, it is in fact generically applicable, regardless of the specific choice of the space-time codes at the source and relays as well as of the irregular components, as exemplified by the family of irregular low-density parity-check (LDPC) codes, etc., provided that the inherent irregularity of the designs used at the source and relays is retained.

After investigating the Ir-CSTC scheme's performance in the single-user scenario, a more practical scenario, where the interference between the relays is taken into account, will be considered in the next chapter, where we will consider operating cooperative systems in a multi-user scenario. In that scenario interference suppression is required not only at the destination, but also at the relays.

Chapter 5

# Relay-Assisted Multiple-Antenna Aided Multi-User SDMA Uplink

## 5.1 Introduction

In the previous chapters, multiple antenna aided techniques have been studied in the context of single-user multiple-input multiple-output (SU-MIMO) systems, such as for example multiplexing-gain-oriented BLAST schemes, diversity-gain-oriented STC schemes and the flexible compromise-scheme of GMLST. In this chapter, we will extend their employment to the multiuser MIMO (MU-MIMO) scenario [148]. In an effort to further increase the achievable system capacity, antenna arrays can be employed for supporting multiple users in a space division multiple access (SDMA) communications scenario [149], which attempts to increase the attainable system throughput in a given bandwidth by incorporating several spatial channels. To gain insight into the multiuser supporting capability of such an SDMA system, it is useful to draw some comparisons with code division multiple access (CDMA) multiuser systems. In a CDMA system each user is identified by a unique user-specific spreading code. By contrast, an SDMA system differentiates each user by the associated unique user-specific channel impulse response (CIR) encountered at the receiver antenna. In a simplistic but conceptually appealing interpretation, we may argue that the unique user-specific CIR plays the role of a user-specific CDMA signature. To be more specific, in this analogy the CIR-signatures of SDMA systems are not orthogonal to each other, but this limitation is not serious, because even the orthogonal spreading codes of CDMA systems become non-orthogonal upon convolution by the CIR. However, owing to the non-orthogonal nature of the CIRs, an efficient multiuser receiver is required for separating the users in an SDMA system.

In conventional SDMA uplink systems, the transmitted signals of $L$ simultaneous mo-

bile stations (MSs) - each equipped with a single transmitter antenna - are received by the $M$ different receiver antennas of the base station (BS). At the BS the individual users' signals are separated with the aid of their unique user-specific spatial signatures. A variety of multiuser detection (MUD) schemes, such as the Least Squares (LS) [148, 150] and Minimum Mean Square Error (MMSE) [148, 150, 151] detectors, or Successive Interference Cancellation (SIC) [148, 150–152], Parallel Interference Cancellation (PIC) [148, 152, 153], Sphere Detection (SD) [154, 155], Minimum Bit Error Rate (MBER) detection [156] and Maximum Likelihood Detection (MLD) [148, 151, 157] schemes may be invoked for the sake of separating the different users at the BS. Among these schemes, the MLD arrangement was found to give the best performance, although this was achieved at the cost of a dramatically increased computational complexity, especially in the context of a high number of users and higher-order modulation schemes. By contrast, MMSE combining exhibits the lowest complexity in this set of detectors, while suffering from a performance loss [152, 158].

Although traditionally only the base station is equipped with more than one transmit/receive antenna elements, ideally the mobile stations should also be equipped with multiple antennas, which would facilitate achieving a high diversity gain and a high peak data rate. Therefore, it is a natural ambition to try and enhance the attainable uplink performance for multiple-antenna aided users. The basic constraint for multiple antenna uplink transmission is that the affordable antenna spacing is limited, since the mobile stations are usually of small size. In the literature, only a limited number of studies were dedicated to the multiple-antenna aided multi-user (MU) SDMA uplink. Against this background, in Section 5.2 of this chapter, we will investigate a multiple-antenna aided MU SDMA uplink system, where each user employs a Space-Time Block Code [8] for the sake of providing transmit diversity. In Section 5.2.2, a generalized MMSE-based SIC multiuser detector will be proposed for the multiple-antenna aided MU SDMA uplink system, which is capable of providing a better performance at low Signal-to-Noise Ratios (SNRs) and is applicable for employment in rank-deficient systems. Naturally, the achievable performance of the SDMA uplink system can be significantly improved, if Forward Error Correction (FEC) schemes, such as for example turbo convolutional codes are incorporated [89]. Hence, an IRregular Convolutional Coded (IRCC) and Unity-Rate Coded (URC) SDMA uplink system will be studied in Section 5.2.3, which significantly improves the uncoded SDMA system's performance, especially for rank-deficient scenarios.

On the other hand, as in Chapter 4, we have investigated the relay-aided single-user scenario, where a single MS is communicating with the BS with the aid of single or multiple relays. As a natural application example, we will also consider the multiuser SDMA

uplink combined with relaying techniques in this chapter. In Section 5.3, instead of considering a single-user scenario, multiple interfering MSs are taken into account, when we evaluate the overall relay-aided multiuser system's performance. Naturally, the multiple MSs interfere with each other and hence degrade the overall system performance achieved at the base station. In this multiuser scenario, interference suppression is required not only at the BS, but also at the relaying MS. Finally, we will also investigate the effects of the spatial correlation on the MS transmitters in Section 5.4, while our conclusions are summarized in Section 5.5.

## 5.2 STBC-Based Multiple-Antenna Aided Multi-User SDMA Uplink

### 5.2.1 SDMA System Model

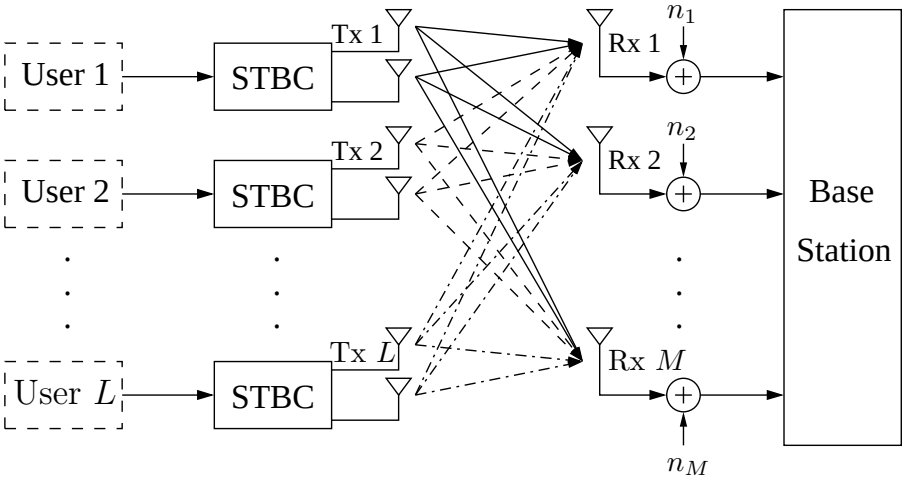


**Figure 5.1:** Schematic of the multiple-antenna aided multi-user SDMA uplink scenario, where each of the $L$ users is equipped with two transmit antennas and the base station's receiver is assisted by an $M$-element antenna array.

We consider an STBC-aided SDMA uplink MU-MIMO system supporting $L$ users, as depicted in Fig. 5.1, where each of the users is equipped with $N_t = 2$ transmit antennas and the base station's receiver is assisted by an $M$-element antenna array. For the sake of simplicity, the well-known STBC scheme proposed by Alamouti in [8] is employed by each user, which is also known as the G2 scheme. The signal seen at each receive antenna-element of the base station is a noisy superposition of the $(L \times N_t)$ transmitted signals corrupted by the flat Rayleigh fading channel. In general, the fading channel is spatially correlated due to the size limitation of the mobile station. For simplicity, in this section we first assume that the fading is statistically independent from one transmit-receive antenna pair to another, while the spatial correlation effects of the MIMO channel will be discussed in Section 5.4. The signal received by antenna $i$ ($1 \leq i \leq M$) at time

instant $k$ at the base station is given by

$$y_k^i = \sum_{l=1}^{L} \sum_{j=1}^{N_t} h_{i,j}^l c_{j,k}^l + n_k^i, \tag{5.1}$$

where $h_{i,j}^l$ is the complex-valued channel coefficient between the $j$-th transmit antenna of user $l$ and the $i$-th receive antenna of the base station, which is modeled by independent complex Gaussian random variables having a zero mean and a variance of 0.5 per dimension. Furthermore, $c_{j,k}^l$ is the symbol transmitted from antenna $j$ of user $l$ at time instant $k$, and $n_k^i$ is the Additive White Gaussian Noise (AWGN) encountered by the $i$-th antenna of the base station at time instant $k$ and modeled by the samples of independent complex Gaussian random variables having a zero mean and a variance of $N_0/2$ per dimension.

For notational simplicity, we define $\mathbf{y}_k$, $\mathbf{c}_k$ and $\mathbf{n}_k$ as

$$\mathbf{y}_k = [y_k^1, y_k^2, \ldots, y_k^M]^T,$$

$$\mathbf{c}_k = [\mathbf{c}_k^1, \mathbf{c}_k^2, \ldots, \mathbf{c}_k^L]^T = \left[[c_{1,k}^1, c_{2,k}^1, \ldots, c_{N_t,k}^1], \ldots, [c_{1,k}^L, c_{2,k}^L, \ldots, c_{N_t,k}^L]\right]^T,$$

and

$$\mathbf{n}_k = [n_k^1, n_k^2, \ldots, n_k^M]^T,$$

respectively. Then the channel model of Eq. (5.1) may be expressed using a more compact matrix notation as

$$\mathbf{y}_k = \mathbf{H}\mathbf{c}_k + \mathbf{n}_k, \tag{5.2}$$

where $\mathbf{H}$ is the $(M \times (L \times N_t))$-element channel matrix, which may be further expressed as

$$\begin{aligned} \mathbf{H} &= [\mathbf{H}_1, \mathbf{H}_2, \ldots, \mathbf{H}_L] \\ &= \begin{bmatrix} h_{1,1}^1 & \ldots & h_{1,N_t}^1 & h_{1,1}^2 & \ldots & h_{1,N_t}^2 & \ldots & h_{1,1}^L & \ldots & h_{1,N_t}^L \\ h_{2,1}^1 & \ldots & h_{2,N_t}^1 & h_{2,1}^2 & \ldots & h_{2,N_t}^2 & \ldots & h_{2,1}^L & \ldots & h_{2,N_t}^L \\ \vdots & \ldots & \vdots & \vdots & \ldots & \vdots & & \vdots & \ldots & \vdots \\ h_{M,1}^1 & \ldots & h_{M,N_t}^1 & h_{M,1}^2 & \ldots & h_{M,N_t}^2 & \ldots & h_{M,1}^L & \ldots & h_{M,N_t}^L \end{bmatrix}. \end{aligned} \tag{5.3}$$

### 5.2.2 Maximum-SINR-Based SIC Multiuser Detection

As mentioned above, at the receiver side of an SDMA uplink MU-MIMO system, multiuser detection schemes have to be invoked for the sake of detecting the received signals of different users. For the conventional single-antenna-user aided SDMA systems [148], a family of various MUD techniques, represented for example by the Maximum Likelihood

Detector (MLD) [148, 151, 157], Sphere Detector (SD) [154, 155], Parallel Interference Canceller (PIC) [148, 152, 153], Successive Interference Canceller (SIC) [148, 150–152], Minimum Mean Square Error (MMSE) [148, 150, 151] and Least Squares (LS) [148, 150] detectors have been extensively studied. Specifically, ML detection is known to exhibit the optimum performance, although this is achieved at the highest complexity. In order to avoid the potentially excessive complexity of optimum ML detection, sub-optimum detection techniques such as the LS- and MMSE-MUD have been devised. Specifically, these linear multiuser detectors exhibit the lowest detection complexity at the cost of a performance degradation [152, 158].

In the linear MUDs, the estimates of the different users' transmitted signals are generated with the aid of the linear combiner. More specifically, the estimated signal vector $\hat{\mathbf{c}}_k$ generated from the transmitted signal $\mathbf{c}_k$ of the $L$ simultaneous users, as shown in Fig. 5.1, is obtained by linearly combining the signals received by the $M$ different receiver antenna elements of the base station with the aid of the array weight matrix, as follows [148]:

$$\hat{\mathbf{c}}_k = \mathbf{W}^H \mathbf{y}_k, \tag{5.4}$$

where the superscript $H$ denotes the Hermitian transpose, and $\mathbf{W}$ is the LS- or MMSE-based weight matrix given by [148]:

$$\mathbf{W}_{LS} = \mathbf{H}(\mathbf{H}^H\mathbf{H})^{-1} \tag{5.5}$$

and

$$\mathbf{W}_{MMSE} = \mathbf{H}(\mathbf{H}^H\mathbf{H} + \sigma_n^2\mathbf{I})^{-1}, \tag{5.6}$$

respectively, while $\mathbf{I}$ is the identity matrix and $\sigma_n^2 = N_0/2$ is the AWGN noise variance.

On the other hand, for the multiple-antenna aided MU SDMA systems [148, 154], the above-mentioned linear MUDs also perform well. However, not all the non-linear MUD schemes designed for single-antenna-user aided SDMA systems can be directly transplanted into the multiple-antenna aided MU SDMA systems. In [154], Sphere Detection was studied in the context of multiple-antenna assisted MU systems, which guarantees a good performance, while imposing a rather low computational complexity. In Chapter 2, a zero-forcing (ZF) based iterative SIC algorithm was proposed for a multi-layer space-time scheme in order to achieve the maximum attainable receive diversity, while imposing only a fraction of the ML's complexity. Obviously, when we consider the different layers of the multi-layer space-time scheme as different SDMA users, the iterative SIC detection algorithm can be employed in the multiple-antenna aided MU SDMA system for the sake of maintaining a balance between the performance obtained and the complexity imposed. It is widely recognized that zero-forcing degrades the performance at low-to-mid

SNRs due to its noise enhancement. A performance improvement is thus expected, if one seeks to strike a trade-off between the interference suppression and noise enhancement. Naturally, MMSE-based SIC [148] is a promising solution for providing a better performance at low SNRs. However, in the multiple-antenna aided MU SDMA system, minimizing the mean squared error (MSE) of the signals involves averaging over the data symbols. Maximizing the signal-to-interference-plus-noise ratio (SINR) may be handled more concisely [86–88]. As an alternative, in this section we will design a multi-user detector based on the maximum SINR array processor for the multiple-antenna aided MU SDMA system. This maximum SINR (MaxSINR) based MUD differs from the conventional MMSE-based detector in that there are more than one desired signal dimensions, each of which corresponding to one of the multiple-antenna aided users. In the following section, we will derive the MaxSINR-based SIC multi-user detector.

#### 5.2.2.1 Maximum-SINR-Based SIC Algorithm

Without loss of generality, we first consider natural ordering based SIC detection of the SDMA users. Let us rewrite Eq. (5.2) as

$$\mathbf{y}_k = \mathbf{H}_1 \mathbf{c}_k^1 + \mathbf{H}_o \mathbf{c}_k^o + \mathbf{n}_k, \tag{5.7}$$

where we have

$$\mathbf{c}_k^1 = [c_{1,k}^1, c_{2,k}^1, \ldots, c_{N_t,k}^1]^T, \tag{5.8}$$

$$\mathbf{c}_k^o = [\mathbf{c}_k^2, \ldots, \mathbf{c}_k^L]^T = \left[[c_{1,k}^2, c_{2,k}^2, \ldots, c_{N_t,k}^2], \ldots, [c_{1,k}^L, c_{2,k}^L, \ldots, c_{N_t,k}^L]\right]^T, \tag{5.9}$$

and

$$\mathbf{H}_1 = \begin{bmatrix} h_{1,1}^1 & \ldots & h_{1,N_t}^1 \\ h_{2,1}^1 & \ldots & h_{2,N_t}^1 \\ \vdots & \cdots & \vdots \\ h_{M,1}^1 & \ldots & h_{M,N_t}^1 \end{bmatrix}, \tag{5.10}$$

$$\begin{aligned} \mathbf{H}_o &= [\mathbf{H}_2, \ldots, \mathbf{H}_L] \\ &= \begin{bmatrix} h_{1,1}^2 & \ldots & h_{1,N_t}^2 & \ldots & h_{1,1}^L & \ldots & h_{1,N_t}^L \\ h_{2,1}^2 & \ldots & h_{2,N_t}^2 & \ldots & h_{2,1}^L & \ldots & h_{2,N_t}^L \\ \vdots & \cdots & \vdots & \cdots & \vdots & \cdots & \vdots \\ h_{M,1}^2 & \ldots & h_{M,N_t}^2 & \ldots & h_{M,1}^L & \ldots & h_{M,N_t}^L \end{bmatrix}. \end{aligned} \tag{5.11}$$

Firstly, in this section we derive the maximum SINR based array processor. Since the space-time coded symbols of the multiple users are unknown at the array processing stage,

the SINR can only be maximized statistically. Therefore, we define the covariance matrices of the desired signal and of the interference, when considering the detection of the first user, as

$$\mathbf{R}_s^1 = \mathbf{H}_1 E\left[\mathbf{c}_k^1 \left(\mathbf{c}_k^1\right)^H\right] \mathbf{H}_1^H, \tag{5.12}$$

$$\mathbf{R}_n^1 = \mathbf{H}_o E\left[\mathbf{c}_k^o \left(\mathbf{c}_k^o\right)^H\right] \mathbf{H}_o^H + N_0\mathbf{I}, \tag{5.13}$$

respectively. Using the MMSE filter representation advocated in [159], the maximum SINR array processor will require the same number of linear filters as the dimension of the signal space for the sake of collecting all the energy representing the specific user's signal. Each of these linear filters can be decomposed into two components: one in the signal space and the other in the orthogonal space. We may consider the linear filtering in two steps. First, we assemble the above-mentioned $k$ linear filters $\mathbf{w}_1, \mathbf{w}_2, \cdots, \mathbf{w}_k$ into a linear filter bank characterized by $\Theta_1 = (\mathbf{w}_1, \mathbf{w}_2, \cdots, \mathbf{w}_k)$ in order to filter the receive antenna outputs at the base station. The outputs of this filter bank are then combined in order to achieve the maximum SINR. Without loss of generality, the interference components of the filter bank outputs are assumed to be uncorrelated with each other. In other words, the matrix $\Theta_1^H \mathbf{R}_n^1 \Theta_1$ is diagonal. This assumption is reasonable since for any filter bank consisting of $k$ linear filters, we can find a nonsingular $(k \times k)$-element matrix to transform it and to diagonalize the interference covariance matrix of its output using the singular value decomposition (SVD) [160] of $\Theta_1^H \mathbf{R}_n^1 \Theta_1$. This transformation is reversible and will not destroy the information contained in the filter bank outputs. Furthermore, we assume that the linear filters constituting this filter bank are linearly independent of each other, which may be readily justified by the fact that if this is not true, we can always combine the corresponding correlated filters to form a linearly independent filter bank constituted by a reduced number of filters.

Based on the above assumptions and on the fact that $\mathbf{R}_n$ is nonsingular, the filter bank outputs hence have nonzero and uncorrelated interference components. Naturally, under these conditions, the maximum SINR based combining of the filter bank outputs becomes identical to maximum ratio combining (MRC). Due to the independence of the different users' transmissions, the expectation of the signal and of the interference, i.e. of $\mathbf{c}_k^1$ and $\mathbf{c}_k^o$, can be taken separately. Hence, the resultant $k$ maximum-SINR linear filters have to satisfy

$$(\mathbf{w}_1, \mathbf{w}_2, \cdots, \mathbf{w}_k) = \arg\left\{\max_{\mathbf{w}_1, \cdots, \mathbf{w}_k} \sum_j \mathbf{w}_j^H \mathbf{R}_s \mathbf{w}_j\right\}, \tag{5.14}$$

which is subject to the constraints of

$$\mathbf{w}_i^H \mathbf{R}_n \mathbf{w}_i = \nu, \quad \forall i, \tag{5.15}$$

where $\nu$ is a predefined constant, which will not affect the results. This constrained optimization may be formulated with the aid of the classic Lagrange multipliers as follows:

$$\frac{\partial}{\partial \mathbf{w}_i^*}\left(\sum_j \mathbf{w}_j^H \mathbf{R}_s \mathbf{w}_j - \sum_j \lambda_j \mathbf{w}_j^H \mathbf{R}_n \mathbf{w}_j\right) = 0, \quad \forall i. \tag{5.16}$$

The solutions to the Lagrangian optimization problem of Eq. (5.16) satisfy

$$(\mathbf{R}_s - \lambda_i \mathbf{R}_n)\mathbf{w}_i = 0, \quad \forall i \tag{5.17}$$

where

$$\lambda_i = \frac{\mathbf{w}_i^H \mathbf{R}_s \mathbf{w}_i}{\mathbf{w}_i^H \mathbf{R}_n \mathbf{w}_i} \tag{5.18}$$

are the corresponding SINRs of the maximum SINR filter outputs.

We can now readily derive the linear maximum SINR array processor $\Theta_1$ for user 1 from Eq. (5.17), which consists of a set of $k$ linearly independent eigenvectors corresponding to the nonzero eigenvalues of the $generalized\ eigenvalue\ problem$[1] of

$$\mathbf{R}_s \mathbf{w} = \lambda \mathbf{R}_n \mathbf{w}, \tag{5.19}$$

where $k$ is the rank of $\mathbf{R}_s$. On the other hand, since we have

$$\begin{aligned} E\left[\mathbf{w}_i^H \mathbf{y}_k \left(\mathbf{w}_j^H \mathbf{y}_k\right)^H\right] &= E\left[\mathbf{w}_i^H \mathbf{y}_k \mathbf{y}_k^H \mathbf{w}_j\right] \\ &= \mathbf{w}_i^H \left(\mathbf{R}_s + \mathbf{R}_n\right) \mathbf{w}_j, \end{aligned} \tag{5.20}$$

and

$$\mathbf{w}_i^H \mathbf{R}_n \mathbf{w}_j = \begin{cases} \nu, & i = j \\ 0, & i \neq j \end{cases} \quad \mathbf{w}_i^H \mathbf{R}_s \mathbf{w}_j = \begin{cases} \lambda_i \nu, & i = j \\ 0, & i \neq j, \end{cases} \tag{5.21}$$

we can observe that the outputs of the maximum SINR filter bank $\left\{\mathbf{w}_i^H \mathbf{y}_k\right\}_{i=1}^k$ are uncorrelated with each other.

Based on the above analysis, we may readily see that the maximum SINR filter generalizes the classic MMSE filtering for multidimensional signals. When we have $N_t = 1$ (single-antenna user) or $c_{1,k}^1 = c_{2,k}^1 = \cdots = c_{N_t,k}^1$ (repetitive transmission), the maximum SINR-based array processor becomes the conventional MMSE filter. Intuitively, the maximum SINR array processor pre-whitens the interference and orthogonalizes the desired users' signal. Following the maximum SINR-based array processing, the resultant output may be expressed as:

$$\tilde{\mathbf{y}}_k = \tilde{\mathbf{H}}_1 \mathbf{c}_k^1 + \tilde{\mathbf{n}}_k, \tag{5.22}$$

[1]The solution of the generalized eigenvalue problem is described in the Appendix.

where we have $\tilde{\mathbf{y}}_k = \Theta_1^H \mathbf{y}_k, \tilde{\mathbf{H}}_1 = \Theta_1^H \mathbf{H}_1$ and $\tilde{\mathbf{n}}_k = \Theta_1^H \mathbf{H}_o \mathbf{c}_k^o + \Theta_1^H \mathbf{n}_k$. When using the Gaussian approximation of the maximum SINR-based array processor outputs [161], Eq. (5.22) becomes the maximum likelihood solution, where the detection result is obtained as:

$$\left(\mathbf{c}_0^1, \mathbf{c}_1^1, \ldots, \mathbf{c}_k^1, \ldots\right) = \arg\left\{ \min_{\left\{\mathbf{c}_k^1\right\}} \sum_k \parallel \Theta_1^H \mathbf{y}_k - \Theta_1^H \mathbf{H}_1 \mathbf{c}_k^1 \parallel^2 \right\}. \tag{5.23}$$

Compared to the classic zero-forcing approach of Chapter 2, the maximum SINR-based approach does not impose any constraint on the number of receive antennas at the base station. In other words, the maximum SINR-based array processor is also applicable to rank-deficient systems. It works even when we have $(M - (L-1)N_t) \leq 0$, although the performance of this scenario will be poor. Once the signal of user 1 is detected, we cancel its contribution from the received signal at the base station and proceed to the detection of all the other SDMA users in the same manner.

#### 5.2.2.2 Ordered Maximum-SINR-Based SIC Detection

As we have seen in Chapter 2 for nonlinear detection schemes, using the appropriate SIC detection order is crucial for the overall SDMA system's performance, which may lead to a substantial performance gain for all users. Similarly to the ZF-based SIC of Chapter 2, according to the 'best first' rule, at every step of interference suppression and interference cancellation, we detect the SDMA user associated with the highest post-suppression SINR and then cancel its contribution from the received signal. Observe from Eq. (5.22) that the total output SINR of user 1 recorded after suppressing all the other users is

$$\text{SINR}_1 = \text{trace}\left( \left(\mathbf{R}_n^1\right)^{-1} \mathbf{R}_s^1 \right), \tag{5.24}$$

where trace(.) indicates the sum of all diagonal elements of the matrix. Similarly, the output SINR of the $l$-th user, provided that it is detected first after suppressing all the other users' signals becomes

$$\text{SINR}_l = \text{trace}\left( \left(\mathbf{R}_n^l\right)^{-1} \mathbf{R}_s^l \right), \tag{5.25}$$

where we have

$$\mathbf{R}_s^l = \mathbf{H}_l E\left[ \mathbf{c}_k^l \left(\mathbf{c}_k^l\right)^H \right] \mathbf{H}_l^H, \tag{5.26}$$

$$\mathbf{R}_n^l = \mathbf{H}_o^l E\left[ \mathbf{c}_k^{l,o} \left(\mathbf{c}_k^{l,o}\right)^H \right] \left(\mathbf{H}_o^l\right)^H + N_0 \mathbf{I}, \tag{5.27}$$

with $\mathbf{H}_o^l = [\mathbf{H}_1, \mathbf{H}_2, \ldots, \mathbf{H}_{l-1}, \mathbf{H}_{l+1}, \ldots, \mathbf{H}_L]$ and $\mathbf{c}_k^{l,o} = [\mathbf{c}_k^1, \mathbf{c}_k^2, \ldots, \mathbf{c}_k^{l-1}, \mathbf{c}_k^{l+1}, \ldots, \mathbf{c}_k^L]^T$. Hence, the determination of the optimal user ordering process imposes some additional

| | |
|---|---|
| Modulation Scheme | QPSK |
| No. of MSs | $L = 1, 2, 3, 4$ or 5 |
| No. of Antenna Elements per MS | $N_t = 2$ |
| No. of Antenna Elements at BS | $M = 4$ |
| STC | STBC [8] |
| Frame Length | 130 symbols per transmit antenna |
| Channel | Temporally uncorrelated flat Rayleigh fading |
| Channel Estimation | Perfect |
| MUD | MaxSINR-based SIC |

**Table 5.1:** SDMA system parameters.

computational complexity in terms of the associated matrix inversion process of Eq. (5.25) than the natural ordering based SIC process, while achieving a significant performance improvement, as will demonstrate in the next section.

#### 5.2.2.3 Simulation Results

In this section, we characterize the attainable performance of the STBC-aided SDMA uplink of Fig. 5.1 in Fig. 5.2, where both the naturally and optimally ordered MaxSINR-based SIC multiuser detectors are employed at the BS for comparison. We assume that all SDMA users have the same transmit power, while all the other system parameters are summarized in Table 5.1. We can see from Fig. 5.2 that as the number of users increases, the BER performance degrades owing to the increased multiuser interference imposed. Furthermore, it is clearly observed in Fig. 5.2 that our MaxSINR-based SIC detection is capable of supporting rank-deficient systems, although naturally the system performance suffers under these conditions. Specifically, there are severe error floors for the rank-deficient 3-user, 4-user and 5-user scenarios, when employing naturally ordered MaxSINR-based SIC detection. On the other hand, the optimally ordered SIC detection significantly improves the multiuser system performances, which dramatically reduces the error floor of the 3-user system to an acceptable BER level of $10^{-4}$. Furthermore, in conjunction with the optimal ordering based SIC detection the system performance of the 2-user scenario was improved by approximately 2.0 dB at the target BER of $10^{-4}$.

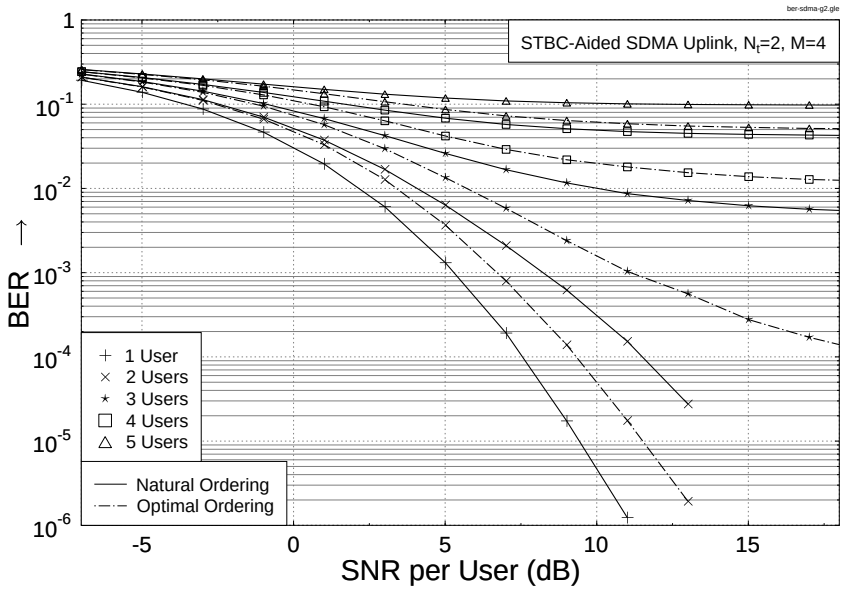


**Figure 5.2:** Average BER versus SNR performance of the STBC-aided SDMA uplink systems of Fig. 5.1, where at the base station a MaxSINR-based SIC multiuser detection algorithm is employed.

## 5.2.3 Channel-Code-Assisted STBC-Aided SDMA Uplink

### 5.2.3.1 Channel-Coded SDMA System

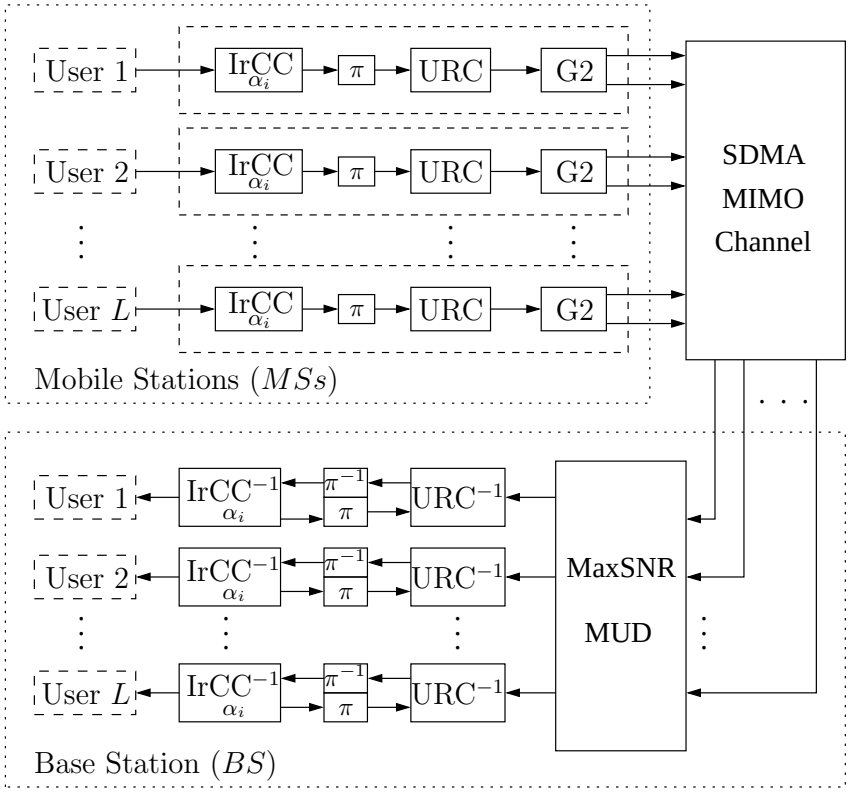


**Figure 5.3:** Schematic of the IRCC- and URC-coded STBC-aided SDMA uplink employing MaxSINR-based multiuser detection.

In Section 5.2.1, we have briefly reviewed the multiuser STBC uplink system of Fig. 5.1. For the sake of improving the multiuser system's performance, especially for the rank-deficient scenario, in this section we characterize the channel-code-assisted STBC-aided multiuser system shown in Fig. 5.3. At the mobile stations of Fig. 5.3, the information bit sequences of the geographically-separated $L$ simultaneous users are firstly encoded by a bank of half-rate IRregular Convolutional Codes (IRCCs). After interleaving, the IRCC coded bits are forwarded to an identical Unity-Rate Code (URC), which is concatenated with the STBC as the inner code for each user. As stated in the previous chapters, the URCs are employed for the sake of eliminating the error floor as well as achieving a near-capacity performance together with the outer IRCC. The power of these simple URCs is a benefit of their infinite impulse response, which allow us to spread the extrinsic information more efficiently without increasing the system's delay. The STBC symbols are then transmitted by the MSs to the base station over the SDMA MIMO channel. Then each element of the receiver antenna array shown at the bottom right of Fig. 5.3 receives the superposition of the AWGN-contaminated and faded signals, which are forwarded to the MaxSINR-based SIC multiuser detector for separating the different users' signals. The detected signals are then successively decoded by the corresponding URC and IRCC decoders. The turbo iterations exchange extrinsic information between the IRCC and URC decoders for the sake of achieving near-capacity performance for each user.

#### 5.2.3.2 System Design and Simulation Results

Similarly, in this section we first design the IRCCs with the aid of EXtrinsic Information Transfer (EXIT) charts for the IRCC- and URC-coded multiuser system. Without loss of generality, we consider the first user in our EXIT chart analysis, while other users can be analysed in the same manner. As presented in Chapter 3, EXIT charts are employed for the sake of analysing the iterative detection/decoding process, which visualize the mutual information exchange between the inner and outer decoders. For our IRCC- and URC-coded SDMA uplink system, a specific user's inner decoder is composed by the MaxSINR-based SIC multiuser detector and the corresponding URC decoder. It is clearly seen in Fig. 5.4 that a specific user's inner EXIT curve is shifted downwards at a given SNR when more interfering mobile stations communicate with the base station simultaneously. This is because the extra interference effectively reduces the SNR. As stated in Chapter 3, we design the outer IRCC's components by employing the EXIT curve matching algorithm of [61] to match the outer IRCC's EXIT curve to the shape of the inner decoder's EXIT curve, as shown in Fig. 5.4, where the Monte-Carlo simulation-based de-

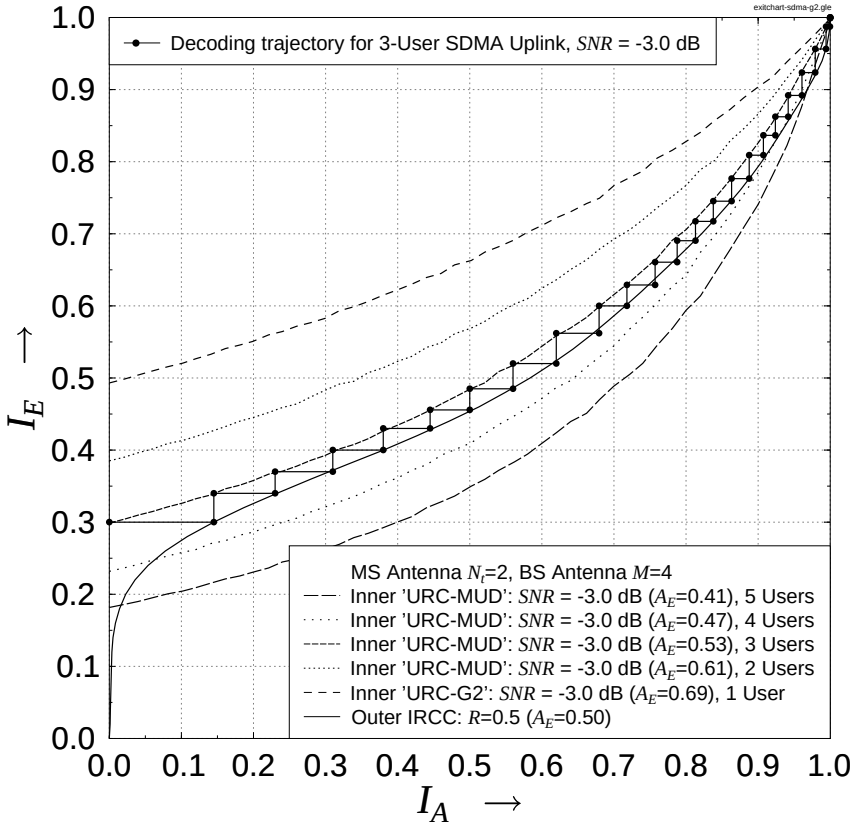


**Figure 5.4:** Exit charts of the IRCC- and URC-coded STBC-aided multiuser SDMA uplink systems of Fig. 5.3.

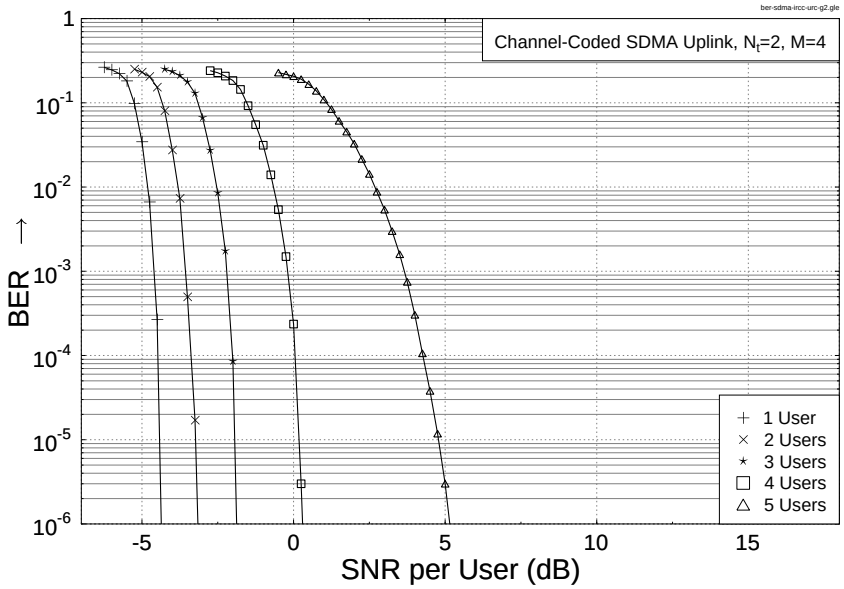


**Figure 5.5:** Average BER versus SNR performance of the IRCC- and URC-coded STBC-aided SDMA uplink systems of Fig. 5.3, where at the base station a MaxSINR multiuser detection algorithm is employed. The system parameters are summarized in Table 5.2.

| | |
|---|---|
| Modulation Scheme | QPSK |
| No. of MSs | $L = 1$, 2, 3, 4 or 5 |
| No. of Antenna Elements per MS | $N_t = 2$ |
| No. of Antenna Elements at BS | $M = 4$ |
| IRCC Coding Rate | 0.5 |
| IRCC Components Coefficients $\alpha_i$ | [0, 0, 0, 0, 0, 0.327442, 0.186505, 0.113412, 0, 0.0885527, 0, 0.0781214, 0.0962527, 0.0114205, 0.0346015, 0.0136955, 0.0500168] |
| Frame Length | 250 000 bits |
| URC Generator | (1, $g_1/g_0$) = (1, $\frac{1}{1+D}$) |
| STC | STBC [8] |
| Channel | Temporally uncorrelated flat Rayleigh fading |
| Channel Estimation | Perfect |
| MUD | MaxSINR-based SIC |
| No. of Iterations at BS | 10 |

**Table 5.2:** Channel-coded SDMA system parameters.

coding trajectory was also plotted for our 3-user scenario for example. Since there is no difference in the inner EXIT curve shapes for different SDMA users, we employ IRCCs in conjunction with the same weighting coefficients, as shown in Table 5.2 for all SDMA users.

Following the EXIT chart analysis of Fig. 5.4, Fig. 5.5 portrays the BER performance of the IRCC- and URC-coded multiuser SDMA uplink, where the system parmeters are summarized in Table 5.2. Similarly, we also assume that all SDMA users transmit at the same power. Fig. 5.5 demonstrates that the BER performances of the iteratively-detected channel-coded SDMA systems closely match the EXIT chart based predictions of Fig. 5.4. As expected, the channel-coded SDMA systems provide dramatic coding gains over their uncoded counterparts. For the $L = 1$ to $L = 5$ scenarios, the systems approach a target BER of $10^{-4}$ at SNRs of -4.5 dB, -3.4 dB, -2 dB, 0 dB and 4.2 dB, respectively, when using 10 iterations at the BS. Compared to the uncoded systems of Fig. 5.2, the channel-coded SDMA systems achieved coding gains of around 9 dB, 9.7 dB and 17.4 dB in terms of $E_b/N_0$ at the target BER of $10^{-4}$ for the $L = 1$ to $L = 3$ scenarios, respectively. On the other hand, for the rank-deficient $L = 4$ and $L = 5$ scenarios, we can

see that powerful turbo detection significantly enhances the multiuser SDMA system's performance and totally eliminates the error floors of the uncoded SDMA systems of Fig. 5.2. Furthermore, the system performance can be further improved at the cost of a higher computational complexity, when employing more iterations between the IRCC and URC decoders of each SDMA user.

## 5.3 Relay-Assisted Multi-User SDMA Uplink

### 5.3.1 System Model

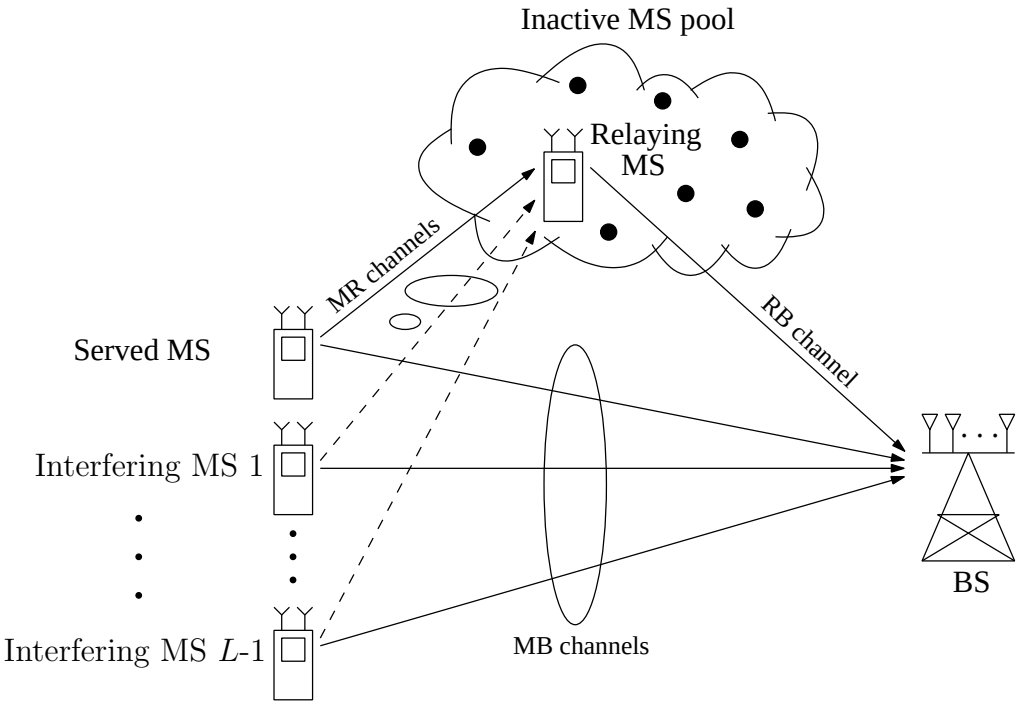


(a) Network topology.

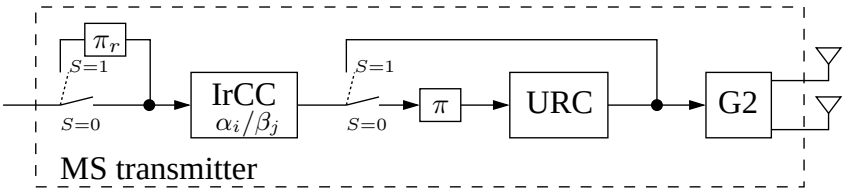


(b) MS's transmitter structure, where the Unity-Rate Code is employed as the intermediate code when MS is in the active transmission mode ($S = 0$). Otherwise, when MS is in the relay mode ($S = 1$), the URC is deactivated and a bit-wise random interleaver is incorporated before the outer IRCC code for the sake of achieving iterative gains at the BS side. The IRCC is then concatenated directly with the inner G2 scheme.

**Figure 5.6:** Relay-assisted multiple-antenna aided MU SDMA uplink system.

In Chapter 4, we have investigated the relay-aided single-user scenario, where a single MS is communicating with the BS with the aid of single or multiple relays. In this section,

we will consider a relay-assisted multiuser SDMA uplink system, in which multiple interfering MSs are considered. Naturally, the multiple MSs will interfere with each other and hence degrade the overall relay-aided multiuser system performance at the base station. In contrast to the single-user scenario of Chapter 4, in this multiuser interference-limited scenario, interference suppression is required not only at the BS, but also at the relaying MS.

Let us now consider the multiuser scenario of Fig. 5.6, where the network is constituted by a group of active MSs and an inactive MS pool. For simplicity, we assume that all the MSs are transmitting at the same power. The served MS is actively communicating with the base station positioned far away, while ($L$-1) interfering MSs are simultaneously transmitting in the same bandwidth. The inactive MS pool consists of all the MSs being in idle mode. For the sake of achieving extra spatial diversity as well as reduced-pathloss based geometrical gains [142], the served MS will attempt to find the geometrically nearest idle MS in the inactive MS pool in order to seek assistance in its communications with the base station. Following the design philosophy of the irregular cooperative space-time coding (Ir-CSTC) schemes of Chapter 4, we can readily extend the Ir-CSTC schemes to multiuser scenarios. Fig. 5.6(b) shows the MS's transmitter structure, where we can see that the MS can readily switch between its active transmission mode and the relaying mode. Specifically, when we have $S = 0$, the MS is in its active transmission mode and its outer IRCC will have the weighting coefficients of $\alpha_i$. When acting as a relaying station ($S = 1$), the MS's intermediate URC is deactivated and the outer IRCC changes its weighting coefficients from $\alpha_i$ to $\beta_j$, which will be directly concatenated with the inner STBC scheme. Meanwhile, a bit-wise interleaver is incorporated before the outer IRCC code, which helps us to achieve distributed turbo coding gains at the base station, as stated in Chapter 4. In contrast to the relay-aided single-user systems of Figs. 4.1 and 4.10, multiuser detection should be employed at the relaying MS of Fig. 5.6(a) since many simultaneous active MSs will interfere the signals received from the served MS. Therefore, we employ the MaxSINR-based MUD at the relaying MS for the active MSs to relaying MS (MR) link. Although the MR link is typically rank-deficient, the MaxSINR-based MUD is capable of separating the signals received at the relaying MS at a moderate complexity. After the MUD, iterative decoding is carried out by exchanging extrinsic information between the IRCC and URC decoders at the relaying MS, until a reliable estimate of the served MS is generated. On the other hand, at the base station, the distributed turbo detection scheme of Fig. 4.13 is employed for the sake of detecting the served MS's signals, where we replace the iterative ZF-based SIC detector of Fig. 4.13 by the MaxSINR-based MUD of Section 5.2.2.

| | |
|---|---|
| Modulation Scheme | QPSK |
| No. of Served MSs | 1 |
| No. of Relaying MSs | 1 |
| No. of Interfering MSs | $(L-1) = 0$, 1, 2, 3 or 4 |
| No. of Antenna Elements per MS | $N_t = 2$ |
| No. of Antenna Elements at BS | $M = 4$ |
| Served MS' IRCC Coding Rate | 0.5 |
| Relaying MS' IRCC Coding Rate | 0.5 |
| Served MS' IRCC Components Coefficients $\alpha_i$ | [0, 0, 0, 0, 0, 0.327442, 0.186505, 0.113412, 0, 0.0885527, 0, 0.0781214, 0.0962527, 0.0114205, 0.0346015, 0.0136955, 0.0500168] |
| Relaying MS' IRCC Components Coefficients $\beta_j$ | [0, 0, 0, 0, 0.233115, 0.0158742, 0.292084, 0.220065, 0.0151108, 0, 0, 0, 0, 0, 0, 0, 0.22375] |
| Geometrical Gain of Relaying MS to BS link | 2 |
| Geometrical Gains of Active MS to BS links | 1 |
| Frame Length | 250 000 bits |
| Channel | long-term path loss + short-term uncorrelated flat Rayleigh fading |
| Channel Estimation at Relaying MS | Perfect |
| Channel Estimation at BS | Perfect |
| MUD at Relaying MS | MaxSINR-based SIC |
| MUD at BS | MaxSINR-based SIC |
| No. of Iterations at Relaying MS | 10 |
| No. of Inner Iterations at BS | 5 |
| No. of Outer Iterations at BS | 10 |

**Table 5.3:** Relay-assisted multiuser SDMA system parameters.

### 5.3.2 EXIT Chart Analysis and Simulation Results

For the sake of realizing a power-efficient multiuser system, we apply the design procedure proposed in Section 4.2.3.2 to our relay-assisted multiuser SDMA uplink system of Fig. 5.6. Specifically, in order to design the optimized IRCC of the served MS, EXIT

chart analysis is required at the relaying MS. Fig. 5.7 provides an example of the served MS and a single interfering MS having the same distance from the relaying MS. Following the MaxSINR-based MUD process at the relaying MS, it is clearly seen in Fig. 5.7 that a 'narrow-but-open' tunnel emerges after careful EXIT chart design using the curve matching algorithm of [61]. Since the inner 'URC-MUD' decoder's EXIT curves remain unchanged, the optimized IRCC observed in Fig. 5.7 is our final scheme, whose weighting coefficients $\alpha_i$ are summarized in Table 5.3. Considering the geometrical gains facilitated by the commensurately reduced distance and path loss of the MR link, it is safe to say that there exists a relaying MS in the inactive MS pool, which will maintain an open EXIT tunnel, as exemplified in Fig. 5.7, as long as it is sufficiently close to the served MS, even in the scenario of many interfering MSs. Therefore, in our forthcoming analysis we will not focus on the detailed iterative detection process at the relaying MS and assume that sufficiently reliable information can always be recovered at the relay.

Furthermore, following the design procedure of Section 4.2.3.2, Figs. 5.8-5.12 portray the EXIT charts recorded at the base station for zero, one, two, three and four interfering-MS scenarios, respectively, where we summarize the optimized relaying mobile station's IRCC weighting coefficients $\beta_j$ in Table 5.3. The minimum required equivalent $\text{SNR}_e$[2] at both the served and relaying MSs are obtained as shown in Figs. 5.8-5.12, when the required 'narrow-but-open' EXIT tunnels emerge. The Monte-Carlo simulation-based decoding trajectories are computed for a frame length of 250 000 bits, while all other system parameters are summarized in Table 5.3.

Following our EXIT chart analysis, in Fig. 5.13 we characterize the BER performance of the relay-assisted multiuser SDMA uplink system of Fig. 5.6. For the sake of generating a reliable estimate of the served MS's information at the relaying MS after several iterations, in the presence of multiple interfering MSs the served MS always attempts to link up with the closest relaying MS in the inactive MS pool, which will result in an open EXIT tunnel, as exemplified in Fig. 5.7. It can be clearly observed in Fig. 5.13 that the BER performances closely match the EXIT chart based performance predictions of Figs. 5.8-5.12. Naturally, relay-assisted systems will benefit from extra spatial diversity and from reduced-pathloss based geometrical gains. As seen in Fig. 5.13, the relay-assisted multiuser SDMA systems outperform their non-relay-aided counterparts of Fig. 5.3 by approximately 5.7 dB, 6.4 dB, 7.3 dB, 8.7 dB and 12.4 dB in terms of the required SNR for the $L = 1$ to $L = 5$ scenarios, respectively, which correspond to 3 dB lower values in terms of $E_b/N_0$, when considering the associated factor two throughput reduction.

[2] Similarly to that of Chapter 4, the equivalent $\text{SNR}_e$ defines the ratio of the signal power at the transmitter side with respect to the noise level at the receiver side.

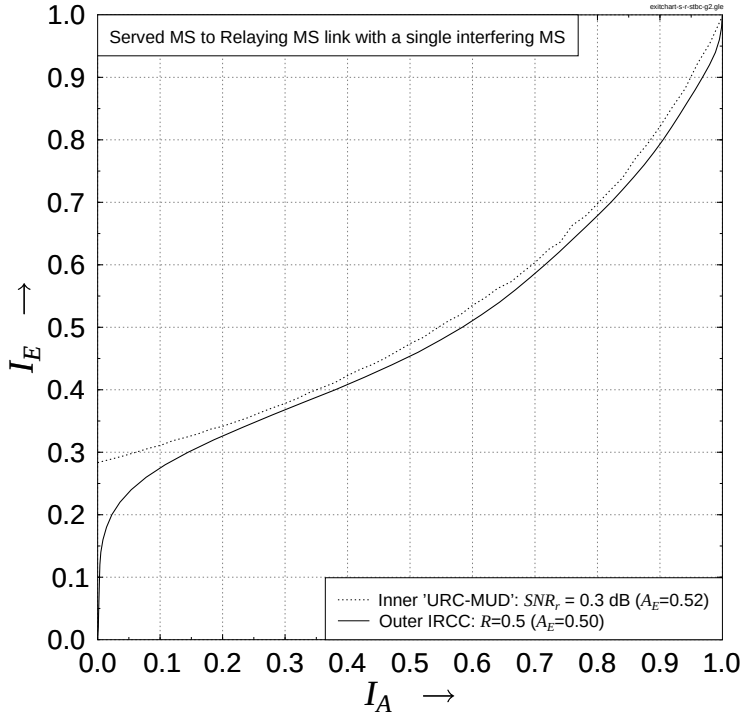


**Figure 5.7:** The EXIT chart for the served MS to relaying MS link of Fig. 5.6 with a single interfering user, where the MaxSINR-based multiuser detection algorithm is employed at the relaying MS. The $\text{SNR}_r$ represents the received SNR at the relaying MS. The system parameters are summarized in Table 5.3.

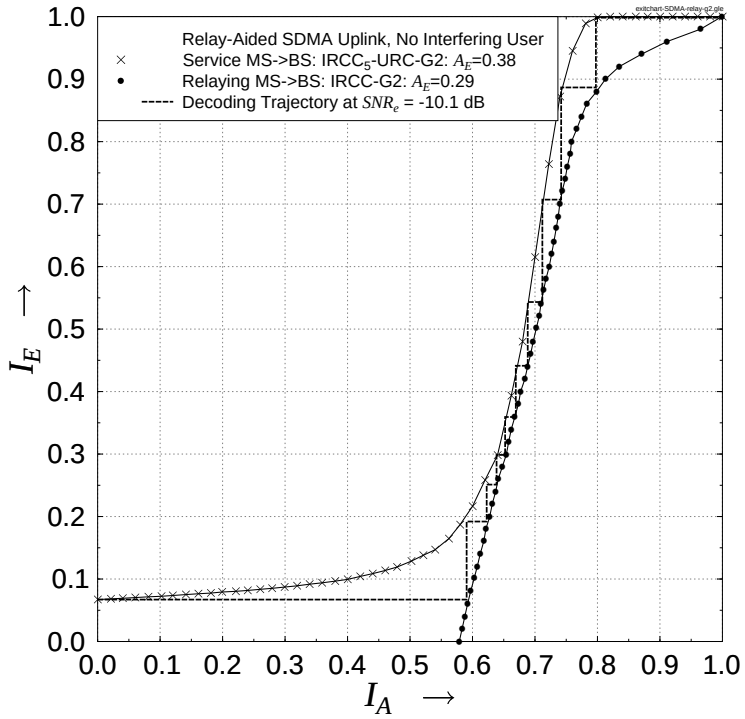


**Figure 5.8:** The EXIT chart for the relay-aided SDMA uplink system of Fig. 5.6 when no interfering user exists. The $\text{SNR}_e$ represents the equivalent SNR at both the service and relaying mobile stations. The MS transmitter structure is shown in Fig. 5.3.1 and the system parameters are summarized in Table 5.3.

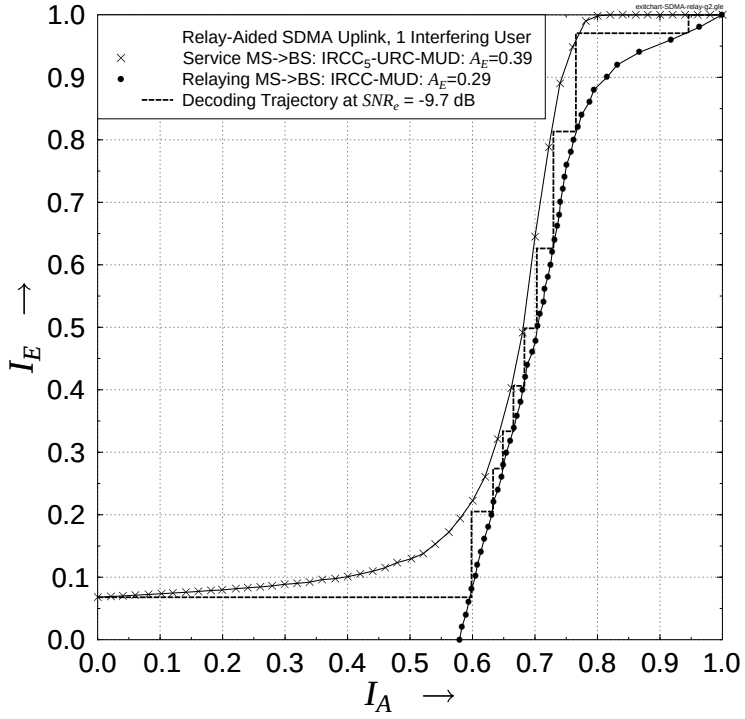


**Figure 5.9:** The EXIT chart for the relay-aided SDMA uplink system of Fig. 5.6 for one interfering user. The $\text{SNR}_e$ represents the equivalent SNR at both the service and relaying mobile stations. The MS transmitter structure is shown in Fig. 5.3.1 and the system parameters are summarized in Table 5.3.

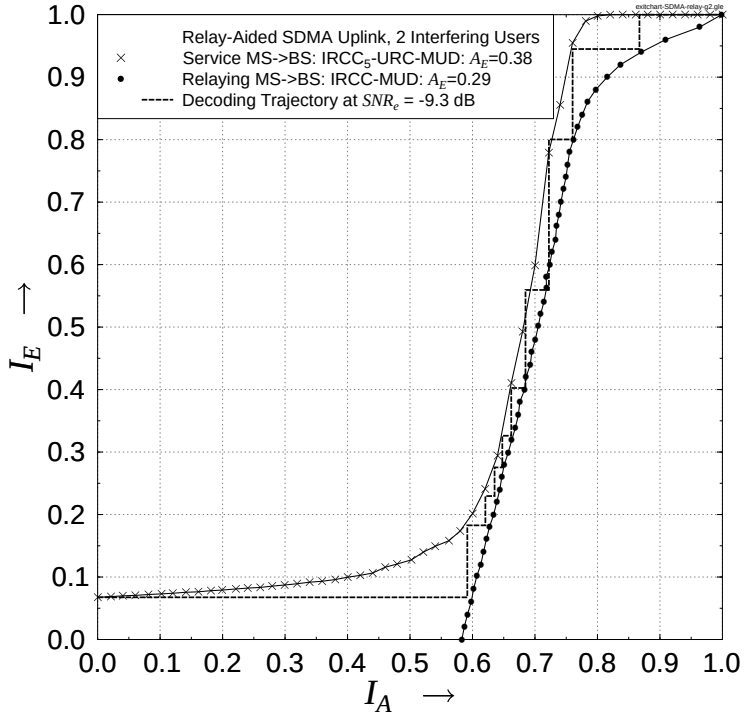


**Figure 5.10:** The EXIT chart for the relay-aided SDMA uplink system of Fig. 5.6 for two interfering users. The $\text{SNR}_e$ represents the equivalent SNR at both the service and relaying mobile stations. The MS transmitter structure is shown in Fig. 5.3.1 and the system parameters are summarized in Table 5.3.

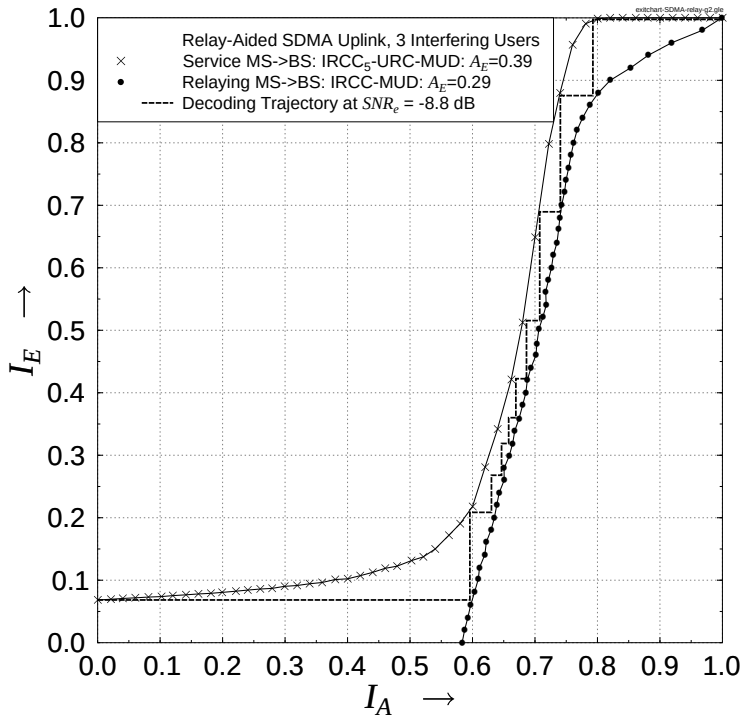


**Figure 5.11:** The EXIT chart for the relay-aided SDMA uplink system of Fig. 5.6 for three interfering users. The $\text{SNR}_e$ represents the equivalent SNR at both the service and relaying mobile stations. The MS transmitter structure is shown in Fig. 5.3.1 and the system parameters are summarized in Table 5.3.

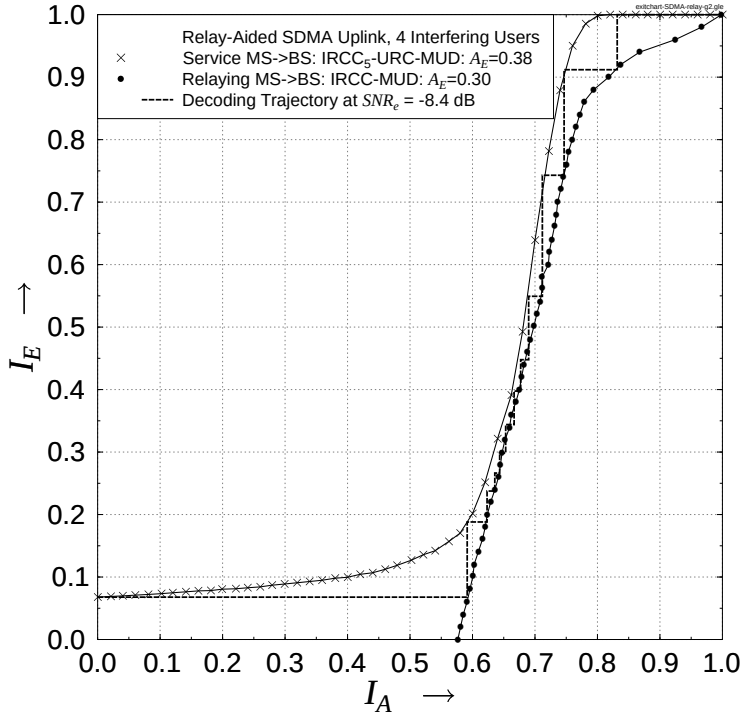


**Figure 5.12:** The EXIT chart for the relay-aided SDMA uplink system of Fig. 5.6 for four interfering users. The $\text{SNR}_e$ represents the equivalent SNR at both the service and relaying mobile stations. The MS transmitter structure is shown in Fig. 5.3.1 and the system parameters are summarized in Table 5.3.

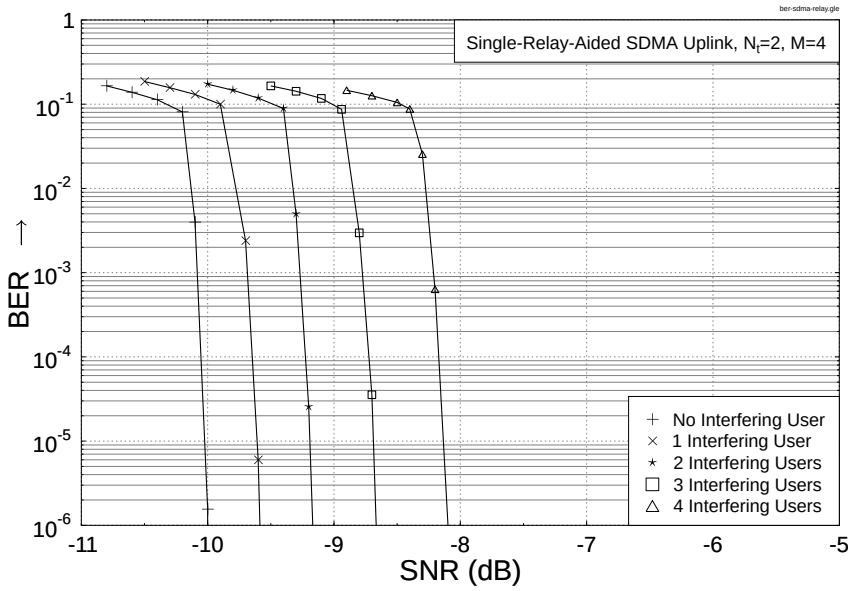


**Figure 5.13:** Average BER versus $\mathrm{SNR}_e$ performance comparison of the single-relay-aided multiuser SDMA uplink system of Fig. 5.6, where the system parameters are summarized in Table 5.3.

## 5.4 Effects of Spatially Correlated MIMO Channels

As specified in Section 5.1, the basic constraint for our multiple-antenna-user SDMA uplink transmission is that the mobile station's antenna spacing is limited due to the limited physical size of MSs. In a realistic radio environment, the low antenna spacing will impose correlation on the MIMO channels [162–170], which is typically regarded as a detrimental factor, since it results in a reduced degree of freedom [162, 163]. In this section, we will briefly investigate the impact of the MIMO channel's spatial correlation on the attainable performance of our multiuser SDMA uplink system.

In this section, we still consider a $L$-user SDMA uplink system communicating over a flat multiple access channel associated with $M$ antennas at the base station and $N_t$ antennas at each MS. Hence, we can rewrite Eq. (5.2) as follows

$$\mathbf{y}_k = \sum_{l=1}^{L} \overline{\mathbf{H}}_l \mathbf{c}_k^l + \mathbf{n}_k, \tag{5.28}$$

where $\overline{\mathbf{H}}_l$ indicates the spatially correlated MIMO channel matrix of the link between $\mathrm{MS}_l$ and the BS. For simplicity, we assume that $\{\overline{\mathbf{H}}_l\}_{l=1}^{L}$ are uncorrelated with each other for the different mobile stations.

Following the common Kronecker correlation model of [163, 164], $\overline{\mathbf{H}}_l$ can be written as

$$\overline{\mathbf{H}}_l = \mathbf{R}_{BS}^{\frac{1}{2}} \mathbf{H}_l \mathbf{R}_{MS}^{\frac{1}{2}}, \tag{5.29}$$

where $\mathbf{H}_l$ is a Rayleigh fading matrix, whose entries are independent and identically dis-

tributed (i.i.d.) complex Gaussian variables with zero mean and unit variance. Furthermore, $(.)^{\frac{1}{2}}$ denotes the matrix square root and can be derived with the aid of eigenvalue decomposition. Furthermore, $\mathbf{R}_{BS} \in \mathbb{C}^{M \times M}$ and $\mathbf{R}_{MS} \in \mathbb{C}^{N_t \times N_t}$ in Eq. (5.29) are semi-definite positive matrices that characterize the spatial correlation effects imposed on the antennas at the receiver and the transmitter, respectively, for the uplink between $\text{MS}_l$ and the BS. For normalization purposes, $\text{tr}(\mathbf{R}_{BS}) = M$ and $\text{tr}(\mathbf{R}_{MS}) = N_t$ are assumed throughout this chapter. More specifically, according to [171, 172], the transmit correlation matrix of $\mathbf{R}_{MS}$ is given as

$$\mathbf{R}_{MS} = \begin{bmatrix} 1 & \beta_{MS} \\ \beta_{MS}^* & 1 \end{bmatrix}, \tag{5.30}$$

where $(.)^*$ denotes the complex conjugate operation. Specifically, $\beta_{MS} = 0$ indicates the presence of no correlation at the MS, while $\beta_{MS} = 1$ represents full correlation at the MS. On the other hand, it is commonly assumed that the antenna elements at the base station are spaced far enough, hence the correlation matrix of $\mathbf{R}_{BS}$ is of full rank and can be represented by the identity matrix.

### 5.4.1 Performance Evaluation

Based on the spatially correlated channel model of Eq. (5.29), Fig. 5.14 portrays the performance of the multiuser SDMA uplink system of Fig. 5.1 in conjunction with transmit antenna correlation in terms of the associated average BER. The MaxSINR-based SIC multiuser detection algorithm is employed at the base station, while all other system parameters are listed in Table 5.1. The correlation coefficient of $\beta_{MS}$ at the MS is set to be as high as 0.9 [172], while the correlation at the BS is zero. For comparison, we also plot the BER curves of the systems associated with $\beta_{MS} = 0$ in Fig. 5.14. It is clearly seen in Fig. 5.14 that for the single-user scenario, the system associated with correlated transmit antennas performs worse than its uncorrelated counterpart. Specifically, at a certain BER of $10^{-4}$, a 1.6 dB SNR loss is encountered by the system in conjunction with correlated transmitters owing to the partial loss of transmit diversity gains. Furthermore, for the $L = 2$ uplink system, a similar performance degradation is observed in the system associated with transmitter correlation, although the loss is reduced. However, when supporting $L = 3$ users or more in the SDMA system, the systems subjected to transmitter correlation outperform their uncorrelated counterparts. Particularly in the $L = 3$ user SDMA system, the error floor of the uncorrelation system is reduced to a BER of $5 \times 10^{-4}$. To elaborate a little further, Fig. 5.15 characterizes the relationship between the average BER and the antenna correlation coefficients $\beta_{MS}$ for the multiuser SDMA systems considered at SNR = 11 dB. It is clearly observed from Fig. 5.15 that for the single-user scenario,

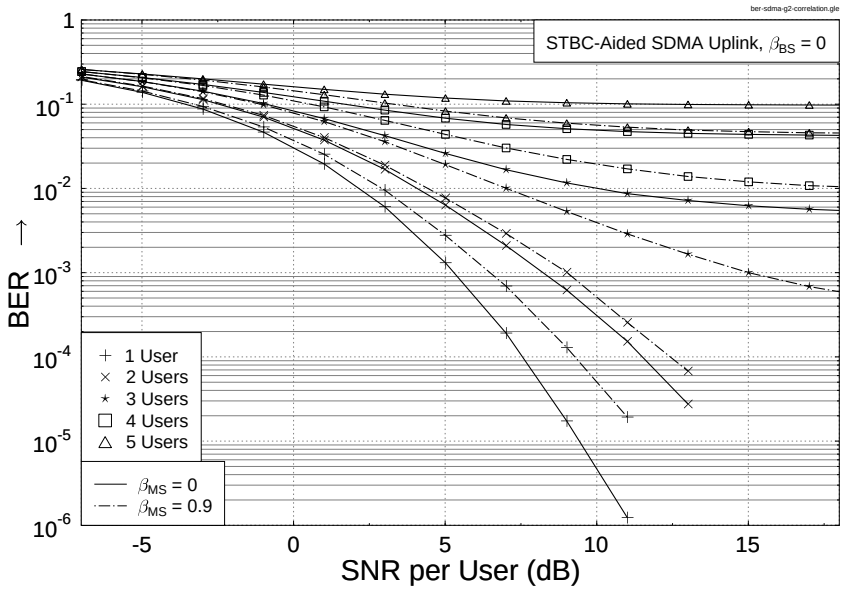


**Figure 5.14:** Average BER versus SNR performance comparison of the multiuser SDMA uplink system of Fig. 5.1 in conjunction with transmit antenna correlation. The system parameters are summarized in Table 5.1.

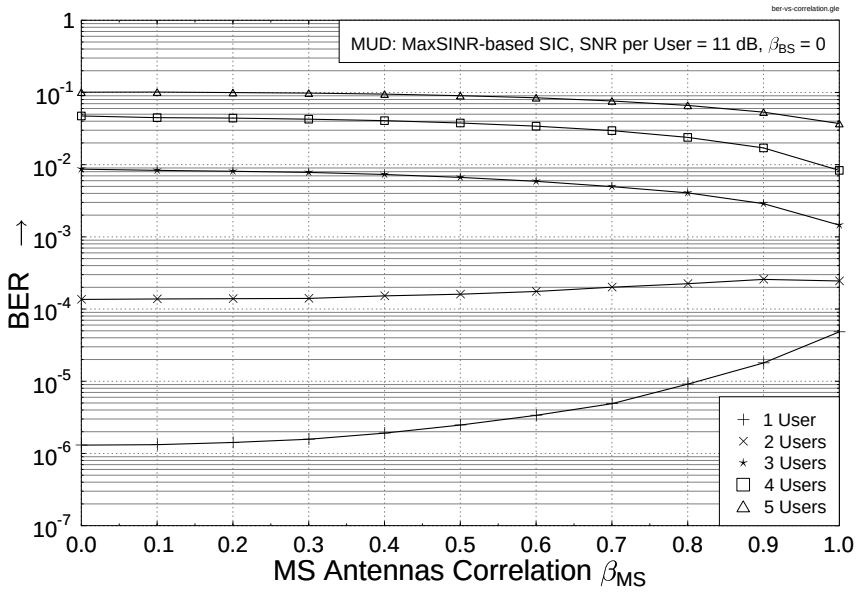


**Figure 5.15:** Average BER as a function of transmit antenna correlation for the multiuser SDMA uplink system of Fig. 5.1. The system parameters are summarized in Table 5.1.

the BER increases with the spatial correlation. For the $L = 2$ user system, the BER initially increases with the correlation and then decreases for high-correlation scenarios. For systems involving more than $L = 2$ users, the BER decreases with the correlation. This observation is due to the fact that in the multiuser system, the transmit diversity loss imposed by correlation for every single user is compensated by the gains achieved by the MUD, since the multiple MSs associated with higher correlations may be more readily separated at the BS. Similar arguments can be found in [173], which indicates that antenna

correlation can be potentially beneficial in a multiuser environment.

## 5.5 Chapter Conclusion

In this chapter, we first investigated a multiple-antenna aided MU SDMA uplink system in Section 5.2, where each MS is equipped with two antennas and employs Alamouti's G2 scheme for the sake of providing transmit diversity. In Section 5.2.2, a maximum-SINR-based SIC MUD was proposed for the multiple-antenna aided MU SDMA uplink system, which is capable of balancing the interference suppression and noise enhancement. More specifically, in contrast to the ZF-based SIC detection, the MaxSINR-based SIC MUD is applicable for rank-deficient systems. Furthermore, we designed an IRCC- and URC-coded multiuser SDMA uplink system in Section 5.2.3 for the sake of improving the system's performance. The IRCC's weighting coefficients were optimally designed with the aid of EXIT charts for the sake of realizing a power-efficient SDMA system, while the URC helped to eliminate the error floors encountered in the rank-deficient uncoded multiuser systems. On the other hand, in Section 5.3 we incorporated relaying techniques in the channel-coded SDMA systems. The system design procedures of Chapter 4 conceived for single-user Ir-CSTC schemes were extended to suit our multiuser systems. In contrast to the single-user scenario, interference suppression was performed at both the BS and the relaying MS in the multiuser scenario. Finally, in Section 5.4 we investigated the effects of spatial correlation at the MS transmitters on the average system BER performance in the context of multiuser scenarios. In conclusion, we summarize all the relevant simulation results of this chapter in Table 5.4.

| System Configuration | Average SNR required at BER of $10^{-4}$ | | | | | System Throughput (b/s/Hz) |
|---|---|---|---|---|---|---|
| | Single-user | 2-user | 3-user | 4-user | 5-user | |
| Uncoded SDMA uplink of Fig. 5.1, Natural Ordering | 7.5 dB | 11.5 dB | error floor of $5 \times 10^{-3}$ | error floor of $4 \times 10^{-2}$ | error floor of $1 \times 10^{-1}$ | $2.0 \times L$ |
| Uncoded SDMA uplink of Fig. 5.1, Optimal Ordering | 7.5 dB | 9.2 dB | error floor of $1 \times 10^{-4}$ | error floor of $1.2 \times 10^{-2}$ | error floor of $5 \times 10^{-2}$ | |
| Uncoded SDMA uplink of Fig. 5.1, $\beta_{MS} = 0.9$ | 9.1 dB | 12.2 dB | error floor of $5 \times 10^{-4}$ | error floor of $1 \times 10^{-2}$ | error floor of $4.5 \times 10^{-2}$ | |
| Channel-coded SDMA uplink of Fig. 5.3 | -4.5 dB | -3.4 dB | -2 dB | 0 dB | 4.2 dB | $1.0 \times L$ |
| Relay-assisted SDMA uplink of Fig. 5.6 | -10.1 dB | -9.7 dB | -9.2 dB | -8.7 dB | -8.3 dB | $0.5 \times L$ |

**Table 5.4:** Performance summary of the multiple-antenna aided MU SDMA uplink systems, where $L$ denotes the number of SDMA users.

Chapter 6

# Conclusions and Future Work

In this final chapter, we will summarise the key contributions of each chapter in Section 6.1. Then some design guidelines for near-capacity communications will be presented in Section 6.2. Our suggestions for future research will be outlined in Section 6.3.

## 6.1 Chapter Summaries

### 6.1.1 Chapter 1

Chapter 1 constitutes the background of our research throughout the thesis. Specifically, a rudimentary overview of colocated and distributed MIMO techniques, iterative detection and near-capacity communications was provided in Sections 1.1-1.3. Furthermore, the outline of the thesis was presented in Section 1.4 and we described our novel contributions in Section 1.5.

### 6.1.2 Chapter 2

In Chapter 2, a combination of V-BLAST and STCs designed for MIMO systems was investigated, which we referred to as Generalized Multi-Layer Space-Time Coding. Two fundamental schemes were designed, namely the GMLST(STBC) and GMLST(STTC) arrangements of Figs. 2.1 and 2.2, where STBCs and STTCs were used as the component space-time codes, respectively. According to the different mapping of the signals to the antennas, the GMLST(STTC) regime was further divided into the H-GMLST(STTC) and D-GMLST(STTC) arrangements. On the other hand, for the GMLST(STBC) scheme of Fig. 2.2, only horizontal mapping was considered, since no additional spatial diversity can be obtained, when employing diagonal mapping. The basic detection procedure de-

vised for the GMLST schemes is constituted by the ordered successive detection scheme combining group-based interference nulling and interference cancellation, as portrayed in Fig. 2.3. Furthermore, in Section 2.4 we introduced Tarokh's power allocation regime conceived for detection using an arbitrary order, which outperformed the conventional schemes relying on equal-power allocation at the same computational complexity. For the H-GMLST systems of Figs. 2.1(b) and 2.2, which relied on equal-power allocation, in Section 2.5 we also discussed the optimal detection order based on the assumption that the channel coefficients are perfectly known at the receiver. Finally, in Section 2.6 an iterative SIC-based detection scheme was advocated for both the GMLST(STTC) and GMLST(STBC) arrangements, in order to exploit the potential of full receive antenna diversity. The simulation results of Figs. 2.10 and 2.11 show that the iterative detection scheme is capable of approaching the same receive diversity order as ML-style joint detection, while imposing only a fraction of the computational complexity of ML-style joint detection. Table 2.2 summarizes the performance versus complexity of various GMLST schemes, where the SNR loss is caused by the SIC-induced error propagation among the different layers of the GMLST scheme. In conclusion, the iterative SIC-based GMLST scheme of Fig. 2.9 provides a promising practical solution for high-data-rate, high-integrity communications in MIMO systems, especially when the number of antennas is high.

### 6.1.3 Chapter 3

Chapter 3 demonstrated that as expected, further performance improvements may be attained by the concatenation of the GMLST schemes with channel codes and upon performing iterative detection by exchanging extrinsic information between the different component decoders/demodulators at the receiver side. Specifically, the proposed serially concatenated IRCC-URC-GMLST system of Fig. 3.10 exploits the advantages of both iterative detection as well as those of the GMLST schemes using STBC and STTC as the component space-time codes. In Section 3.2.1.1, an APP-based iterative multistage SIC detection algorithm has been invoked for the GMLST schemes instead of the previous Viterbi-decoding-aided SIC detection for the sake of supporting the iterative detection process at the receiver side. Furthermore, in Section 3.2.1.2 we presented a significantly more complex iterative ML detection scheme designed for the GMLST(STTC) regime of Fig. 2.1 in the context of serially concatenated systems for comparison, which invokes a concept similar to that of classic BICM-ID schemes. On the other hand, the benefit of URC precoders was characterized in Section 3.3.3.1, which was used as an intermediate code and assisted us in eliminating the system's error-floor, hence improving the attainable decoding convergence. Moreover, our investigations demonstrated in Section 3.3.3

that the proposed low-complexity SIC-based iteratively decoded IRCC-URC-GMLST scheme of Fig. 3.10 is capable of achieving a near-capacity performance, when designed with the aid of EXIT chart analysis. Table 3.3 presents the achievable coding gains, the SNR-distance from the maximum achievable rate limit as well as that from the DCMC capacity limit for the various near-capacity iteratively-decoded IRCC-URC-GMLST systems. Based on these simulation results, we found that the iterative IRCC-URC-GMLST scheme of Fig. 3.10 using SIC detection strikes an attractive trade-off between the complexity imposed and the effective throughput achieved. It is demonstrated further that the design procedure is generically applicable, regardless of the specific choice of the inner and outer decoder components, as exemplified by other detectors, such as Sphere Detectors, MCMC detectors as well as by different outer channel codes, such as an irregular LDPC codes, etc.

### 6.1.4 Chapter 4

Following the investigation of near-capacity communication schemes using colocated MIMO elements in Chapter 3, Chapter 4 proposed relay-aided schemes for the sake of near-capacity communications in distributed MIMO systems. Specifically, in Section 4.2 an Ir-CSTC scheme was designed for near-capacity communications in the conventional single-relay-aided network seen in Figs. 4.2 and 4.3. The encoding and decoding processes of Figs. 4.2 and 4.3 designed for our Ir-CSTC scheme were specified in Section 4.2.2, where we employed a serially concatenated three-component IRCC-URC-STBC scheme at the source and a two-component IRCC-STBC at the relay. In Section 4.2.3.1, we derived the CCMC capacity and the constrained information-rate bounds of Alamouti's G2 scheme for the half-duplex single-relay channel of Fig. 4.5. A joint source-and-relay mode design procedure designed with the aid of EXIT charts analysis was proposed in Section 4.2.3.2 for the sake of finding the optimal Ir-CSTC scheme, which performs closest to the single-relay channel's capacity as well as achieves the maximum effective throughput, which is an extra benefit of the joint mode design procedure. The numerical results seen in Fig. 4.9 of Section 4.2.4 demonstrated that the joint source-and-relay mode design based on EXIT chart analysis is capable of near-capacity cooperative communications in the single-relay-aided network. Furthermore, in Section 4.3 an extended Ir-CSTC scheme was studied in the context of the twin-relay aided network of Fig. 4.10, in which the successive relaying protocol was employed. The factor two multiplexing loss of the single-relay-aided network was recovered by the successive relaying protocol, although this was achieved at the cost of an additional relay. Similarly, the CCMC capacity and the constrained information-rate bounds of Alamouti's STBC scheme were derived for the successive relaying aided schemes of Figs. 4.11 and 4.12

in Section 4.3.4.1. It was observed in Figs. 4.14 and 4.15 that the factor two multiplexing loss of the single-relay-aided network may be recovered by the successive relaying protocol with the aid of an additional relay, which is a more practical technique than the assumption of a full-duplex system. The generalized joint source-and-relay mode design procedure advocated relies on the proposed procedure of finding the optimal cooperative coding scheme, which performs close to the capacity limit, in the context of twin-relay-aided network, as demonstrated by the BER performance results of Fig. 4.18 discussed in Section 4.3.5. It is further demonstrated that the Ir-CSTC schemes proposed in Chapter 4 are insensitive to the network's geometry. In other words, as long as the number of antennas as well as the space-time coding schemes used at the source and relays are fixed, the irregular components employed at the source and relays also remain unchanged, regardless of the network topology considered. The topology only affects the transmit power thresholds to be used at the source and relays, when the EXIT tunnels are open, as shown in Figs. 4.6-4.8 and 4.16-4.17. However, if the number of antennas, or the space-time coding schemes used at the source and relays are changed, we have to redesign the irregular components both at the source and relays. More specifically, the joint source-and-relay mode design procedures advocated in Sections 4.2.3.2 and 4.3.4.2 operate off-line in order to find the optimal distributed code components. In other words, they do not have to operate on-line in order to adapt the parameters according to the instantaneous channel conditions. Once the irregular components at the source and relays were determined, they remain fixed during the transmit and receive periods. However, the knowledge of the channel state information is required during the off-line search procedure, which was assumed to be perfectly known at both the relay and destination in Chapter 4. Furthermore, the code design procedure is not limited to a specific networking scenario, but applicable under virtually any network configuration. Most importantly, it is in fact generically applicable, regardless of the specific choice of the space-time codes at the source and relays as well as of the irregular components, provided that the inherent irregularity of the designs used at the source and relays is retained.

### 6.1.5 Chapter 5

In contrast to the noise-limited single-user scenario of Chapter 4, Chapter 5 investigated the Ir-CSTC schemes in the context of our interference-limited multiuser SDMA scenario, where the multiple access interference (MAI) significantly degrades the overall system performance. Specifically, in Section 5.2.2 a MaxSINR-based SIC multiuser detector was proposed for the multiple-antenna-user aided SDMA uplink system, which is capable of striking a trade-off between the interference suppression capability and noise enhancement, as shown in Fig. 5.2, while supporting rank-deficient systems. Furthermore, in Sec-

tion 5.2.3 the multiuser SDMA system was combined with channel codes, which assisted us in eliminating the typical BER floors of rank-deficient systems, as depicted in Fig. 5.5. Referring to the Ir-CSTC scheme for the single-user scenario of Chapter 4, in Section 5.3 relay aided techniques were incorporated in channel-coded SDMA systems, which benefit from extra spatial diversity and reduced-pathloss based geometrical gains. In contrast to the single-user Ir-CSTC schemes, interference suppression was required at both the base station and the relaying mobile station. Finally, a more practical scenario where the MSs have spatially correlated transmit antennas was studied in Section 5.4. In contrast to the conventional views, the simulation results of Figs. 5.14 and 5.15 demonstrated that the transmitter's spatial correlation is potentially beneficial in multiuser SDMA uplink systems, when employing efficient MUDs.

## 6.2 Design Guidelines

In this section, we summarize the general design guidelines of near-capacity transceivers in the context of both colocated and distributed MIMO systems by examining the various schemes investigated throughout Chapter 2 to Chapter 5.

1. Near-capacity operation is of particular interest in digital multimedia broadcast applications. In conventional colocated MIMO systems, following the advent of turbo codes near-capacity communications may be facilitated by concatenating simple constituent codes and employing efficient iterative decoding. EXIT charts constitute convenient tools, which may be used to analyse the iterative extrinsic information exchange process among the constituent decoders. An 'open-but-narrow' EXIT tunnel indicates that near-capacity performance may be achieved, provided that the Monte-Carlo simulation based decoding trajectory matches the EXIT curves.

2. Hence, near-capacity transceiver designs may involve several design aspects, such as the choice of the parallel versus serial concatenation structure, the appropriate selection of the constituent codes, the interleaver length, the detection algorithm, which complement the transmission scheme. The best attainable performance is determined by the DCMC capacity.

3. Firstly, the choice of the inner code of a serially concatenated scheme has to be resolved. In Chapter 2 we considered a multi-layer space-time coding scheme referred to as GMLST, which provides both multiplexing and diversity gains. Hence a high configuration flexibility spanning the entire range of options between the full-multiplexing and the full-diversity oriented systems may be attained. As a design example, a novel iterative multi-stage SIC scheme was proposed in Section 2.6,

which is capable of achieving the maximum attainable receive diversity of the potentially excessive-complexity classic ML detection, while imposing only a fraction of the ML complexity.

4. Once the choice of the inner code was resolved, we should opt for an appropriate outer channel code, which leads itself to so-called irregular designs, yielding diverse EXIT-curve shapes. In Chapter 3, a powerful IRCC was employed. Then, the area of the EXIT tunnel between the outer and inner decoders' EXIT curves may be minimized by employing a curve-matching algorithm, which indicates the possibility of near-capacity performance.

5. On the other hand, for the sake of eliminating the error floor, a recursive URC was also needed as an intermediate code in the serially concatenated scheme, as demonstrated in Section 3.3. The resultant near-capacity transceiver based on EXIT-chart-matching designs in Chapter 3 is generically applicable, regardless of the specific choice of the inner and outer decoder components, as long as the inherent irregularity of the inner or outer codes is retained. Since they are capable of reducing the area of the open EXIT-tunnel, they facilitate decoding convergence to an infinitesimally low BER at near-capacity SNRs.

6. Naturally, invoking more IRCC components is capable of providing more diverse EXIT curves, hence matching the inner codes' EXIT functions more accurately, which indicates that a 'very-near-capacity' performance is achievable, as shown in Section 3.3.3.3.

7. The above-mentioned advances may also be exploited in the context of distributed MIMO systems. More specifically, parallel concatenation of the geographically separated transceivers may be invoked as shown in Chapter 4. More specifically, a three-stage serially concatenated scheme may be employed at the source for the sake of approaching the SR link capacity, while another irregular scheme may be employed at the relay for the sake of assisting the near-capacity operation of the distributed system following the philosophy of distributed turbo codes. As a design example, in Chapter 4, an Ir-CSTC scheme was designed using the following joint source-and-relay mode design procedure:

   (a) Firstly, optimized irregular components are designed at the source using EXIT-curve-matching for the SR link.

   (b) Then, the irregular components to be used at the relay are optimized by another EXIT curve matching process at the destination, where the EXIT curve of the RD link is matched against that of the SD link.

(c) Finally, the decoding convergence threshold of the Ir-CSTC scheme is calculated. More specifically, when the EXIT tunnel area between the EXIT curves of the SD link and the RD link is minimized, a near-capacity performance may be achieved in the distributed MIMO system considered.

## 6.3 Future Work

The research presented in this thesis can be extended in several directions. In this section, a brief overview of some ideas for potential future work are presented as follows:

**Differential Multi-functional MIMO Scheme**

The multi-functional GMLST schemes presented in Chapter 2 use coherent detection, while assuming perfect channel knowledge at the receiver. In a realistic scenario, however, channel estimation is required when employing coherent detection, which will degrade the system's performance due to channel estimation errors. Additionally, the channel estimation complexity increases with the product of the number of transmit and receive antennas. Therefore, an attractive solution for eliminating the potentially high-complexity channel estimation as well as the performance degradation due to channel estimation errors is to design non-coherent receivers that do not require any channel knowledge. As a further extension of the multi-functional GMLST schemes of Chapter 2, we can design differential multi-functional MIMO schemes that do not require any channel knowledge. Naturally, it is expected that the differential scheme will have a 3 dB performance degradation when compared to the corresponding coherent scheme assuming perfect channel knowledge at the receiver. However, when channel estimation is employed, differential detection eliminates the complexity of channel estimation and we may even attain a better BER performance than that of the coherent scheme, when a practical, finite-precision channel estimation scheme is considered.

**Adaptive Multi-functional MIMO Systems**

In Chapter 2, the proposed multi-functional GMLST scheme provides flexibility in terms of multiplexing and diversity oriented system benefits. Hence, an adaptive multi-functional MIMO system is worth investigating in our future research. Specifically, the sophisticated multi-functional system will adaptively switch between the full-multiplexing oriented BLAST, partial-multiplexing, partial-diversity oriented GMLST and full-diversity STC schemes according to the quality of the channel experienced. When the channel is gravely faded, the system will automatically adapt itself to STC mode, which provides diversity gains to combat the effects of the fading channel. On the other hand, BLAST will be employed in a rather benign channel environments for the sake of maximizing

system throughput, while maintaining an acceptable BER level at the receiver side. Otherwise, we use the flexible GMLST scheme to strike an attractive trade-off between the multiplexing gain and diversity gain.

**Employing Symbol-Based URC in Near-Capacity IRCC-URC-GMLST Schemes**

In Chapter 3, a bit-based URC was invoked as the intermediate code in the three-stage serially concatenated IRCC-URC-GMLST scheme. It was observed in Fig. 3.26 that a significant amount of information/throughput loss occurs in iterative ML detected IRCC-URC-GMLST(STTC-4) schemes when converting the output symbol probabilities of the GMLST(STTC-4) decoder to LLR values used for the bit-based URC decoder. Hence, as an explicit benefit, a symbol-based URC can be used to recover the above-mentioned information loss, since no conversion from symbol probabilities to LLR values is needed between the GMLST decoder and the symbol-based URC decoder. However, the complexity of the symbol-based URC is higher than that of the bit-based URC.

**Joint Power Allocation and Relay-Position Optimization for Ir-CSTC Schemes**

In Chapter 4, an irregular cooperative space-time coding scheme was proposed for the sake of achieving the corresponding relay channel's single-link DCMC capacity. However, from a perspective of maximizing the multiuser network's capacity, the network's configuration used in Chapter 4 is not optimal. As seen from Eq. (4.25) of Chapter 4, the three-terminal network's capacity is dependent on the equivalent SNRs (transmit powers) at the source and relay nodes as well as the distance (power gain) between the relay and destination nodes. On the other hand, in [174] a closed-form approximation of the MIMO capacity was proposed, which is capable of approximately calculating the corresponding MIMO channel's DCMC capacity without invoking time-consuming Monte-Carlo simulations. Hence, we can employ a joint power allocation and relay location optimization scheme to maximize the three-terminal network's DCMC capacity, which is still approachable by our proposed Ir-CSTC scheme. Hence, the joint power allocation and relay-position optimization algorithm can be further simplified to a convex optimization problem as follows.

Assuming that the source and relay nodes have the same coding rate of 0.5, the three-terminal network's capacity of Eq. (4.25) can be rewritten as:

$$C_{\text{DCMC}}^{\text{coop-g2}}(P_t^s, P_t^r, G_{rd}) = \min\left\{1.0, \frac{1}{2}C_{\text{DCMC}}^{\text{s}\to\text{d}}(P_t^s) + \frac{1}{2}C_{\text{DCMC}}^{\text{r}\to\text{d}}(P_t^r, G_{rd})\right\}. \tag{6.1}$$

Our objective is to maximize $\frac{1}{2}C_{\text{DCMC}}^{\text{s}\to\text{d}}(P_t^s) + \frac{1}{2}C_{\text{DCMC}}^{\text{r}\to\text{d}}(P_t^r, G_{rd})$, which is subject to the

conditions of

$$\begin{cases} 0 \leqslant P_t^s \leqslant 1, \\ P_t^s + P_t^r = 1, \\ P_t^s + 10\log_{10}(G_{sr}) \geqslant P_{r,min}^r, \\ G_{sr} + G_{rd} + 2\sqrt{G_{sr}G_{rd}} \geq G_{sr}G_{rd}, \end{cases} \tag{6.2}$$

where $P_t^s$ and $P_t^r$ are the transmit powers at the source and relay nodes, respectively, while $P_{r,min}^r$ is the minimum receive power required at the relay node to maintain an open EXIT tunnel as in Fig. 4.6.

**Channel Estimation in Multiuser SDMA Uplink Systems**

In Chapter 5, we have considered multiuser SDMA systems assuming perfectly accurate channel knowledge at the base station. However, it is well known that SDMA systems are sensitive to channel estimation errors, which will significantly degrade the overall system performance. Therefore, it is worth exploring efficient channel estimation techniques for the sake of minimizing the performance loss due to inaccurate channel knowledge in a realistic SDMA uplink scenario.

Appendix A

# Mathematical Preliminaries

## A.1 The Nulling Matrix

For the sake of nulling the effects of interference imposed by the interfering groups in Eq. (2.5), the following condition must be satisfied in Section 2.3:

$$\mathbf{W}_k^j \cdot [\mathbf{H}_{(j+1)',k}, \ldots, \mathbf{H}_{q',k}] = \mathbf{0}, \tag{A.1}$$

which can be reformulated using the matrix transpose notation as:

$$[\mathbf{H}_{(j+1)',k}, \ldots, \mathbf{H}_{q',k}]^T \cdot [\mathbf{W}_k^j]^T = \mathbf{0}. \tag{A.2}$$

Since the null space of a matrix $\mathbf{A}$ is the set of all vectors $\mathbf{v}$, which solves the equation $\mathbf{Av} = \mathbf{0}$, where $\mathbf{v}$ is also referred to as the kernel of $\mathbf{A}$, in set-construction notation we have:

$$\text{Null}(\mathbf{A}) = \{\mathbf{v} \in \mathbf{V} : \mathbf{Av} = \mathbf{0}\}.$$

Hence, we can mathematically deduce the nulling matrix $\mathbf{W}_k^j$ in Eq. (A.1) from the null space of $[\mathbf{H}_{(j+1)',k}, \ldots, \mathbf{H}_{q',k}]^T$. For the sake of maximizing the receive diversity order, we choose a nulling matrix $\mathbf{W}_k^j$ having the largest rank, which is equal to the dimension of the null space. There are several computational approaches for determining the null space of $\mathbf{A}$ and the choice of the specific method used depends on both the structure and size of $\mathbf{A}$. A popular approach which can be used, even when $\mathbf{A}$ is large, is to invoke the singular value decomposition (SVD) of $\mathbf{A}$ and use the resultant right-hand-side singular vectors corresponding to the singular values of zero as a basis for the null space. Below we generate the nulling matrix $\mathbf{W}_k^j$ in details as follows:

As $[\mathbf{H}_{(j+1)',k}, \ldots, \mathbf{H}_{q',k}]^T$ is an $[(N_t - N_t^{1'} \cdots - N_t^{j'}) \times N_r]$-element matrix, its SVD

is given by:

$$[\mathbf{H}_{(j+1)',k}, \ldots, \mathbf{H}_{q',k}]^T = \mathbf{U} \begin{bmatrix} \Sigma_{r\times r} & \mathbf{0} \\ \mathbf{0} & \mathbf{0} \end{bmatrix} \mathbf{V}^H, \tag{A.3}$$

where we have $\mathbf{U} \in \mathbb{C}^{(N_t - N_t^{1'} \cdots - N_t^{j'}) \times (N_t - N_t^{1'} \cdots - N_t^{j'})}$, $\mathbf{V} \in \mathbb{C}^{N_r \times N_r}$ and $\Sigma_{r\times r}$ is a diagonal matrix having singular values on the diagonal and $r = \text{rank}([\mathbf{H}_{(j+1)',k}, \ldots, \mathbf{H}_{q',k}]^T)$. Since the subchannels are uncorrelated and random, the matrix $[\mathbf{H}_{(j+1)',k}, \ldots, \mathbf{H}_{q',k}]^T$ is of full rank and $r = N_t - N_t^{1'} \cdots - N_t^{j'} < N_r$. As a result, the matrix $\begin{bmatrix} \Sigma_{r\times r} & \mathbf{0} \\ \mathbf{0} & \mathbf{0} \end{bmatrix}$ can be reformulated as $\begin{bmatrix} \Sigma_{r\times r} & \mathbf{0}_{r\times(N_r-r)} \end{bmatrix}$. Upon substituting Eq. (A.3) into Eq. (A.2), we have

$$\mathbf{U} \begin{bmatrix} \Sigma_{r\times r} & \mathbf{0}_{r\times(N_r-r)} \end{bmatrix} \mathbf{V}^H [\mathbf{W}_k^j]^T = \mathbf{0} \tag{A.4}$$

if and only if

$$\begin{bmatrix} \Sigma_{r\times r} & \mathbf{0}_{r\times(N_r-r)} \end{bmatrix} \mathbf{V}^H [\mathbf{W}_k^j]^T = \mathbf{0}. \tag{A.5}$$

When choosing $\mathbf{V}^H [\mathbf{W}_k^j]^T = \begin{bmatrix} \mathbf{0}_{r\times(N_r-r)} \\ \mathbf{I}_{(N_r-r)\times(N_r-r)} \end{bmatrix}$, the nulling matrix $\mathbf{W}_k^j$ is obtained as

$$\begin{aligned} \mathbf{W}_k^j &= \left\{ \mathbf{V} \begin{bmatrix} \mathbf{0}_{r\times(N_r-r)} \\ \mathbf{I}_{(N_r-r)\times(N_r-r)} \end{bmatrix} \right\}^T \\ &= \left\{ \begin{bmatrix} \tilde{\mathbf{V}}_{N_r\times r} \bar{\mathbf{V}}_{N_r\times(N_r-r)} \end{bmatrix} \begin{bmatrix} \mathbf{0}_{r\times(N_r-r)} \\ \mathbf{I}_{(N_r-r)\times(N_r-r)} \end{bmatrix} \right\}^T \\ &= \bar{\mathbf{V}}_{N_r\times(N_r-r)}^T. \end{aligned} \tag{A.6}$$

## A.2 Maximum SINR Array Processor

For the sake of deriving the maximum SINR array processor, we have to find the solution of the following generalized eigenvalue equation in Section 5.2.2:

$$\mathbf{R}_s \mathbf{w} = \lambda \mathbf{R}_n \mathbf{w}. \tag{A.7}$$

To be consistent with the assumption of uncorrelated interference components, as stated in Section 5.2.2, we can decompose the covariance matrix $\mathbf{R}_n$ of the interference by Cholesky decomposition [160] as

$$\mathbf{R}_n = \mathbf{L}\mathbf{L}^H, \tag{A.8}$$

since $\mathbf{R}_n$ is Hermitian and positive definite, where $\mathbf{L}$ is a lower triangular matrix having strictly positive diagonal entries. When both sides of Eq. (A.7) are left-multiplied by $\mathbf{L}^{-1}$,

we obtain

$$\mathbf{C}\left(\mathbf{L}^H\mathbf{w}\right) = \lambda\left(\mathbf{L}^H\mathbf{w}\right), \tag{A.9}$$

where

$$\mathbf{C} = \mathbf{L}^{-1}\mathbf{R}_s\left(\mathbf{L}^{-1}\right)^H \tag{A.10}$$

is the Hermitian and nonnegative definite with the same rank $k$ as that of $\mathbf{R}_s$. According to Eq. (5.12), $k$ cannot be larger than the rank of $\mathbf{H}_1$, so we have $k \leq \min(M, N_t)$. Obviously, the eigenvalues of $\mathbf{C}$ are the same as those of the original generalized eigenvalue equation of (A.7). There are $k$ nonzero eigenvalues, and a set of orthogonal eigenvectors $\left\{\mathbf{L}^H\mathbf{w}_i\right\}_{i=1}^{k}$ can be found by using the SVD on $\mathbf{C}$.

As $\mathbf{C} = \mathbf{L}^{-1}\mathbf{R}_s\left(\mathbf{L}^{-1}\right)^H$ is an $[M \times M]$-element Hermitian semi-positive definite matrix, its SVD is given by:

$$\mathbf{C} = \mathbf{U}\begin{bmatrix}\Sigma_{k\times k} & \mathbf{0}\\ \mathbf{0} & \mathbf{0}\end{bmatrix}\mathbf{U}^H, \tag{A.11}$$

where $\mathbf{U} \in \mathbb{C}^{M\times M}$ and $\Sigma_{k\times k}$ is a diagonal matrix having singular values on the diagonal, which correspond to the $k$ number of nonzero eigenvalues of $\mathbf{C}$. With the aid of matrix manipulation, Eq. (A.11) can be further simplified to

$$\mathbf{C} = [\mathbf{U}_1, \mathbf{U}_2]\begin{bmatrix}\Sigma_{k\times k} & \mathbf{0}\\ \mathbf{0} & \mathbf{0}\end{bmatrix}[\mathbf{U}_1, \mathbf{U}_2]^H = \mathbf{U}_1\Sigma_{k\times k}\mathbf{U}_1^H, \tag{A.12}$$

where $\mathbf{U}_1 \in \mathbb{C}^{M\times k}$ and $\mathbf{U}_2 \in \mathbb{C}^{M\times(M-k)}$. The columns of the matrix $\mathbf{U}_1$ are the eigenvectors of $\mathbf{C}$, which correspond to the eigenvalues on the diagonal of $\Sigma_{k\times k}$, respectively. Finally, we obtain the linear maximum SINR array processor of Section 5.2.2 as follows

$$\begin{aligned}\Theta &= [\mathbf{w}_1, \mathbf{w}_2, \cdots, \mathbf{w}_k]\\ &= (\mathbf{L}^{-1})^H\left[\mathbf{L}^H\mathbf{w}_1, \mathbf{L}^H\mathbf{w}_2, \cdots, \mathbf{L}^H\mathbf{w}_k\right]\\ &= (\mathbf{L}^{-1})^H\mathbf{U}_1.\end{aligned} \tag{A.13}$$

# Glossary

| | |
|---|---|
| **4QAM** | 4-level Quadrature Amplitude Modulation |
| **AF** | Amplify-and-Forward |
| **APP** | A Posteriori Probability |
| **AWGN** | Additive White Gaussian Noise |
| **BCJR** | Bahl-Cocke-Jelinek-Raviv algorithm |
| **BEC** | Binary Erasure Channel |
| **BER** | Bit Error Ratio |
| **BICM-ID** | Bit-Interleaved Coded Modulation scheme using Iterative Decoding |
| **BLAST** | Bell-labs LAyered Space-Time architecture |
| **BPS** | Bits Per modulated Symbol |
| **BPSK** | Binary Phase Shift Keying |
| **BS** | A common abbreviation for Base Station |
| **CCMC** | Continuous-input Continuous-output Memoryless Channel |
| **CDMA** | Code Division Multiple Access |
| **CF** | Compress-and-Forward |
| **CIR** | Channel Impulse Response |
| **CSI** | Channel State Information |
| **D-BLAST** | Diagonal Bell-labs LAyered Space-Time architecture |

| | |
|---|---|
| **DCMC** | Discrete-input Continuous-output Memoryless Channel |
| **DF** | Decode-and-Forward |
| **D-GMLST** | Diagonal Generalized Multi-Layer Space-Time architecture |
| **DSTC** | Differential Space-Time Coding scheme |
| **DTC** | Distributed Turbo Code |
| **DTTCM** | Distributed Turbo Trellis Coded Modulation |
| $E_b/N_0$ | Ratio of bit energy to noise power spectral density. |
| **EGC** | Equal Gain Combining |
| **EXIT** | EXtrinsic Informathion Transfer |
| **FEC** | Forward Error Correction |
| **FER** | Frame Error Ratio |
| **GMLST** | Generalized Multi-Layer Space-Time architecture |
| **GMLST(STBC)** | GMLST schemes using STBC as the component codes |
| **GMLST(STTC)** | GMLST schemes using STTC as the component codes |
| **H-GMLST** | Horizontal Generalized Multi-Layer Space-Time architecture |
| **IC** | Interference Cancellation |
| **i.i.d.** | independent and identically distributed |
| **IN** | Interference Nulling |
| **IRCCs** | IRregular Convolutional Codes |
| **Ir-CSTC** | Irregular Cooperative Space-Time Coding scheme |
| **i.u.d.** | independent and uniformly distributed |
| **JD** | Joint Detection |
| **LDC** | Linear Dispersion Code |
| **LDPC** | Low Density Parity Check code |
| **LLR** | Log-Likelihood Ratio |
| **log-domain** | logarithmic-domain |

| | |
|---|---|
| **Log-MAP** | Log Maximum Aposteriori Probability |
| **LOS** | Line of Sight |
| **LS** | Least Square |
| **MAI** | Multiple Access Interference |
| **MAP** | Maximum A Posteriori |
| **MaxSINR** | Maximum Signal-to-Interference-plus-Noise Ratio |
| **MBER** | Minimum Bit Error Rate detection |
| **MCMC** | Markov Chain Monte Carlo detection |
| **MIMO** | Multi-Input Multi-Output |
| **ML** | Maximum Likelihood |
| **MLSE** | Maximum Likelihood Sequence Estimator |
| **MMSE** | Minimum Mean Square Error |
| **MR** | The active MSs to Relaying MS link |
| **MRC** | Maximum Ratio Combining |
| **MS** | Mobile Station |
| **MU** | Multi-User |
| **MUD** | Multi-User Detector |
| **MU-MIMO** | Multiple-User MIMO system |
| **MSE** | Mean Square Error |
| **OSTBC** | Orthogonal Space-Time Block Coding |
| **PDF** | Probability Density Function |
| **PIC** | Parallel Interference Cancellation |
| **PSD** | Power Spectral Density |
| **PSK** | Phase Shift Keying |
| **PWEP** | Pair-Wise Error Probability |
| **QAM** | Quadrature Amplitude Modulation |

| | |
|---|---|
| **QPSK** | Quadrature Phase Shift Keying |
| **RD** | Relay-to-Destination link |
| **RSC** | Recursive Systematic Convolutional |
| **Rx** | Receiver |
| **SD** | Selection Diversity or Sphere Detection / Source-to-Destination link |
| **SDMA** | Space Division Multiple Access |
| **SER** | Symbol Error Ratio |
| **SIC** | Successive Interference Cancellation |
| **SINR** | Signal-to-Interference-plus-Noise Ratio |
| **SISO** | Soft-Input Soft-Output/Single-Input Single-Output |
| **SNR** | Signal to Noise Ratio, noise energy compared to the signal energy |
| **SP** | Set Partitioning |
| **S/P** | Serial-to-Parallel |
| **SR** | Source-to-Relay link |
| **STBC** | Space-Time Block Code |
| **STC** | Space-Time Coding |
| **STTC** | Space-Time Trellis Code |
| **STTC-4** | 4-state based Space-Time Trellis Code |
| **STTC-16** | 16-state based Space-Time Trellis Code |
| **SU-MIMO** | Single-User MIMO system |
| **SVD** | Singular-Value Decomposition |
| **TCM** | Trellis Coded Modulation |
| **Tx** | Transmitter |
| **URC** | Unity-Rate Code |
| **VA** | Viterbi Algorithm |

| | |
|---|---|
| **VAA** | Virtual Antenna Arrays |
| **V-BLAST** | Vertical Bell-lab LAyered Space-Time architecture |
| **ZF** | Zero Forcing. |

# Bibliography


[1] C. E. Shannon, "A mathematical theory of communication," *Bell Systems Technical Journal*, vol. 27, pp. 379–423 and 623–656, June and October 1948.

[2] D. Gesbert, M. Shafi, D. Shiu, P. J. Smith, and A. Naguib, "From theory to practice: An overview of MIMO space-time coded wireless systems," *IEEE Journal on Selected Areas in Communications*, vol. 21, pp. 281–302, April 2003.

[3] G. J. Foschini and M. J. Gans, "On limits of wireless communications in a fading environment when using multiple antennas," *Wireless Personal Communications*, vol. 6, pp. 311–335, March 1998.

[4] I. E. Telatar, "Capacity of multi-antenna Gaussian channels," *European Transactions on Telecommunication*, vol. 10, pp. 585–595, Nov./Dec. 1999.

[5] M. S. Alouini and A. J. Goldsmith, "Capacity of Rayleigh fading channels under different adaptive transmission and diversity-combining techniques," *IEEE Transactions on Vehicular Technology*, vol. 48, pp. 1165–1181, July 1999.

[6] S. X. Ng and L. Hanzo, "On the MIMO channel capacity of multidimensional signal sets," *IEEE Transactions on Vehicular Technology*, vol. 55, pp. 528–536, March 2006.

[7] G. J. Foschini, "Layered space-time architecture for wireless communication in a fading environment when using multiple antennas," *Bell Labs Technical Journal*, vol. 1, pp. 41–59, Autumn 1996.

[8] S. M. Alamouti, "A simple transmit diversity technique for wireless communications," *IEEE Journal on Selected Areas in Communications*, vol. 16, pp. 1451–1458, Oct. 1998.

[9] V. Tarokh, N. Seshadri, and A. R. Calderbank, "Space-time codes for high data rate wireless communication: Performance criterion and code construction," *IEEE Transactions on Information Theory*, vol. 45, pp. 744–765, Mar. 1998.

[10] V. Tarokh, A. Naguib, N. Seshadri, and A. R. Calderbank, "Combined array processing and space-time coding," *IEEE Transactions on Information Theory*, vol. 45, pp. 1121–1128, May 1999.

[11] M. Tao and R. S. Cheng, "Generalized layered space-time codes for high data rate wireless communications," *IEEE Transactions on Wireless Communications*, vol. 3, pp. 1067–1075, July 2004.

[12] A. J. Paulraj, D. A. Gore, R. U. Nabar, and H. Boelcskei, "An overview of MIMO communications – A key to gigabit wireless," *Proceedings of the IEEE*, vol. 92, pp. 198–218, Feb. 2004.

[13] A. Paulraj and T. Kailath, *Increasing capacity in wireless broadcast systems using distributed transmission/directional reception*. U.S. Patent 5 345 599, Feb. 1992.

[14] J. G. Proakis, *Digital Communications*. 4th ed. New York: McGraw-Hill, 2001.

[15] G. D. Golden, C. J. Foschini, R. A. Valenzuela, and P. W. Wolniansky, "Detection algorithm and initial laboratory results using V-BLAST space-time communication architecture," *Electronics Letters*, vol. 35, pp. 14–16, Jan. 1999.

[16] P. W. Wolniansky and G. J. Foschini and G. D. Golden and R. A. Valenzuela, "V-BLAST: an architecture for realizing very high data rates over the rich-scattering wireless channel," in *1998 URSI International Symposium on Signals, Systems, and Electronics*, (Pisa, Italy), pp. 295–300, 1998.

[17] G. J. Foschini and G. D. Golden and R. A. Valenzuela and P. W. Wolniansky, "Simplified processing for high spectral efficiency wireless communications employing multi-element arrays," *IEEE Journal on Selected Areas in Communications*, vol. 17, pp. 1841–1852, Nov. 1999.

[18] S. Baro and G. Bauch and A. Pavlic and A. Semmler, "Improving BLAST performance using space-time block codes and turbo decoding," in *IEEE Global Telecommunications Conference (GLOBECOM'00)*, vol. 2, pp. 1067–1071, 2000.

[19] A. Benjebbour and H. Murata and S. Yoshida, "Comparison of ordered successive receivers for space-time transmission," in *IEEE Vehicle Technology Conference (VTC-Fall)*, (Atlantic City, New Jersey, USA), pp. 2053–2057, Oct. 2001.

[20] M. Sellathurai and S. Haykin, "TURBO-BLAST for wireless communications: theory and experiments," *IEEE Transactions on Signal Processing*, vol. 50, pp. 2538–2546, Oct. 2002.

[21] A. Benjebbour and H. Murata and S. Yoshida, "Performance of iterative successive detection algorithm with space-time transmission," in *IEEE Vehicle Technology Conference (VTC-Spring)*, (Rhodes, Greece), pp. 1287–1291, May 2001.

[22] S. Loyka and F. Gagnon, "Performance analysis of the V-BLAST algorithm: An analytical approach," *IEEE Transactions on Wireless Communications*, vol. 3, pp. 1326–1337, July 2004.

[23] G. J. Foschini and D. Chizhik and M. J. Gans and C. Papadias and R. A. Valenzuela, "Analysis and performance of some basic space-time architectures," *IEEE Journal on Selected Areas in Communications*, vol. 21, pp. 303–320, Apr. 2003.

[24] D. G. Brennan, "Linear diversity combining techniques," in *Proceedings of the IEEE*, vol. 91, pp. 331–356, Feb. 2003.

[25] T. Eng, N. Kong, and L. B. Milstein, "Comparison of diversity combining techniques for Rayleigh-fading channels," *IEEE Transactions on Communications*, vol. 44, pp. 1117–1129, Sept. 1996.

[26] N. Seshadri and J. H. Winters, "Two signalling schemes for improving the error performance of frequency-division-duplex (FDD) transmission systems using transmitter antenna diversity," in *IEEE Vehicle Technology Conference (VTC-Spring)*, (Secaucus, New Jersey, USA), pp. 508–511, May,1993.

[27] A. Wittneben, "A new bandwidth efficient transmit antenna modulation diversity scheme for linear digital modulation," in *IEEE International Conference on Communications (ICC)*, (Geneva, Switzerland), pp. 1630–1634, May,1993.

[28] G. Ungerböck, "Trellis-coded modulation with redundant signal sets, Part I," *IEEE Communications Magazine*, pp. 5–11, February 1987.

[29] G. Ungerböck, "Trellis-coded modulation with redundant signal sets, Part II," *IEEE Communications Magazine*, pp. 12–21, February 1987.

[30] V. Tarokh, H. Jafarkhani, and A. R. Calderbank, "Space-time block coding for wireless communications: Performance Results," *IEEE Journal on Selected Areas in Communications*, vol. 17, pp. 451–460, March 1999.

[31] V. Tarokh, H. Jafarkhani, and A. R. Calderbank, "Space-time block codes from orthogonal designs," *IEEE Transactions on Information Theory*, vol. 45, pp. 1456–1467, July 1999.

[32] L. Zhao and V. K. Dubey, "Detection schemes for space-time block code and spatial multiplexing combined system," *IEEE Communications Letters*, vol. 9, pp. 49–51, Jan. 2005.

[33] F. S. Ostuni and B. Abdool-Rassool and M. R. Nakhai and H. Aghvami, "Layered space-time codes with iterative receiver and space-time soft-output decoding in a Rayleigh fading environment," in *IEEE International Symposium on Personal, Indoor, and Mobile Radio Communications (PIMRC)*, (Pavilhao Atlantico, Lisboa, Portugal), pp. 418–422, Sept. 2002.

[34] Y. Wu and Y. Yang and X. Luo, "Improving the performance of V-BLAST with STTC," in *IEEE International Conference on Communication Systems (ICCS)*, (Singapore), pp. 174–177, Nov. 2002.

[35] H. E. Gamal and J. A. R. Hammons, "A new approach to layered space-time coding and signal processing," *IEEE Transactions on Information Theory*, vol. 47, pp. 2321–2334, Sept. 2001.

[36] H. Huang and H. Viswanathan, "Multiple antennas and multiuser detection in high data rate CDMA systems," in *IEEE Vehicular Technology Conference (VTC-Spring)*, (Tokyo, Japan), pp. 556–560, May 2000.

[37] H. Huang, H. Viswanathan, and G. Foschini, "Multiple antennas in cellular CDMA systems: transmission, detection and spectral efficiency," *IEEE Transactions on Wireless Communications*, vol. 1, pp. 383–392, July 2002.

[38] A. Sendonaris, E. Erkip, and B. Aazhang, "User cooperation diversity–Part I: System Description," *IEEE Transactions on Communications*, vol. 51, pp. 1927–1938, Nov. 2003.

[39] A. Sendonaris, E. Erkip, and B. Aazhang, "User cooperation diversity–Part II: Implementation Aspects and Performance Analysis," *IEEE Transactions on Communications*, vol. 51, pp. 1939–1948, Nov. 2003.

[40] E. C. V. der Meulen, "Three-terminal communication channels," *Advanced Applied Probability*, vol. 3, no. 1, pp. 120–154, 1971.

[41] T. Cover and A. E. Gamal, "Capacity theorems for the relay channel," *IEEE Transactions on Information Theory*, vol. 25, no. 5, pp. 572–584, 1979.

[42] A. Sendonaris and E. Erkip and B. Aazhang, "Increasing uplink capacity via user cooperation diversity," in *IEEE International Symposium on Information Theory (ISIT'98)*, (Cambridge, MA, USA), p. 156, Aug. 1998.

[43] M. Dohler and E. Lefranc and H. Aghvami, "Space-time block codes for virtual antenna arrays," in *The 13th IEEE International Symposium on Personal, Indoor and Mobile Radio Communications (PIMRC)*, vol. 1, pp. 414–417, Sept. 2002.

[44] J. Laneman and G. Wornell, "Distributed space-time-coded protocols for exploiting cooperative diversity in wireless networks," *IEEE Transactions on Information Theory*, vol. 49, pp. 2415–2425, Oct. 2003.

[45] T. E. Hunter and A. Nosratinia, "Cooperation diversity through coding," in *IEEE International Symposium on Information Theory (ISIT'02)*, p. 220, 2002.

[46] M. Janani, A. Hedayat, T. E. Hunter, and A. Nosratinia, "Coded cooperation in wireless communications: space-time transmission and iterative decoding," *IEEE Transactions on Signal Processing*, vol. 52, pp. 362–371, Feb. 2004.

[47] A. Stefanov and E. Erkip, "Cooperative coding for wireless networks," *IEEE Transactions on Communications*, vol. 52, pp. 1470–1476, Sept. 2004.

[48] J. Laneman, D. Tse, and G. Wornell, "Cooperative diversity in wireless networks: Efficient protocols and outage behavior," *IEEE Transactions on Information Theory*, vol. 50, pp. 3062–3080, Dec. 2004.

[49] B. Zhao and M. Valenti, "Distributed turbo coded diversity for relay channel," *Electronics Letters*, vol. 39, pp. 786–787, May 2003.

[50] S. X. Ng, Y. Li and L. Hanzo, "Distributed turbo trellis coded modulation for cooperative communications," in *IEEE International Conference on Communications (ICC'09)*, (Dresden, Germany), pp. 1–5, 14-18 June 2009.

[51] C. Berrou and A. Glavieux and P. Thitimajshima, "Near Shannon Limit Error-Correcting Coding and Decoding: Turbo Codes," in *IEEE International Conference on Communications (ICC'93)*, (Geneva, Switzerland), pp. 1064–1070, May 1993.

[52] D. Divsalar and F. Pollara, "Multiple turbo codes for deep-space communications," in *Telecommunication and Data Acquisition Progress Report 42-121, Jet Propulsion Laboratory*, (Pasadena, CA), pp. 66–77, May 1995.

[53] S. Benedetto and G. Montorsi, "Iterative decoding of serially concatenated convolutional codes," *Electronics Letters*, vol. 32, pp. 1186–1188, June 1996.

[54] S. Benedetto, D. Divsalar, G. Montorsi, and F. Pollara, "Analysis, design, and iterative decoding of double serially concatenated codes with interleavers," *IEEE Journal on Selected Areas in Communications*, vol. 16, pp. 231–244, Feb. 1998.

[55] R. G. Gallager, "Low-density parity-check codes," *IRE Transactions on Information Theory*, vol. 8, pp. 21–28, Jan. 1962.

[56] D. J. C. MacKay and R. M. Neal, "Near shannon limit performance of low density parity check codes," *Electronics Letters*, vol. 32, pp. 457–458, Aug. 1996.

[57] R. G. Gallager, *Low Density Parity Check Codes*. Cambridge, Mass.: MIT Press, 1963.

[58] R. Tanner, "A recursive approach to low complexity codes," *IEEE Transactions on Information Theory*, vol. 27, pp. 533–547, Sept. 1981.

[59] M. Luby and M. Mitzenmacher and A. Shokrollahi and D. Spielman and V. Stemann, "Practical loss-resilient codes," in *Proceedings of the ACM Symposium on Theory of Computing*, (El Paso, TX, USA), pp. 150 –159, May 1997.

[60] M. J. Frey and D. J. C. Mackay, "Irregular turbo-like codes," in *Proceedings of the International Symposium on Turbo Codes*, (Brest, France), pp. 67 –72, Sept. 2000.

[61] M. Tüchler and J. Hagenauer, "EXIT charts of irregular codes," in *Proceeding of the 36th Annual Conference on Information Sciences and Systems [CDROM]*, (Princeton, NJ, USA), March 2002.

[62] Z. Zhang and T. Duman, "Capacity-approaching turbo coding and iterative decoding for relay channels," *IEEE Transactions on Communications*, vol. 53, pp. 1895–1905, Nov. 2005.

[63] Z. Zhang and T. Duman, "Capacity-approaching turbo coding for half-duplex relaying," *IEEE Transactions on Communications*, vol. 55, pp. 1895–1906, Oct. 2007.

[64] S. ten Brink, "Designing Iterative Decoding Schemes with the Extrinsic Information Transfer Chart," *AEÜ International Journal of Electronics and Communications*, vol. 54, pp. 389–398, Nov. 2000.

[65] J. Hagenauer, "The EXIT chart - introduction to extrinsic information transfer in iterative processing," in *European Signal Processing Conference*, (Vienna, Austria), pp. 1541–1548, Sept. 2004.

[66] S. ten Brink, "Convergence of multidimensional iterative decoding schemes," in *the 35th Asilomar Conference on Signals, Systems and Computers*, vol. 1, (Pacific Grove, CA, USA), pp. 270–274, 2001.

[67] M. Tüchler, "Convergence prediction for iterative decoding of threefold concatenated systems," in *IEEE Global Telecommunications Conference (GLOBECOM'02)*, vol. 2, (Taipei, Taiwan), pp. 1358–1362, 17-21 November 2002.

[68] F. Brännström, L. K. Rasmussen, and A. J. Grant, "Convergence analysis and optimal scheduling for multiple concatenated codes," *IEEE Transactions on Information Theory*, vol. 51, no. 9, pp. 3354–3364, 2005.

[69] L. Kong, S. X. Ng and L. Hanzo, "Near-Capacity Three-Stage Downlink Iteratively Decoded Generalized Layered Space-Time Coding with Low Complexity," in *IEEE Global Telecommunications Conference (GLOBECOM'08)*, (New Orleans, LA, USA), pp. 1–6, 30 Nov.-04 Dec. 2008.

[70] L. Kong and S. X. Ng and R. G. Maunder and L. Hanzo, "Irregular Distributed Space-Time Code Design for Near-Capacity Cooperative Communications," in *IEEE Vehicular Technology Conference (VTC-Fall)*, (Anchorage, Alaska, USA), pp. 1–6, 20-23 Sept. 2009.

[71] L. Kong, S. X. Ng, R. G. Maunder, and L. Hanzo, "Successive relaying aided near-capacity irregular distributed space-time coding," in *IEEE Global Telecommunications Conference (GLOBECOM'09)*, (Honolulu, Hawaii, USA), pp. 1–5, 30 Nov.-04 Dec. 2009.

[72] W. Liu, L. Kong, S. X. Ng, and L. Hanzo, "Near-capacity iteratively decoded markov-chain monte-carlo aided BLAST system," in *IEEE Global Telecommunications Conference (GLOBECOM'09)*, (Honolulu, Hawaii, USA), pp. 1–5, 30 Nov.-04 Dec. 2009.

[73] L. Wang, L. Kong, S. X. Ng, and L. Hanzo, "To cooperate or not: A capacity perspective," in *IEEE Vehicular Technology Conference (VTC-Spring)*, (Taipei, Taiwan), pp. 1–5, 16-19, May 2010.

[74] L. Wang, L. Kong, S. X. Ng, and L. Hanzo, "A near-capacity differentially encoded non-coherent adaptive multiple-symbol-detection aided three-stage coded scheme," in *IEEE Vehicular Technology Conference (VTC-Spring)*, (Taipei, Taiwan), pp. 1–5, 16-19, May 2010.

[75] S. Sugiura, S. X. Ng, L. Kong, S. Chen, and L. Hanzo, "Multiple-relay aided distributed turbo coding assisted differential unitary space-time spreading for asynchronous cooperative networks," in *IEEE Vehicular Technology Conference (VTC-Spring)*, (Taipei, Taiwan), pp. 1–5, 16-19, May 2010.

[76] L. Kong, S. X. Ng, R. Y. S. Tee, R. G. Maunder, and L. Hanzo, "Reduced-complexity near-capacity downlink iteratively decoded generalized multi-layer space-time coding using irregular convolutional codes," *IEEE Transactions on Wireless Communications*, vol. 9, pp. 684–695, Feb. 2010.

[77] L. Kong, S. X. Ng, R. G. Maunder, and L. Hanz, "Maximum-throughput irregular distributed space-time code for near-capacity cooperative communications," *IEEE Transactions on Vehicular Technology*, vol. 59, pp. 1511–1517, March 2010.

[78] L. Kong, S. X. Ng, R. G. Maunder, and L. Hanz, "Near-capacity cooperative space-time coding employing irregular design and successive relaying," *IEEE Transactions on Communications*, vol. 58, pp. 2232–2241, Aug. 2010.

[79] L. Wang, L. Kong, S. X. Ng, and L. Hanzo, "Code-rate-optimized differentially modulated near-capacity cooperation," *submitted to IEEE Transactions on Communications*, 2010.

[80] S. Sugiura, S. X. Ng, L. Kong, S. Chen, and L. Hanzo, "Multiple-relay aided differential distributed turbo coding for asynchronous cooperative networks," *submitted to IEEE Transactions on Vehicular Technology*, 2010.

[81] M. Tüchler, "Design of serially concatenated systems depending on the block length," *IEEE Transactions on Communications*, vol. 52, pp. 209–218, Feb. 2004.

[82] L. Zheng and D. N. C. Tse, "Diversity and Multiplexing: A Fundamental Tradeoff in Multiple-Antenna Channels," *IEEE Transactions on Information Theory*, vol. 49, pp. 1073–1096, May 2003.

[83] J. C. Guey, M. P. Fitz, M. R. Bell, and W. Y. Kuo, "Signal design for transmitter diversity wireless communication systems over Rayleigh fading channels," *IEEE Transactions on Communications*, vol. 47, pp. 527–537, April 1999.

[84] Da-shan Shiu and J. M. Kahn, "Layered space-time codes for wireless communications using multiple transmit antennas," in *IEEE International Conference on Communications (ICC'99)*, (Vancouver, British Columbia, Canada), pp. 436–440, 6-10, June 1999.

[85] Da-shan Shiu, "Iterative decoding for layered space-time codes," in *IEEE International Conference on Communications (ICC'00)*, (New Orleans, Louisiana, USA), pp. 297–301, June 2000.

[86] H.-J. Su and E. Geraniotis, "Maximum signal-to-noise ratio array processing for space-time coded systems," *IEEE Transactions on Communications*, vol. 50, pp. 1419–1422, Sep 2002.

[87] Z. Lei, Y. Dai, and S. Sun, "Ordered maximum SNR array processing for space time coded systems," *Electronics Letters*, vol. 39, pp. 561–562, March 2003.

[88] Y. Dai, Z. Lei, and S. Sun, "Iterative interference cancellation and ordered array processing for groupwise space time trellis coded (GSTTC) systems," in *IEEE Wireless Communications and Networking Conference*, vol. 4, pp. 2323–2328, March 2004.

[89] L. Hanzo, T.H. Liew and B.L. Yeap, *Turbo Coding, Turbo Equalisation and Space Time Coding for Transmission over Wireless channels*. New York, USA: John Willy IEEE Press, 2002.

[90] L.R. Bahl, J. Cocke, F. Jelinek and J. Raviv, "Optimal Decoding of Linear Codes for Minimising Symbol Error Rate," *IEEE Transactions on Information Theory*, vol. 20, pp. 284–287, March 1974.

[91] R. A. Horn and C. R. Johnson, *Matrix Analysis*. Cambridge University Press, 1985.

[92] J. Hagenauer, "The turbo principle: Tutorial introduction and state of the art," in *Proceedings of International Symposium on Turbo Codes and related topics*, (Brest, France), pp. 1–11, September 1997.

[93] L. Hanzo, J. P. Woodard, and P. Robertson, "Turbo decoding and detection for wireless applications," in *Proceedings of the IEEE*, pp. 1178–1200, June 2007.

[94] S. Benedetto and G. Montorsi, "Iterative decoding of serially concatenated convolutional codes," *Electronics Letterrs*, vol. 32, pp. 1186–1188, June 1996.

[95] S. Benedetto, D. Divsalar, G. Montorsi, and F. Pollara, "Analysis, design, and iterative decoding of double serially concatenated codes with interleavers," *IEEE Journal on Selected Areas in Communications*, vol. 16, pp. 231–244, Feb. 1998.

[96] O. Alamri, B. L. Yeap, and L. Hanzo, "A turbo detection and sphere-packing-modulation-aided space-time coding scheme," *IEEE Transactions on Vehicular Technology*, vol. 56, pp. 575–582, March 2007.

[97] D. Divsalar and S. Dolinar and F. Pollara, "Low complexity turbo-like codes," in *2nd International Symposium on Turbo Codes and Related Topics*, (Brest, France), pp. 73–80, Sept. 2000.

[98] T. J. Richardson and R. Urbanke, "The capacity of low-density parity-check codes under message-passing decoding," *IEEE Transactions on Information Theory*, vol. 47, pp. 599–618, Feb. 2001.

[99] T. J. Richardson, A. Shokrollahi, and R. Urbanke, "Design of capacity-approaching low-density parity-check codes," *IEEE Transactions on Information Theory*, vol. 47, pp. 619–637, Feb. 2001.

[100] H. E. Gamal and A. R. Hammons, "Analyzing the turbo decoder using the Gaussian approximation," *IEEE Journal on Selected Areas in Communications*, vol. 47, pp. 671–686, Feb. 2001.

[101] S. ten Brink, "Convergence behaviour of iteratively decoded parallel concatenated codes," *IEEE Transactions on Communications*, vol. 49, pp. 1727–1737, Oct. 2001.

[102] M. Tüchler and S. ten Brink and J. Hagenauer, "Measures for tracing convergence of iterative decoding algorithms," in *Proceedings of the 4th International ITG Conference on Source and Channel Coding*, (Berlin, Germany), pp. 53 –60, Jan. 2002.

[103] S. Y. Chung, G. D. Forney, T. J. Richardson, and R. Urbanke, "On the design of low-density parity-check codes within 0.0045 db of the Shannon limit," *IEEE Communication Letter*, vol. 5, pp. 58–60, Feb. 2001.

[104] M. Peleg, I. Sason, S. Shamai, and A. Elia, "On interleaved differentially encoded convolutional codes," *IEEE Transactions on Information Theory*, vol. 45, pp. 2572–2582, Nov. 1999.

[105] D. Divsalar, S. Dolinar and F. Pollara, "Serial turbo trellis coded modulation with rate-1 inner code," in *International Symposium on Information Theory (ISIT'00)*, (Sorrento, Italy), p. 194, 25-30 June 2000.

[106] S. X. Ng, J. Wang, M. Tao, L.-L. Yang, and L. Hanzo, "Iteratively decoded variable-length space-time coded modulation: code construction and convergence analysis," *IEEE Transactions on Wireless Communications*, vol. 6, pp. 1953–1963, May 2007.

[107] M. El-Hajjar, O. Alamri, S. X. Ng, and L. Hanzo, "Turbo detection of precoded sphere packing modulation using four transmit antennas for differential space-time

spreading," *IEEE Transactions on Wireless Communications*, vol. 7, pp. 943–952, March 2008.

[108] S. X. Ng, and J. Wang and L. Hanzo, "Unveiling Near-Capacity Code Design: The Realization of Shannon's Communication Theory for MIMO Channels," in *IEEE International Conference on Communications (ICC'08)*, (Beijing, China), pp. 1415–1419, 19-23 May 2008.

[109] V.B. Balakirsky, "Joint source-channel coding with variable length codes," in *IEEE International Symposium on Information Theory*, (Ulm, Germany), p. 419, June 1997.

[110] P. Robertson and E. Villebrun and P. Hoeher, "A Comparison of Optimal and Sub-Optimal MAP Decoding Algorithms Operating in the Log Domain," in *IEEE International Conference on Communications (ICC'95)*, (Seattle, USA), pp. 1009–1013, June 1995.

[111] J. Hagenauer, E. Offer, and L. Papke, "Iterative decoding of binary block and convolutional codes," *IEEE Transactions on Information Theory*, vol. 42, no. 2, pp. 429–445, 1996.

[112] S. Benedetto and G. Montorsi, "Serial concatenation of block and convolutional codes," *Electronics Letters*, vol. 32, pp. 887–888, May 1996.

[113] E. Zehavi, "8-PSK trellis codes for a Rayleigh fading channel," *IEEE Transactions on Communications*, vol. 40, pp. 873–883, May 1992.

[114] X. Li and J.A. Ritcey, "Bit-interleaved coded modulation with iterative decoding," *IEEE Communications Letters*, vol. 1, pp. 169–171, November 1997.

[115] X. Li and J.A. Ritcey, "Bit-interleaved coded modulation with iterative decoding — Approaching turbo-TCM performance without code concatenation," in *Proceedings of CISS*, (Princeton University, USA), March 1998.

[116] X. Li and J.A. Ritcey, "Bit-interleaved coded modulation with iterative decoding using soft feedback," *IEE Electronics Letters*, vol. 34, pp. 942–943, May 1998.

[117] X. Li and J.A. Ritcey, "Bit-interleaved coded modulation with iterative decoding," in *IEEE International Conference on Communications (ICC'99)*, vol. 2, pp. 885–863, 1999.

[118] X. Li and J.A. Ritcey, "Trellis-Coded Modulation with Bit Interleaving and Iterative Decoding," *IEEE Journal on Selected Areas in Communications*, vol. 17, pp. 715–724, April 1999.

[119] J. Kliewer, S. X. Ng, and L. Hanzo, "Efficient computation of EXIT functions for nonbinary iterative decoding," *IEEE Transactions on Communications*, vol. 54, pp. 2133–2136, Dec. 2006.

[120] T. M. Cover and J. A. Thomas, *Elements of information theory*. New York, USA: Wiley, 2006.

[121] B. Scanavino and G. Montorsi and S. Benedetto, "Convergence properties of iterative decoders working at bit and symbol level," in *IEEE Global Telecommunications Conference (GLOBECOM'01)*, (San Antonio, TX, USA), pp. 1037–1041, 25-29 Nov. 2001.

[122] A. Ashikhmin, G. Kramer, and S. ten Brink, "Extrinsic information transfer functions: model and erasure channel properties," *IEEE Transactions on Information Theory*, vol. 50, pp. 2657–2673, Nov. 2004.

[123] A. Ashikhmin and G. Kramer and S. ten Brink, "Code rate and the area under extrinsic information transfer curves," in *International Symposium on Information Theory (ISIT'02)*, (Lausanne, Switzerland), p. 115, June 2002.

[124] H. Jafarkhani, "A quasi-orthogonal space-time block code," *IEEE Communications Letter*, vol. 49, pp. 1–4, January 2001.

[125] R. Calderbank, S. Diggavi, S. Da and N. Al-Dhahir, "Construction and Analysis of a New 4x4 Orthogonal Space-Time Block Code," in *International Symposium on Information Theory (ISIT'04)*, p. 309, 27 June - 2 July 2004.

[126] R. Calderbank, S. Das, N. Al-Dhahir and S. Diggavi, "Construction and analysis of a new quaternionic space-time code for 4 transmit antennas," *Communication in Information and Systems*, vol. 5, no. 1, pp. 97–122, 2005.

[127] S. X. Ng, S. Das, J. Wang and L. Hanzo, "Near-Capacity Iteratively Decoded Space-Time Block Coding," in *IEEE Vehicle Technology Conference (VTC-Spring)*, (Marina Bay, Singapore), pp. 590 – 594, 11-14 May 2008.

[128] T. Rappaport, *Wireless Communications Principles and Practice*. Englewood Cliffs, NJ, USA: Prentice-Hall, 1996.

[129] A. Sendonaris, E. Erkip, and B. Aazhang, "Diversity through coded cooperation," *IEEE Transactions on Wireless Communications*, vol. 5, pp. 283–289, Feb. 2006.

[130] A. Nosratinia, T. E. Hunter, and A. Hedayat, "Cooperative communication in wireless networks," *IEEE Communications Magazine*, vol. 42, pp. 74–80, Oct. 2004.

[131] T. M. Cover and A. E. Gamal, "Capacity theorems for the relay channel," *IEEE Transactions on Information Theory*, vol. 25, pp. 572–584, Sept. 1979.

[132] A. Høst-Madsen and J. Zhang, "Capacity bounds and power allocation for wireless relay channel," *IEEE Transactions on Information Theory*, vol. 51, pp. 2020–2040, June 2005.

[133] R. U. Nabar, H. Bölcskei, and F. W. Kneubühler, "Fading relay channels: Performance limits and space-time signal design," *IEEE Journal on Selected Areas on Communications*, vol. 22, pp. 1099–1109, Aug. 2004.

[134] G. Kramer, M. Gastpar, and P. Gupta, "Cooperative strategies and capacity theorems for relay networks," *IEEE Transactions on Information Theory*, vol. 51, pp. 3037–3063, Sept. 2005.

[135] B. Wang, J. Zhang, and A. Høst-Madsen, "On the capacity of mimo relay channels," *IEEE Transactions on Information Theory*, vol. 51, pp. 29–43, Jan. 2005.

[136] A. Reznik, S. R. Kulkarni, and S. Verdú, "Capacity and optimal resource allocation in the degraded Gaussian relay channel with multiple relays," in *40th Allerton Conference on Communication, Control, and Computing*, pp. 377–386, Oct. 2002.

[137] B. Rankov and A. Wittneben, "Achievable Rate Regions for the Two-way Relay Channel," in *IEEE International Symposium on Information Theory (ISIT'06)*, (Seattle, USA), pp. 1668–1672, July 2006.

[138] K. Azarian, H. El Gamal, and P. Schniter, "On the achievable diversity-multiplexing tradeoff in half-duplex cooperative channels," *IEEE Transactions on Information Theory*, vol. 51, pp. 4152–4172, Dec. 2005.

[139] T. Hunter and A. Nosratinia, "Cooperation diversity through coding," in *IEEE International Symposium on Information Theory (ISIT'02)*, p. 220, 2002.

[140] B. Wang and J. Zhang, "MIMO relay channel and its applications for cooperative communication in ad hoc networks," in *41st Allerton Conference on Communication, Control, and Computing*, pp. 1556–1565, Oct. 2003.

[141] Y. Fan, C. Wang, J. Thompson, and H. Poor, "Recovering multiplexing loss through successive relaying using repetition coding," *IEEE Transactions on Wireless Communications*, vol. 6, pp. 4484–4493, December 2007.

[142] H. Ochiai, P. Mitran, and V. Tarokh, "Design and analysis of collaborative diversity protocols for wireless sensor networks," *IEEE Vehicular Technology Conference (VTC-Fall)*, vol. 7, pp. 4645–4649, Sept. 2004.

[143] A. Høst-Madsen, "Capacity bounds for cooperative diversity," *IEEE Transactions on Information Theory*, vol. 52, pp. 1522–1544, April 2006.

[144] S. Yang and J.-C. Belfiore, "On slotted amplify-and-forward cooperative diversity schemes," *IEEE International Symposium on Information Theory (ISIT'06)*, pp. 2446–2450, July 2006.

[145] J. Luo, R. S. Blum, L. J. Cimini, L. J. Greenstein, and A. M. Haimovich, "Decode-and-forward cooperative diversity with power allocation in wireless networks," *IEEE Transactions on Wireless Communications*, vol. 6, pp. 793–799, March 2007.

[146] L. Zuari, A. Conti and V. Tralli, "Effects of relay position and power allocation in space-time coded cooperative wireless systems," in *the 6th IEEE International Symposium on Wireless Communication Systems*, (Siena-Tuscany, University of Siena, Italy), pp. 700–704, 7-10 Sept. 2009.

[147] A. Conti, V. Tralli, and M. Chiani, "Pragmatic space-time codes for cooperative relaying in block fading channels," *EURASIP Journal on Advances in Signal Processing*, vol. 2008, Article ID 872151, 11 pages, 2008.

[148] S. Verdú, *Multiuser Detection*. Cambridge, UK: Cambridge University Press, 1998.

[149] L. Hanzo, Y. Akhtman, L. Wang, and M. Jiang, *MIMO-OFDM for LTE, WiFi and WiMAX - Coherent versus Non-coherent and Cooperative Turbo Transceivers*. New York, USA: John Wiley IEEE, 2010.

[150] C. Hassell, J. Thompson, B. Mulgrew, and P. Grant, "A comparison of detection algorithms including BLAST for wireless communication using multiple antennas," in *The 11th IEEE International Symposium on Personal, Indoor and Mobile Radio Communications (PIMRC)*, vol. 1, pp. 698–703, 2000.

[151] P. Vandenameele, L. Van Der Perre, M. Engels, B. Gyselinckx, and H. De Man, "A novel class of uplink of OFDM/SDMA algorithms: a statistical performance analysis," in *IEEE Vehicular Technology Conference (VTC-Fall)*, vol. 1, pp. 324–328, 1999.

[152] M. Münster and L. Hanzo, "Co-channel interference cancellation techniques for antenna array assisted multiuser OFDM systems," in *the First International Conference on 3G Mobile Communication Technologies*, (London, United Kingdom), pp. 256–260, March 2000.

[153] M. Sellathurai and S. Haykin, "A simplified diagonal BLAST architecture with iterative parallel-interference cancellation receivers," in *IEEE International Conference on Communications (ICC'01)*, vol. 10, pp. 3067–3071, 2001.

[154] L. Wang, O. Alamri, and L. Hanzo, "K-best sphere detection for the sphere packing modulation aided SDMA/OFDM uplink," in *IEEE Global Telecommunications Conference (GLOBECOM'08)*, pp. 1–5, Nov. 2008.

[155] L. Wang, L. Xu, S. Chen, and L. Hanzo, "Three-stage irregular convolutional coded iterative center-shifting K-best sphere detection for soft-decision SDMA-OFDM," *IEEE Transactions on Vehicular Technology*, vol. 58, pp. 2103 –2109, May 2009.

[156] S. Chen, L. Hanzo, and A. Livingstone, "MBER space-time decision feedback equalization assisted multiuser detection for multiple antenna aided SDMA systems," *IEEE Transactions on Signal Processing*, vol. 54, pp. 3090 –3098, Aug. 2006.

[157] P. Vandenameele, L. Van Der Perre, M. Engels, B. Gyselinckx, and H. De Man, "A combined OFDM/SDMA approach," *IEEE Journal on Selected Areas in Communications*, vol. 18, pp. 2312 –2321, Nov. 2000.

[158] L. Hanzo, M. Münster, B. J. Choi, and T. Keller, *OFDM and MC-CDMA for Broadband Multi-User Communications, WLANs and Broadcasting*. New York, USA: Wiley-IEEE Press, 2003.

[159] M. Honig, U. Madhow, and S. Verdú, "Blind adaptive multiuser detection," *IEEE Transactions on Information Theory*, vol. 41, pp. 944 –960, Jul. 1995.

[160] S. Haykin, *Adaptive Filter Theory*. Englewood Cliffs, NJ, USA: Prentice-Hall, 1996.

[161] H. Poor and S. Verdú, "Probability of error in MMSE multiuser detection," *IEEE Transactions on Information Theory*, vol. 43, pp. 858 –871, May 1997.

[162] D.-S. Shiu, G. Foschini, M. Gans, and J. Kahn, "Fading correlation and its effect on the capacity of multielement antenna systems," *IEEE Transactions on Communications*, vol. 48, pp. 502 –513, Mar. 2000.

[163] C.-N. Chuah, D. Tse, J. Kahn, and R. Valenzuela, "Capacity scaling in MIMO wireless systems under correlated fading," *IEEE Transactions on Information Theory*, vol. 48, pp. 637 –650, Mar. 2002.

[164] R. Louie, M. McKay, and I. Collings, "Impact of correlation on the capacity of multiple access and broadcast channels with MIMO-MRC," *IEEE Transactions on Wireless Communications*, vol. 7, pp. 2397 –2407, June 2008.

[165] N. Zhang and B. Vojcic, "Multiuser diversity scheduling in MIMO systems with correlated fading," in *IEEE Global Telecommunications Conference (GLOBECOM'05)*, vol. 3, p. 5, Nov. 2005.

[166] P. Viswanath, D. Tse, and R. Laroia, "Opportunistic beamforming using dumb antennas," *IEEE Transactions on Information Theory*, vol. 48, pp. 1277 –1294, Jun. 2002.

[167] J. Kermoal, L. Schumacher, K. Pedersen, P. Mogensen, and F. Frederiksen, "A stochastic MIMO radio channel model with experimental validation," *IEEE Journal on Selected Areas in Communications*, vol. 20, pp. 1211 – 1226, Aug. 2002.

[168] K. Yu, M. Bengtsson, B. Ottersten, D. McNamara, P. Karlsson, and M. Beach, "Second order statistics of NLOS indoor MIMO channels based on 5.2 ghz measurements," in *IEEE Global Telecommunications Conference (GLOBECOM'01)*, vol. 1, pp. 156 –160, 2001.

[169] D. Chizhik, F. Rashid-Farrokhi, J. Ling, and A. Lozano, "Effect of antenna separation on the capacity of BLAST in correlated channels," *IEEE Communications Letters*, vol. 4, pp. 337 –339, Nov. 2000.

[170] S. Loyka, "Channel capacity of MIMO architecture using the exponential correlation matrix," *IEEE Communications Letters*, vol. 5, pp. 369 –371, Sept. 2001.

[171] E. G. Larsson and P. Stoica, *Space-Time Block Coding for Wireless Communications*. Cambridge, UK: Cambridge University Press, 2003.

[172] S. Sesia and I. Toufik and M. Baker, *LTE - the UMTS long term evolution: from theory to practice*. New York, USA: Wiley-IEEE Press, 2009.

[173] H. Wang, P. Li, and X. Lin, "Gain from antenna correlation in multi-user MIMO systems," in *Information Theory and Applications Workshop (ITA)*, (University of California, San Diego, USA), Feb. 2010.

[174] J. Akhtman and L. Hanzo, "Closed-form approximation of MIMO capacity," *Electronics Letters*, vol. 45, pp. 68–69, Jan. 2009.

# Index

# Author Index